

Manipulation and Simulation of Cold Atoms in Optical Lattices

DISSERTATION

zur Erlangung des akademischen Grades

Doktor der Naturwissenschaften

an der

Fakultät für Mathematik, Informatik und Physik

der

Leopold-Franzens-Universität Innsbruck

vorgelegt von

Andrew John Daley, MSc (Hons.)

Juli 2005

To my parents and my brothers.

ZUSAMMENFASSUNG

Kalte Atome in optischen Gittern haben ein großes Potenzial für die Untersuchung von stark korrelierten Systemen und für Anwendungen auf dem Gebiet der Quanteninformationsbearbeitung. Dieses System zeichnet sich insbesondere durch ein gutes Verständnis der mikroskopischen Dynamik und eine umfangreiche Kontrolle dieser Dynamik durch äußere Felder aus.

In dieser Dissertation werden zwei Hauptthemen behandelt. Das erste Thema befasst sich mit der Manipulation von Atomen in optischen Gittern, um folgende zwei Ziele zu erreichen: (i) Die Erzeugung von speziellen Vielteilchenzuständen, die als Ausgangspunkt für Anwendungen auf dem Gebiet der Quanteninformation oder für die Simulation von stark korrelierten Systemen benötigt werden, und (ii) die Bewegung der Atome im Gitter durch einen Mechanismus zu kühlen, der zu keiner Dekohärenz der internen Zustände führt. In diesem Zusammenhang werden zwei Methoden zur Präparation von reinen Zuständen vorgeschlagen. Eine Methode basiert auf einem kohärenten Filterprozess, die andere auf einem fehlertoleranten Schema, um Atome aus einem Reservoirgas, welches nicht im optischen Gitter gefangen ist, in das Gitter zu laden. Der Prozess des sympathetischen Kühlens, welches für die zweite Methode benützt wird, führt unter geeigneten Bedingungen auch zu einem raschen Kühlen der atomaren Bewegung, ohne dabei den internen Zustand zu beeinflussen.

Das zweite Hauptthema dieser Dissertation widmet sich der numerischen Berechnung der Vielteilchendynamik in optischen Gittern. Diese Dynamik ist im Allgemeinen analytisch nicht lösbar und kann mit traditionellen Methoden auch numerisch nur für kleine Systeme exakt berechnet werden. Durch die Adaption von erst kürzlich entwickelten numerischen Verfahren werden exakte zeitabhängige Berechnungen der Dynamik von Atomen in eindimensionalen optischen Gittern durchgeführt. Diese Verfahren stehen in Beziehung mit gängigen Density Matrix Renormalisation Group (DMRG) Methoden, welche zur Berechnung von Grundzuständen in eindimensionalen Systemen verwendet werden. Es wird gezeigt, dass die zeitabhängigen Algorithmen in existierenden DMRG Programme implementiert werden können.

Die numerischen Methoden werden zur Untersuchung des “Ein-Atom-Transistors” verwendet. In diesem System wird der Transport von Atomen durch ein einzelnes Störstellen-Atom geschaltet. Der Fluss der Atome durch die Störstelle zeigt eine signifikante Abhängigkeit von ihrer gegenseitigen Wechselwirkung, ein Effekt, der in einer experimentellen Realisierung dieses Systems direkt beobachtet werden kann.

ABSTRACT

Systems of cold atoms in optical lattices have a great deal of potential as tools in the study of strongly correlated condensed matter systems and in the implementation of quantum information processing. There exists both a good understanding of the microscopic dynamics in these systems, and extensive control over those dynamics via external fields.

In this thesis two primary issues are addressed. The first is the manipulation of atoms in optical lattice to achieve two goals: (i) the production of initial many-body states required for applications to strongly correlated systems and to quantum information processing, and (ii) cooling of the atoms in the lattice using a mechanism that does not cause decoherence for their internal states. In this context, two methods for preparation of high-fidelity patterns of atoms in optical lattices are proposed, one being a coherent filtering process that leaves single atoms in selected lattice sites, and the other a fault-tolerant scheme to load atoms from a reservoir gas, which is not trapped by the lattice. Under appropriate conditions, the sympathetic cooling process between the reservoir gas and lattice atoms that forms part of the second method gives rise to rapid cooling of the motional states of the atoms, without altering their internal states.

The second primary issue is the numerical computation of coherent many-body dynamics for atoms in optical lattices. These dynamics are generally intractable analytically, and can only be treated for very small systems by traditional exact numerical methods (in which the full Hilbert space is retained in the calculation). Through the adaption of recently proposed numerical methods, exact time dependent calculations for atoms in one dimensional optical lattices are performed. These methods are also related to the widespread Density Matrix Renormalisation Group (DMRG) methods, which are used to compute ground states for one dimensional systems, and it is shown that the time-dependent algorithms can be straightforwardly implemented in existing DMRG codes.

The numerical methods are applied in the study of the “Single Atom Transistor”, a system in which a single impurity atom is used to switch the transport of probe atoms in one dimension. We observe that the current of probe atoms passing the impurity depends significantly on interactions between the probe atoms, an effect which should be directly observable in experimental implementations of this system.

ACKNOWLEDGEMENTS

Living and studying in Austria for the last three years has been a wonderful experience for me: I don't believe that I could possibly have found somewhere that would have been better for me in terms of either physics or general life experiences, and I have a lot of people to thank for the part that they played in making this period a success. Unfortunately it is never possible in a short list of acknowledgements to thank everyone who deserves to be thanked, and I both apologise to and thank profusely the many people not listed here who have played a significant role during my time so far in Innsbruck.

Foremost, I would like to thank my supervisor, Peter Zoller, who gave me the opportunity to come to Innsbruck in the first place, who has given me the opportunity to partake in many interesting projects, and who has spent large amounts of time guiding me and discussing work related to those projects. He has taught me a lot of physics and a lot about how to approach the systems we study, and the work contained in this thesis strongly reflects his creativity and insight.

I have had the opportunity to collaborate with many other physicists over the last three years, and I would especially like to thank my co-authors on the publications contained in this thesis, Peter Rabl, Peter Fedichev, Ignacio Cirac, Andi Micheli, Andi Griessner, Dieter Jaksch, Ulrich Schollwöck, Corina Kollath, Guifré Vidal, and Stephen Clark for their part in these projects. I have also had very fruitful discussions and collaborations on work contained in this thesis with Hans-Peter Büchler and Adrian Kantian; and I would particularly like to thank Andi Griessner, Adrian Kantian, Peter Rabl, Viktor Steixner, Dunja Peduzzi and Anna Renzl for their help in proof-reading parts of this thesis.

I also enjoyed the stimulating discussions I have had with experimentalists in our field, particularly those with members of Rudi Grimm and Rainer Blatt's groups here in Innsbruck (especially Selim Jochim, Markus Bartenstein, Johannes Hecker-Denschlag, Florian Schreck, and Eric Wille), with Immanuel Bloch and his coworkers from the University of Mainz, with Trey Porto at NIST in Gaithersburg, Giovanni Modugno and Massimo Inguscio from LENS in Firenze, and Tilman Esslinger and his co-workers at the ETH in Zürich.

Over the last three years our research group has been an extremely stimulating and enjoyable environment in which to work. In alphabetical order, I would like to thank Michiel Bijlsma (whose arrival in Innsbruck was a comedy of errors), Hans-Peter Büchler (who offered his flat for our Lord of the Rings marathon), Tommaso Calarco (the only person I know who can obtain free entry to art galleries in Firenze), Uwe Dorner (the first person I met after I got off the plane here, he will do most things for Weissbier), Peter Fedichev (who knows more

about the NZ defence forces than me), Andi Griessner (who played squash and explored Oxford with me), Dieter Jaksch (who told me that if I worked 60 hours a week I would be finished inside three years), Konstanze Jähne (who always smiles at my jokes), Adrian Kantian (who introduced me to real chocolate), Andi Micheli (who has regular coffee breaks at half past one in the morning), Sarah Morrison (who put up with my Australian jokes and linguistic sense of humour), Peter Rabl (who won our Stadtlauf competition for the “Diplom Students”), Alessio Recati (who discovered Japan with me), and Viktor Steixner (who despite being a mountain-person explored the coast of Corsica with me) for their discussions on physics and their friendship during my time as a student here.

I would like also to thank Marion Grünbacher and Nicole Jorda for their help with many practical and administrative matters over the last three years, as well as Hans Embacher, Julio Lamas-Knapp, and Thomas Mayr for their organisation of the computer systems here, and Markus Knabl for his organisation of our move to the new academy institute.

I have had many opportunities to partake in activities outside of physics, and I would especially like to thank the members of the Musikkapelle Allerheiligen for showing me a side of Tirolean culture that no tourist ever has the opportunity to see, and the Innsbruck Uni Big Band for giving me the opportunity to return to my favourite form of performance music.

It is, a priori, not easy for a New Zealander (an extra-hemispherical!) to come to the middle of Europe, to a country where he does not speak the native language, and to live there for three years whilst studying for a PhD. That I have enjoyed my time so much here is a tribute to the many extremely kind people I have met here during my time in Innsbruck, both inside and outside physics. I do not have space to begin to thank every one of these people, but would particularly like to mention Martina DeMattio, Elisa Vianello, Régis Danielian, Petra Weiler, Viktor Steixner, Andi Griessner, Peter Rabl, Helga Richter, and Simon Bailey for their friendship, support, and sanity (of sorts) during a substantial part of my time as a student here. I would also like to thank my friends in New Zealand who have kept in contact and (in some cases!) even visited me here in Innsbruck.

That I chose to study for a PhD was the result of five and a half stimulating years in the Physics department at the University of Auckland, which convinced me of my strong interest in this subject, and my choice to come to Innsbruck was also the result of much advice I was given by people in Auckland. For this I would especially like to thank Scott Parkins, who was a wonderful MSc supervisor, and who both recommended Peter Zoller’s group to me and helped me immensely in making my decision to come here. I would also like to thank Peter Wills, Paul Barker, Matthew Collett, and Rainer Leonhardt, without whose encouragement and convincing arguments I may not have had the courage to come to a country where English is not the native language. I also thank all my enthusiastic teachers, colleagues, and supervisors who inspired me to study for a PhD in physics, and particularly, in addition to the people I have already named in this paragraph, Gary Bold, Sze Tan, Tom Barnes, Chris Tindle, Steve Buckman, and the late Tom Rhymes.

And, finally, but most importantly, I could not be where I am today without the enormous amount of support and love that my parents, Paul and Robyn, and my brothers, Chris and Nic, have given me over the last $26\frac{1}{2}$ years. This thesis is dedicated to them, for being the best, most caring and supportive family anyone could ever have.

Andrew Daley, July 4, 2005.

CONTENTS

Zusammenfassung	v
Abstract	vii
Acknowledgments	ix
Contents	xi
I Introduction	1
Chapter 1. General Introduction	3
Chapter 2. Background: Cold Atoms in Optical Lattices	13
2.1 Optical Lattices	13
2.1.1 Periodic Potential	14
2.1.2 Spontaneous Emissions	15
Blue-detuned lattices	16
Red-detuned lattices	16
2.2 Bloch Waves	16
2.2.1 Band Structure	17
2.2.2 Wannier Functions	17
2.3 The Bose-Hubbard Model	19
2.3.1 Derivation of the Bose-Hubbard Hamiltonian	19
2.3.2 Basic Properties of the Bose-Hubbard Model	22
2.4 The Hubbard Model for Fermions	23
2.5 Spin-Dependent Optical Lattices	23

II Manipulation of Atoms in Optical Lattices	27
Chapter 3. Manipulation of Cold Atoms in an Optical Lattice	29
3.1 Coherent Laser-Assisted Filtering of Atoms	29
3.1.1 Adiabatic Transfer	30
3.2 Sympathetic Cooling of Atoms in an Optical Lattice by a Cold Reservoir	31
3.3 Dissipative loading of Fermions	31
Chapter 4. Publication: Defect-Suppressed Atomic Crystals in an Optical Lattice	33
Chapter 5. Publication: Single Atom Cooling by Superfluid Immersion	41
5.1 Introduction	41
5.2 Overview	42
5.3 The Model	45
5.3.1 Avoiding Decoherence	45
5.3.2 Hamiltonian for the Oscillator-Superfluid Interaction	46
5.3.3 Damping Equations	47
5.3.4 Supersonic and Subsonic Motion Regimes	49
5.4 Results	50
5.4.1 Supersonic Case	50
5.4.2 Subsonic Case	52
5.4.3 Finite Temperature Effects	55
5.5 Decoherence for non-symmetric interactions	56
5.6 The Semi-Classical Approximation	60
5.6.1 Supersonic Case	60
5.6.2 Subsonic Motion	63
5.7 Immersion in a Strongly Correlated 1D Superfluid	64
5.8 Summary	66
5.A Foreign Particle in a Superfluid	67
5.B Derivation of the Master Equation	68
5.C Estimation of $\delta\hat{\Psi}^\dagger\delta\hat{\Psi}$ Terms	69

Chapter 6. Publication: Dissipative Preparation of Atomic Quantum Registers	75
6.1 Introduction	75
6.2 Laser-Assisted Loading	78
6.2.1 The Model	78
6.2.2 The Fast and Slow Loading Regimes	80
6.2.3 Analysis of the Loading Regimes	82
Fast Loading Regime	82
Slow Loading Regime	84
6.3 Cooling Atoms to the Lowest Band	89
6.4 Combined Process	91
6.5 Summary	93
6.A Heisenberg Equations for Coherent Loading	93
6.B Derivation of the Master Equation	94
6.C Equations of motion for Combined Dynamics	95
III Exact Time-Dependent Simulation of Many Atoms in 1D Optical Lattices	99
Chapter 7. Exact Calculations for 1D Many-Body Systems using Vidal's Algorithm	101
7.1 Time-Dependent Calculations for 1D Systems	101
7.2 Vidal's State Representation	102
7.2.1 Schmidt Decompositions	103
7.2.2 The State Decomposition	104
7.2.3 Use and Validity of Truncated Decompositions	105
7.3 Vidal's TEBD Algorithm	106
7.3.1 Single-Site Operations	107
7.3.2 Two-Site Operations	107
7.3.3 Coherent Time Evolution of a State	108
7.3.4 Finding Initial States	109
Imaginary Time Evolution: Non-conservation of good quantum numbers	109
Imaginary Time Evolution: Orthogonalisation	109
Imaginary Time Evolution: Testing the Ground State	110
7.4 Implementation of the Algorithm	111
7.4.1 Choosing simulation parameters	111

Chapter 8. Extensions to the Method and Short Examples	113
8.1 Calculating Correlation Functions	113
8.2 Conserved Quantities and Vidal's Algorithm	115
8.3 Superfluid and MI Ground States in 1D	116
8.3.1 Box Trap	116
8.3.2 Harmonic Trap	118
8.4 Time Dependence of the MI-Superfluid Transition	120
Chapter 9. Publication: Adaptive time-dependent DMRG	123
9.1 Introduction	124
9.2 Time-dependent simulation using DMRG	126
9.3 Matrix product states	131
9.4 TEBD Simulation Algorithm	133
9.5 DMRG and matrix-product states	138
9.6 Adaptive time-dependent DMRG	141
9.7 Case study: time-dependent Bose-Hubbard model	142
9.8 Conclusion	147
IV A Single Atom Transistor in a 1D Optical Lattice	151
Chapter 10. The Single Atom Transistor: Introduction	153
Chapter 11. Publication: A Single Atom Transistor in a 1D Optical Lattice	155
Chapter 12. Publication: Numerical Analysis of Many-Body Currents in a SAT	165
12.1 Introduction	165
12.2 Overview	167
12.2.1 The Single Atom Transistor	167
The System	167
Single Atoms	168
Many Atoms	169
12.2.2 Atomic Currents through the SAT	169
12.2.3 Time-Dependent Numerical Algorithm for 1D Many-Body Systems	171

12.3	Numerical Results	172
12.3.1	Time Dependence of the current for bosonic probe atoms	173
12.3.2	Diffusive evolution, with initial mean momentum ($\langle \hat{k} \rangle_{t=0} = 0$)	176
	Dependence of the current on impurity-probe coupling, Ω	176
	Dependence of the current on interaction strength, U/J	176
	Dependence of the current on initial density, n	179
12.3.3	Kicked evolution, with initial mean momentum ($\langle \hat{k} \rangle_{t=0} \neq 0$)	179
	Dependence of the current on kick strength p_k	179
	Dependence of the current on impurity-probe coupling, Ω	182
12.4	Summary	182
Chapter 13. Future Directions		185
Curriculum Vitae		187

Part I

Introduction

CHAPTER 1

GENERAL INTRODUCTION

Cold Atoms

The first realisations of Bose-Einstein Condensation (BEC) [1–5] in dilute gases in 1995 [6–8] opened a myriad of opportunities to study quantum phenomena on a macroscopic scale. These opportunities arise from the three distinguishing properties of the BEC experiments: (i) That we have a detailed microscopic (Hamiltonian) description of the experimental system; (ii) That we have extensive control over the parameters of the system via external fields; and (iii) That we can probe both the spectroscopic and coherent properties of the system in unprecedented detail, e.g., via density measurements and interference experiments.

During the past ten years, over fifty experiments in this field have been developed, using a variety of atomic species (to date, Bose Einstein Condensates (BECs) had been produced in the atomic species of Rubidium, Sodium, Lithium, Hydrogen, metastable Helium, Potassium, Caesium, Ytterbium, and Chromium). The experiments use laser cooling techniques [9] and evaporative cooling [10] to obtain temperatures on the scale of a few nanoKelvin or microKelvin required for BEC at the typical densities found in the experiment, $\sim 10^{13} - 10^{15} \text{cm}^{-3}$. Through such work, fundamental progress has been made in the study of many phenomena, including atomic and molecular collisional properties [11], superfluid properties (e.g., vortices and vortex arrays), aspects of matter-wave coherence (e.g., interference experiments, and coupled BECs acting as a Josephson Junction), and collective excitations in trapped Bose gases.

More recently, there has also been extensive progress in the study of degenerate Fermi gases in similar experiments [12–19], where laser cooling can be followed either by sympathetic cooling of the Fermi gas with a BEC, or via evaporative cooling if more than one fermionic species is present. Typical densities reached are $\sim 10^{13} - 10^{14} \text{cm}^{-3}$, which are smaller than for Bosons due to the Fermi pressure of the gases. These systems exhibit the same level of controllability found for trapped Bosons.

For both Bosons and Fermions, magnetic [20] and optical [21] Feshbach resonances make it possible to modify the strength of collisional interactions by providing effective off-resonant coupling into a bound molecular state. By ramping the effective detuning of the atomic state from the molecular state across the resonance, ultra-cold molecules can be formed from pairs of atoms. In two-component Fermi gases, these molecules have been observed to condense and form a molecular BEC [16–19].

The dilute gases in experiments are weakly interacting, which has contributed to the success in using these systems to study superfluid properties and coherence properties. However, it also leads to questions as to how to use these systems for wider applications, especially to investigate strongly correlated systems that are of particular interest in modern condensed matter physics and, potentially, to allow the engineering of entanglement and quantum information processing.

Optical Lattices

As was first discussed by Jaksch et. al [22] and demonstrated by Greiner et al. [23], strongly correlated systems can be engineered with cold gases by loading them into an optical lattice. Such lattices are formed by standing waves of laser light in three dimensions (see chapter 2), and the resulting atomic dynamics are described by Hubbard-type lattice models, which can be reduced or extended in an experiment form many different spin and lattice models of interest in condensed matter physics.

The available control over the system means that these Hamiltonians can be engineered in experiments with unprecedented control over most relevant parameters. Combined with the many accessible measurement techniques, this allows investigations of these models that would be impossible if the same system were realised in traditional condensed matter experiments. In addition, the same setup offers many possibilities to engineer entanglement and has potential applications in quantum computing.

Using different combinations of optical lattice parameters and external fields, there exists a veritable toolbox of techniques with which to control the dynamics of atoms in optical lattices [24]. For example, interaction energies in the system can be controlled by varying the depth of the lattice, as deeper lattices lead both to lower tunnelling rates between lattice sites, and to tighter on-site confinement and hence stronger interactions amongst multiple atoms on a single site. These interactions can then be further tailored using optical [21] and magnetic [20] Feshbach resonances [25] to control the interatomic interactions, as in other cold gases experiments. The laser setups used to produce optical standing waves are themselves very versatile, potentially allowing the creation of many different lattice geometries by repositioning the standing waves that form the lattice (e.g., it is relatively straightforward to produce either triangular lattices [24] or Kagomé lattices [26] in this manner). By making lattices very deep in a particular dimension (or two dimensions) compared with other energy scales in the system, it is even possible to restrict the system to the ground state in that dimension, making the system behave as an effective 2D or 1D system, as has been demonstrated in experiments [27, 28]. Whilst optical lattice potentials are normally extremely uniform, it is also possible to offset the energy of particular lattice sites by applying commensurate superlattices [29], or to produce pseudo-random disorder in the lattice by applying a non-commensurate superlattice. Better random disorder could also be deliberately generated in these systems, either by adding a laser speckle pattern, or via the introduction of an additional atomic species. By including several species simultaneously in the lattice, many different models can be generated, and the standing wave detuning can be used to make the parameters species-dependent. For two internal states of the same atomic species, spin-dependent optical lattices can also be produced by manipulating the polarisation of the laser light [30].

Similarly, there are many possibilities for making measurement on systems of atoms in optical lattices, including measurement of interference patterns when atoms are released from the lattice [23], and coincidence detection [31, 32] for density-density correlation functions. There are also proposals for measuring various properties of spin systems on a lattice [33].

This range of techniques finds many important applications in the study of models from condensed matter physics. In addition to the original realisation of the superfluid-Mott Insulator transition in the Bose-Hubbard model [23], various properties of the Fermi Hubbard model [34], and of strongly correlated systems of 1D Bosons (in the Tonks gas limit) [27, 28] have been observed in experiments. Many theoretical proposals exist for applying these techniques to other lattice and spin systems. These include aspects of spin models with interesting phases in various lattice configurations [35–37], the Kondo and other similar impurity problems [38, 39], spin glass systems [40], lattice gauge theories [41], and properties of Luttinger liquids [42]. There are also proposals for the implementation of effective magnetic fields [43], the study of superfluidity of fermions [44], and the investigation of complicated phases that arise from Bose-Fermi mixtures in optical lattices [45–47]. In addition, many other so-called toy models of condensed matter physics, which describe phenomena that are yet to be properly understood, could be implemented. These include models for important problems such as high T_C superconductivity, and experimental implementations of these models would allow investigation of properties that are analytically inaccessible.

One major difference between atoms in optical lattices and most systems in condensed matter physics is their excellent isolation from their environment, which leads to coherent dynamics on long timescales. For example, the timescale for spontaneous emission events, one of the dominant sources of decoherence, can be made of the order of seconds in these systems (see chapter 2). Such long coherence times can be utilised for the implementation of quantum information processing [48, 49], and several proposals exist for engineering entanglement with systems of atoms in optical lattices. Mostly, these take qubit states to be two long-lived internal states of atoms localised at each site in a deep lattice. This is inherently scalable, as a large array of atoms, with a single atom each lattice site, can be produced either for Bosons (in the Mott Insulator regime [22]) or for Fermions (by using Pauli blocking to prevent double-occupation [50]). Gate operations in this system can be performed via collisional [51, 52] or dipole interactions [53] between the atoms themselves. Entanglement of a large array of atoms via controlled collisions has already been performed in an experiment [30], producing a 1D version of the so-called cluster state required for measurement-based quantum computing schemes [54]. Other gate schemes have also been proposed, based, for example, on the tunnelling of atoms between neighbouring sites [55, 56], on the motional states of atoms [57], or on strong dipole-dipole interactions between Rydberg atoms [58]. At the present time, individual addressing of atoms in particular sites presents the greatest difficulty in implementing general purpose quantum computing in optical lattices, although there are several possibilities to overcome this problem in the future, such as a scheme using marker atoms [59]. However, the most immediate application of atoms in optical lattices to quantum computing is as a quantum simulator [60]. This is the role already described above, in which we use atoms in optical lattices to simulate lattice models from condensed matter physics.

Manipulation and Simulation

Thus, atoms in optical lattices provide us with the means to investigate previously intractable many body problems, and to engineer entangled states that could be used for quantum computation. However, engineering the appropriate Hamiltonian dynamics is not sufficient to properly study strongly correlated systems or to perform quantum information processing. In addition, extensive quantum control over atoms is required to prepare initial states and to correct for imperfections that occur during experiments. For example, in order to simulate strongly correlated systems, we must prepare sufficiently cold initial states with chosen filling factors in the lattice and control additional defects in that state. To prepare an atomic qubit register for quantum computation, we must ensure that we have a single atom in every lattice site; and to perform quantum computation, we must have a way of repeatedly cooling the system without destroying information encoded on the atomic qubits.

Manipulation of atoms in optical lattices in this manner is addressed in Part II of this thesis. Here, two schemes for initial state preparation and a scheme for sympathetic cooling of atoms in the lattice are presented. The first state preparation scheme consists of a laser-assisted coherent filtering scheme, which, beginning from a state with more than one atom per lattice site and a low probability of zero-occupation, produces a high-fidelity state of one atom in every lattice site. This scheme can be extended to produce essentially arbitrary patterns of atoms loaded into an optical lattice, and examples are given of the use of this scheme to produce a BCS state for fermions with a chosen filling factor. The second preparation scheme achieves a similar goal, but instead of utilising a coherent single-shot process, it includes an irreversible step. This makes it possible to prepare a state with the probability for there being one fermion per site in the lowest Bloch band of the lattice improves in time in a fault-tolerant manner. The dissipative process used as part of this preparation scheme is the cooling of atoms within the lattice by creation of excitations in an cold reservoir gas, which is not trapped by the lattice. This setup is introduced in the cooling scheme of Part II, which was originally proposed as a means to cool the motional state of atomic qubits in an optical lattice without causing decoherence for the information encoded on their internal states. As demonstrated by its application in the fault-tolerant loading scheme, this dissipative process has wider applications, which are discussed briefly in chapter 13.

Another complication with atoms in optical lattices is in the theoretical analysis of the coherent many-body dynamics, which are often analytically intractable, and can only be treated exactly numerically for very small systems (when traditional techniques involving dynamics computed on the full Hilbert space are used). However, in many cases it is very useful to have insight into these dynamics in experimentally relevant situations, e.g., to compute the state prepared as the result of a particular Hamiltonian time evolution, or to predict basic properties of systems that can be measured in the laboratory.

Simulation of systems of atoms in a 1D optical lattice is addressed in parts III and IV of this thesis. We make use of a new simulation method proposed by Vidal [61, 62], which makes possible the exact computation of time evolutions for low energy states of 1D systems. This is achieved by adaptively selecting a reduced Hilbert space, in a manner related to similar algorithms proposed by Verstrate and Cirac [63, 64], uses similar formalisms to those used in Density Matrix Renormalisation Group (DMRG) methods [65] (see chapter 7 for more historical and technical details). We apply this algorithm to study the lattice models that

describe systems of cold atoms in 1D lattices, as well as providing extensions and optimisations of the simulation algorithm which are important in this context. We also discuss formally the relationship between Vidal’s algorithm and DMRG and explain how Vidal’s algorithm can be incorporated directly within widespread existing implementations of DMRG methods.

We apply these time-dependent simulation methods to the study of a “Single Atom Transistor” (SAT), in which a single impurity atom can be used to switch the transport of a many-body system of probe atoms. To complement analytical calculations for non-interacting Fermions and for single atoms, we compute the atomic currents past the impurity atom, and find interesting effects that derive from interactions between the probe atoms. Using the numerical methods we are able to make quantitative predictions for currents that would be directly measurable in an experimental implementation of the SAT.

This thesis is thus focussed on techniques to manipulate atoms in optical lattices, and techniques to simulate their dynamics. The resulting state preparation and cooling techniques, as well as the results from our numerical simulations have significant applications in the context of present experimental systems; applications which are intended to enhance the application of atoms in optical lattices both to the study of strongly correlated systems, and to quantum information processing.

Overview

This thesis contains six articles, together with additional chapters that give extra information on the background and details of the article. At the beginning of each article, there is a short note indicating the primary contributions of the author of this thesis to that article.

Part I of this thesis provides an introduction to systems of cold atoms in optical lattices. This general introduction is completed in chapter 2, which gives the technical background for these systems, and for the Hubbard and Bose-Hubbard models that describe their dynamics.

In Part II of the thesis, *Manipulation of Cold Atoms in Optical Lattices*, we elaborate on the schemes mentioned above for initial state preparation and sympathetic cooling of atoms in optical lattices. The introduction in chapter 3 is followed by three publications. The first, in chapter 4, *Defect-Suppressed Atomic Crystals in and Optical Lattice*, describes the production of high-fidelity patterns of atoms by means of a laser-assisted coherent filtering scheme. The second, in chapter 5, *Single Atom Cooling by Superfluid Immersion: A Non-Destructive Method for Qubits*, discusses a scheme to cool the motional states of atoms in an optical lattice without causing decoherence for the internal states. The third, in chapter 6, *Fault-Tolerant Dissipative Preparation of Atomic Quantum Registers with Fermions*, gives an alternative application for the cooling scheme discussed in chapter 5, in which creation of excitations in an external reservoir is used as a dissipative process that gives rise to a fault-tolerant loading scheme.

In Part III of the thesis, *Exact Time-Dependent Simulation of Many Atoms in 1D Optical Lattices*, we discuss the exact numerical computation of coherent many-body dynamics for atoms in optical lattices. Chapter 7 details the background of Vidal’s algorithm essentially as it was originally presented, together with some comments on its practical implementation. Chapter 8 discusses extensions to the method that have been implemented, and provides

two simple example calculations illustrating the power of the algorithm. Chapter 9 is then a publication, *Time-dependent density-matrix renormalisation-group using adaptive effective Hilbert spaces*, which discusses the relationship between Vidal's algorithm and DMRG, and provides a prescription for users of existing DMRG implementations to extend these to time-dependent calculations in a straight-forward manner.

In Part IV, *A Single Atom Transistor in a 1D Optical Lattice*, we use these simulation methods as part of the investigation of the Single Atom Transistor system. After a brief introduction in chapter 10, two publications are presented. Chapter 11, *A Single Atom Transistor in a 1D Optical Lattice* details the system and its basic properties, whilst chapter 12, *Numerical Analysis of Coherent Many-Body Currents in a Single Atom Transistor* provides more details on the application of the simulation methods from part III, and gives further examples of interaction effects on the many-body currents through the SAT.

The thesis concludes with an outline of future directions for this work in chapter 13.

Bibliography

- [1] L. Pitaevskii and S. Stringari, *Bose-Einstein Condensation*, (Oxford University Press, Oxford, 2003).
- [2] C. Pethick and H. Smith, *Bose-Einstein Condensation in Dilute Gases*, (Cambridge University Press, Cambridge, 2001).
- [3] For a review see *Nature* **416**, 205 [Insight section] (2002).
- [4] F. Dalfovo, S. Giorgini, L. Pitaevskii and S. Stringari, *Rev. Mod. Phys.* **71**, 463 (1999).
- [5] A. Leggett, *Rev. Mod. Phys.* **73**, 307 (2001).
- [6] M. H. Anderson, J. R. Ensher, M. R. Matthews, C. E. Wieman, and E. A. Cornell, *Science* **269**, 198 (1995).
- [7] K. B. Davis, M.-O. Mewes, M. R. Andrews, N. J. van Druten, D. S. Durfee, D. M. Kurn, and W. Ketterle, *Phys. Rev. Lett.* **75**, 3969 (1995).
- [8] C. C. Bradley, C. A. Sackett, J. J. Tollett, and R. G. Hulet, *Phys. Rev. Lett.* **75**, 1687 (1995); C. C. Bradley, C. A. Sackett, and R. G. Hulet, *Phys. Rev. Lett.* **78**, 985 (1997).
- [9] See, for example, H. J. Metcalf and P. van der Straten, *Laser Cooling and Trapping*, (Springer-Verlag, New York, 1999).
- [10] For a review see W. Ketterle and N. J. van Druten, *Adv. At. Mol. Opt. Phys.* **37**, 181 (1996).
- [11] For a review on ultracold collisions, see J. Weiner, V. S. Bagnato, S. Zilio, and P. S. Julienne, *Rev. Mod. Phys.* **71**, 1 (1999).
- [12] B. DeMarco and D. S. Jin, *Science* **285**, 1703 (1999).
- [13] G. Roati, F. Riboli, G. Modugno, and M. Inguscio, *Phys. Rev. Lett.* **89**, 150403 (2002).

- [14] K. E. Strecker, G. B. Partridge, and R. G. Hulet, *Phys. Rev. Lett.* **91**, 080406 (2003).
- [15] J. Kinast, S. L. Hemmer, M. E. Gehm, A. Turlapov, and J. E. Thomas, *Phys. Rev. Lett.* **92**, 150402 (2004).
- [16] S. Jochim, M. Bartenstein, A. Altmeyer, G. Hendl, S. Riedl, C. Chin, J. Hecker Denschlag, and R. Grimm, *Science* **302**, 2101 (2003).
- [17] M. Greiner, C. A. Regal, and D. S. Jin, *Nature* **426**, 537 (2003).
- [18] M. W. Zwierlein, C. A. Stan, C. H. Schunck, S. M. F. Raupach, S. Gupta, Z. Hadzibabic, and W. Ketterle *Phys. Rev. Lett.* **91**, 250401 (2003).
- [19] T. Bourdel, L. Khaykovich, J. Cubizolles, J. Zhang, F. Chevy, M. Teichmann, L. Tarruell, S. J. J. M. F. Kokkelmans, and C. Salomon, *Phys. Rev. Lett.* **93**, 050401 (2004).
- [20] See, for example, E. A. Donley, N. R. Claussen, S. T. Thompson, and C. E. Wieman, *Nature* **417**, 529 (2002); T. Loftus, C. A. Regal, C. Ticknor, J. L. Bohn, and D. S. Jin, *Phys. Rev. Lett.* **88**, 173201 (2002).
- [21] M. Theis, G. Thalhammer, K. Winkler, M. Hellwig, G. Ruff, R. Grimm, J. Hecker Denschlag, *Phys. Rev. Lett.* **93**, 123001 (2004).
- [22] D. Jaksch, C. Bruder, J. I. Cirac, C. W. Gardiner, and P. Zoller, *Phys. Rev. Lett.* **81**, 3108 (1998).
- [23] M. Greiner, O. Mandel, T. W. Hänsch and I. Bloch *Nature* **415**, 39 (2002); M. Greiner, O. Mandel, T. Esslinger, T.W. Hänsch and I. Bloch, *Nature* **419** 51 (2002).
- [24] For a review on techniques for manipulating atoms in optical lattices, see D. Jaksch and P. Zoller, *Annals of Physics* **315**, 52 (2005), and references therein.
- [25] E. L. Bolda, E. Tiesinga, and P. S. Julienne, *Phys. Rev. A* **66**, 013403 (2002).
- [26] For example see L. Santos, M. A. Baranov, J. I. Cirac, H.-U. Everts, H. Fehrmann, and M. Lewenstein, *Phys. Rev. Lett.* **93** 030601 (2004).
- [27] T. Stöferle, H. Moritz, C. Schori, M. Köhl, and T. Esslinger, *Phys. Rev. Lett.* **92**, 130403 (2004).
- [28] B. Paredes, A. Widera, V. Murg, O. Mandel, S. Fölling, I. Cirac, G. V. Shlyapnikov, T. W. Hänsch, and I. Bloch, *Nature* **429**, 277 (2004).
- [29] S. Peil, J. V. Porto, B. Laburthe Tolra, J. M. Obrecht, B. E. King, M. Subbotin, S. L. Rolston, and W. D. Phillips, *Phys. Rev. A* **67**, 051603(R) (2003).
- [30] O. Mandel, M. Greiner, A. Widera, T. Rom, T. W. Hänsch, and I. Bloch, *Phys. Rev. Lett.* **91**, 010407 (2003).
- [31] S. Fölling, F. Gerbier, A. Widera, O. Mandel, T. Gericke and I. Bloch, *Nature* **434**, 481 (2005).

-
- [32] E. Altman, E. Demler, and M. D. Lukin, Phys. Rev. A **70**, 013603 (2004).
- [33] J. J. Garcia-Ripoll M. A. Martin-Delgado, and J. I. Cirac, Phys. Rev. Lett. **93**, 250405 (2004).
- [34] M. Köhl, H. Moritz, T. Stöferle, K. Günter, and T. Esslinger, Phys. Rev. Lett. **94**, 080403 (2005).
- [35] A. Sorensen and K. Molmer, Phys. Rev. Lett. **83**, 2274 (1999).
- [36] L.-M. Duan, E. Demler and M. Lukin, Phys. Rev. Lett. **91**, 090402 (2003).
- [37] J.K. Pachos and M.B. Plenio, Phys. Rev. Lett. **93**, 056402 (2004).
- [38] L.-M. Duan, Europhys. Lett., **67**, 721 (2004).
- [39] B. Paredes, C. Tejedor, and J. I. Cirac, Phys. Rev. A **71**, 063608 (2005).
- [40] B. Damski, J. Zakrzewski, L. Santos, P. Zoller, M. Lewenstein, Phys. Rev. Lett. **91**, 080403 (2003).
- [41] H. P. Büchler, M. Hermele, S. D. Huber, M. P. A. Fisher, and P. Zoller, Phys. Rev. Lett., in press, (e-print cond-mat/0503254).
- [42] B. Paredes and J.I. Cirac, Phys. Rev. Lett. **90**, 150402 (2003).
- [43] D. Jaksch and P. Zoller, New J. Phys. **5**, 56 (2003).
- [44] W. Hofstetter, J. I. Cirac, P. Zoller, E. Demler, and M. D. Lukin, Phys. Rev. Lett. **89**, 220407 (2002).
- [45] M. Lewenstein, L. Santos, M. Baranov and H. Fehrmann, Phys. Rev. Lett. **92**, 050401 (2004).
- [46] R. Roth and K. Burnett, Phys. Rev. A **69** 021601(2004).
- [47] H. Büchler and G. Blatter, Phys. Rev. A **69**, 063603 (2004).
- [48] M. A. Nielsen and I. L. Chuang, *Quantum Computation and quantum communication*, (Cambridge University Press, Cambridge, 2000).
- [49] *Experimental Quantum Computation and Information*, Proceedings of the International School of Physics “Enrico Fermi”, Course CXLVIII (IOS Press, Amsterdam, 2002).
- [50] L. Viverit, C. Menotti, T. Calarco, A. Smerzi, Phys. Rev. Lett. **93**, 110401 (2004).
- [51] D. Jaksch, H.-J. Briegel, J. I. Cirac, C. W. Gardiner, and P. Zoller, Phys. Rev. Lett. **82**, 1975 (1999).
- [52] T. Calarco, H.-J. Briegel, D. Jaksch, J.I. Cirac, and P. Zoller, Fortschr. Phys. **48**, 945 (2000).
- [53] G. K. Brennen, C. M. Caves, P. S. Jessen, and I. H. Deutsch, Phys. Rev. Lett. **82**, 1060 (1999); G. K. Brennen, I. H. Deutsch, and P. S. Jessen, Phys. Rev. A **61**, 62309 (2000).

-
- [54] R. Raussendorf and H. J. Briegel, Phys. Rev. Lett. **86**, 5188 (2001).
- [55] J. Mompart, K. Eckert, W. Ertmer, G. Birkel, and M. Lewenstein, Phys. Rev. Lett. **90**, 147901 (2003).
- [56] J. K. Pachos and P. L. Knight, Phys. Rev. Lett **91** 107902 (2003).
- [57] E. Charron, E. Tiesinga, F. Mies, and C. Williams, Phys. Rev. Lett **88**, 077901 (2002).
- [58] D. Jaksch, J. I. Cirac, P. Zoller, S. Rolston, R. Côté, and M. D. Lukin, Phys. Rev. Lett. **85** 2208 (2000).
- [59] T. Calarco, U. Dorner, P. Julienne, C. Williams, P. Zoller, Phys. Rev. A **70**, 012306 (2004).
- [60] E. Jane, G. Vidal, W. Dür, P. Zoller, and J. I. Cirac, Quantum Inform. Comput. **3**, 15 (2003).
- [61] G. Vidal, Phys. Rev. Lett. **91**, 147902 (2003); G. Vidal, Phys. Rev. Lett. **93**, 040502 (2004).
- [62] M. Zwolak and G. Vidal, Phys. Rev. Lett. **93**, 207205 (2004).
- [63] F. Verstraete, J. J. Garcia-Ripoll, and J. I. Cirac, Phys. Rev. Lett. **93**, 207204 (2004).
- [64] F. Verstraete, and J. I. Cirac, cond-mat/0407066.
- [65] S. R. White, Phys. Rev. Lett. **69**, 2863 (1992); S. R. White, Phys. Rev. B **48**, 10345 (1993); U. Schollwöck, Rev. Mod. Phys., **77**, 259 (2005).

CHAPTER 2

BACKGROUND: COLD ATOMS IN OPTICAL LATTICES

As discussed in chapter 1, the recent success of systems in optical lattices has been the possibility to take a relatively uncomplicated physical system and use it to engineer important model Hamiltonians, especially the Bose-Hubbard and Hubbard models. In this chapter the fundamental physics of these systems is outlined, beginning with the basic properties of cold atoms in an optical standing wave, and proceeding to the Wannier basis description and the derivation of the Bose-Hubbard model. The basic properties of this model are also discussed.

2.1 Optical Lattices

We begin by considering the basic physics of an atom coupled to classical, single-mode laser light with wavenumber k_l and frequency ω_l , forming a standing wave in 1D, as depicted schematically in Fig. 2.1. The atom is initially in an electronic ground state $|g\rangle$, and this state is coupled by the laser light to an excited internal state $|e\rangle$. We assume that the frequency ω_l is sufficiently far from the frequencies required to couple $|g\rangle$ to internal states other than $|e\rangle$, that intensity of the light is sufficiently weak so that other internal states do not play a role in the dynamics and may be eliminated in perturbation theory. (In practice we will use far detuned laser light for an optical lattice, in which case the resulting potential will be a sum over contributions from all excited states. See the paragraph at the end of section 2.1.1.) The energy difference between the states $|e\rangle$ and $|g\rangle$ is $\hbar\omega_{eg}$. In the interaction picture, the behaviour of the system, including the motion of the atom and spontaneous emissions of photons from the atom in the state $|e\rangle$, is described by the stochastic Schrödinger equation [1, 2] (with $\hbar \equiv 1$),

$$d|\Psi(t)\rangle = \left(-i\hat{H}_{\text{eff}}dt + \sqrt{\Gamma} \int_{-1}^1 du \sqrt{N(u)} e^{-ik_{eg}u\hat{x}} d\hat{B}_u^\dagger(t) |g\rangle\langle e| \right) |\Psi(t)\rangle, \quad (2.1)$$

$$\hat{H}_{\text{eff}} = \frac{\hat{p}^2}{2m} + \left(\delta - i\frac{\Gamma}{2} \right) |e\rangle\langle e| - \frac{\Omega(\hat{x})}{2} (|g\rangle\langle e| + |e\rangle\langle g|). \quad (2.2)$$

Here, the effective Hamiltonian \hat{H}_{eff} consists of three parts: The kinetic energy term, where \hat{p} is the momentum operator, and m is the atomic mass; a term accounting for the detuning, $\delta = \omega_l - \omega_{eg}$, of the laser from resonance, and the influence of spontaneous emissions with rate Γ ; and a term describing the coupling of the states $|g\rangle$ and $|e\rangle$ with effective Rabi frequency

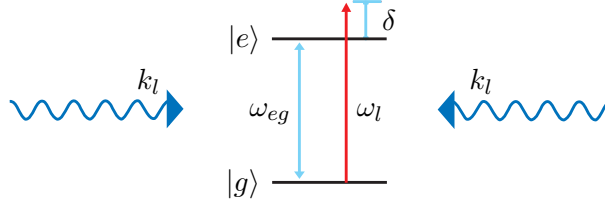


Figure 2.1. Schematic diagram showing a two level atom with states $|g\rangle$ and $|e\rangle$ separated by energy $\hbar\omega_{eg}$ interacting with a standing wave of light formed by two lasers with wavenumber k_l and frequency ω_l . The detuning of the lasers from resonance $\delta = \omega_l - \omega_{eg}$.

$\Omega(\hat{x}) = 2\boldsymbol{\mu}_{eg} \cdot \mathbf{E}(\hat{x}, t)$, which depends on the applied electric field $\mathbf{E}(\hat{x}, t)$ and the dipole matrix element for the states $|g\rangle$ and $|e\rangle$, $\boldsymbol{\mu}_{eg} = \langle e | \hat{\boldsymbol{\mu}} | g \rangle$. The second term in Eq. 2.1 describes the quantum jumps associated with spontaneous emission of a photon and transition from $|e\rangle \rightarrow |g\rangle$, with a normalised distribution of momentum recoil projected onto the axis of the standing wave $N(u)$, and spontaneous emission rate $\Gamma = |\boldsymbol{\mu}_{eg}|^2 \omega_{eg}^3 / (3\pi\epsilon_0 \hbar c^3)$. The operator $d\hat{B}_u^\dagger(t)$ corresponds to an Ito noise increment in this process[1].

2.1.1 Periodic Potential

If we write the state $|\Psi(t)\rangle = |\psi_e(t)\rangle \otimes |e\rangle + |\psi_g(t)\rangle \otimes |g\rangle$, then the equations of motion for $|\psi_e(t)\rangle$ and $|\psi_g(t)\rangle$ are given by

$$\frac{d|\psi_e\rangle}{dt} = -i \left(\delta - i\frac{\Gamma}{2} + \frac{\hat{p}^2}{2m} \right) |\psi_e(t)\rangle + i\frac{\Omega(\hat{x})}{2} |\psi_g(t)\rangle \quad (2.3)$$

and

$$d|\psi_g(t)\rangle = -i \left(\frac{\hat{p}^2}{2m} \right) dt |\psi_g(t)\rangle + \left(i\frac{\Omega(\hat{x})}{2} dt + \sqrt{\Gamma} \int_{-1}^1 du \sqrt{N(u)} e^{-ik_{eg}u\hat{x}} d\hat{B}_u^\dagger(t) \right) |\psi_e(t)\rangle. \quad (2.4)$$

In the limit where the detuning $|\delta| \gg |\Omega|, \Gamma$, and where the detuning is also larger than the kinetic energy (and thus the recoil energy $E_R = \hbar^2 k_l^2 / (2m)$), the excited state may be adiabatically eliminated. Setting $d|\psi_e\rangle/dt \approx 0$ and neglecting the kinetic energy term in Eq. 2.3, we obtain

$$|\psi_e(t)\rangle = \frac{\Omega(\hat{x})}{2\delta - i\Gamma} |\psi_g(t)\rangle. \quad (2.5)$$

The resulting equation of motion for the atom in the ground state is then given by

$$d|\psi_g(t)\rangle \approx \left[-i \left(\frac{\hat{p}^2}{2m} - \frac{\Omega^2(\hat{x})\delta}{4\delta^2 + \Gamma^2} - \frac{i\Gamma}{2} \hat{c}^\dagger \hat{c} \right) dt + \sqrt{\Gamma} \int_{-1}^1 du \sqrt{N(u)} e^{-ik_{eg}u\hat{x}} d\hat{B}_u^\dagger(t) \hat{c} \right] |\psi_g(t)\rangle, \quad (2.6)$$

where $\hat{c} = \Omega(\hat{x}) / (2\delta - i\Gamma)$. The resulting optical potential is then

$$V(x) = -\frac{\Omega^2(x)\delta}{4\delta^2 + \Gamma^2} \approx -\frac{\Omega^2(x)}{4\delta} = -\frac{\Omega_0^2}{4\delta} \sin^2(k_l x) = V_0 \sin^2(k_l x), \quad (2.7)$$

where we have used the spatial dependence of Ω for the 1D standing wave, $\Omega(x) = \Omega_0 \sin(k_l x)$, and defined the depth of the lattice $V_0 = \Omega_0^2/(4\delta)$. This potential can be easily modified using additional lasers and a variety of geometries to change the spatial dependence of $\Omega(x)$, or using the polarisation of the laser light to make the potential state-dependent (by varying μ_{eg}). This versatility is discussed in more detail in section 2.5.

In a deep lattice, the ground state wavefunction of an atom trapped in one of the potential minima will be much smaller than the lattice periodicity. In this limit, the optical potential for the atom may also be approximated by a Harmonic potential,

$$V_{\text{HO}} = \frac{m\omega_T^2 x^2}{2}, \quad (2.8)$$

with trapping frequency

$$\omega_T = \frac{\Omega_0 k_l}{\sqrt{2m\delta}} = \sqrt{\frac{2V_0 k_l^2}{m}} = 2\sqrt{V_0 E_R}. \quad (2.9)$$

The ground state wavefunction for the atom is then well approximated by the Harmonic Oscillator wavefunction,

$$\psi_0^{\text{HO}}(x) = \sqrt{\frac{1}{\pi^{1/2} a_0}} e^{-x^2/(2a_0^2)}, \quad (2.10)$$

with the size of the ground state $a_0 = \sqrt{\hbar/(m\omega_T)}$. Note that this approximation is valid in the regime where $a_0 \ll a$, where $a = \pi/k_l$ is the lattice periodicity.

In the case of a 3D optical lattice, the basic physics is the same, and there are only a few minor adjustments. A potential is formed in three dimensions by three independent standing waves, with interference effects amongst the different standing waves suppressed by either the choice of orthogonal light polarisations or by slightly detuning the standing waves from one another. In practice, the laser(s) will be far-detuned, and the resulting potential will not result from coupling to one excited state, $|e\rangle$, but instead will be given by a sum of the contributions from all internal states of the atom. For the purposes of estimating the effective spontaneous emission rate, Γ_{eff} , we can normally consider the coupling to a single (or to few) excited states, as the relative detuning varies sufficiently from state to state that the contributions from most states are extremely small.

2.1.2 Spontaneous Emissions

Providing that the effective rate of spontaneous emissions, Γ_{eff} , is small, the dynamics of the atom will obey a Schrödinger equation with a periodic potential provided by the optical standing wave. For many applications with which we are concerned in this thesis, spontaneous emissions constitute one of the largest sources of decoherence, and it is mostly preferable and often imperative to limit the experiment to times small in comparison with $1/\Gamma_{\text{eff}}$. Here we estimate the rate of spontaneous emission for an atom localised near one of the potential minima, which (as we will see) is a good approximation for the system in the limit which is well described by Bose-Hubbard and Hubbard models. As we are primarily interested in these results when the lattice is deep, we will use the Harmonic oscillator approximation in our calculations.

Blue-detuned lattices

If the optical standing wave is blue-detuned, i.e., $\omega_l > \omega_{eg}$, then the potential minima will be the points of zero intensity in the standing wave. The effective spontaneous emission rate is then given by

$$\Gamma_{\text{eff}} \approx \Gamma \langle \psi_0^{\text{HO}} | \hat{c}^\dagger \hat{c} | \psi_0^{\text{HO}} \rangle \approx -\frac{\omega_T}{4\delta} \Gamma, \quad (2.11)$$

which can be made extremely small in a far detuned lattice ($\delta \ll \Omega_T, \Gamma$). For example, a blue-detuned optical lattice with wavelength $\lambda = 514$ nm for ^{23}Na , inducing an $S_{1/2} \rightarrow P_{3/2}$ transition with $\lambda_{eg} = 589$ nm, $\Gamma = 2\pi \times 10$ MHz, and $E_R \approx 2\pi \times 33$ kHz, gives a detuning $\delta = -2.3 \times 10^9 E_R$. For a lattice depth $V_0 = 25E_R$ with trapping frequency $\omega_T = 10E_R$, the resulting effective spontaneous emission rate $\Gamma_{\text{eff}} \sim 10^{-2} s^{-1}$, which corresponds a time scale of the order of minutes.

Red-detuned lattices

If the optical standing wave is red-detuned, i.e., $\omega_l < \omega_{eg}$, then the potential minima will be the points of maximum light intensity in the standing wave. The resulting effective spontaneous emission rate is, in general, significantly higher than in the blue-detuned case,

$$\Gamma_{\text{eff}} \approx \Gamma \langle \psi_0^{\text{HO}} | \hat{c}^\dagger \hat{c} | \psi_0^{\text{HO}} \rangle \approx -\frac{\Gamma}{4\delta} \left(\frac{\Omega_0^2}{\delta} - \omega_T \right) \approx \frac{V_0}{\delta} \Gamma. \quad (2.12)$$

In a typical experiment, the rate of spontaneous emission events can also be heavily reduced by using far-detuned lattices. For a typical current experiment with a red-detuned optical lattice with wavelength $\lambda = 852$ nm for ^{87}Rb , inducing an $S_{1/2} \rightarrow P_{1/2}$ transition with $\lambda_{eg} = 795$ nm, $\Gamma = 2\pi \times 6$ MHz, and $E_R \approx 2\pi \times 3.1$ kHz, gives a detuning $\delta = 8.0 \times 10^9 E_R$. For a lattice depth $V_0 = 25E_R$ with trapping frequency $\omega_T = 10E_R$, the resulting effective spontaneous emission rate $\Gamma_{\text{eff}} \sim 0.2 \times 10^{-2} s^{-1}$, giving a timescale which is again of the order of minutes.

In practice, when the detuning of the lattice is chosen, other factors must be taken into account, especially the possibility for loss of atoms from the lattice due to light-assisted inelastic collisions. These occur when the effective detuning from resonances changes as a result of the interatomic potential, leading to resonant coupling of two free atoms either to a bound molecular states or different unbound states (for a red or blue-detuned lattice respectively) [3].

2.2 Bloch Waves

On timescales where spontaneous emissions can be neglected, the coherent dynamics of a single atom in the standing wave will then be described by the Hamiltonian

$$\hat{H} = \frac{\hat{p}^2}{2m} + V_0 \sin^2(k_l x). \quad (2.13)$$

2.2.1 Band Structure

The eigenstates of this Hamiltonian are then the Bloch eigenstates [4], which have the form

$$\phi_q^{(n)}(x) = e^{iqx} u_q^{(n)}(x), \quad (2.14)$$

where q is the quasimomentum of the eigenstate, $q \in [-\pi/a, \pi/a]$, and $u_q^{(n)}(x)$ are the eigenstates of the Hamiltonian

$$H_q = \frac{(p+q)^2}{2m} + V_0 \sin^2(k_l x), \quad (2.15)$$

and have the same periodicity as the potential ($u_q^{(n)}(x+a) = u_q^{(n)}(x)$). The Bloch eigenstates are normalised so that

$$\frac{2\pi}{a} \int_0^a |\phi_q^{(n)}(x)|^2 dx = 1. \quad (2.16)$$

Whilst $u_q(x)$ are, in general, complicated functions, they are relatively simple to compute numerically, e.g., by writing the Fourier expansion

$$u_q^{(n)}(x) = \frac{1}{\sqrt{2\pi}} \sum_{j=-\infty}^{\infty} c_j^{(n,q)} e^{i2k_l x j}, \quad (2.17)$$

which allows us to reduce Eq. 2.15 to a linear eigenvalue equation in the complex coefficients c_j ,

$$\sum_{j'=-l}^l H_{jj'} c_{j'}^{(n,q)} = E_q^{(n)} c_j^{(n,q)}. \quad (2.18)$$

Here, $H_{jj} = (2j + q/k_l)^2 E_R + V_0/2$ for $j = j'$, $H_{jj'} = -V_0/4$ for $|j - j'| = 1$, and $H_{jj'} = 0$ otherwise. This problem can be diagonalised by restricting $j \in \{-l, \dots, l\}$, and we find for the lowest few bands that good results are obtain for relatively small $l \sim 10$. The resulting band structure, given by the energy eigenvalues, $E_q^{(n)}$, taken as a function of the quasimomentum, q are plotted in Fig. 2.2. Depending in each case on the depth of the lattice, particles in the lowest bands, with $E_q^{(n)} < V_0$ are in bound states of the potential, whilst the higher bands $E_q^{(n)} > V_0$ correspond to free particles. The lowest two bands are separated in energy approximately by the trapping frequency, ω_T . When we derive the Bose-Hubbard model we will assume that the temperature and all other energy scales in the system are smaller than ω_T , allowing us to restrict the system to the lowest Bloch band.

2.2.2 Wannier Functions

It is often very convenient to express the Bloch functions in terms of Wannier functions, which form a complete set of orthogonal basis states. The Wannier functions are given in 1D by

$$w_n(x - x_i) = \sqrt{\frac{a}{2\pi}} \int_{-\pi/a}^{\pi/a} dq u_q^{(n)}(x) e^{-iqx_i}, \quad (2.19)$$

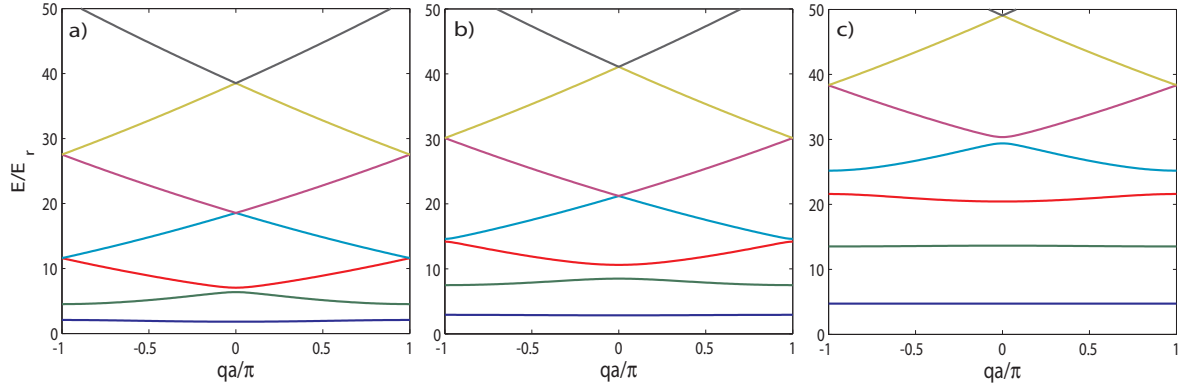


Figure 2.2. Band energies E/E_R in 1D as a function of q for the optical potential $V_0 \sin^2(k_l x)$, for (a) $V_0 = 5E_R$, (b) $V_0 = 10E_R$, and (c) $V_0 = 25E_R$. The lattice spacing, $a = \pi/k_l$.

where x_i are the minima of the standing wave. Each set of Wannier functions for a given n can be used to express the Bloch functions in that band,

$$u_q^{(n)}(x) = \sqrt{\frac{a}{2\pi}} \sum_{x_i} w_n(x - x_i) e^{ix_i q}. \quad (2.20)$$

The Wannier functions have the advantage of being localised on particular sites, which makes them useful for describing local interactions between particles.

The Wannier functions are not uniquely defined by Eq. 2.19, because the wavefunctions $\phi_q^{(n)}(x)$ are arbitrary up to a complex phase. However, as shown by Kohn in 1959 [5], there exists for each band only one real Wannier function $w_n(x)$ that is either symmetric or antisymmetric about either $x = 0$ or $x = a/2$, and falls off exponentially, i.e., $|w_n(x)| \sim \exp(-h_n x)$ for some $h_n > 0$ as $x \rightarrow \infty$. These Wannier functions are known as the *maximally localised* Wannier functions, and we will use this choice for the Wannier functions in the rest of our discussions. If the Bloch functions are computed as described in section 2.2.1, the maximally localised Wannier functions can be produced from the integral in Eq. 2.19 if all $c_m^{n,q}$ are chosen to be real for the even bands, $n = 0, 2, 4, \dots$, and imaginary for the odd bands $n = 1, 3, 5, \dots$, and are chosen to be smoothly varying as a function of q . (Numerically, one can ensure smoothness by choosing, e.g., that $c_l^{n,q} \geq 0$ for some particular l).

Examples of maximally localised Wannier functions for $n = 0, 1$ are plotted in Fig. 2.3. On the central site these functions bear strong relationship to the ground and first excited state wavefunctions for the harmonic oscillator, and indeed for many analytical estimates of onsite properties the Wannier functions may be replaced by harmonic oscillator wavefunctions if the lattice is sufficiently deep. The major difference between the two is that the Wannier functions are exponentially localised (as see in the lower plots of Fig. 2.3), whereas the harmonic oscillator wavefunctions decay more rapidly in the tails as $\exp[-x^2/(2a_0)^2]$.

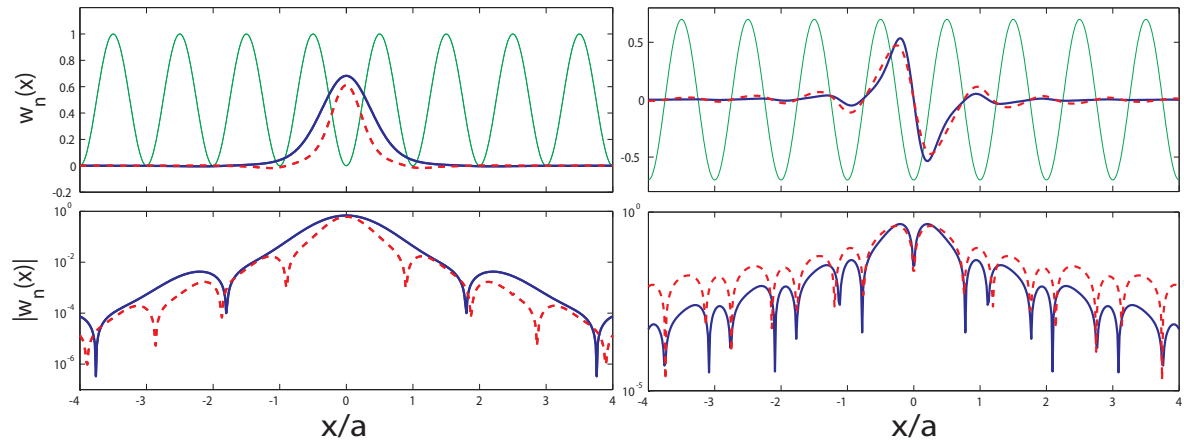


Figure 2.3. Wannier Functions $w_n(x)$ in units $\sqrt{2\pi/a}$ for $n = 0$ (left) and $n = 1$ (right), plotted for $V_0 = 10E_R$ (solid line) and $V_0 = 5E_R$ (dashed line). The lower plots show the absolute version of the Wannier functions on a logarithmic scale. The position of the periodic potential is indicated on the upper plots.

2.3 The Bose-Hubbard Model

In its simplest form, the Bose-Hubbard model describes bosonic particles on a lattice, which have a hopping amplitude J to transfer between neighbouring sites, and which exhibit local interactions with an onsite energy shift U when two atoms are present on one site. The Hamiltonian, in terms of bosonic creation and annihilation operators \hat{b}_i^\dagger and \hat{b}_i that obey the standard commutator relations, is given ($\hbar = 1$) by

$$\hat{H} = -J \sum_{\langle i,j \rangle} \hat{b}_i^\dagger \hat{b}_j + \frac{U}{2} \sum_i \hat{n}_i (\hat{n}_i - 1) + \sum_i \epsilon_i \hat{n}_i, \quad (2.21)$$

where $\langle i,j \rangle$ denotes a sum over all combinations of neighbouring sites, $\hat{n}_i = \hat{b}_i^\dagger \hat{b}_i$ and ϵ_i is the local energy offset of each site. For bosonic atoms in optical lattices, ϵ_i can include, for example, the effects of background trapping potentials, superlattice, or fixed disorder.

2.3.1 Derivation of the Bose-Hubbard Hamiltonian

Under certain conditions, the Bose-Hubbard Hamiltonian can be derived directly from the microscopic description of a cold atomic gas, as was first performed by Jaksch et al. [6]. In the limit of low energies, where the only significant contribution to the interactions between atoms comes from s-wave scattering, the interatomic potential $U(\mathbf{x})$ can be replaced by a contact-interaction pseudopotential [7],

$$U(\mathbf{x}) = \frac{4\pi\hbar^2 a_s}{m} \delta(\mathbf{x}) = g \delta(\mathbf{x}), \quad (2.22)$$

with the scattering length a_s as the only parameter. In the presence of a potential $V(\mathbf{x})$, the second-quantised Hamiltonian in terms of the bosonic field operators $\hat{\Psi}(\mathbf{x})$ is

$$\hat{H} = \int d\mathbf{x} \hat{\Psi}^\dagger(\mathbf{x}) \left(-\frac{\hbar^2}{2m} \nabla^2 + V(\mathbf{x}) \right) \hat{\Psi}(\mathbf{x}) + \frac{g}{2} \int d\mathbf{x} \hat{\Psi}^\dagger(\mathbf{x}) \hat{\Psi}^\dagger(\mathbf{x}) \hat{\Psi}(\mathbf{x}) \hat{\Psi}(\mathbf{x}) \quad (2.23)$$

We now expand the field operators in terms of Wannier functions,

$$\hat{\Psi}(\mathbf{x}) = \sum_{i,n} w_n(\mathbf{x} - \mathbf{x}_i) \hat{b}_{n,i}, \quad (2.24)$$

where for a 3D cubic lattice the Wannier function $w_n(\mathbf{x})$, $\mathbf{x} = (x, y, z)$ is a product of the 1D Wannier functions, $w_n(\mathbf{x}) = w_{n_x}(x)w_{n_y}(y)w_{n_z}(z)$. It is then possible to reduce Eq. 2.23 to Eq. 2.21 with the parameters J , U , and ϵ_i given by

$$J = - \int dx w_0(x) \left(-\frac{\hbar^2}{2m} \nabla^2 + V_0 \sin^2(k_l x) \right) w_0(x - a), \quad (2.25)$$

$$U = g \int d\mathbf{x} |w_0(\mathbf{x})|^4, \quad (2.26)$$

$$\epsilon_i = \int d\mathbf{x} |w_0(\mathbf{x} - \mathbf{x}_i)|^2 (V(\mathbf{x} - \mathbf{x}_i)), \quad (2.27)$$

under the following assumptions:

1. That the tunnelling matrix elements between neighbouring sites J are much larger than those between next-nearest neighbours, i.e.,

$$- \int dx w_0(x) \left(-\frac{\hbar^2}{2m} \nabla^2 + V_0 \sin^2(k_l x) \right) w_0(x - la), \quad (2.28)$$

for integer $l > 1$.

2. That the onsite interaction terms, e.g.,

$$g \int d\mathbf{x} |w_0(\mathbf{x} - \mathbf{x}_i)|^2 |w_0(\mathbf{x} - \mathbf{x}_j)|^2, \quad (2.29)$$

are small compared with the other quantities in the model.

3. That the Temperature T , and interaction energies $U\langle\hat{n}\rangle/2$ are much less than the trapping frequency ω_T , which gives the separation between the Bloch Bands, so that we may restrict the system to Wannier states in the lowest band, eliminating the others in perturbation theory.

All of these conditions are fulfilled provided that the lattice is deeper than $V_0 \sim 2E_R$. Typical corresponding parameter values as a function of V_0 are plotted in Fig. 2.4. We see that even for $V_0 = 1E_R$ the onsite interaction energies (Fig. 2.4a) are an order of magnitude smaller than the onsite interaction energies, and that they decrease rapidly as the lattice becomes deeper and the Wannier functions better localised. The same occurs for the second-neighbour and third-neighbour hopping as compared with the nearest neighbour hopping (Fig. 2.4b).

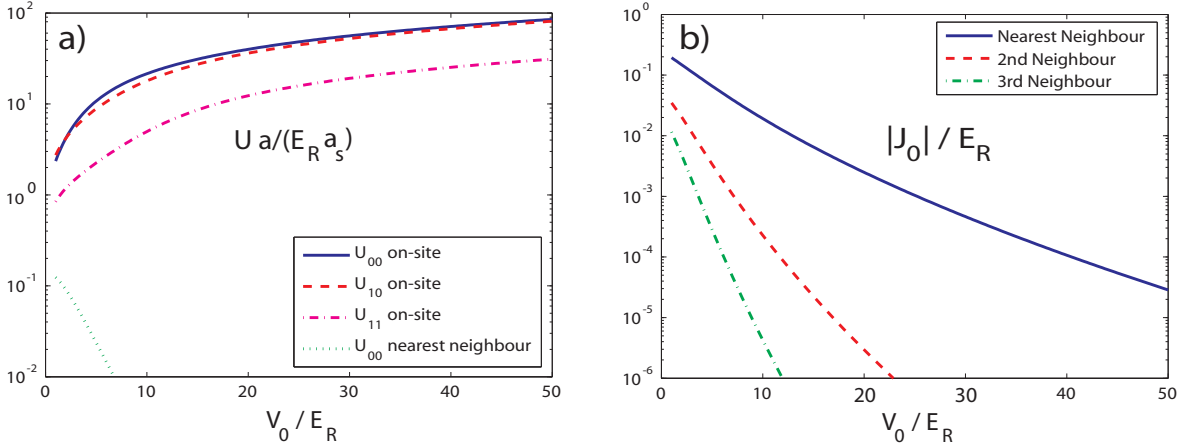


Figure 2.4. (a) Interaction energies U in units of $E_R a_s/a$ calculated from Wannier functions as a function of V_0/E_R . Values are shown for onsite interaction energies in the lowest band U_{00} , in the first excited Bloch band U_{11} , and for one atom in each band, U_{10} . Note that U_{10} is twice the single matrix element in Wannier functions. Nearest neighbour contributions to U_{00} are also shown. All values are for an isotropic 3D lattice. (b) Tunnelling matrix elements in the lowest band J_0/E_R calculated for nearest neighbours, and for 2nd and third neighbours along one dimension.

We also see that as the lattice becomes deeper and the Wannier functions are better localised U increases whilst J decreases. This can be used in an experiment to tune the ratio U/J .

By taking the Fourier transform of the Bose-Hubbard Hamiltonian, we see that the hopping term in position space corresponds to the normal tight-binding model [4] dispersion relation, with $\varepsilon_k = -2J \cos(ka)$. Thus, J can be most easily computed as a quarter the energy range for the Bloch band.

It is also possible to create multi-band Hubbard models, of the form

$$\begin{aligned} \hat{H}_{2\text{ Band}} = & - \sum_{\langle i,j \rangle} \left(J_0 \hat{b}_{0,i}^\dagger \hat{b}_{0,j} + J_1 \hat{b}_{1,i}^\dagger \hat{b}_{1,j} \right) + \frac{1}{2} \sum_i [U_{00} \hat{n}_{0,i} (\hat{n}_{0,i} - 1) + U_{11} \hat{n}_{1,i} (\hat{n}_{1,i} - 1)] \\ & + U_{10} \sum_i \hat{n}_{0,i} \hat{n}_{1,i} + \sum_{n,i} \epsilon_{n,i} \hat{n}_{n,i}, \end{aligned} \quad (2.30)$$

with the same assumptions applied as in the single-band model. Because the higher bands are not as deeply bound as lower bands, $|J_n|$ increases with n . Whilst the interaction energy in the upper bands is smaller than that in lower bands, (see, e.g., U_{11} in Fig. 2.4a), the interaction energy for two atoms in different bands is reasonably large, and the energy shift for two atoms, one in the band $n = 0$ and the other in the band $n = 1$ approaches U_{00} for deep lattices (in the Harmonic oscillator approximation these energy shifts are identical).

2.3.2 Basic Properties of the Bose-Hubbard Model

The zero-temperature phase diagram of the Bose-Hubbard Model with $\epsilon_i = 0$ was first investigated by Fisher et al. [8], and has since been extensively studied. This phase diagram is qualitatively similar in all dimensions, despite substantial quantitative differences, and this phase diagram is schematically plotted in Fig. 2.5. In the limit $(U/J) \rightarrow 0$, the ground state of the system is superfluid, and the atoms are delocalised around the lattice. For a lattice of M sites, this ideal superfluid state can be written as

$$|\Psi_{SF}\rangle = \left(\frac{1}{\sqrt{M}} \sum_{i=1}^M \hat{b}_i^\dagger \right)^N |0\rangle, \quad (2.31)$$

which for $N, M \rightarrow \infty$ at fixed N/M tends to

$$|\Psi_{SF}\rangle = \prod_{i=1}^M \left[\exp \left(\sqrt{\frac{N}{M}} \hat{b}_i^\dagger \right) |0\rangle_i \right], \quad (2.32)$$

which is locally a coherent state with Poisson number statistics. In 3D, this state is an ideal BEC in which all N atoms are in the Bloch state $\phi_{\mathbf{q}=0}^{(n=0)}(x)$. Superfluid states at ($T=0$) exhibit off-diagonal long-range order (or quasi-long range order in 1D), with the off diagonal elements of the single particle density matrix, $\langle \hat{b}_i^\dagger \hat{b}_j \rangle$ decaying polynomially with $|i - j|$.

As U/J increases, a regime exists in which the onsite interactions make it less favourable to particles to hop to neighbouring sites. Provided that the number of particles and lattice sites are commensurate, a phase transition then occurs to the Mott Insulator (MI) regime, in which particles are essentially localised at particular sites in the sense that their mean square displacement is finite. In the limit $J/U \rightarrow 0$, this state corresponds to a fixed number of atoms on each site,

$$|\Psi_{MI}\rangle = \prod_i |\bar{n}\rangle_i, \quad (2.33)$$

where $\bar{n} = \langle \hat{n} \rangle = N/M$ is the average filling factor. The MI regime appears as lobes in the phase diagram corresponding to an integer fixed filling factor (see Fig. 2.5). For finite J/U , the off diagonal elements of the single particle density matrix, $\langle \hat{b}_i^\dagger \hat{b}_j \rangle$, decay exponentially for a MI state as a function of $|i - j|$.

At fixed integer \bar{n} , the transition point in 2D or 3D is well described by mean-field theories, with $(U/J)_c = 5.8z$ for $\bar{n} = 1$ and $(U/J)_c = 4\bar{n}z$ for $\bar{n} > 1$, where z is the number of nearest neighbours for each lattice site (in a 3D cubic lattice, $\bar{n} = 6$). In 1D, the deviations from mean-field results are large, and $(U/J)_c = 3.37$ [9] for $\bar{n} = 1$ and $(U/J)_c = 2.2\bar{n}$ for $\bar{n} > 1$.

If \bar{n} is fixed and non-integer (see, e.g., the line $\langle \hat{n} \rangle = 1 + \varepsilon$ in Fig. 2.5), then even in the limit $U \ll J$, there is a fraction of atoms which can remain superfluid on top of a frozen Mott-Insulator core (which will exist for $\bar{n} > 1$) provided $J > 0$. Indeed these atoms need not be affected by increasing U/J , as they can gain kinetic energy by delocalising over the lattice without two of them being present at the same site.

In an external Harmonic trap, $\epsilon_l = \Omega l^2$ with a fixed number of particles, the local chemical potential, μ , varies across the trap, decreasing from the centre to the edges. As a result, regions exhibiting alternately the superfluid and MI phases appear (See chapter 8 for example calculations of the ground state of such systems).

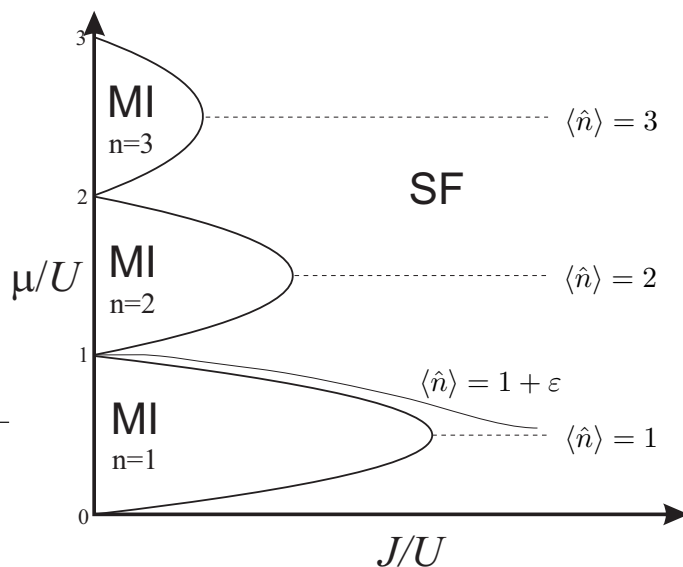


Figure 2.5. *Schematic Phase Diagram for the Bose-Hubbard Model at zero temperature, showing lobes for the Mott Insulator phases with fixed average particle number $\langle \hat{n} \rangle = 1, 2, 3$. The critical values of J/U , indicated by the intersection of the Mott lobes with dashed lines indicating fixed average particle number, decrease as the density increases. For non-integer filling, the lines of fixed average filling factor (e.g., $\langle \hat{n} \rangle = 1 + \varepsilon$) do not intersect the Mott lobes, as some fraction of the particles remain in a superfluid phase for all $J > 0$.*

2.4 The Hubbard Model for Fermions

In a similar manner to the procedure in section 2.3.1, one can show that the microscopic Hamiltonian for two fermionic spin species reduces to the Hubbard model,

$$\hat{H} = -J \sum_{\langle i,j \rangle, \sigma} \hat{c}_{i\sigma}^\dagger \hat{c}_{j\sigma} + U \sum_i \hat{n}_{i\uparrow} \hat{n}_{i\downarrow} + \sum_{i,\sigma} \epsilon_i \hat{n}_{i\sigma}, \quad (2.34)$$

with fermionic operators \hat{c}_i , which obey the standard anti-commutator relations, and $\sigma \in \{\uparrow, \downarrow\}$. This is a simple example of the many two-species models that can be engineered with atoms in optical lattices.

2.5 Spin-Dependent Optical Lattices

As discussed in chapter 1, the greatest strength of atoms in optical lattices is our ability to engineer a wide range of Hamiltonians with excellent control over system parameters [10]. One technique in this context that is mentioned throughout this thesis is the possibility to create spin dependent lattices for different internal states of a single atomic species. This is based on the strong dependence of the dipole matrix elements μ , and hence the Rabi frequency $\Omega(x)$ in Eq. 2.6, on the polarisation of the light forming the standing wave.

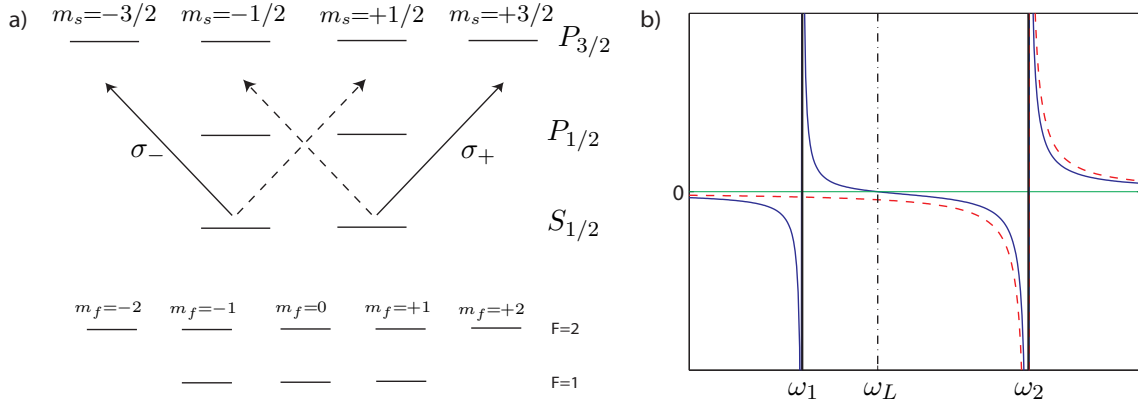


Figure 2.6. (a) Diagram showing the Fine structure and Hyperfine structure for Alkali atoms with nuclear spin $I = 3/2$, e.g., ^{23}Na and ^{87}Rb . The arrows on the diagram indicate the dipole couplings produced by circularly polarised light. (b) Schematic plot of the AC Stark shift as a function of laser tuning generated with σ^+ polarised light for the atomic level $S_{1/2}$ with $m_s = -1/2$ (solid line) and $m_s = +1/2$ (dashed line). Resonant tunings to the $P_{1/2}$ and $P_{3/2}$ levels are denoted ω_1 and ω_2 respectively. When the tuning $\omega = \omega_L$, the shift for the state with $m_s = -1/2$ is zero.

A specific example of this is shown in Fig. 2.6 for alkali atoms with nuclear spin $I = 3/2$, which includes the species ^{23}Na and ^{87}Rb which are commonly used in lattice experiments. Circularly polarised σ^+ light couples the level $S_{1/2}$ with $m_s = -1/2$ to the $m_s = +1/2$ states in both the $P_{3/2}$ level and the $P_{1/2}$ level. The sum of the resulting AC Stark shifts (with opposite detuning) gives rise to a point at which the total shift of the $m_s = -1/2$ state is zero ($\omega = \omega_L$ in Fig. 2.6b). As σ_+ light couples the $S_{1/2}$, $m_s = +1/2$ state only to the $P_{3/2}$, $m_s = +3/2$ level, the level shift for this state is non-zero. At the same frequency as this occurs, $\omega = \omega_L$, the AC-Stark shift due to σ_- light for the $S_{1/2}$, $m_s = +1/2$ state is zero, so that the potentials V_{\pm} for the $S_{1/2}$, $m_s = \pm 1/2$ states are independently generated by light with polarisation σ_{\pm} . The level shifts for the hyperfine states are then related to the level shifts for the fine structure states via Clebsch-Gordan coefficients, so that, e.g., $V(F = 2, m_F = 2) = V_+(x)$, $V(F = 1, m_F = 1) = 3V_+(x)/4 + V_-(x)/4$, and $V(F = 1, m_F = -1) = V_+(x)/4 + 3V_-(x)/4$.

These techniques were demonstrated in an experiment by Bloch and his coworkers [11], who showed that by changing the angle of polarisation φ between two running waves, it was possible to shift the nodes of potentials for two states, so that $V_{\pm}(x) = \sin^2(k_1 x \pm \varphi)$.

Bibliography

- [1] C. W. Gardiner and P. Zoller, *Quantum Noise*, Third Edition (Springer, Berlin, 2005).

-
- [2] P. Zoller and C. W. Gardiner, *Quantum Noise in Quantum Optics: the Stochastic Schrödinger Equation*, quantum-ph/9702030.
- [3] K. Burnett, P. S. Julienne, and K.-A. Suominen, *Phys. Rev. Lett.* **77**, 1416 (1996).
- [4] See, for example, C. Kittel, *Introduction to Solid State Physics*, 7th Ed., (Wiley, New York, 1996).
- [5] W. Kohn, *Phys. Rev.* **115**, 809 (1959).
- [6] D. Jaksch, C. Bruder, J. I. Cirac, C. W. Gardiner, and P. Zoller, *Phys. Rev. Lett.* **81**, 3108 (1998).
- [7] See, for example, C. J. Pethick and H. Smith, *Bose-Einstein Condensation in Dilute Gases* (Cambridge University Press, Cambridge, 2002).
- [8] M. P. A. Fisher, P. B. Weichmann, G. Grinstein, and D. S. Fisher, *Phys. Rev. B* **40**, 546 (1989).
- [9] T. D. Kühner, S. White, and H. Monien, *Phys Rev. B* **61**, 12474 (2000).
- [10] See D. Jaksch and P. Zoller, *Annals of Physics* **315**, 52 (2005), and references therein.
- [11] O. Mandel *et al.*, *Phys. Rev. Lett.* **91**, 010407 (2003).

Part II

Manipulation of Atoms in Optical Lattices

CHAPTER 3

MANIPULATION OF COLD ATOMS IN AN OPTICAL LATTICE

In part II of this thesis we discuss techniques to manipulate atoms in optical lattices in order to achieve two primary objectives:

1. The production of initial states required for quantum computing (an atomic qubit “register”, with one atom in every lattice site), and for the study of strongly correlated systems (e.g., states of precisely known filling factors)
2. The cooling of the motional states of atoms in an optical lattice without causing decoherence for the internal states.

The first objective is addressed by two state preparation schemes, which are designed to produce high fidelity arrays of atoms in optical lattices. These arrays are patterns of occupied and unoccupied sites, which can be determined by using a superlattice to shift the energy level at each site. The first scheme relies on coherently filtering an existing state (chapter 4) so that one atom is left in every lattice site, and the second scheme involves filling the lattice from an external reservoir gas, which is not trapped by the lattice. In this second scheme, cooling of the motional state of atoms in the lattice due to interactions with the atoms still in the reservoir gas makes the dynamics irreversible and the scheme fault-tolerant (chapter 6). This sympathetic cooling mechanism was originally investigated as a method to achieve the second objective, i.e., cooling the motional states of atoms in the lattice by dissipating energy in the form of excitations in the reservoir gas, without altering the internal state of the atoms (chapter 5).

3.1 Coherent Laser-Assisted Filtering of Atoms

The first state preparation scheme, presented in the publication in chapter 4 begins by taking a Mott Insulator state of bosons with a filling factor greater than one, where the probability that a lattice site is unoccupied is small. Then the initial internal atomic state $|a\rangle$ is coupled to a second internal state $|b\rangle$, using either an oscillating microwave field or a Raman setup (which consists of two lasers that can couple two hyperfine states via an off-resonant coupling

to an excited level). State $|b\rangle$ is trapped by an independent lattice, and by sweeping the detuning of the coupling transition over a range of frequencies, exactly one atom per lattice site is transferred adiabatically (see below) into $|b\rangle$, regardless of how many atoms were initially present in the site. This range is, in general, different for each possible number of atoms initially present on the site, and is determined by the interaction strengths between atoms in the same and different internal states. The key to the filtering process is to adjust those interaction strengths, so that the detuning can be swept over a range of frequencies that will produce the transfer of exactly one atom irrespective of the initial site occupation. The resulting fidelities are potentially very high, and are fundamentally limited primarily by the probability that a site is initially unoccupied.

This scheme can be extended to arbitrary patterns of atoms by using a superlattice to shift the relative energy of the internal states, and thus prevent atoms in particular lattice sites from being coupled to state $|b\rangle$. This technique can also be applied to fermions, where it is particularly useful for selecting the filling factor of an initial state, and can also be used to aid in the calculation of correlation functions. This is illustrated in chapter 4 by a scheme to produce a BCS state of fermions with a chosen filling factor.

3.1.1 Adiabatic Transfer

The concept of adiabatic transfer from one state to another is the key to this coherent filtering scheme. This process occurs because if a parameter of the Hamiltonian is changed sufficiently slowly in time, then the system will remain in a particular energy eigenstate as the system evolves. At the beginning of the evolution the initial state corresponds to one of the energy eigenstates, and at the end it corresponds to the same energy eigenstate, but potentially a different physical state, as the Hamiltonian, and thus the eigenstates have been changed. The eigenstates as a function of the parameter being varied are often referred to as the *dressed states* of the system.

To write the adiabatic approximation explicitly, we can express the state of the system in terms of the energy eigenstates, $\hat{H}(t)|\psi_n(t)\rangle = E_n(t)|\psi_n(t)\rangle$, of the Hamiltonian \hat{H} , i.e., $|\Psi\rangle = \sum_k c_k(t)|\psi_k(t)\rangle$. Then, from the Schrödinger equation we obtain the coefficients $c_k(t)$,

$$i\hbar \frac{d}{dt} c_k(t) = \left(E_k - \langle \psi_k(t) | i\hbar \frac{d}{dt} | \psi_k(t) \rangle \right) c_k(t) - \sum_{n \neq k} \frac{\langle \psi_k(t) | \left(\frac{d}{dt} \hat{H}(t) \right) | \psi_n(t) \rangle}{E_n(t) - E_k(t)} c_n(t). \quad (3.1)$$

In the limit where $\hat{H}(t)$ changes sufficiently slowly, specifically,

$$\left| \langle \psi_k(t) | \left(\frac{d}{dt} \hat{H}(t) \right) | \psi_n(t) \rangle \right| \ll |E_n(t) - E_k(t)|, \quad (3.2)$$

we can then neglect the coupling terms between different energy eigenstates, and the system will remain in the same dressed state as the Hamiltonian is modified.

In a non-ideal case, the coupling into other dressed states, known as Landau-Zener tunnelling [1, 2] depends on the separation of the eigenvalues and the rate with which the

3.2 Sympathetic Cooling of Atoms in an Optical Lattice by a Cold Reservoir 31

Hamiltonian changes in time. In the case originally studied by Zener, the Hamiltonian for a two level system in the state basis $|a\rangle, |b\rangle$ has the form

$$\hat{H}(t) = \frac{\Omega}{2} (|a\rangle\langle b| + |b\rangle\langle a|) - V(t)|b\rangle\langle b|, \quad (3.3)$$

where $V(t) = -vt$ for some constant v . If we start in the state $|\psi\rangle = |a\rangle$ at $t = -\infty$ then provided $v \ll \Omega$, we can estimate the occupation probability for the state $|b\rangle$ for $t \rightarrow \infty$ as $|\langle 1|\psi\rangle|^2 \approx \exp[-\pi\Omega^2/(2v)]$.

3.2 Sympathetic Cooling of Atoms in an Optical Lattice by a Cold Reservoir

The cooling scheme presented in chapter 5 was originally designed to approach the problem of cooling the motional state of atoms in a deep optical lattice without causing decoherence for the internal state of the atom, which can potentially encode qubit information. In this case we approximate each lattice site as a harmonic trap, and consider this trap to be immersed in a cold, weakly interacting Bose gas [3]. The atoms interact with this cold reservoir reservoir via a density-density interaction, and can generate Bogoliubov excitations in the Bose gas. We show that provided the internal states of the atoms in the lattice used to encode qubit states are chosen carefully, together with the internal state for the reservoir gas, that decoherence can be eliminated by making the interaction between the lattice atoms and the atoms in the reservoir symmetric for the two qubit internal states.

We derive the resulting cooling rates, and find that the problem divides into two clear limiting cases. The first is when the motion of the atoms in the lattice is typically subsonic with respect to the sound velocity in the reservoir gas, and the other is when the motion of the atom is typically supersonic with respect to the velocity of sound. The latter case is the experimentally relevant limit, and we show that in this case cooling of the lattice atom from the first excited state to the ground state occurs on the order of 10 oscillator cycles. We also study the effects of finite temperature in the reservoir gas, and see that the atoms in the lattice are cooled to a thermal distribution, but that for typical experimental parameters this amounts for all practical purposes to full ground state cooling.

The cooling rates are derived twice, once with a full quantum master equation treatment and once applying Fermi's golden rule, and then evaluating the resulting matrix elements in the semiclassical approximation. Specifically, we use the relationship between the matrix elements of an operator in the energy eigenbasis and the Fourier components of the particle's classical trajectory [4]. This relationship is derived from the WKB wavefunctions [4], and is technically only valid for highly excited oscillator levels. Here, however, the semiclassical result agrees exactly in the subsonic limit with the full quantum result, and differs only by 10% from that result in the supersonic limit.

3.3 Dissipative loading of Fermions

Controlled dissipation of energy into a reservoir gas, as discussed in chapter 5 is not simply a method for cooling the motional states of atomic qubits, but instead has much broader

potential applications in cooling and the introduction of controlled dissipation for atoms in optical lattices. This fact is illustrated in chapter 6, where this dissipative process is used as the key element in an irreversible loading scheme to prepare high fidelity initial states. In contrast to the coherent filtering scheme in 4, this scheme is fault tolerant, and the state being prepared always improves in time.

The basic element of this scheme is a cold reservoir of fermions, which plays a dual role as both a source for atoms to be loaded into the lattice via a Raman process, and as a heat bath for sympathetic cooling of lattice atoms. We use the Raman transition to couple atoms into an excited motional state in each lattice site, from where they decay to the ground state whilst creating particle-hole pairs in the reservoir. These excitations are analogous to the Bogoliubov excitations discussed for the Bose reservoir in the original cooling scheme. Atoms transferred into the ground motional level are no longer coupled back to the reservoir, and are effectively in a “dark state” with respect to the coupling laser. This scheme thus has strong conceptual connections with optical pumping processes, in which atoms are repeatedly transferred using a laser into excited electronic states, undergoing spontaneous emission events and being re-excited until they reach the target “dark state”, where they are no longer coupled by the laser.

This is discussed in detail in chapter 6, beginning with transfer of atoms from the reservoir into the lattice via Raman processes. The decay of atoms due to interactions with the external reservoir (in this case a Fermi gas) is then treated, as is the combination of these two parts into the complete scheme.

Bibliography

- [1] C. Zener, Proc. R. Soc. London A **137**, 696 (1932).
- [2] L. D. Landau and E. M. Lifshitz, *Quantum Mechanics*, (Butterworth-Heinemann, Oxford, 1977).
- [3] E. M. Lifshitz and L. P. Pitaevskii, *Statistical Physics, Part 2*, (Pergamon Press, Oxford, 1980).
- [4] A. B. Migdal, *Qualitative Methods in Quantum Theory*, (W. A. Benjamin, Massachusetts, 1977).

CHAPTER 4

PUBLICATION

Defect-Suppressed Atomic Crystals in an Optical Lattice[†]

Phys. Rev. Lett. **91**, 110403 (2003)

P. Rabl¹, A. J. Daley¹, P. O. Fedichev¹, J. I. Cirac², and P. Zoller¹

*1) Institut für Theoretische Physik, Universität Innsbruck,
A-6020 Innsbruck, Austria*

2) Max-Planck Institut für Quantenoptik, D-85748 Garching, Germany

We present a coherent filtering scheme which dramatically reduces the site occupation number defects for atoms in an optical lattice, by transferring a chosen number of atoms to a different internal state via adiabatic passage. With the addition of superlattices it is possible to engineer states with a specific number of atoms per site (atomic crystals), which are required for quantum computation and the realisation of models from condensed matter physics, including doping and spatial patterns. The same techniques can be used to measure two-body spatial correlation functions.

There has been a vast amount of recent interest in the study of Bose-Einstein Condensates (BECs) [1] and degenerate Fermi gases [2] in optical lattices [3–5]. Such systems have many potential applications in quantum computing, and also make possible the study of strongly correlated systems from condensed matter theory with unprecedented control over system parameters.

However, the study of strongly correlated systems or entangled atoms in optical lattices requires not only that the corresponding (Hubbard) Hamiltonian [3, 4] be properly engineered, but also that the system is placed in a well defined (pure) initial state with high precision. Whilst it is possible to load a BEC into an optical lattice in the Mott Insulator (MI) phase, which corresponds to having a definite number of atoms at each lattice site [3, 4], non-ideal conditions will always result in defects in that phase (i.e., missing atoms and overloaded

[†]The primary contribution of the author of the present thesis to this publication was the analysis of the loading scheme for Fermions, together with the related measurement scheme and applications found in the second half of the publication. He also acted as a discussion partner for the other aspects of this work.

sites). The removal (or precise control) of such defects is then a necessary condition for the application of atoms in optical lattices to quantum computing and the study of strongly correlated systems. In this letter, we propose a coherent filtering scheme which, beginning with an uncertain number of atoms in each site, provides a method to transfer a definite number of atoms at each site into a different internal state, and so load a new lattice of atoms with an exact number of particles per site. This process dramatically reduces the site occupation number defects, and can be extended, under experimentally reasonable conditions, to allow the production of doped or pattern loaded initial states with almost unit fidelity (i.e., atomic crystals). The scheme is also applicable to the production of high fidelity initial states in fermion systems (including doped states and the loading of composite objects), and when combined with moving optical lattices, can be used to measure two-body correlation functions. We illustrate this by presenting an example of how this scheme could be used to both produce and characterise superconducting states in an optical lattice with a chosen filling factor.

We begin by considering a system of bosons loaded into an optical lattice such that they do not tunnel between neighbouring sites. The atoms are in a particular internal state, $|a\rangle$, and have onsite interaction strength (with $\hbar = k_B = 1$) $U_a = 4\pi a_s \int d^3\mathbf{x} |w(\mathbf{x})|^4 / m$, (valid for U_a less than the separation of the two lowest motional states at each site) where a_s is the scattering length and $w(\mathbf{x})$ is a Wannier function [3]. We then couple the atoms into a second internal state, $|b\rangle$, (which is trapped by a second lattice potential) via an off-resonant Raman transition with Rabi frequency $\Omega(t)$, which is detuned from state $|b\rangle$ by $\delta(t)$. If we denote the onsite interaction between particles in state $|b\rangle$ as U_b and the onsite interaction between particles in different internal states as U_{ab} , and follow the derivation in [3], we obtain the Hamiltonian

$$\begin{aligned} \hat{H} = & \frac{U_a}{2} \hat{n}_a (\hat{n}_a - 1) + \frac{U_b}{2} \hat{n}_b (\hat{n}_b - 1) + U_{ab} \hat{n}_a \hat{n}_b \\ & - \frac{\Omega(t)}{2} (a^\dagger b + b^\dagger a) - \delta(t) \hat{n}_b, \end{aligned} \quad (4.1)$$

where \hat{a} and \hat{b} are the annihilation operators for particles in states $|a\rangle$ and $|b\rangle$ respectively, and $\hat{n}_a = \hat{a}^\dagger \hat{a}$, $\hat{n}_b = \hat{b}^\dagger \hat{b}$. We can then write the state of the site as $|n_a, n_b\rangle$, where n_a and n_b are the number of particles in the internal states $|a\rangle$ and $|b\rangle$ respectively. We know that the initial state at a particular lattice site is $|N, 0\rangle$, where $N \in 1, 2, \dots, N_{\max}$. Our goal is to transfer exactly one particle from state $|a\rangle$ to state $|b\rangle$, so that for any N , the final state is $|N - 1, 1\rangle$. In order to do this we must choose the initial and final values of the detunings, δ_i and δ_f so that the system evolves along the avoided crossing in the energy eigenvalues, undergoing an adiabatic passage from $|N, 0\rangle \rightarrow |N - 1, 1\rangle$, and does not evolve along any other such avoided crossings. These values have to be simultaneously chosen for all values of N , as shown in Fig. 4.1. Once the system is in state $|N - 1, 1\rangle$, we can turn off the lattice trapping state $|a\rangle$, leaving a pure state with exactly one atom per lattice site.

The relative locations of the avoided crossings in the energy eigenvalues are determined by the values of U_a/U_b and U_{ab}/U_b . In the adiabatic limit ($\dot{\delta} \rightarrow 0$), we can set $\Omega = 0$, and for a given N_{\max} it is then straight forward to find the parameter range for which an appropriate choice of δ_i and δ_f is possible. We consider the locations at which the energy eigenvalues of \hat{H} cross in this limit, and then attempt to find a parameter range for which the crossings between

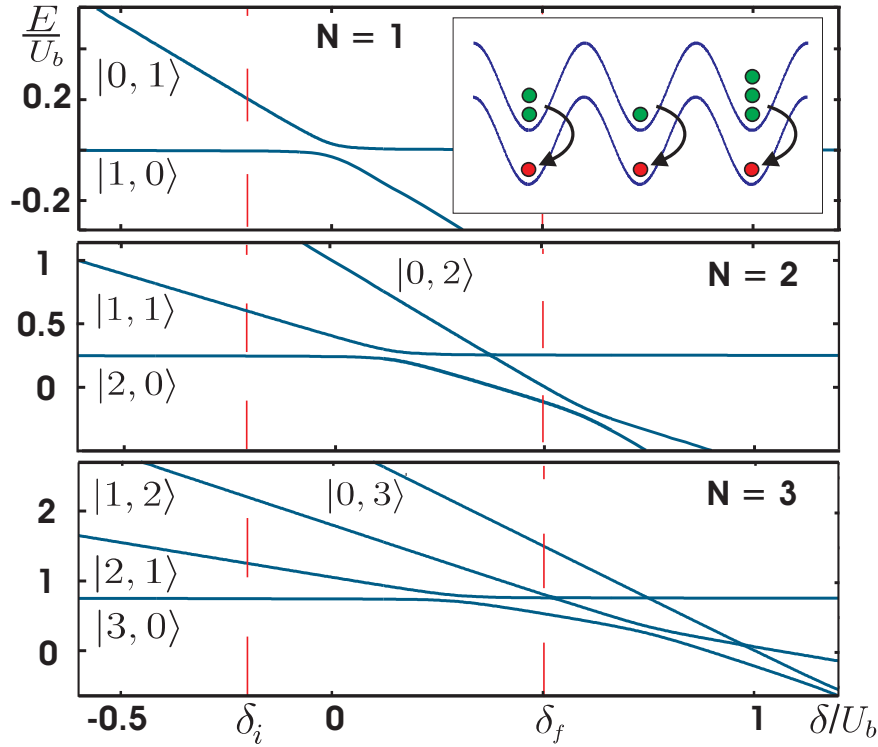


Figure 4.1. *Plots showing avoided crossings in the energy eigenvalues for $N = 1, 2, 3$ (Note the vertical scale variation). We must choose δ_i and δ_f (dashed vertical lines) so that we cross only from $|N, 0\rangle \rightarrow |N - 1, 1\rangle$, as illustrated in the inset.*

$|N, 0\rangle$ and $|N - 1, 1\rangle$ for all N fall within a range of detunings $[\delta_i, \delta_f]$ which isolates them from all other crossings. The resulting boundaries for the allowed parameter space are given by $U_{ab} = (1 - k_i)U_a + k_i U_b$, for $i = 1, 2$, where for $U_{ab} > U_a$, $k_1 = 1/N_{\max}$, $k_2 = 1/(2N_{\max} - 4)$, and for $U_{ab} < U_a$, $k_1 = 1/(2N_{\max} - 2)$, $k_2 = 1/(N_{\max} - 3)$. These boundaries are shown in Fig. 4.2a for $N_{\max} = 4$. Larger values of N_{\max} result in a more restrictive allowed parameter range. Substantially different values of U_a and U_b are required, which is possible using either spin-dependent lattices [5], where U_a and U_b are independently controlled via the different lattice shape for atoms in each internal state, or Feshbach Resonances [6], near which the scattering length a_s is different for atoms in different internal states as we tune an external magnetic field. U_{ab} can also be independently controlled by slightly displacing the lattices trapping internal states $|a\rangle$ and $|b\rangle$.

In the case of finite-time laser pulses, the adiabatic crossings have a finite size, and must be crossed on a timescale dictated by the separation of the energy eigenvalues at the crossings. From the Landau-Zener formula, we can estimate the transfer error ε for each N , when $\sqrt{N}\Omega(t) \ll U_a, U_b$, as $\varepsilon_N \approx \exp[-\pi N\Omega^2/(2\dot{\delta})]$, where $\dot{\delta} \sim |\delta_f - \delta_i|/\tau$ and τ is the total transfer time. Numerical calculations of ε_N are shown in Figs. 4.2b, 4.2c, and predict values of the order of 10^{-4} for typical $\tau \sim 100/U_b$, which could be significantly improved upon by coherent control optimisation of $\Omega(t)$ and $\delta(t)$. This analysis is valid for τ values

well within the decoherence time (including spontaneous emissions, collisional losses, and external parameter fluctuations, [4]) of the optical lattice.

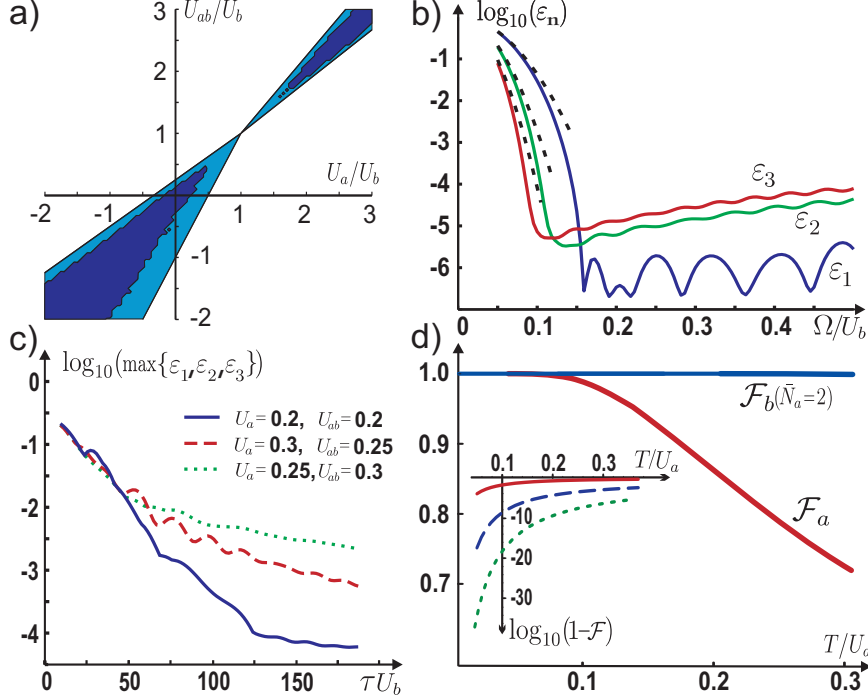


Figure 4.2. (a) The parameter range for which appropriate values of δ_i and δ_f can be found when $N_{\max} = 4$, in the adiabatic limit (light shading) and from numerical simulations with a smoothed rectangular pulse which rises and falls with a $\sin^2(t/\tau)$ shape, $\tau = 100/U_b$ and $\max \Omega = 0.3U_b$, giving a transfer error $\epsilon < 1\%$ (dark shading). (b) Transfer errors ϵ_N as a function of Ω for $U_a = U_{ab} = 0.2U_b$ and $\tau = 200/U_b$ (The dashed lines show the corresponding results from the Landau-Zener formula). (c) Maximum transfer errors from $N = 1, 2, 3$ as a function of τ for example values of U_a and U_{ab} (parameters are shown in units of U_b). (d) Initial and final state fidelities, \mathcal{F}_a and \mathcal{F}_b , as a function of temperature, T , for an initial MI state described at each site using the GCE. The inset shows values of $1 - \mathcal{F}_a$ (solid line) and $1 - \mathcal{F}_b$ for $\bar{N}_a = 2$ (dashed) and $\bar{N}_a = 3$ (dotted) on a logarithmic scale.

This filtering scheme naturally cannot correct occupation number defects in which no atoms are present at particular lattice site in state $|a\rangle$. Because in principle extremely low transfer errors, ϵ , are obtainable, this is the fundamental limit for the filtering scheme. The initial single-site fidelity of a state where we choose to have N_a particles in each lattice site is defined as $\mathcal{F}_a = \langle N_a, 0 | \hat{w}_0 | N_a, 0 \rangle$, where \hat{w}_0 is the initial density operator for the site. Similarly, the final state single-site fidelity (for 1 transferred atom) is $\mathcal{F}_b = \langle 1 | \hat{w}_b | 1 \rangle$, where $\hat{w}_b = \text{Tr}_a \hat{w}$, and \hat{w} is the final density operator for the site. In each case the overall fidelity for M sites is given by $\mathcal{F}_M = \mathcal{F}^M$. If the probability of zero occupation in a particular site

is p_0 , then $\mathcal{F}_b = (1 - \varepsilon)(1 - p_0)$. Thus to obtain the highest possible fidelities we should start in a MI phase with an average filling factor of 2 or more particles per site, where p_0 is small. For such a MI phase, with an average filling factor of \bar{N}_a at temperature T , we model the particle number fluctuations using a Grand Canonical Ensemble (GCE). For integer \bar{N}_a and low initial temperature, $\exp[-U_a/(2T)] \ll 1$, we obtain $p_0 = \exp[-U_a\bar{N}_a^2/(2T)]$, so that for $\varepsilon \rightarrow 0$, $\mathcal{F}_b \approx (1 - \exp[-U_a\bar{N}_a^2/(2T)])$. Under the same conditions, we can write $\mathcal{F}_a = p(N = \bar{N}_a) \approx 1 - 2\exp[-U_a/(2T)]$. We see (Fig. 4.2d) that coherent filtering increases the fidelity by several orders of magnitude, even when the fidelity \mathcal{F}_a is already reasonably high. Moreover, as $(1 - F_b) = [(1 - F_a)/2]^{\bar{N}_a^2}$, we see that the error in the initial state is exponentially suppressed with exponent \bar{N}_a^2 . For example, if we assume $\varepsilon \rightarrow 0$, an initial state with $\bar{N}_a = 2$ and a defect at every tenth lattice site, $\mathcal{F}_a = 0.9$, $T/U_a = 0.17$, results in a final state with $1 - \mathcal{F}_b \approx 3 \times 10^{-6}$, i.e., less than one defect every three hundred thousand sites. In an attempt to reduce number fluctuations even further we also considered a regime in which the atoms were allowed to move between neighbouring sites during the filtering process. However, for a fixed mean filling factor and transfer time this produces a lower final state fidelity than performing the filtering in the MI regime.

Taking Poisson statistics instead of the GCE, which corresponds to the BEC being loaded by suddenly switching on the lattice (this can be seen by computing the reduced density operator of the original superfluid state), and assuming a perfect transfer ($\varepsilon = 0$), we obtain $\mathcal{F}_b = 1 - \exp(-\bar{N}_a)$. Thus, to achieve high fidelities $\mathcal{F} > 0.99$ in the final state requires $\bar{N}_a \sim 5$. Such \bar{N}_a values might ultimately be limited by the increase in 3-body collisional losses with many atoms on each site.

This filtering can clearly be extended to transfer multiple atoms into state $|b\rangle$ by choosing δ_f so that the system evolves along more than one avoided crossing (but the same number for all initial N). Similarly, it is possible to choose δ_i and δ_f so that the transfer $|N, 0\rangle \rightarrow |N-1, 1\rangle$ occurs only for initial states with a particular value of N . Thus, we can measure the defects in the initial state, for example by mapping sites with $N_a = \bar{N}_a + 1$ or $N = \bar{N}_a - 1$ atoms onto occupied sites in state $|b\rangle$.

Spatial patterns can be created by adding a superlattice to the lattice trapping atoms in state $|b\rangle$, site-dependently shifting the energy level of $|b\rangle$ and preventing atoms in particular sites from coupling to the Raman transition. This allows the engineering of many high-fidelity spatial states because of the wide range of possible superlattice configurations which can be formed using overlapping laser beams.

Coherent filtering can also be applied to a degenerate Fermi gas [2, 7] in an optical lattice (Fig. 4.3a). We consider spin up and spin down fermions (in states $|a \uparrow, \downarrow\rangle$) loaded into the motional levels of each lattice site according to the Pauli principle. Atoms in any chosen motional level (normally the lowest, as for low temperature and high filling factors it will almost always be occupied) may then be transferred by adiabatic passage to a different internal state, $|b \uparrow, \downarrow\rangle$. An example of appropriate states can be taken from the $2S_{1/2}$ level of ${}^6\text{Li}$ in a strong magnetic field (i.e., in the Paschen-Back regime). We choose $|a \uparrow, \downarrow\rangle = |m_s = \frac{1}{2}; m_I = 0, -1\rangle$ and $|b \uparrow, \downarrow\rangle = |m_s = -\frac{1}{2}; m_I = 1, 0\rangle$, where m_s and m_I denote the magnetic spin quantum number for the electronic and nuclear spins respectively. (Where required, spin-dependent lattices for these states could be implemented for the short times required by coupling the ground states between the $2P_{1/2}$ and $2P_{3/2}$ levels.) As was the case for Bosons, we can apply

a superlattice to the lattice which traps state $|b\rangle$, and hence engineer very high fidelity spatial patterns (Fig. 4.3b). By applying different superlattices during the transfer of different spin states, the ratio of spin up to spin down particles in the final state can also be very precisely controlled.

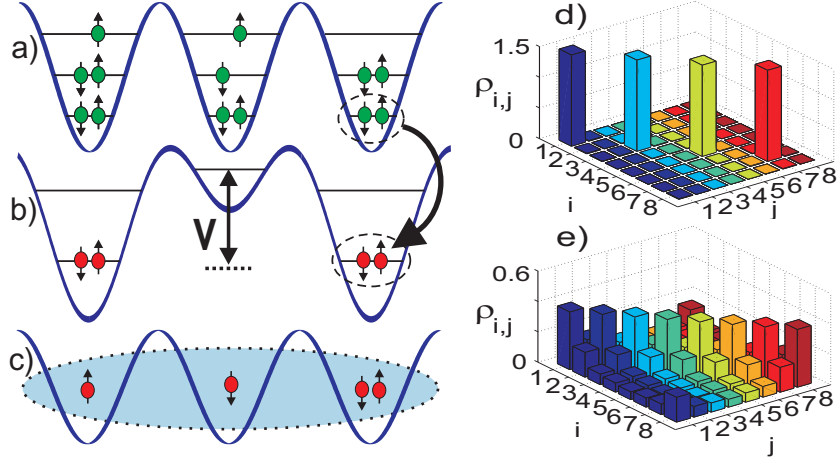


Figure 4.3. The production of (c) a BCS state at exactly half filling in an optical lattice from (a) a degenerate Fermi gas using pattern loading techniques described in the text (a→b). The 3D Plots show the pair correlation function $\rho_{i,j,0}$, illustrating the crossover from (d) localized pairs [$V = 10J$, $U = -10J$, MI Regime (b)] to (e) delocalised pairs [$V = 0$, $U = -0.1J$, BCS regime (c)]. Information about these correlations can be obtained from $\gamma_l = \sum_i \rho_{i-l,i+l}$. These results are from numerical diagonalisation of (4.2) for 8 sites and half filling with periodic boundary conditions.

These techniques, when combined with the ability to move spin-dependent optical lattices [5], can be used to measure two body correlation functions. Currently, single-body correlation functions can be studied using the interference patterns produced when atoms are released from the lattice, and many-body correlation functions for a single site can be estimated from collisional loss rates. However, for fermion systems in a lattice, fourth order correlation functions of the form $\rho_{i,j,l} = \langle \hat{c}_{i+l\uparrow}^\dagger \hat{c}_{i-l\downarrow}^\dagger \hat{c}_{j-l\downarrow} \hat{c}_{j+l\uparrow} \rangle$ (where $c_{i\sigma}$ is the annihilation operator for an atom of spin σ in site i) are of particular interest because they provide information about both about the long range order and the pair correlation length in the system. Specifically, $\kappa_l = \sum_i \langle \hat{c}_{i+l\uparrow}^\dagger \hat{c}_{i-l\downarrow}^\dagger \hat{c}_{i-l\downarrow} \hat{c}_{i+l\uparrow} \rangle$ characterises the correlation as a function of the separation $2l$ between spin up and spin down particles, and $\gamma_k = \sum_i \langle \hat{c}_{i-k\uparrow}^\dagger \hat{c}_{i-k\downarrow}^\dagger \hat{c}_{i+k\downarrow} \hat{c}_{i+k\uparrow} \rangle$ gives us information about the long range order as a function of the separation $2k$ between the pairs. These two functions can be measured by firstly making the lattice potential very deep, and performing the measurement on a timescale shorter than that on which atoms can move to neighbouring sites. Then, to measure κ_l , we first transfer all of the spin down atoms from their current state, $|b \downarrow\rangle$ via an adiabatic passage to the internal state $|a \downarrow\rangle$. We then shift the lattice trapping the state $|a \downarrow\rangle$ $2l$ sites to the left. If we now transfer the particles in state $|a \downarrow\rangle$ to state $|b \downarrow\rangle$ selectively, based on the condition that no particle exists (at a particular site) in

the state $|b \uparrow\rangle$, then the number of atoms left in state $|a \downarrow\rangle$ is proportional to the value of κ_l . This is made possible by the onsite interaction between particles with different spins shifting the detunings at which avoided crossings occur in the energy eigenvalues. A similar process can be used to measure γ_l , but requires an additional step in which we flip the spin of particles in state $|b \downarrow\rangle \rightarrow |b \uparrow\rangle$. Whilst these processes would be difficult to implement experimentally, they can be seen as providing an eventual way to perform a complete tomography of pair correlations in fermion systems.

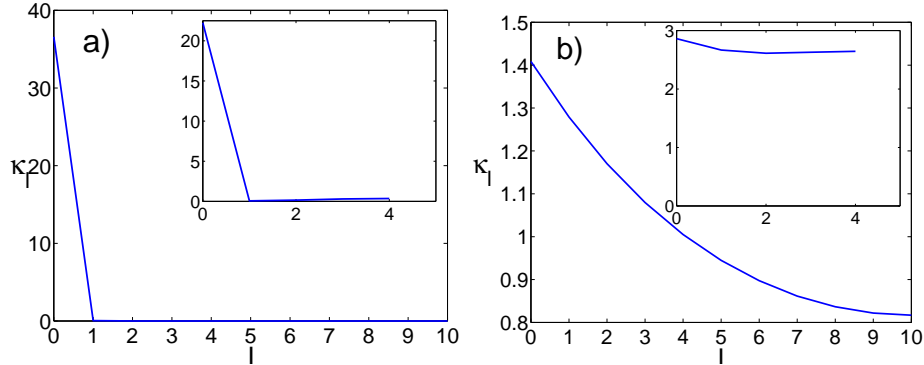


Figure 4.4. Numerical values of κ_l , which describes the pair correlation length. These results are examples from numerical diagonalisation of (4.2) for 40 sites and 1 particle of each spin type and 16 sites and 2 particles of each spin type (inset) with a) $V = 0$, $U = -10J$ and b) $V = 0$, $U = -0.1J$.

Such a characterisation would be particularly useful in the study of the BEC - BCS crossover in an optical lattice [8]. Along with initial state preparation, this is well illustrated by the method to study the MI to BCS state transition in fermions at exactly half-filling shown in Fig. 4.3. We begin by transferring particles of both spin types from a degenerate Fermi gas loaded into an optical lattice (Fig. 4.3a) via adiabatic passage to a different internal state, whilst a superlattice is used to offset even-numbered sites in the final state by a potential V (Fig. 4.3b). This system is then described by the Hamiltonian

$$\hat{H} = -J \sum_{\langle i,j \rangle, \sigma} \hat{c}_{i\sigma}^\dagger \hat{c}_{j\sigma} + U \sum_{i=1}^N \hat{n}_{i\uparrow} \hat{n}_{i\downarrow} + \frac{V}{2} \sum_{i,\sigma} (-1)^i \hat{n}_{i,\sigma}, \quad (4.2)$$

where $\langle i, j \rangle$ denotes all nearest neighbour combinations and $\hat{n}_{i,\sigma} = \hat{c}_{i,\sigma}^\dagger \hat{c}_{i,\sigma}$. U denotes the onsite interaction between particles of different spin, which we choose to make initially large and negative, using a combination of lattice parameters, and, if necessary, a Feshbach resonance [7]. Thus we prepare a state with exactly half-filling (note that other filling factors are possible with different superlattices), consisting of pre-formed pairs in the odd numbered sites (Fig. 4.3b, 4.3d). We slowly decrease V to a small value, $V < J \ll U$, allowing the pairs to delocalise. For small V but large $|U|$, the pairs behave as a gas of hard-core Bosons. Following the discussion in [9], we find that the system is protected throughout this process by an energy gap of V . This resulting state is characterised by a very short inter-particle correlation length, measurable through the correlation function κ_l (Fig. 4.4a).

We then lower the onsite interaction until $|U| < J$, so that the spin up and spin down particles can move independently. A meanfield treatment [10] shows that even in the weak coupling limit the state is protected by an energy gap which is no less than V . Once the BCS state of Cooper pairs sets in [8], we can set $V \rightarrow 0$ by completely removing the superlattice. The system thus undergoes a transition into a BCS state (Fig. 4.3c, 4.3e), characterised by its long pair correlation length, again measurable using κ_l (Fig. 4.4b).

In summary, the coherent filtering scheme presented here allows the production of high-fidelity atomic crystals, and the measurement of important correlation functions. These features will greatly enhance the application of atoms in optical lattices to quantum computation and to the precise modeling of condensed matter systems.

We thank D. Jaksch, L. Tian, M. Bijlsma, and members of R. Grimm's group for discussions. Work was supported in part by the Austrian Science Foundation, E.U. Networks, and the Institute for Quantum Information.

Bibliography

- [1] For a review, see Nature **416** (2002).
- [2] B. DeMarco and D. S. Jin, Science **285**, 1703 (1999); A. G. Truscott, K. E. Strecker, W. I. McAlexander, G. B. Partridge, and R. G. Hulet, *ibid.* **291**, 2570 (2001); G. Roati, F. Riboli, G. Modugno, and M. Inguscio, Phys. Rev. Lett. **89**, 150403 (2002).
- [3] D. Jaksch, C. Bruder, J. I. Cirac, C. W. Gardiner, and P. Zoller, Phys. Rev. Lett. **81**, 3108 (1998).
- [4] M. Greiner, O. Mandel, T. W. Hänsch, and I. Bloch, Nature **415**, 39 (2002); M. Greiner *et al.*, *ibid.* **419**, 51 (2002); W. Hofstetter, J. I. Cirac, P. Zoller, E. Demler, and M. D. Lukin, Phys. Rev. Lett. **89**, 220407 (2002); D. Jaksch *et al.*, *ibid.* **82**, 1975 (1999); E. Charron, E. Tiesinga, F. Mies, and C. Williams, *ibid.* **88**, 077901 (2002); G. K. Brennen, C. M. Caves, P. S. Jessen, and I. H. Deutsch, *ibid.* **82**, 1060 (1999); L.-M. Duan, E. Demler, and M. D. Lukin, cond-mat/0210564 (2002) [Phys. Rev. Lett. **91**, 090402 (2003)]; S. L. Rolston, Private Communication.
- [5] O. Mandel *et al.*, Phys. Rev. Lett. **91**, 010407 (2003).
- [6] E. L. Bolda, E. Tiesinga, and P. S. Julienne, Phys. Rev. A **66**, 013403 (2002); E. A. Donley, N. R. Claussen, S. T. Thompson, and C. E. Wieman, Nature **417**, 529 (2002).
- [7] T. Loftus, C. A. Regal, C. Ticknor, J. L. Bohn, and D. S. Jin, Phys. Rev. Lett. **88**, 173201 (2002); S. Jochim *et al.*, *ibid.* **89**, 273202 (2002); K. Dieckmann *et al.*, *ibid.* **89**, 203201 (2002); T. Bourdel *et al.*, cond-mat/0303079 (2003) [Phys. Rev. Lett. **91**, 020402 (2003)].
- [8] R. Micnas, J. Ranninger, and S. Robaszkiewicz, Rev. Mod. Phys. **62**, 113 (1990)
- [9] H. P. Büchler, G. Blatter, and W. Zwerger, cond-mat/0208391 (2002) [Phys. Rev. Lett. **90**, 130401 (2003)].
- [10] A. J. Daley and P. O. Fedichev, unpublished.

CHAPTER 5

PUBLICATION

Single Atom Cooling by Superfluid Immersion: A Non-Destructive Method for Qubits[†]

Phys. Rev. A **69**, 022306 (2004)

A. J. Daley, P. O. Fedichev, and P. Zoller

*Institut für Theoretische Physik, Universität Innsbruck,
A-6020 Innsbruck, Austria*

We present a scheme to cool the motional state of neutral atoms confined in sites of an optical lattice by immersing the system in a superfluid. The motion of the atoms is damped by the generation of excitations in the superfluid, and under appropriate conditions the internal state of the atom remains unchanged. This scheme can thus be used to cool atoms used to encode a series of entangled qubits non-destructively. Within realisable parameter ranges, the rate of cooling to the ground state is found to be sufficiently large to be useful in experiments.

5.1 Introduction

Neutral atoms are one of the most promising candidates as carriers for the storage and manipulation of quantum information [1]. Qubits may be stored in long-lived internal atomic states with very low levels of decoherence, and may be manipulated using interactions between the atoms and external devices (such as lasers) or interactions amongst the atoms themselves.

An experimental prerequisite for this is the development of techniques to trap single atoms, and there has been much progress over the last five years both in optical traps [2, 3] and in magnetic microtraps [4]. In addition, specific implementation of quantum computing usually requires cooling of atoms to the vibrational ground state of the trap, or at least to the Lamb-Dicke limit. Many techniques have been developed including the widespread use of laser cooling [5].

[†]The author of the present thesis performed all of the calculations in this publication, except those of the dispersion relation for a foreign particle in a superfluid found in Appendix A.

One of the most promising routes to quantum computation with neutral atoms is the use Bose Einstein Condensates (BECs) [6] loaded in optical lattices [7, 8], a system which has been realised in part in a number of recent experiments [3, 9–11]. There are several theoretical proposals for the implementation of quantum logic gates in such systems [12–16], and the first steps towards the fundamental experimental techniques required for some of these have been recently realised. For example, the recent demonstration of spin-dependent transport in an optical lattice [9] makes possible the implementation of a fundamental quantum phase gate by cold controlled collisions [12] in which qubits are encoded using two different internal states of the atoms in the optical lattice.

However, most of these proposals require the transport of qubits, which is usually associated with heating of the atomic motion [9]. A question then arises as to how that motion may be cooled back to the ground state without changing the internal state of the atoms, and thus destroying the qubits or their entanglement. Laser cooling, for example, is clearly not applicable here as the process of light scattering causes decoherence. The same problem arises in scalable ion trap quantum computing, and there it has been overcome using sympathetic cooling schemes, in which ions used to encode qubits are cooled via a coulomb interaction with either a single ion which is directly laser-cooled [17] or another species of ions which are directly laser-cooled [18]. In a different context, sympathetic cooling schemes are also widely used in the field of cold quantum gases, where they have been used to cool different spin states of the same atomic species [19], to cool different Bosonic species [20], and to cool Fermi gases brought into contact with a BEC [21].

In this article we consider the sympathetic cooling of a single atom in a harmonic trap in contact with a superfluid. This is readily expanded to the case of many harmonic traps, which is a good approximation for an optical lattice without tunneling. The motion of the atom is damped by the generation of excitations in the superfluid, and the resulting cooling rates are sufficiently large to be useful experimentally. In addition, decoherence of a qubit encoded on the atoms can be eliminated in this scheme provided that the internal atomic states used to encode the qubit are chosen carefully in order to satisfy particular collisional requirements.

5.2 Overview

In this section we give a short summary of the most important results contained in this article. Derivations and further discussions of these results follow in the remaining sections.

Our goal is to cool a single trapped atom representing a qubit $|0\rangle, |1\rangle$ without destroying the superposition state of the qubit (or the entangled state in case of many atoms). Cooling of the atom is achieved by sympathetic cooling, immersing the atom in a superfluid, which plays the role of a very cold reservoir. By a proper encoding of the qubit in internal atomic states, and choice of the atomic level for the superfluid reservoir (see section 5.3.1) we can ensure that (i) the qubit is not destroyed by opening collisional channels to unwanted final states, and (ii) the $|0\rangle$ and $|1\rangle$ states have identical collisional properties with respect to the collisional interactions with the superfluid, and thus the collisions do not randomise the relative phases of the qubit.

Cooling is considered within a model in which the atoms are treated as being trapped in independent 1D Harmonic oscillator potentials with trapping frequency ω , and interact with the superfluid via a density-density interaction, generating excitations in the superfluid, which are modeled as Bogoliubov excitations in a weakly interacting Bose gas (section 5.3) and have momentum $\hbar\mathbf{q}$ and energy ε_q . In discussing this cooling process we can restrict ourselves to a single component of the qubit $|0\rangle$ (or $|1\rangle$). Justification for the use of a density-density interaction is provided in appendix 5.A, where the dispersion relation for a free foreign particle interacting with a superfluid is derived.

A master equation is derived for the density operator of this system (section 5.3.3 and appendix 5.B), from which the time evolution of the probability p_n that the atom is in the n th motional state of the Harmonic oscillator potential is shown to be

$$\dot{p}_m = \sum_{n>m} F_{n\rightarrow m} p_n - \sum_{n'<m} F_{m\rightarrow n'} p_m + \sum_n H_{n,m} (p_n - p_m). \quad (5.1)$$

The terms with coefficient $F_{n\rightarrow m}$,

$$F_{n\rightarrow m} = \frac{2\pi}{\hbar} \sum_{\mathbf{q}} |Z_{n,m}(\mathbf{q})|^2 \delta(\hbar\omega(n-m) - \varepsilon_q), \quad (5.2)$$

where $Z_{n,m}$ are the matrix elements of the interaction Hamiltonian in the basis of Harmonic oscillator energy eigenstates (Fock states), describe the transitions from state n to state m due to generation of excitations in the superfluid, and the terms with coefficient $H_{n,m}$,

$$H_{m,n} = \frac{2\pi}{\hbar} \sum_{\mathbf{q}} N(\mathbf{q}) |Z_{n,m}(\mathbf{q})|^2 \delta(\hbar\omega|n-m| - \varepsilon_q), \quad (5.3)$$

describe the transitions between state n and state m due to interactions with thermal excitations at finite temperatures. This is illustrated in Fig. 5.1.

If the speed of sound in the superfluid is u , and the mass of superfluid atoms is m_b , then the behaviour of the cooling process can be separated into two regimes - where the motion of the oscillating atom is subsonic ($\hbar\omega \ll m_b u^2/2$) or supersonic ($\hbar\omega \gg m_b u^2/2$). In the supersonic regime, cooling from any excited oscillator state occurs directly to all lower energy states, including a significant transition rate directly to the ground state (section 5.4.1). The resulting rate of energy loss $\dot{\varepsilon}(n)$ for a particle in the n th oscillator state is not linear in n , but instead (for lattice and superfluid atoms of equal mass m) is found to be

$$\dot{\varepsilon}(n) \approx -\frac{g_{ab}^2 \rho_0 m^{3/2}}{\pi \hbar^4 \sqrt{2}} \alpha [\varepsilon(n)]^{3/2}, \quad (5.4)$$

where g_{ab} is the coupling constant for interactions between the atoms in the lattice and the superfluid, ρ_0 is the condensate density, $\varepsilon(n) = \hbar\omega n$, and $\alpha \sim 0.3$ is a constant.

If we consider the slowest transition rate, that from the first excited state to the ground state, we find that the characteristic transition time, τ , is given by

$$\frac{\omega \tau_{1\rightarrow 0}}{2\pi} \sim 1.2 \times 10^{-2} \times \frac{1}{\rho_0 a_{ab}^3} \frac{a_{ab}}{l_0}, \quad (5.5)$$

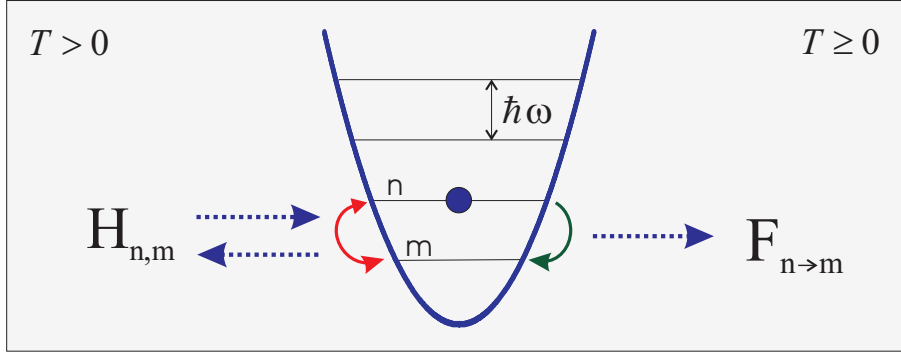


Figure 5.1. *The motion of an atom in a harmonic trap immersed in a superfluid is cooled by the generation of excitations in the superfluid. Terms in the equations of motion with coefficients $F_{n \rightarrow m}$ describe transitions from oscillator state $|n\rangle$ to state $|m\rangle$ by creation of excitations, whilst finite temperature contributions with coefficients $H_{n,m}$ account for the interaction of the system with thermal excitations.*

where a_{ab} is the scattering length for the interaction between atoms in the lattice and the superfluid, and $l_0 = \sqrt{\hbar/(m\omega)}$ is the size of the harmonic oscillator ground state. Thus, as l_0 is typically an order of magnitude larger than a_{ab} , and $\rho_0 a_{ab}^3 \sim 10^{-4}$, τ is of the order of 10 oscillator cycles. This is a sufficiently rapid cooling rate to be useful experimentally.

In the subsonic regime, damping still occurs because the oscillatory motion of the atom is accelerated (section 5.4.2). Significant rates are found only for transitions between neighbouring oscillator levels, and $\dot{\epsilon}(n)$ is found to be linear in n ,

$$\dot{\epsilon}(n) \approx -\frac{g_{ab}^2 \rho_0 \omega^4}{12\pi m_a m_b u^7} \epsilon(n). \quad (5.6)$$

When the superfluid is at a finite superfluid temperature T , the system is cooled to the temperature T of the superfluid. The final distribution of occupation probabilities is shown to be a Boltzmann distribution,

$$\bar{p}_n = \bar{p}_0 e^{-n\hbar\omega/(k_B T)} = \left(1 - e^{-\hbar\omega/(k_B T)}\right) e^{-n\hbar\omega/(k_B T)}, \quad (5.7)$$

where k_B is the Boltzmann constant (section 5.4.3). If the temperature corresponds to an energy much smaller than the Harmonic oscillator spacing, $k_B T \ll \hbar\omega$, then the population in excited motional states is negligible. For example, if $\omega \sim 2\pi \times 10^5 \text{s}^{-1}$, $\hbar\omega/k_B \sim 5\mu\text{K}$, so that for $T = 500\text{nK}$, we then obtain $1 - \bar{p}_0 \approx 5 \times 10^{-5}$.

The situation in which the collisional interaction between atoms in the lattice and superfluid atoms are not identical for the two qubit states $|0\rangle$ and $|1\rangle$ is considered in section 5.5. If the scattering lengths for interactions between atoms in the qubit states and atoms in the superfluid, a_{ab} is expressed as a_0 and a_1 for atoms from each of the two qubit states, then the rate of decoherence is found to be proportional to $(a_1 - a_0)^2$. This rate is also proportional to the transition rate between motional states, except for an ‘‘initial slip’’ in the decoherence

(also proportional to $(a_1 - a_0)^2$) which occurs on the timescale of approximately one oscillator cycle.

A semiclassical treatment of this system in the WKB approximation (section 5.6) gives a result for the supersonic case which is different from the full quantum result by only 12%. A similar treatment in the strongly subsonic regime gives exact agreement with the earlier result.

In section 5.7 we investigate a somewhat different model for the excitations, in the context of a quasi-1D superfluid. The resulting damping rates are found to be small except in the regime where the superfluid is very strongly interacting, which is a difficult regime to obtain experimentally. Finally, appendix 5.C contains semiclassical estimates for small additional damping terms which arise at finite temperatures and have been neglected in earlier calculations.

5.3 The Model

5.3.1 Avoiding Decoherence

The total Hamiltonian of the cooling process for a single atom can be written as

$$\hat{H}_{\text{tot}} = \hat{H}_{\text{qubit}} + \hat{H}_{\text{motion}} + \hat{H}_{\text{superfluid}} + \hat{H}_{\text{int}}, \quad (5.8)$$

where \hat{H}_{qubit} is the Hamiltonian for the internal states of the atom, denoted $|0\rangle$ and $|1\rangle$, on which the qubit is encoded, \hat{H}_{motion} is the Hamiltonian for the atomic motion of the atom which is to be cooled, $\hat{H}_{\text{superfluid}}$ is the Hamiltonian for the superfluid, and \hat{H}_{int} describes the interaction between the atom and the superfluid. In order to cool a qubit without decoherence, the internal state of the atom being cooled should remain unchanged during the cooling process. If we write the initial internal state of an atom in a particular lattice site as $|\psi\rangle$, and the combined density operator for the initial mixed motional state of the atom and the state of the superfluid as $\hat{R}(0)$, so that the total initial density operator is $|\psi\rangle\langle\psi| \otimes \hat{R}(0)$, then the overall Hamiltonian for the cooling process, \hat{H}_{tot} , must satisfy

$$e^{-i\hat{H}_{\text{tot}}t/\hbar} |\psi\rangle\langle\psi| \otimes \hat{R}(0) e^{i\hat{H}_{\text{tot}}t/\hbar} = |\psi\rangle\langle\psi| \otimes \hat{R}(t). \quad (5.9)$$

Thus \hat{H}_{tot} must be of the form $\hat{H}_{\text{tot}} = (|0\rangle\langle 0| + |1\rangle\langle 1|) \otimes \hat{H}$. This requirement is satisfied provided that the interaction Hamiltonian, \hat{H}_{int} is independent of the internal state of the atom in the lattice. Thus, the trap potential must be the same for the two internal states $|0\rangle$ and $|1\rangle$, and the scattering length a_{ab} between atoms in the superfluid and atoms in the lattice [22] must also be the same for the two internal states. The identical scattering lengths can be arranged by choosing symmetric spin configurations, for example, by choosing $|0\rangle$ and $|1\rangle$ to be internal states with angular momentum quantum number $F = 1$ and magnetic quantum numbers $m_F = \pm 1$, and the superfluid atoms to be in an internal state with $F = 1$ and $m_F = 0$. In order to make such a configuration stable against spin-exchanging collisions [23], these states should all be in the ground state of the manifold, and to prevent the creation of pairs of lattice atoms from superfluid atoms [24], the energy of the $m_F = 0$ level should be lowered with respect to the $m_F = \pm 1$ states (for example by using a laser [25]).

We must also ensure that when we have N qubits ($N > 1$), the entanglement between them is not destroyed when the motion of one or more of them is cooled. The condition in Eq. (5.9) is once again sufficient for the suppression of decoherence, but now $|\psi\rangle$ is the total internal state of the N -qubit system, and \hat{W} is the total combined density operator for the motional state of each qubit and the state of the environment. Physically, the condition is now modified so that the interaction between any atom and the superfluid must be both independent of the internal state of that atom, and independent of the internal state of all other atoms. Because the interaction is a density-density interaction, this second requirement is always fulfilled. Note that when the correlation length of the superfluid is shorter than the separation between atoms, it is possible for the motional state of different atoms to become entangled. However, this will not affect the state of the N -qubit system, as the qubits are encoded solely on the internal states of the atoms, which remain at all times separable from the motional states. The situation in which the states used to encode the qubit are not appropriately chosen to ensure symmetry in the collisional interactions is considered in section 5.5.

5.3.2 Hamiltonian for the Oscillator-Superfluid Interaction

After imposing the requirement from the preceding section, we consider only the motional degrees of freedom of the atoms in the optical lattice, which are assumed to be confined in particular lattice sites where the motional states can be approximated as those of an harmonic oscillator. Coupling to the superfluid occurs in the form of a density-density interaction that generates excitations in the superfluid, which we model as Bogoliubov excitations in a weakly interacting Bose gas [26]. The Hamiltonian for the combined system of an atom in a lattice site and the superfluid (for the motional atomic degrees of freedom only) is given by

$$\hat{H} = \hat{H}_{\text{motion}} + \hat{H}_{\text{superfluid}} + \hat{H}_{\text{int}}, \quad (5.10)$$

where \hat{H}_{motion} is a 3D harmonic oscillator Hamiltonian with frequency ω , which describes the motional state of the atom, $\hat{H}_{\text{superfluid}}$ is the Hamiltonian for the superfluid excitations, and \hat{H}_{int} is the interaction Hamiltonian.

$$\hat{H}_{\text{superfluid}} = E_0 + \sum_{\mathbf{q} \neq 0} \varepsilon(\mathbf{q}) \hat{b}_{\mathbf{q}}^\dagger \hat{b}_{\mathbf{q}}, \quad (5.11)$$

where $\hat{b}_{\mathbf{q}}^\dagger$ and $\hat{b}_{\mathbf{q}}$ are creation and annihilation operators for Bogoliubov excitations in the superfluid with momentum $\hbar\mathbf{q}$ and energy $\varepsilon(\mathbf{q})$, and E_0 is the ground state energy of the superfluid.

$$\begin{aligned} \hat{H}_{\text{int}} &= g_{ab} \int \delta\hat{\rho}(\mathbf{r}) \delta\hat{\rho}_{\text{atom}}(\mathbf{r}) d^3\mathbf{r} \\ &= g_{ab} \int \delta\hat{\rho}(\mathbf{r}) \delta(\mathbf{r} - \hat{\mathbf{r}}) d^3\mathbf{r} = g_{ab} \delta\hat{\rho}(\hat{\mathbf{r}}), \end{aligned} \quad (5.12)$$

where $\delta\hat{\rho}_{\text{atom}}$ is the density operator for the motion of the atom, $\hat{\mathbf{r}}$ is the position operator for the atomic motional states, $\delta\hat{\rho}$ is the density fluctuation operator in the superfluid, and $g_{ab} = 4\pi\hbar^2 a_{ab}/(2\mu)$ is the coupling constant for the interaction, with a_{ab} the scattering

length for interactions between superfluid atoms and atoms in the lattice [22], and $\mu = (m_a m_b)/(m_a + m_b)$ the reduced mass of an atom in the lattice with mass m_a and a superfluid atom with mass m_b . The density fluctuation operator may be expressed as $\delta\hat{\rho} = \hat{\Psi}^\dagger \hat{\Psi} - \rho_0$ where $\hat{\Psi} = \sqrt{\rho_0} + \delta\hat{\Psi}$ is the second quantised field operator for the superfluid and ρ_0 is the mean condensate density. In terms of the creation and annihilation operators for Bogoliubov excitations, we can write

$$\delta\hat{\Psi} = \frac{1}{\sqrt{V}} \sum_{\mathbf{q}} \left(u_{\mathbf{q}} \hat{b}_{\mathbf{q}} e^{i\mathbf{q}\cdot\mathbf{r}} + v_{\mathbf{q}} \hat{b}_{\mathbf{q}}^\dagger e^{-i\mathbf{q}\cdot\mathbf{r}} \right), \quad (5.13)$$

where V is the normalisation volume,

$$u_{\mathbf{q}} = \frac{L_{\mathbf{q}}}{\sqrt{1 - L_{\mathbf{q}}^2}}, \quad v_{\mathbf{q}} = \frac{1}{\sqrt{1 - L_{\mathbf{q}}^2}}, \quad (5.14)$$

and

$$L_{\mathbf{q}} = \frac{\varepsilon_{\mathbf{q}} - (\hbar\mathbf{q})^2/(2m) - mu^2}{mu^2}. \quad (5.15)$$

The energy of excitations with momentum $\hbar\mathbf{q}$ is

$$\varepsilon_{\mathbf{q}} = [u^2(\hbar\mathbf{q})^2 + (\hbar\mathbf{q})^4/(2m_b)^2]^{1/2}, \quad (5.16)$$

and the speed of sound can be expressed as, $u = \sqrt{g_{bb}\rho_0/m_b}$, where $g_{bb} = 4\pi\hbar a_{bb}/m_b$ with a_{bb} the scattering length for interactions between atoms in the superfluid [26]. In a weakly interacting Bose gas at sufficiently low temperatures (where the condensate density is much smaller than the density of the normal component), the term from $\delta\hat{\Psi}^\dagger \delta\hat{\Psi}$ may be neglected (see appendix 5.C). In this case we can write

$$\delta\hat{\rho} = \sqrt{\frac{\rho_0}{V}} \sum_{\mathbf{q}} \left((u_{\mathbf{q}} + v_{\mathbf{q}}) \hat{b}_{\mathbf{q}} e^{i\mathbf{q}\cdot\mathbf{r}} + (u_{\mathbf{q}} - v_{\mathbf{q}}) \hat{b}_{\mathbf{q}}^\dagger e^{-i\mathbf{q}\cdot\mathbf{r}} \right). \quad (5.17)$$

For the motion of atoms in the lattice, we make the approximation that the damping of in each dimension can be considered independently, and thus we treat the atom as a 1D oscillator with frequency ω , i.e.,

$$\hat{H}_{\text{atom}} = \hbar\omega \left(\hat{a}^\dagger \hat{a} + \frac{1}{2} \right), \quad (5.18)$$

where \hat{a} is the lowering operator for the motional state of the atom. The position operator for the 1D oscillator is $\hat{x} = \sqrt{\hbar/(2m_a\omega)}(\hat{a} + \hat{a}^\dagger)$, where m_a is the mass of the atoms in the lattice. We can also write $\mathbf{q}\cdot\hat{\mathbf{r}} \rightarrow q_x \hat{x}$, where q_x is the component of \mathbf{q} in the direction of the oscillator motion.

5.3.3 Damping Equations

In deriving equations for the damping of the system we assume that the cooling rate is significantly slower than the period of the oscillator, and we treat the BEC as a reservoir in

which the correlation time is much shorter than the correlation time of atoms in the lattice. Under these assumptions, the master equation for reduced density operator describing the motional state of an atom in the lattice, $\hat{w}(t) = \text{Tr}_R[\hat{W}(t)]$, where Tr_R denotes the trace over the superfluid states, is derived in Appendix 5.B.

We define the projection operator, $\hat{\mathcal{P}}$, onto a basis diagonal in the oscillator Fock states $|m\rangle$ ($H_{\text{motion}}|m\rangle = \hbar\omega(m + 1/2)|m\rangle$) as

$$\hat{\mathcal{P}}\hat{X} = \sum_m |m\rangle\langle m| \langle m|\hat{X}|m\rangle, \quad (5.19)$$

so that

$$\hat{\mathcal{P}}\hat{w}(t) = \sum_m |m\rangle\langle m|p_m. \quad (5.20)$$

Because we assumed that the oscillator trap frequency $\omega \gg \tau^{-1}$, where τ is the characteristic timescale on which transitions take place due to interaction with the superfluid, the coupling to off-diagonal elements of $\hat{w}(t)$ in the Fock state basis is very small, and the state occupation probabilities p_n satisfy a closed set of equations. From appendix 5.B we then see that

$$\dot{p}_m = \sum_{n>m} F_{n\rightarrow m}p_n - \sum_{n'<m} F_{m\rightarrow n'}p_m + \sum_n H_{n,m}(p_n - p_m). \quad (5.21)$$

Here $F_{n\rightarrow m}$ is the damping coefficient at zero temperature for transitions from state n to state m , and $H_{n,m}$ are the coefficients of the finite temperature corrections due to the absorption and scattering of thermal excitations. The zero temperature damping coefficients are

$$F_{n\rightarrow m} = \frac{2\pi}{\hbar} \sum_{\mathbf{q}} |Z_{n,m}(\mathbf{q})|^2 \delta(\hbar\omega(n - m) - \varepsilon_{\mathbf{q}}), \quad (5.22)$$

and the

system matrix elements of the interaction Hamiltonian are given by

$$Z_{n,m}(\mathbf{q}) = \langle m|\hat{H}_{\text{int}}|n\rangle = (u_{\mathbf{q}} + v_{\mathbf{q}})g_{ab}\sqrt{\frac{\rho_0}{V}}\langle m|e^{-iq_x\hat{x}}|n\rangle. \quad (5.23)$$

Note that (5.22) is Fermi's Golden rule for the transition from state $|m\rangle$ to state $|n\rangle$ via interaction with density fluctuations in the superfluid, and that the restrictions on the summation in (5.21) are written for clarity, but actually result from the delta function in (5.22), due to which $F_{n\rightarrow m}$ is only nonzero when $n > m$.

The finite temperature corrections are given by

$$H_{m,n} = \frac{2\pi}{\hbar} \sum_{\mathbf{q}} N(\mathbf{q})|Z_{n,m}(\mathbf{q})|^2 \delta(\hbar\omega|n - m| - \varepsilon_{\mathbf{q}}), \quad (5.24)$$

where $N(\mathbf{p}) = (\exp[\varepsilon_p/(k_B T)] - 1)^{-1}$ is the mean number of thermal Bogoliubov excitations with momentum $\hbar\mathbf{p}$ present in the superfluid, with T being the temperature in the normal component of the gas and k_B the Boltzmann constant. Because we are interested in cooling the system to its ground state, we assume that the temperature of the superfluid is small,

$k_B T \ll \hbar\omega$. This is very realistic experimentally, and in this regime we can make the approximation $H_{n,m} \approx 0$. The consequences of these terms are described in section 5.4.3.

Also note that in the derivation of these equations we assume that the terms in $\delta\hat{\rho}$ arising from $\delta\hat{\Psi}\delta\hat{\Psi}^\dagger$ may be neglected. This approximation holds when the temperature is much smaller than the critical temperature, so that the condensate density, ρ_0 , is much larger than the density of the thermal component. The contribution from these terms at finite temperatures is estimated in appendix 5.C.

From the transition rates, the energy dissipation rate of an oscillator in the state $|n\rangle$ can then be calculated as

$$\dot{\epsilon}(n) = \sum_m \hbar\omega(n-m)H_{m,n} - \sum_{m<n} \hbar\omega(n-m)F_{n\rightarrow m}. \quad (5.25)$$

The total energy dissipation rate for an atom in a mixed state can be written as $\dot{\epsilon} = \sum_n \hbar\omega n \dot{p}_n$, which in terms of (5.25) is given by $\dot{\epsilon} = \sum_n \dot{\epsilon}(n)p_n$.

5.3.4 Supersonic and Subsonic Motion Regimes

We note that for typical experimental parameters in the lattice and the BEC, $\hbar\omega \gg m_b u^2/2$. For example, a Rubidium BEC with density $\rho_0 \sim 10^{14} \text{ cm}^{-3}$ and scattering length $a_{bb} \sim 100a_0$, where a_0 is the Bohr Radius, has $m_b u^2/(2\hbar) = 2\pi \times 3.7 \times 10^2 \text{ s}^{-1}$, whilst typically for an atom trapped in an optical lattice, $\omega \sim 2\pi \times 10^5 \text{ s}^{-1}$. Thus, as the maximum velocity of the atom may be estimated as $\sqrt{2\hbar\omega/m_a}$, we see that for a typical experimental system and $m_a \sim m_b$, the atom velocities are supersonic. In this strongly supersonic regime the requirements of energy conservation in (5.22) mean that even for a transition between states where m and n differ only by 1, the excitations are in the particle branch of the Bogoliubov excitation spectrum. In this regime, the momentum of excitations generated in the superfluid $\hbar q \gg m_b u$ as $\hbar^2 q^2/(2m_b) \geq \hbar\omega \gg m_b u^2/2$. Hence, $\epsilon_q \approx \hbar^2 q^2/(2m_b)$, and $|u_q + v_q|^2 \approx 1$.

If the superfluid was made sufficiently dense or strongly interacting, or the oscillator frequency ω was made sufficiently small that the motion of the oscillating atom was subsonic for all oscillator states which are initially excited, then energy conservation would cause the excitations to be in the phonon branch of the spectrum. In this regime, the momentum of excitations generated in the superfluid $\hbar q \ll m_b u$, so that $\epsilon_q \approx \hbar u q$, and $|u_q + v_q|^2 \approx \hbar k/(2m_b u)$.

Note that the coefficients $u_{\mathbf{q}}$ and $v_{\mathbf{q}}$ can be related to the dynamic structure factor $S(\mathbf{k}, \tilde{\omega})$ of the superfluid which is often used in relevant literature [27]. In terms of the symbols used here, $S(\mathbf{k}, \tilde{\omega}) = |u_k + v_k|^2$. In the same way as previously discussed, $S(\mathbf{k}, \tilde{\omega}) \approx 1$ for large values of $k \gg m_b u/\hbar$, whilst for small k , $S(\mathbf{k}, \tilde{\omega}) \propto k$.

In the following, we treat both the supersonic and subsonic regimes. As discussed previously, the supersonic regime is the more relevant of the two in current experiments. However, the subsonic regime could be specifically engineered in experiments, and provides an interesting comparison in terms of the physics of the damping mechanism.

5.4 Results

The matrix elements in (5.23) can be expressed in the position representation as

$$\langle m | e^{-iq_x \hat{x}} | n \rangle = \int_{-\infty}^{\infty} e^{-iq_x x} \psi_n^*(x) \psi_m(x) dx, \quad (5.26)$$

where $l_0 = \sqrt{\hbar/(m_a \omega)}$ is the oscillator length, q_x is the component of \mathbf{q} in the direction of the oscillator, $\psi_n(x) = e^{-x^2/(2l_0^2)} H_n(x/l_0) / \sqrt{l_0 2^n n! \sqrt{\pi}}$ is the position wavefunction for the state $|n\rangle$, and $H_n(x)$ is a Hermite Polynomial. Using the identity $\int_{-\infty}^{\infty} dx e^{-(x-y)^2} H_m(x) H_n(x) dx = 2^n \sqrt{\pi} m! y^{n-m} L_m^{n-m}(-2y^2)$, which assumes $m \leq n$, we can express the matrix elements (for $m < n$) as

$$\langle m | e^{-iq_x \hat{x}} | n \rangle = \sqrt{\frac{m!}{n!}} e^{-l_0^2 q_x^2 / 4} \left(\frac{-il_0 q_x}{\sqrt{2}} \right)^{n-m} L_m^{n-m} \left(\frac{l_0^2 q_x^2}{2} \right), \quad (5.27)$$

so that

$$\begin{aligned} F_{n \rightarrow m} &= \frac{g_{ab}^2 \rho_0}{2\pi \hbar} \frac{m!}{n!} \int_0^\infty q^2 dq \delta(\hbar\omega(n-m) - \varepsilon_q) \frac{\sqrt{2}}{l_0 q} |u_q + v_q|^2 \\ &\times \int_{-l_0 q / \sqrt{2}}^{l_0 q / \sqrt{2}} d\xi e^{-\xi^2} \xi^{2(n-m)} |L_m^{n-m}(\xi^2)|^2. \end{aligned} \quad (5.28)$$

This expression can be further analysed separately in the supersonic and subsonic motion regimes, where the resulting behaviour is remarkably different.

5.4.1 Supersonic Case

Applying to (5.28) the approximations given in section 5.3.4 for the case of supersonic motion yields the expression

$$\begin{aligned} F_{n \rightarrow m} &= \int_{-\sqrt{(n-m)(m_b/m_a)}}^{\sqrt{(n-m)(m_b/m_a)}} d\xi e^{-\xi^2} \xi^{2(n-m)} |L_m^{n-m}(\xi^2)|^2 \\ &\times \frac{g_{ab}^2 \rho_0 m_b}{\pi \hbar^3 l_0 \sqrt{2}} \frac{m!}{n!}. \end{aligned} \quad (5.29)$$

The dimensionless function $F'_{n \rightarrow m} = \pi \hbar^3 l_0 \sqrt{2} F_{n \rightarrow m} / (g_{ab}^2 \rho_0 m_b)$ is plotted in Fig. 5.2, and shows the dependence of $F_{n \rightarrow m}$ on n and m . It is immediately clear that for all $m < n$ the transition rate coefficient is significant. In fact, for all states $|n\rangle$, the transition rate directly to the ground state is of the same order as all other allowed transitions. This corresponds to the atomic motion generating a rich distribution of superfluid excitations, which is characteristic of the regime where the motion of the atom is supersonic with respect to the velocity of sound in the superfluid (see section 5.4.2 for a comparison).

If we consider the energy dissipation rate (5.25) for a system in state $|n\rangle$ in the low temperature limit ($k_B T \ll \hbar\omega$), then we see that the largest contribution comes from transitions

directly to the ground state or first excited state (Fig. 5.3). In addition, the complicated excitation spectrum results in a non-exponential energy damping law, i.e., the energy dissipation rate for a state n is not proportional to the energy of the state. We find instead for $m_a = m_b = m$ (Fig. 5.4) that

$$\dot{\varepsilon}(n) = -\frac{g_{ab}^2 \rho_0 m^{3/2}}{\pi \hbar^4 \sqrt{2}} \alpha [\varepsilon(n)]^{3/2}, \quad (5.30)$$

where $\alpha = 0.3$, and $\varepsilon(n) = \hbar \omega n$ is the energy of state n measured with respect to the ground state. The total energy with respect to the ground state is then $\varepsilon = \sum_n \varepsilon(n) p_n$, so that $\dot{\varepsilon} = -\tilde{\alpha} \sum_n [\varepsilon(n)]^{3/2} p_n \approx -\tilde{\alpha} \varepsilon^{3/2}$, provided that $\varepsilon^{3/2} \approx \sum_n \varepsilon(n)^{3/2} p_n$. The time dependence of the total energy is then approximately given by

$$\varepsilon(t) \approx \left(\frac{1}{\varepsilon^{-1/2}(t=0) + \tilde{\alpha} t/2} \right)^2, \quad (5.31)$$

where $\tilde{\alpha} = -g_{ab}^2 \rho_0 m^{3/2} \omega^{3/2} \alpha / (\pi \hbar^{5/2} \sqrt{2})$.

The non-exponential damping law we obtain here can be understood in terms of a simple classical argument for a “foreign” atom moving uniformly through the superfluid at a supersonic velocity. If σ_{ab} is the scattering cross-section for the foreign atom interacting with the superfluid, then the average number of collisions per unit time is $\rho_0 \sigma_{ab} p / m_a$, where p/m_a is the velocity of the lattice atom propagating through the superfluid. The momentum of the excitation generated in a collision is $q \propto p$. Because the motion of the foreign atom is supersonic, the energy of the excitation is approximately $q^2/(2m_b)$, and the energy dissipation rate $\dot{\varepsilon} \propto \rho_0 \sigma_{ab} p^3 / m_a^2 \propto \varepsilon^{3/2}$, which is the same energy dependence that we observe here.

In practice, this algebraic energy decay will be limited by the slowest transition in the process, that from the first excited state to the ground state. On shorter timescales, population in higher motional states will be transferred to lower states (including direct transfer to the ground state) until the only significant population in an excited motional state is that in the first motional state. Then the rate of transition to the ground state will be exponential, as will the decay of the total system energy.

The transition from the first excited state to the ground state is also the most important case for the low energy excitations which are likely to arise in quantum computing applications. Numerically we find that for $m_a = m_b$, $F_{1 \rightarrow 0} = 0.3789$. Thus,

$$F_{1 \rightarrow 0} = 0.3789 \frac{g_{ab}^2 \rho_0 m}{\pi \hbar^3 l_0 \sqrt{2}}. \quad (5.32)$$

The characteristic time for the transition from the first excited state to the ground state is then expressed in terms of the number of cycles by

$$\begin{aligned} \frac{\omega \tau_{1 \rightarrow 0}}{2\pi} &= \frac{1}{0.3789} \frac{\hbar^3 l_0 \omega}{\sqrt{2} g_{ab}^2 \rho_0 m} \\ &= \frac{1}{0.3789} \frac{1}{16\sqrt{2} \pi^2} \frac{1}{\rho_0 a_{ab}^3} \frac{a_{ab}}{l_0}, \end{aligned} \quad (5.33)$$

assuming that $m_a \approx m_b$. In experiments, l_0 will typically be an order of magnitude larger than a_{ab} , and the parameter $\rho_0 a_{ab}^3 \sim 10^{-4}$, so the characteristic transition time from the first

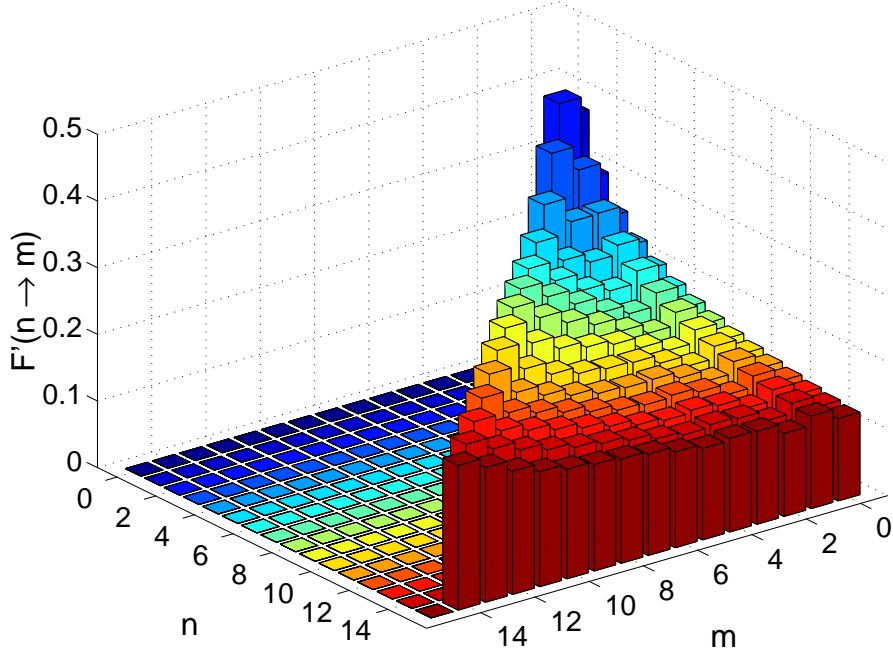


Figure 5.2. The value of $F'_{n \rightarrow m} = \pi \hbar^3 l_0 \sqrt{2} F_{n \rightarrow m} / (g_{ab}^2 \rho_0 m_b)$, showing the coefficients of the transition rate from state n to state m in the case of supersonic motion, as computed numerically from equation (5.29) with $m_a = m_b$.

excited state to the ground state will be of the order of 10 cycles. It is interesting that the small prefactor in this expression is very important in giving such a rapid cooling rate. This rate is sufficiently fast to be useful experimentally, particularly given that the transition rates from states with higher quantum number to the ground state are all of the same order.

5.4.2 Subsonic Case

Applying the approximations given in section 5.3.4 for the subsonic case to (5.28), we obtain

$$F_{n \rightarrow m} = \int_{-l_0 \omega (n-m)/(u\sqrt{2})}^{l_0 \omega (n-m)/(u\sqrt{2})} d\xi e^{-\xi^2} \xi^{2(n-m)} |L_m^{n-m}(\xi^2)|^2 \times \frac{g_{ab}^2 \rho_0 \omega^3}{4\pi m_b \hbar} \frac{m!}{n!} \frac{u\sqrt{2}}{l_0 \omega}. \quad (5.34)$$

Fig. 5.5 shows $\tilde{F}_{n \rightarrow m} = 4\pi m_b \hbar u^5 F_{n \rightarrow m} / (g_{ab}^2 \rho_0 \omega^3)$ plotted as a function of n and m . In contrast to the supersonic case, we see that $F_{n \rightarrow m}$ is very sensitive to the difference $(n - m)$, and for sufficiently small $\hbar \omega / m_a u^2$, the only significant contribution to transitions from the state $|n\rangle$ are transitions to state $|n - 1\rangle$. This can be seen very clearly in Fig. 5.6, which shows the contributions to the overall energy dissipation from the state $|n\rangle$.

If we investigate the rate of energy loss $\dot{\epsilon}(n)$ from the state $|n\rangle$ as given by (5.25), the only significant contribution comes from the term where $m = n - 1$. For very small $\hbar \omega / m_a u^2$, we

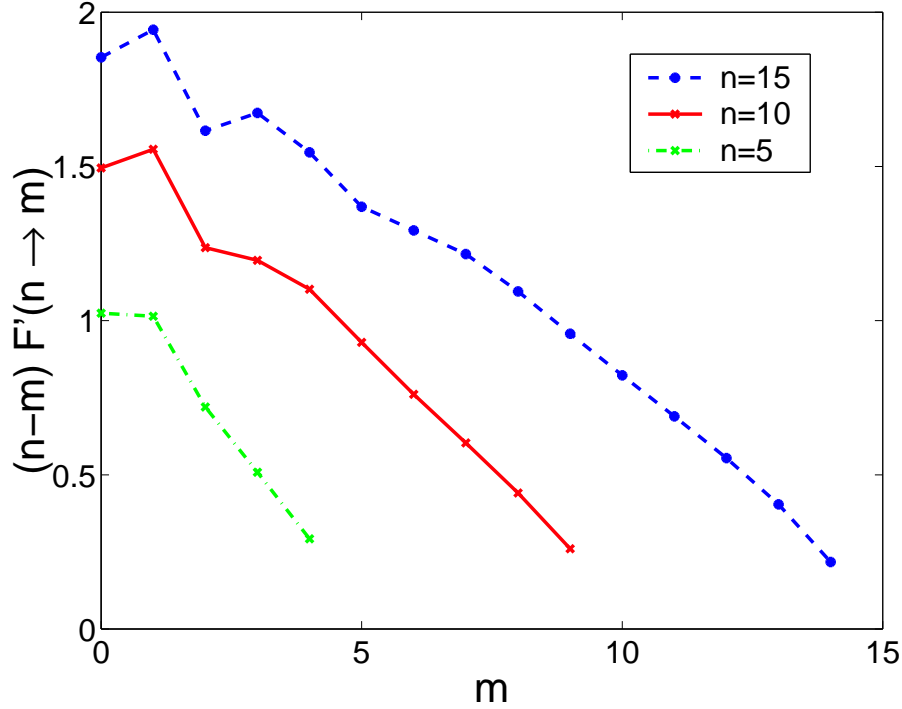


Figure 5.3. The value of $(n - m)F'_{n \rightarrow m}$, showing the contributions to the energy dissipation of the system from transitions from state n to state m in the case of supersonic motion. These results are computed numerically from equation (5.29) with $m_a = m_b$.

can then expand the integrand near $\xi = 0$, and, noting that $L_{n-1}^1(0) = n$, obtain

$$\begin{aligned} \dot{\varepsilon}(n) &\approx -\frac{g_{ab}^2 \rho_0 \omega^3}{4\pi m_b \hbar} \frac{(n-1)!}{n!} \frac{2l_0^2 \omega^2}{6u^2} \hbar \omega n^2 \\ &= -\frac{g_{ab}^2 \rho_0 \omega^4}{12\pi m_a m_b u^2} \hbar \omega n. \end{aligned} \quad (5.35)$$

Thus, as the energy of state $|n\rangle$ measured with respect to the ground state is $\varepsilon(n) = \hbar \omega n$, the energy damping law is exponential. This is a direct consequence of the fact that, in contrast to the supersonic case, only the decay mode into the next lowest oscillator state is significant in the damping process. Fig. 5.7 illustrates from numerical calculations the linear dependence of the damping rate on n . Note that damping still occurs in this regime despite the fact that the velocity of the atom is slower than the speed of sound in the superfluid. This apparently contradicts the Landau derivation of the critical velocity in the superfluid. However, we note that the Landau criterion is a thermodynamic argument, and cannot be applied here, as the motion is accelerated. In fact, this damping law has an analogy with that for dipole radiation in classical electrodynamics (see section 5.6.2).

An analogy also exists between the supersonic and subsonic motion regimes here and regimes of large and small Lamb-Dicke parameter respectively in the context of laser cooling

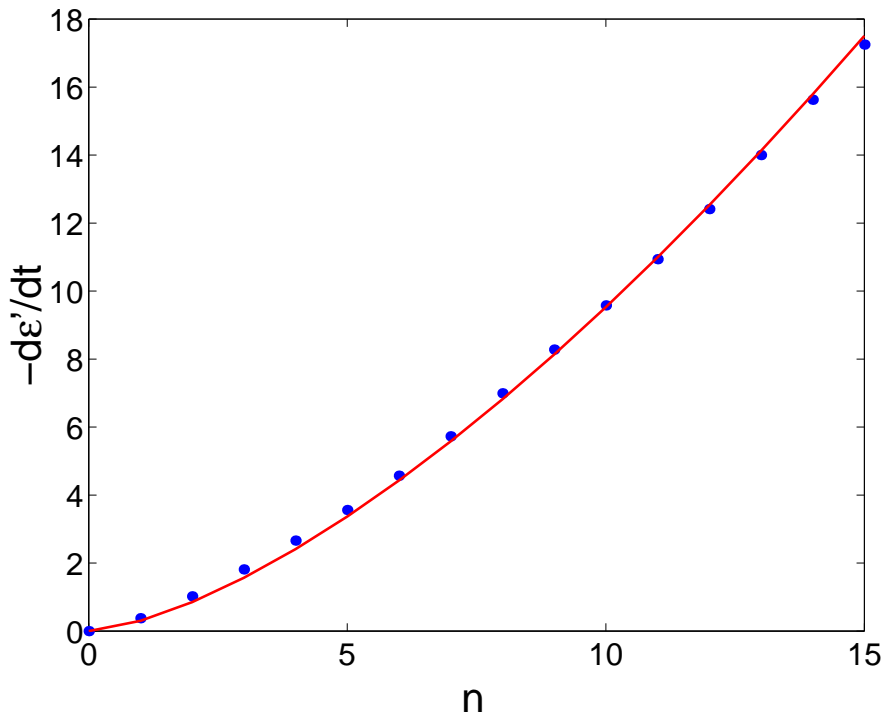


Figure 5.4. The value of $d\varepsilon'/dt = \sum_{(m < n)} (n - m) F'_{n \rightarrow m}$ plotted as a function of n for supersonic motion, showing the total rate of energy dissipation for a system instantaneously in a oscillator state with quantum number n . The points show the values computed numerically from equation (5.29) with $m_a = m_b$, and the solid line is a fitted curve of the form $d\varepsilon'/dt = \alpha n^{3/2}$, with $\alpha = 0.301$.

of trapped ions in a harmonic potential. In that system the Lamb-Dicke parameter, η , is the ratio of the size of the ground state wavefunction to the wavelength of the cooling laser, and the interaction Hamiltonian for the system is proportional to $e^{ik\hat{x}} = e^{i\eta(\hat{a} + \hat{a}^\dagger)}$ [1]. Here the interaction Hamiltonian is proportional to $e^{iq_x\hat{x}}$, and whilst η is a fixed parameter and q_x is not, q_x is constrained to be a small or large parameter by the conservation of momentum when excitations are generated in the superfluid.

During the cooling process, the coupling that exists between two states, which is proportional to $|\langle m | \exp(-i\eta\hat{x}) | n \rangle|^2$ is then analogous in the two cases. We observe cooling directly to the ground state from all excited states in the supersonic regime, and this is also a characteristic of cooling schemes in ion traps with a large Lamb-Dicke parameter. When η or q_x are small (the subsonic regime or small Lamb-Dicke parameter limit), the matrix elements simplify for $m \neq n$, $\langle m | \exp[i\eta(a + a^\dagger)] | n \rangle \approx \langle m | i\eta(\hat{a} + \hat{a}^\dagger) | n \rangle$, and coupling only exists between nearest neighbour states (this is known in ion trap cooling as coupling to the red and blue sidebands only).

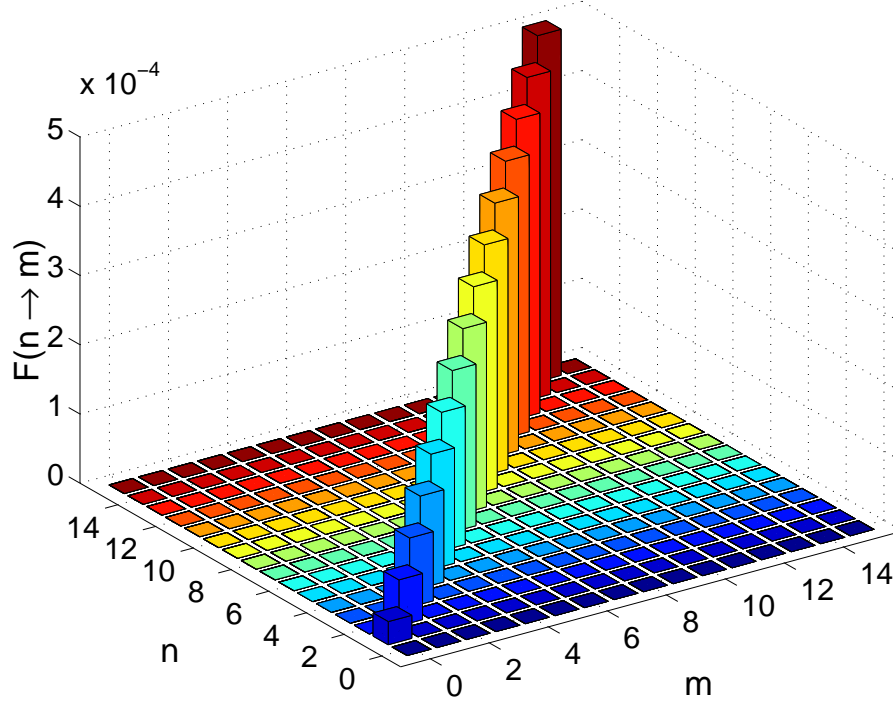


Figure 5.5. The value of $\tilde{F}_{n \rightarrow m} = 4\pi m_b \hbar u^5 F_{n \rightarrow m} / (g_{ab}^2 \rho_0 \omega^3)$, showing the coefficients of the transition rate from state n to state m in the case of subsonic motion, as computed numerically from equation (5.34) for $l_0 \omega / u = 0.01$.

5.4.3 Finite Temperature Effects

At finite temperatures, the terms proportional to $H_{n,m}$ in (5.21) contribute heating effects due to the absorption of thermal excitations in the superfluid. When the temperature is significant, the final equilibrium motional state distribution will contain non-zero excited state probabilities. These can be calculated using the detailed balance condition [28]. Considering the transfer rates for atoms between oscillator states with consecutive quantum numbers, we write for the equilibrium probability distribution $\bar{p}_n = p_n(t \rightarrow \infty)$,

$$F_{n+1 \rightarrow n} \bar{p}_{n+1} = H_{n+1,n} (\bar{p}_n - \bar{p}_{n+1}), \quad (5.36)$$

so that

$$\bar{p}_{n+1} = \frac{H_{n+1,n}}{F_{n+1 \rightarrow n} + H_{n+1,n}} \bar{p}_n. \quad (5.37)$$

Substituting the expressions from (5.22) and (5.24), and integrating over the modulus of \mathbf{q} , this expression simplifies to

$$\bar{p}_{n+1} = \frac{N(q_1)}{N(q_1) + 1} \bar{p}_n, \quad (5.38)$$

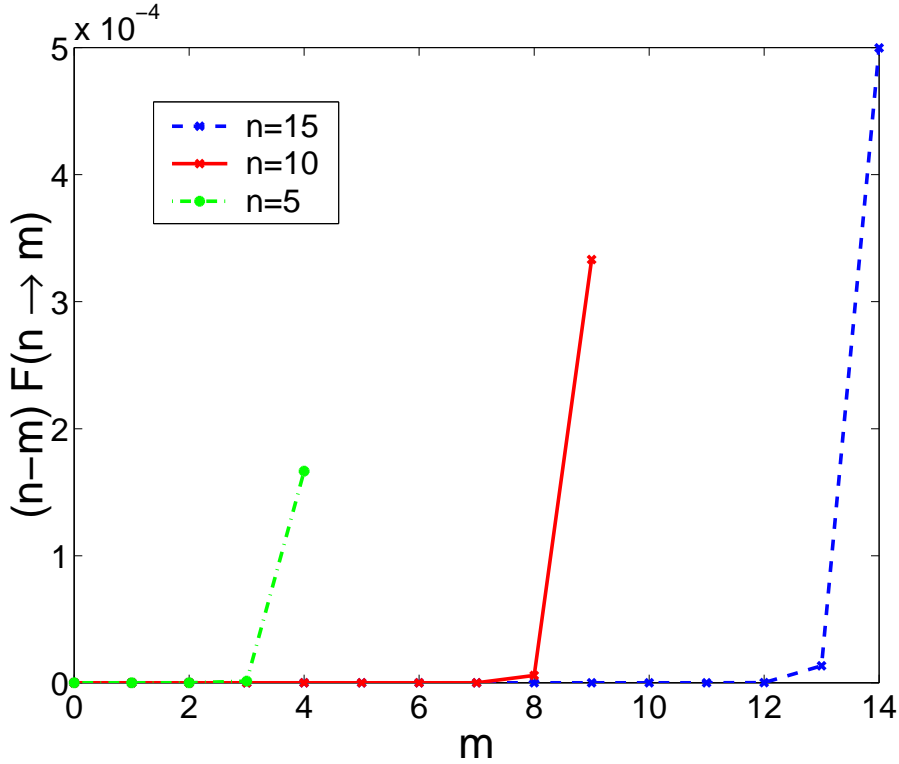


Figure 5.6. The value of $(n-m)\tilde{F}_{n \rightarrow m}$, showing the contributions to the energy dissipation of the system from transitions from state n to state m in the case of subsonic motion. These results are computed numerically from equation (5.34) for $l_0\omega/u = 0.01$.

where $\hbar q_1 = \sqrt{2\hbar m_b \omega}$ is momentum of excitations with energy $\varepsilon_{q_1} = \hbar\omega$. Thus, $\bar{p}_n = [N(q_1)/(N(q_1) + 1)]^n \bar{p}_0$, and using the normalisation condition $\sum_{n=0}^{\infty} \bar{p}_n = 1$, we obtain

$$\bar{p}_n = \bar{p}_0 e^{-n\hbar\omega/(k_B T)} = \left(1 - e^{-\hbar\omega/(k_B T)}\right) e^{-n\hbar\omega/(k_B T)}. \quad (5.39)$$

Hence, the equilibrium state occupation probabilities are simply given by the Boltzmann distribution, and the probability that an atom is in the ground motional state is $\bar{p}_0 = 1 - e^{-\hbar\omega/(k_B T)}$. Provided $k_B T \ll \hbar\omega$, the absorption of thermal excitations will not significantly decrease the cooling rate, and will not prevent the cooling of essentially all of the population to the ground state. This obtainable under reasonable experimental conditions, for example, if $\omega \sim 2\pi \times 10^5 \text{ s}^{-1}$, $\hbar\omega/k_B \sim 5 \mu\text{K}$, so that for $T = 500 \text{ nK}$, we then obtain $1 - \bar{p}_0 \approx 5 \times 10^{-5}$.

5.5 Decoherence for non-symmetric interactions

In the case where the interaction between the atoms in the lattice and the superfluid atoms is not made symmetric as described in section 5.3.1, decoherence of the internal state will occur

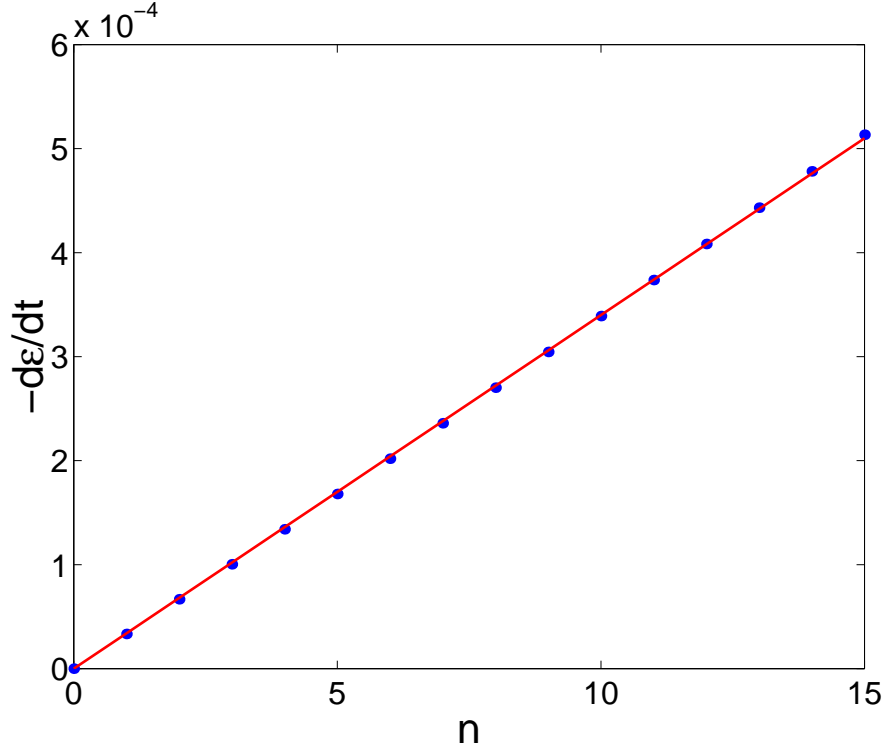


Figure 5.7. The value of $d\tilde{\epsilon}/dt = \sum_{(m<n)}(n-m)\tilde{F}_{n\rightarrow m}$ plotted as a function of n for subsonic motion, showing the total rate of energy dissipation for a system instantaneously in a oscillator state with quantum number n . The points show the values computed numerically from equation (5.34), and the solid line is a fitted straight line of the form $d\tilde{\epsilon}/dt = \alpha n$, with $\alpha = 3.40 \times 10^{-5}$.

as the relative phase of the qubit is randomised by collisional interactions with the superfluid. This process can be modelled by writing the interaction Hamiltonian for atoms in the internal states $|0\rangle$ and $|1\rangle$ as $\hat{H}_0 = a_0\hat{H}_{\text{int}}$ and $\hat{H}_1 = a_1\hat{H}_{\text{int}}$ respectively. Because $\hat{H}_{\text{int}} \propto g_{ab} \propto a_{ab}$, a_0 and a_1 are proportional to the scattering lengths for interactions between superfluid atoms and atoms in the lattice in states $|0\rangle$ and $|1\rangle$ respectively.

Initially the internal atomic state was neglected in the derivation of the master equation in appendix 5.B, as the interaction Hamiltonian was assumed to be independent of the internal state. In order to estimate the rate of decoherence, we must compute the master equation for a density operator which includes the internal atomic state. Once again projecting the density operator onto states which are diagonal in a motional state basis, we write

$$\hat{\mathcal{P}}\hat{W} = \sum_{i,j \in \{0,1\}} \sum_n |n\rangle_{\text{mot}} \text{mot} \langle n| \otimes |i\rangle \langle j| p_{ij,n}, \quad (5.40)$$

where $|n\rangle_{\text{mot}}$ denotes the motional (harmonic oscillator) state of the atom, and $|i\rangle$, where $i \in \{0,1\}$ denotes the internal atomic state. If we take the trace of $\hat{\mathcal{P}}\hat{W}$ over the motional states, and obtain for the density operator, $\text{Tr}_{\text{mot}}(\hat{W}) = \sum_{i,j} |i\rangle \langle j| p_{ij}$, then the rate of decoherence

is the rate of decay of the off-diagonal elements, p_{01} and p_{10} , of this reduced density operator for the internal states.

In the long time limit (for time scales larger than the oscillator period), all of the standard approximations made in the derivation of the master equation in appendix 5.B once again apply. Rewriting the original master equation for the new interaction Hamiltonian and neglecting the heating terms, we obtain

$$\dot{p}_{ij,m} = a_i a_j \sum_{n>m} F_{n \rightarrow m} p_{ij,n} - \frac{a_i^2 + a_j^2}{2} \sum_{n'<m} F_{m \rightarrow n'} p_{ij,m}. \quad (5.41)$$

Thus, the equation of motion for the elements diagonal in the internal states are identical to those given in (5.21), except that they are multiplied by a_0^2 for p_{00}, m and a_1^2 for p_{11}, m , as is expected.

Taking the trace of \hat{W} over the motional states, we obtain the equation of motion for the reduced density operator,

$$\dot{p}_{ij} = \sum_m \dot{p}_{ij,m} = -\frac{(a_i - a_j)^2}{2} \sum_m \sum_{n<m} F_{m \rightarrow n} p_{ij,m}. \quad (5.42)$$

For $i = j$, $\dot{p}_{ij} = 0$, so the populations in each internal state are constant, as we expect. The rate of decoherence is given by the decay of the off-diagonal elements, which by comparison with (5.21) is seen to be the rate of cooling transitions, multiplied by $(a_0 - a_1)^2/2$. In the long time limit with the superfluid at zero temperature, where the motional states are all cooled to the ground state and cooling transitions cease, the rate of decoherence also goes to zero. If $(a_1 - a_0)^2 \ll (a_1 + a_0)^2$, so that the timescale on which the cooling occurs is much faster than that of the decoherence, the total decoherence should be small. However, it is important to note that in the case of finite temperature, transitions between motional states will continue to occur after the atoms are cooled to their steady state distribution, resulting in finite levels of decoherence in the steady state regime.

For time scales shorter than the oscillator period, the observed decoherence will be strongly dependent on the manner in which the atom is introduced into the superfluid. The limiting case in which the atom is suddenly immersed in superfluid (so that the initial overall density matrix is factorised into the system and the superfluid), an ‘‘initial slip’’ in the coherence occurs, a behaviour which can be analysed by directly performing the time integral in (5.67) for the combined density operator and interaction Hamiltonian. At zero temperature, we obtain equations of motion for the elements of the reduced density operator for the internal states given by

$$\dot{p}_{ij} \approx -\frac{(a_i - a_j)^2 g_{ab}^2 \rho_0}{V \hbar} \sum_{\mathbf{q}} (u_{\mathbf{q}} + v_{\mathbf{q}})^2 \sum_{m,n} p_{ij,m} \frac{i(e^{-i[\varepsilon_{\mathbf{q}} - (m-n)\hbar\omega]\tau/\hbar} - 1)}{\varepsilon_{\mathbf{q}} - (m-n)\hbar\omega} \left| \langle n | e^{-i\mathbf{q} \cdot \hat{x}} | m \rangle \right|^2. \quad (5.43)$$

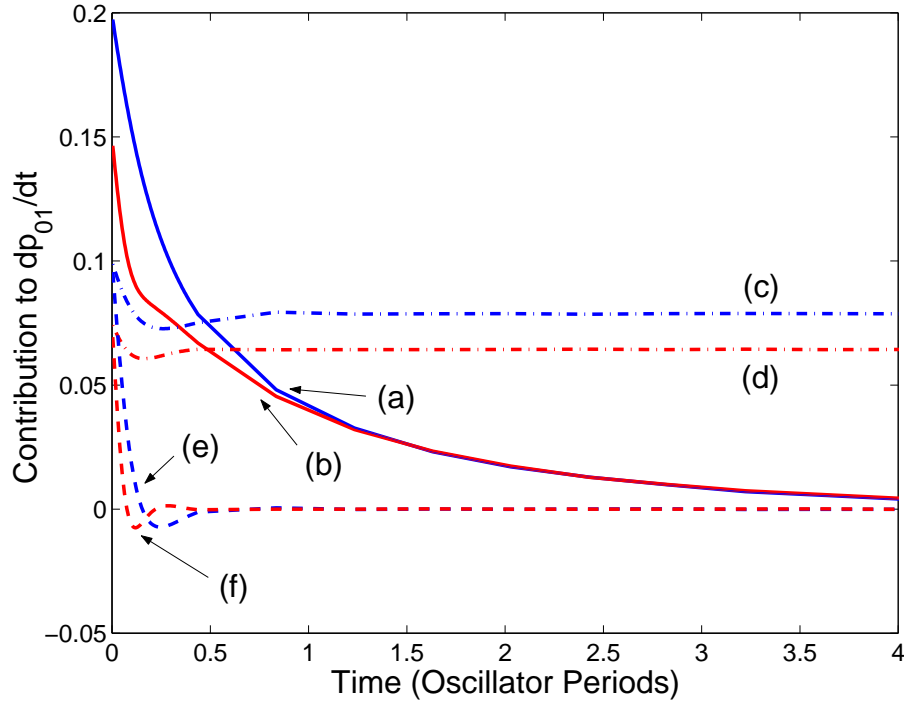


Figure 5.8. Numerical calculations of the contributions to the initial decoherence slip from terms in (5.43), in the supersonic regime with $\hbar\omega = 25m\mu^2$. The quantities plotted are dimensionless, and expressed in terms of $-(a_i - a_j)^2 g_{ab}^2 \rho_0 / (\hbar^3 l_0)$. For (a) $m = 0, n = 0$ and (b) $m = 1, n = 1$ (solid lines), we observe an initial decoherence slip which decays on a time scale of a few oscillator cycles. For (c) $m = 1, n = 0$ and (d) $m = 2, n = 0$ (dash-dot lines), the contributions settle in less than one oscillator cycle to the same long time values given by (5.42). For (e) $m = 0, n = 1$ and (f) $m = 0, n = 2$ (dashed lines), the contributions decay rapidly to zero in less than one oscillator cycle.

Note that as $t \rightarrow \infty$, the factor involving the exponential approximates a delta function, and we recover the behaviour described by (5.42). For short times the real part of the terms in this expression for particular combinations of n and m exhibit three different types of time dependent behaviour, examples of which are shown in Fig. 5.8. For $n < m$, the terms in this expression settle rapidly within one oscillator cycle to the same values that they produce in the long time limit, (5.42), and within the first oscillator cycle give contributions of the same order as their long time values. For $n > m$, the terms correspond to a small initial rate of coherence loss, which decays to zero in much less than one oscillator cycle, a timescale which becomes rapidly shorter as $(n - m)$ increases. Thus, the total decoherence arising from these terms is very small. From the terms where $m = n$ we obtain the most significant contributions to the initial decoherence slip that are not accounted for by the long time behaviour. These contributions decay to zero on a timescale of about 2 oscillator cycles, and at their peak values produce decoherence rates of the same order as terms in the expression for the long time rates. The significant point about these terms is that they describe

decoherence which will occur even if the atoms are in the motional ground state, in contrast with decoherence in the long time regime. If there is a significant population in the excited motional state, then the initial slip will give a small contribution to the total decoherence as compared with the long time behaviour. However, if the atoms are essentially all in the ground state, then this initial slip produces decoherence which would not otherwise arise. In all cases, the rate of decoherence is proportional to $(a_0 - a_1)^2$, so that if the scattering lengths for the states $|0\rangle$ and $|1\rangle$ differ only by a small amount, then the total decoherence introduced will be small.

5.6 The Semi-Classical Approximation

5.6.1 Supersonic Case

It is interesting to compare the fully quantum calculation of the damping rates to the calculation in the semi-classical approximation. Using this approximation, the calculation is performed similarly to the calculation of damping due to radiation from an oscillating charge, which provides a useful physical analogy between the two situations.

In this calculation we make use of the relationship between quantum matrix elements and the Fourier components of the classical trajectory of the system [29]. Strictly speaking, this approximation is valid only when the equivalent quantum matrix elements are taken between states of large quantum number, and where the difference in the quantum numbers is small relative to the quantum numbers. We will discuss the validity of the approximation in practice at the end of the calculation. The classical trajectory of the atom in the lattice may be written in 1D as $\mathbf{r}(t) \rightarrow r_{\max} \cos(\omega t) \hat{\mathbf{z}}$, where $\hat{\mathbf{z}}$ is the axial unit vector along the lattice. Because the motion is periodic with period $2\pi/\omega$, the frequency spectrum of the resulting excitations will be discrete with frequencies ωn for integer n . Analogously to (5.22), we then write the rate of energy dissipation for the atom in the lattice (at zero temperature) as

$$\dot{\varepsilon} = -\frac{2\pi}{\hbar} \sum_{\mathbf{q}} \sum_n |T_{\mathbf{q}}(\omega n)|^2 \delta(\hbar\omega n - \varepsilon_{\mathbf{q}}) \hbar\omega n, \quad (5.44)$$

where

$$\sum_{\mathbf{q}} |T_{\mathbf{q}}(\omega n)|^2 = \sum_{N_f} \left| \frac{\omega}{2\pi} \int_0^{2\pi/\omega} \langle N_f | \hat{H}_{\text{int}} | N_i \rangle e^{-i\omega n t} dt \right|^2, \quad (5.45)$$

with $|N_f\rangle$ the final state of the superfluid (normally a state with a particular number of excitations of momentum $\hbar\mathbf{q}$). This expression is also averaged over the initial state of the system $|N_i\rangle$, which will usually correspond to a thermal distribution of excitations.

Assuming that we are in the supersonic motion regime and applying the approximations given in section 5.3.4, we obtain

$$T_{\mathbf{q}}(\omega n) = \frac{g_{ab} \sqrt{\rho_0}}{\sqrt{V}} \frac{\omega}{2\pi} \int_0^{2\pi/\omega} e^{-iq_x r_{\max} \cos(t)} e^{-i\omega n t} dt. \quad (5.46)$$

Using the identity

$$\left| \frac{1}{2\pi} \int_0^{2\pi} e^{-iz \cos(\zeta)} e^{-in\zeta} d\zeta \right|^2 = J_n^2(z), \quad (5.47)$$

where $J_n(z)$ is an ordinary Bessel Function, and integrating over the angular values of \mathbf{q} in spherical coordinates then gives

$$\begin{aligned} \dot{\varepsilon} &= -\frac{g_{ab}^2 \rho_0}{2\pi} \sum_n \int_0^\infty dq q^2 \int_{-1}^1 d\xi J_n^2(qr_{\max} \xi) \\ &\quad \times \delta(\hbar\omega n - \varepsilon_q) \omega n. \end{aligned} \quad (5.48)$$

We now integrate over q to give

$$\dot{\varepsilon} = -\frac{g_{ab}^2 \rho_0 m_b^{3/2} \omega^{3/2}}{\sqrt{2} \pi \hbar^{5/2}} \sum_n n^{3/2} \int_{-1}^1 d\xi J_n^2(\xi a \sqrt{n}), \quad (5.49)$$

where $a = r_{\max} \sqrt{2m_b \omega / \hbar}$. We can see that many values of n contribute significantly to this sum, which is analogous to the full quantum result, in which many different transitions between oscillator levels had significant coefficients $F_{n \rightarrow m}$. As noted in section 5.4.1, this fact arises from the the motion of the oscillating atom being faster than the speed of sound in the superfluid. This spectrum of generated excitations can be seen as being analogous to the result for electromagnetic radiation from a charge moving faster than the speed of light (in a dielectric), which can be computed semi-classically using a similar method to that used here.

It is possible to determine analytically the functional dependence of (5.49) on r_{\max} by finding an approximate expression for the integral over ξ . In the limit where the argument of the Bessel function is large, we can write

$$\begin{aligned} F(a, n) &= \int_{-1}^1 d\xi J_n^2(\xi a \sqrt{n}) \\ &\approx 2 \int_{\xi_0}^1 d\xi \frac{2 \cos^2(\xi a \sqrt{n} - n\pi/2 - \pi/4)}{\pi \xi a \sqrt{n}} \\ &\approx \frac{2}{\pi a \sqrt{n}} \int_{\xi_0}^1 d\xi \frac{1}{\xi} = \frac{2}{\pi a \sqrt{n}} \ln \left(\frac{a}{\sqrt{n}} \right), \end{aligned} \quad (5.50)$$

where $\xi_0 = \sqrt{n}/a$ is the lower limit for ξ in which the cosine approximation of the Bessel function is valid. This expression is strictly only valid for $n \ll a^2 = 2r_{\max}^2 m_b \omega / \hbar$. At larger values of n , $F(a, n)$ is exponentially small, and the functional dependence of $\sum_n n^{3/2} F(a, n)$ on a can be found from the point at which the summation is cut off, and for a system of energy $m_a \omega r_{\max}^2 / 2$, $n_{\max} = m_a \omega r_{\max}^2 / (2\hbar) = a^2 m_a / (4m_b)$. Approximating the sum by an integral, we can then write

$$\dot{\varepsilon} = -C \frac{g_{ab}^2 \rho_0 m_a^2 m_b [1 + 2 \ln(4m_b/m_a)] \omega^3 r_{\max}^3}{32\pi^2 \hbar^4}, \quad (5.51)$$

where C is a constant which for large values of a is independent of a . Fig. 5.9 shows a numerical calculation of $C(a)$, from which we observe that for large a , $C \sim 1.75$. Moreover,

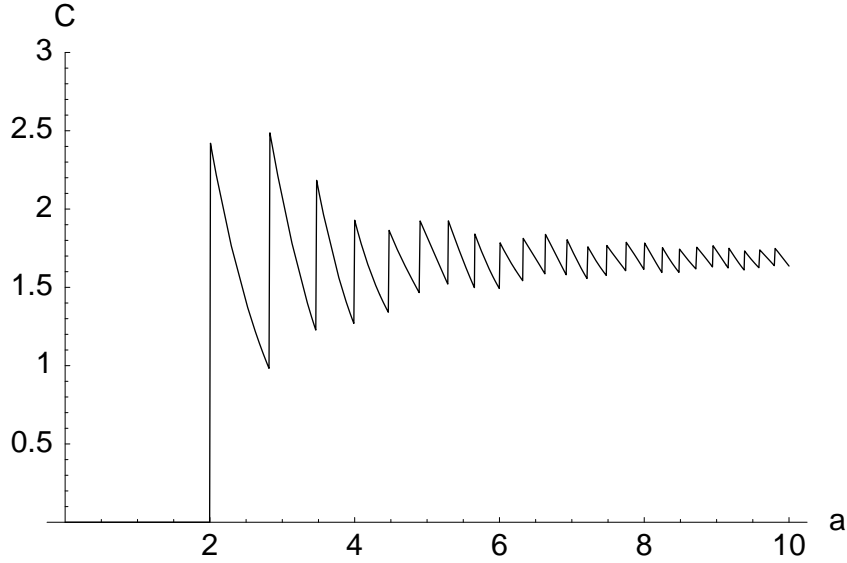


Figure 5.9. The value of C computed numerically as a function of $a = \sqrt{2} r_{\max}/l_0$ by comparison of the results from (5.49) and (5.51). Note that this curve is discontinuous because of the discrete sum in (5.49), which was cut off at the highest integer less than a , and that $C = 0$ for $a < 2$, because $a < 2$ corresponds to a sum cut off at $n = 0$. The value of this function in the limit as $a \rightarrow \infty$ gives $C \sim 1.75$.

the approximation is also very good for small values of $a > 2$, so that C is essentially a constant for all physical values of a .

If we use the classical expression $r_{\max} = \sqrt{2\varepsilon/(m_a\omega^2)}$, where ε is the energy of the oscillating atom, we can rewrite (5.51) as

$$\dot{\varepsilon} = -C[1 + 2 \ln(4m_b/m_a)] \frac{\sqrt{2} g_{ab}^2 \rho_0 m_a^{1/2} m_b}{16\pi^2 \hbar^4} \varepsilon^{3/2}. \quad (5.52)$$

As in the quantum case, the damping is non-exponential as a result of the rich distribution of generated excitations and instead $\dot{\varepsilon} \propto \varepsilon^{3/2}$. If we compare this result to that from equation (5.30), the ratio of the semi-classical result to the quantum result for $m_a = m_b$ is $C[1 + 4 \ln(2)]/(8\alpha\pi) \approx 0.88$. The reason for this becomes clear when we examine the terms of the series $\sum_k k^{3/2} F(2n, k)$ (Noting that if we begin in the initial state $|n\rangle$ then $a = 2n$), and compare them to the equivalent terms in the quantum calculation, $\sum_k k F_{n \rightarrow (n-k)}$. This is shown for an initial state $n = 10$ in Fig. 5.10. We see that the terms agree well for small k but that they diverge as $k \rightarrow n$. This is because the equivalence between the semi-classical result from the Fourier spectrum and the quantum matrix elements is strictly only valid when k is small. Because in the calculation of energy dissipation rates the terms are weighted by an additional factor of k , the terms where the largest discrepancy arises are always significant in the calculation of the damping rates, and thus this discrepancy does not significantly decrease as $n \rightarrow \infty$.

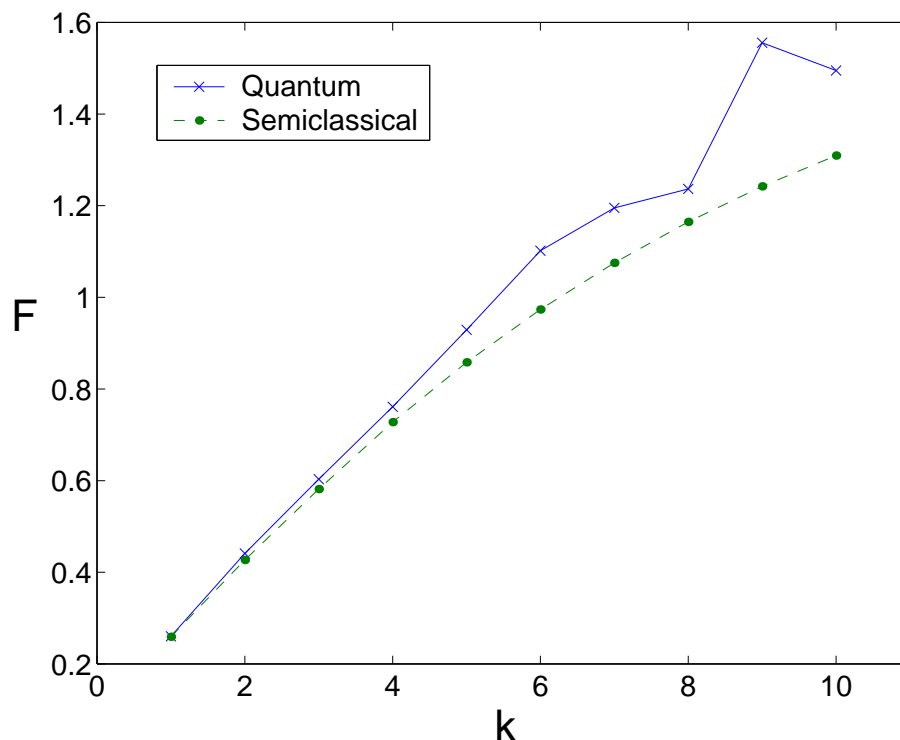


Figure 5.10. Numerical values of the quantum result $F_{10 \rightarrow (10-k)}$ (solid line) and the semi-classical result $F(20, k)$ (dotted line) in the supersonic regime. Note that we observe very good agreement for small k , but the results diverge for higher values of k .

5.6.2 Subsonic Motion

In addition to the approximations given in section 5.3.4, we note that for the purposes of the semi-classical calculation in the subsonic regime, $|\mathbf{q} \cdot \mathbf{r}_{\max}| \leq qv_{\max}/\omega = v_{\max}/u \ll 1$. Thus,

$$\begin{aligned} & \frac{1}{2\pi} \int_0^{2\pi} e^{-iq_x r_{\max} \cos \zeta} e^{-in\zeta} d\zeta \\ & \approx \frac{1}{2\pi} \int_0^{2\pi} q_x r_{\max} \cos(\zeta) e^{-in\zeta} d\zeta = i \frac{q_x r_{\max}}{2} \delta_{n, \pm 1}, \end{aligned} \quad (5.53)$$

and so

$$\begin{aligned} \dot{\varepsilon} &= -\frac{g_{ab}^2 \rho_0}{4\pi m_b u} \int_0^\infty dq q^3 \int_{-1}^1 d\xi \left| \frac{qr_{\max}\xi}{2} \right|^2 \\ & \quad \times \delta(\hbar\omega - \varepsilon_q) \hbar\omega \\ &= \frac{-g_{ab}^2 \rho_0 \omega^4}{12\pi u^7 m_b m_a} \varepsilon \end{aligned} \quad (5.54)$$

As mentioned in section 5.4.2, damping occurs here despite the fact that the velocity of the atom being slower than the speed of sound in the superfluid appears to contradict the Landau

derivation of the critical velocity in the superfluid, and we obtain an exponential damping law. In the same sense that the previously discussed case of supersonic motion is analogous to radiation from a charge moving faster than the speed of light in a dielectric, this case is analogous to dipole radiation from an accelerating charge. The approximation made that results in only one term in the sum being significant, (5.53), similarly corresponds to the dipole approximation in non-relativistic quantum electrodynamics.

Note that if we substitute $\varepsilon = \hbar\omega n$ into (5.54), then we obtain exactly the same result we obtained from the quantum case (5.35). The semi-classical approximation works extremely well here, because the only significant contribution to the quantum calculation comes from matrix elements between states with quantum numbers differing by one.

5.7 Immersion in a Strongly Correlated 1D Superfluid

In this section we investigate the damping that occurs when the lattice is immersed in a quasi-one dimensional superfluid, which is an example of strongly correlated quantum liquid. In a real experiment this setup is not particularly practical for cooling the motion of the atoms. For a gas to be quasi-one dimensional, the excitation modes in the transverse directions must have energies larger than all other significant energy scales in the system, and so the oscillator energies for lattice atoms, $\hbar\omega$ must be much smaller than the energies of the transverse excitations in the superfluid. Furthermore, the motion of the oscillator will only be damped in one dimension (along the direction of the quasi-1D superfluid), and so the oscillator should be made strongly anisotropic so that in the transverse directions the oscillator is always in the motional ground state and need not be cooled. However, the study of the cooling process in this context is still interesting, for example, because the lattice atom in this setup could be used as a probe to provide spectroscopic information about the 1D Bose gas.

In general the excitation spectrum of such a one-dimensional Bose gas is complicated. In the case of short-range interactions between the particles exact analytical solution exists both for the ground state wavefunction and for the excitation spectrum [30] for arbitrary strength of the interparticle interactions and the excitation energies. However, in the limit of long wavelength the excitations are phonons and the system can be described within a hydrodynamic approach. Following [31] we represent the field (Bose-particle annihilation) operator in the form: $\hat{\Psi}(x) \propto \sqrt{\rho_0 + \delta\rho} e^{i\hat{\phi}}$, where $\hat{\phi}$ and $\delta\hat{\rho}$ are phase and density fluctuation fields respectively and obey the commutation relation $[\delta\hat{\rho}(x), \hat{\phi}(y)] = i\delta(x-y)$, and ρ_0 is the 1D density (averaged, in practice, over the transverse directions). The low-energy effective Hamiltonian for the liquid is then

$$\hat{H}_0 = \frac{\hbar}{2\pi} \int_{-\infty}^{\infty} dx [v_J (\partial_x \hat{\phi})^2 + v_N (\pi \delta\hat{\rho})^2], \quad (5.55)$$

where $v_J = \pi\hbar\rho_0/m_b$, $v_N = \kappa/(\pi\hbar\rho_0)$, and κ is compressibility per unit length. The excitation spectrum corresponding to this Hamiltonian satisfies a linear dispersion relation $\varepsilon_q = \hbar v_s q$, where the velocity of sound is given by $v_s = (v_J v_N)^{1/2}$.

The parameters v_J and v_N are phenomenological and can be found from the exact Lieb-Liniger solution [30]. The dependence on the interaction strength between gas particles can be

described using the dimensionless parameter, $\gamma = m_b g_{bb} / (\hbar^2 \rho_0)$. In the weak interaction limit, $\gamma \ll 1$, the velocity of sound is given by the usual Gross-Pitaevskii value: $v_s = \sqrt{g_{bb} \rho_0 / m_b}$. If the interaction is very strong, $\gamma \gg 1$, then the interaction effectively makes the particles impenetrable, and hence in a true 1D system, indistinguishable from Fermions. This is called the Tonks gas regime, and the sound velocity is equal to the effective Fermi velocity: $v_s = \pi \hbar \rho_0 / m_b$. The energy spectrum is linear for $\varepsilon_q \ll g_{bb} \rho_0$ (the chemical potential of a weakly interacting Bose-gas) and $\varepsilon_q \ll \pi \hbar^2 \rho_0^2 / (2m_b)$ (the Fermi energy of the Tonks gas) for the cases of weak and strong interactions, respectively. At higher energies the excitation spectrum is no longer universal and depends on the details of the interparticle interactions. Because ε_q and the trapping frequency ω in the lattice are related via energy conservation, the motion of the lattice atoms must then be subsonic with respect to v_s for the model to be valid.

The operator for density fluctuations in this regime is given by

$$\delta \hat{\rho} = \sum_q \left(\frac{2q\sqrt{K}}{\pi L} \right)^{1/2} \left(\hat{b}_q e^{iqx} + \hat{b}_q^\dagger e^{-iqx} \right), \quad (5.56)$$

where L is the length of the BEC and $K = (v_J/v_N)^{1/2}$. The quantity K depends on the interparticle interactions and is related to the scaling dimension of the particle field operator: $\langle \hat{\Psi}^\dagger(x) \hat{\Psi}(x') \rangle \sim |x - x'|^{-1/(2K)}$ for large $|x - x'|$. The function $K(\gamma)$ monotonically decreases as γ grows, so that $K(\gamma \rightarrow 0) \approx \pi[\gamma - (1/2\pi)\gamma^{3/2}]^{-1/2}$ and $K(\gamma \rightarrow \infty) \approx (1 + 2/\gamma)^2$ [30]. Note also that for the quasi one-dimensional system, $g_{bb} = 4\pi \hbar^2 a_{bb} / m_b l_\perp^2$, where l_\perp is the transverse confinement length of the BEC, provided that $a_s \ll l_\perp$ [32].

In the limit of small oscillation frequencies ω , we apply the same approximation (5.53) used in section 5.6.2, and obtain

$$\begin{aligned} \dot{\varepsilon} &= -\frac{2\omega g_{ab}^2 \sqrt{K}}{\pi} \int_0^\infty dq q \left| \frac{qr_{\max}}{2} \right|^2 \delta(\hbar\omega - \hbar v_s q) \\ &= \frac{-g_{ab}^2 \sqrt{K} \omega^2}{\pi \hbar m_a v_s^4} \varepsilon \end{aligned} \quad (5.57)$$

For small γ , $K \approx \pi \hbar \sqrt{\rho_0 / (m_b g_{bb})}$ and $v_s = \sqrt{g_{bb} \rho_0 / m_b}$, so

$$\dot{\varepsilon} \approx \frac{-g_{ab}^2 \omega^2 m_b^{7/4}}{\sqrt{\pi \hbar m_a \rho_0}^{7/4} g_{bb}^{9/4}} \varepsilon. \quad (5.58)$$

The transition rate constant is then $\Gamma_\varepsilon \sim \omega (g_{ab}/g_{bb})^2 (\hbar\omega / \rho_0 g_{bb}) (m_b g_{bb} / \hbar^2 \rho_0)^{3/4} (m_b/m_a) / \sqrt{\pi} \ll \omega$ and hence is generally small. In the opposite limiting case for large γ , $K \approx 1$ and $v_s = \pi \hbar \rho_0 / m_b$, so

$$\dot{\varepsilon} \approx \frac{-g_{ab}^2 \omega^2 m_b^4}{\pi^5 \hbar^5 m_a \rho_0^4} \varepsilon. \quad (5.59)$$

Here, $\Gamma_\varepsilon \sim \omega (m_b g_{ab} / \hbar^2 \rho_0)^2 (\omega m_b / \hbar \rho_0^2) (m_b/m_a) / \pi^5$. Thus, in this regime, the damping rates can be made very fast, provided that $\gamma_{ab} = m_b g_{ab} / \hbar^2 \rho_0 = g_{ab} \gamma / g_{bb}$ is made very large.

However, this regime is difficult to obtain experimentally, and in most current experiments $\gamma \sim 1$.

In both cases the damping that we obtain is exponential, which again arises because the motion we consider is subsonic, and produces excitations at only one significant momentum. The energy exchange rate grows as a function of ω , in a manner analogous to dipole radiation in quantum electrodynamics.

5.8 Summary

We have shown that the immersion of a system of atoms in an optical lattice in a superfluid causes damping of atoms in excited motional states, and that this damping can be used to transfer these atoms to the ground motional state whilst preserving their initial internal state and any entanglement between the atoms. For typical experimental parameters, this transfer occurs in a characteristic time of around 10 oscillator cycles, which is sufficiently rapid to be useful experimentally. These typical parameters come from a regime in which the atoms in the lattice are moving faster than the velocity of sound in the superfluid, which generates a rich distribution of excitations, involving significant transitions from all levels directly to the ground state. In the opposite regime, where the velocity of the atoms in the lattice is significantly slower than the speed of sound in the superfluid, damping still occurs because the motion is accelerated, but only transitions between neighbouring oscillator levels contribute significantly to the damping process.

Provided that the temperature in the non-superfluid fraction of the gas is much smaller than the oscillator level spacing in the lattice, heating effects due to absorption of thermal excitations is not a significant effect in this process. This is the case for experimentally realisable conditions. At higher temperatures, the system would be cooled not to the ground state, but to a thermal distribution of motional states corresponding to a Boltzmann distribution with the same temperature as that in the normal component.

The supersonic motion regime discussed here is readily realisable in present experiments. Together with a careful choice of internal atomic states used to encode a qubit, this damping mechanism thus provides a decoherence-free means to cool an atomic qubit to its motional ground state.

Note added in proof: Recently, we became aware of a related study done by Astracharchik and Pitaevski [36], in which the drag force on an impurity traveling with a constant velocity through a condensate is computed. The present work differs in that we consider the motion of an oscillating atom immersed in a superfluid, and deal specifically with the application of the resulting drag force to decoherence suppressed cooling of an atomic qubit.

Acknowledgements

This work was supported in part by the Austrian Science Foundation FWF, E.U. Networks and the Institute for Quantum Information.

5.A Dispersion Relation for a Foreign Particle in a Superfluid

When a foreign particle is immersed in a superfluid, its interaction with the condensed atoms can be described as a collective excitation, which represents both the injected particle and the cloud of the condensed atoms. This leads to a modification of the dispersion relation as well as to the appearance of frictional forces. Since the goal of the current work is to calculate the damping of atomic motion due to the friction force experienced by an alien particle in a harmonic trap, we first calculate the dispersion relation for a free foreign particle immersed into a superfluid of atoms, which moves at a constant velocity. This situation is conceptually simpler, and allows us to consider the validity of treating the interaction between the superfluid and the foreign particle as a simple density-density interaction.

For a given momentum, p , the energy of the resulting collective excitation is given by

$$E = \frac{p^2}{2m_{\text{eff}}} + g_{ab}\rho_0 + \delta E^{(2)}, \quad (5.60)$$

where $m_{\text{eff}} \approx m_a$ is the effective mass of the foreign atoms, g_{ab} is the coupling coefficient for the interaction between the foreign particles and the superfluid, and ρ_0 is the condensate density.

$$\delta E^{(2)} = g^2 \rho_0 \sum_q \left(\frac{(u_q + v_q)^2}{p^2/2m_a - \epsilon_q - (p-q)^2/2m_a + i0} + \frac{1}{q^2/2\mu} \right), \quad (5.61)$$

and $\mu^{-1} = m_b^{-1} + m_a^{-1}$ is the reduced mass. This expression is a trivial generalisation of the standard superfluid ground state energy calculation (see [26]). The counterterm (the second term in the brackets) is obtained by replacing the Fourier component of the interaction potential in the Hamiltonian by the scattering length, a_{ab} . It is possible to simplify (5.61) in two particularly relevant cases.

If the momentum, p , is small (the foreign particle moves at subsonic velocities, $p/m_a \ll u$), then the integral in (5.61) converges at $q \sim \mu$. The analysis of the energy denominator leads to the Landau critical velocity condition for subsonic particles and thus $\text{Im} \delta E^{(2)} = 0$. For the calculation of $\text{Re} \delta E^{(2)}$ we can first set $p = 0$ and find:

$$\delta E^{(2)} = g_{ab}^2 \rho_0 \sum_q \left(-\frac{(u_q + v_q)^2}{\epsilon_q + q^2/2m_a} + \frac{1}{q^2/2\mu} \right). \quad (5.62)$$

The calculation of the integral over q is straight forward. For example, in the case $m_a = m_b$, we find $\delta E^{(2)} = 4g_{ab}\rho_0(\rho_0 g_{ab}^3)^{1/2}/3\pi^2$, which is a small correction to the leading order ($(\rho_0 g_{ab}^3)^{1/2} \ll 1$) and hence can further be neglected. One can expand $\delta E^{(2)}$ in powers of $p^2/(m_a \mu)$ to find a similar small correction to the effective mass of the immersed particle, $(m_{\text{eff}} - m_a)/m_a \sim (\rho_0 g_{ab}^2)^{1/2} \ll 1$. Therefore, interaction effects up to leading order in the gaseous parameter do not lead to damping for subsonic motion. Both the mass of the particle and the effective interaction are changed by a small quantity $\sim (\rho_0 a^3)^{1/2} \ll 1$, which can be neglected. This means that the cooling may only originate from accelerated motion.

In the other limiting case, where the motion of the foreign particle is supersonic, $p/m_a \gg u$, $\text{Re} \delta E^{(2)} = 0$, and the imaginary part gives the damping (see [33])

$$\text{Im} \delta E^{(2)} = \frac{8\pi \rho_0 a_{ab}^2 p}{m_a}. \quad (5.63)$$

Here, the effects of the interaction between the foreign particle and the the superfluid (to leading order) generate damping only, which is nothing else but the classical result for a particle moving through a gas of classical scatterers of a given density ρ_0 . The difference between the real mass and the effective mass can once again be neglected, so that in both subsonic and supersonic regimes, the interaction between a foreign particle and a superfluid may be treated as a density-density interaction.

5.B Derivation of the Master Equation

We treat the superfluid with Bogoliubov excitations as a reservoir, with density operator \hat{R} . In the interaction picture, and after making the Born-Markov approximation, the master equation for the density operator \hat{w} of a system which interacts with a reservoir via an interaction Hamiltonian \hat{H}_{int} can be shown to be given by [34]

$$\dot{\hat{w}} = -\frac{1}{\hbar^2} \int_0^t dt' \text{Tr}_R[\hat{H}_{\text{int}}(t), [\hat{H}_{\text{int}}(t'), \hat{w}(t) \otimes \hat{R}]], \quad (5.64)$$

where Tr_R denotes the trace over the reservoir states.

We write $\hat{s}_{\mathbf{q},1} = e^{iq_x \hat{x}}$, $\hat{s}_{\mathbf{q},2} = e^{-iq_x \hat{x}}$, $\hat{\Gamma}_{\mathbf{q},1} = \hat{b}_{\mathbf{q}}$ and $\hat{\Gamma}_{\mathbf{q},2} = \hat{b}_{\mathbf{q}}^\dagger$, so that

$$\hat{H}_{\text{int}} = g_{ab} \sqrt{\frac{\rho_0}{V}} \sum_{\mathbf{q}} (u_{\mathbf{q}} + v_{\mathbf{q}}) \sum_{i=1,2} \hat{s}_i \hat{\Gamma}_i, \quad (5.65)$$

and then substitute this expression into (5.64) to give

$$\begin{aligned} \dot{\hat{w}} = & -\frac{g_{ab}^2 \rho_0}{V \hbar^2} \sum_{\mathbf{q}} (u_{\mathbf{q}} + v_{\mathbf{q}})^2 \sum_{i,j=\{1,2\}} \int_0^t dt' \\ & [\hat{s}_i(t) \hat{s}_j(t') \hat{w}(t) - \hat{s}_j(t') \hat{w}(t) \hat{s}_i(t)] \langle \hat{\Gamma}_i(t) \hat{\Gamma}_j(t') \rangle_R \\ & + [\hat{w}(t) \hat{s}_j(t') \hat{s}_i(t) - \hat{s}_i(t) \hat{w}(t) \hat{s}_j(t')] \langle \hat{\Gamma}_j(t') \hat{\Gamma}_i(t) \rangle_R, \end{aligned} \quad (5.66)$$

where we have used the cyclic property of the trace, dropped the operator subscript \mathbf{q} , and written $\text{Tr}_R(\hat{R} \hat{A}) = \langle \hat{A} \rangle_R$. We have also used the fact that $\langle \hat{\Gamma}_{\mathbf{q},i}(t') \hat{\Gamma}_{\mathbf{q}',j}(t) \rangle_R = 0$ for $\mathbf{q} \neq \mathbf{q}'$.

Proceeding in the standard way, we change the variable of integration to $\tau = t - t'$, and note that $\hat{b}_{\mathbf{q}}(t - \tau) = e^{-i\hat{H}_b \tau / \hbar} \hat{b}_{\mathbf{q}}(t) e^{i\hat{H}_b \tau / \hbar} = e^{i\varepsilon_{\mathbf{q}} \tau / \hbar} \hat{b}_{\mathbf{q}}(t)$ and similarly $e^{-i\hat{H}_b \tau / \hbar} \hat{b}_{\mathbf{q}}^\dagger(t) e^{i\hat{H}_b \tau / \hbar} = e^{-i\varepsilon_{\mathbf{q}} \tau / \hbar} \hat{b}_{\mathbf{q}}^\dagger(t)$.

We then make use of the assumption that $\hat{w}(t) \approx \hat{\mathcal{P}} \hat{w}(t)$ (see (5.19)), and write the master equation in a Fock state representation. Noting also that $\langle \hat{b}_{\mathbf{q}}(t) \hat{b}_{\mathbf{q}}(t) \rangle_R = \langle \hat{b}_{\mathbf{q}}^\dagger(t) \hat{b}_{\mathbf{q}}^\dagger(t) \rangle_R = 0$, we obtain

$$\begin{aligned} \dot{\hat{w}} = & -\frac{2g_{ab}^2 \rho_0}{V \hbar^2} \sum_{\mathbf{q}} (u_{\mathbf{q}} + v_{\mathbf{q}})^2 \sum_{m,n} \int_0^t d\tau \left[|m\rangle \langle m| e^{-iq_x \hat{x}} |n\rangle \langle n| e^{iq_x \hat{x}} |m\rangle \langle m| p_m e^{i\omega \tau (m-n)} \right. \\ & \left. - |m\rangle \langle m| e^{-iq_x \hat{x}} |n\rangle \langle n| e^{-iq_x \hat{x}} |m\rangle \langle m| p_n e^{i\omega \tau (n-m)} \right] \left(e^{-i\varepsilon_{\mathbf{q}} \tau / \hbar} \langle \hat{b}_{\mathbf{q}} \hat{b}_{\mathbf{q}}^\dagger \rangle_R + e^{i\varepsilon_{\mathbf{q}} \tau / \hbar} \langle \hat{b}_{\mathbf{q}}^\dagger \hat{b}_{\mathbf{q}} \rangle_R \right) \end{aligned} \quad (5.67)$$

Assuming that the correlation time of the superfluid reservoir is much shorter than that in the system we can extend the integration over $\tau \rightarrow \infty$, and making the replacement $\int_0^\infty d\tau e^{i(\varepsilon-\varepsilon_0)\tau/\hbar} \rightarrow \pi\hbar\delta(\varepsilon-\varepsilon_0)$, we obtain

$$\begin{aligned} \dot{p}_m = & \frac{2\pi g_{ab}^2 \rho_0}{V\hbar} \sum_{\mathbf{q}} (u_q + v_q)^2 \sum_n \left| \langle m | e^{-iqx\hat{x}} | n \rangle \right|^2 \{ \\ & [\delta(\hbar\omega(n-m) - \varepsilon_{\mathbf{q}}) p_n - \delta(\hbar\omega(m-n) - \varepsilon_{\mathbf{q}}) p_m] \langle \hat{b}_{\mathbf{q}} \hat{b}_{\mathbf{q}}^\dagger \rangle_R \\ & + [\delta(\hbar\omega(m-n) - \varepsilon_{\mathbf{q}}) p_n - \delta(\hbar\omega(n-m) - \varepsilon_{\mathbf{q}}) p_m] \langle \hat{b}_{\mathbf{q}}^\dagger \hat{b}_{\mathbf{q}} \rangle_R \}. \end{aligned} \quad (5.68)$$

The first two terms here (those proportional to $\langle \hat{b}_{\mathbf{q}} \hat{b}_{\mathbf{q}}^\dagger \rangle_R$) describe the damping by creation of excitations in the superfluid, whilst the second two terms (those proportional to $\langle \hat{b}_{\mathbf{q}}^\dagger \hat{b}_{\mathbf{q}} \rangle_R$) describe heating effects by absorption of thermally generated excitations. At finite temperatures, the reservoir correlation functions are given by the number of thermal excitations $N(\mathbf{q})$ with momentum $\hbar\mathbf{q}$, $\langle \hat{b}_{\mathbf{q}}^\dagger \hat{b}_{\mathbf{q}} \rangle_R = N(\mathbf{q})$.

5.C Estimation of $\delta\hat{\Psi}^\dagger\delta\hat{\Psi}$ Terms

The heating effects due to absorption of thermal excitations has already been discussed in section 5.4.3, where the equilibrium distribution at finite temperatures was shown to be a Boltzmann distribution. The small additional damping terms arising at finite temperatures from the $\delta\hat{\Psi}^\dagger\delta\hat{\Psi}$ term, which are small when the condensate density, ρ_0 is large and which were omitted when the density fluctuation operator $\delta\hat{\rho}$ was originally written, may be estimated using a semi-classical treatment. The operator for the additional density fluctuation terms is given by

$$\begin{aligned} \delta\hat{\rho}' = & \delta\hat{\Psi}^\dagger\delta\hat{\Psi} = \frac{1}{V} \sum_{\mathbf{p},\mathbf{p}'} u_{\mathbf{p}} u_{\mathbf{p}'} \hat{a}_{\mathbf{p}} \hat{a}_{\mathbf{p}'}^\dagger e^{i(\mathbf{p}-\mathbf{p}')\cdot\mathbf{r}} \\ & + v_{\mathbf{p}} v_{\mathbf{p}'} \hat{a}_{\mathbf{p}}^\dagger \hat{a}_{\mathbf{p}'} e^{-i(\mathbf{p}-\mathbf{p}')\cdot\mathbf{r}} + u_{\mathbf{p}} v_{\mathbf{p}'} \hat{a}_{\mathbf{p}} \hat{a}_{\mathbf{p}'} e^{i(\mathbf{p}+\mathbf{p}')\cdot\mathbf{r}} \\ & + u_{\mathbf{p}} v_{\mathbf{p}'} \hat{a}_{\mathbf{p}}^\dagger \hat{a}_{\mathbf{p}'}^\dagger e^{-i(\mathbf{p}+\mathbf{p}')\cdot\mathbf{r}}. \end{aligned} \quad (5.69)$$

The first two terms in this expression correspond to the inelastic scattering of thermal excitations with momentum $\hbar\mathbf{p}$ to excitations with momentum $\hbar\mathbf{p}'$, and the second two correspond to the absorption and emission respectively of two excitations with momenta $\hbar\mathbf{p}$ and $\hbar\mathbf{p}'$.

For the case of supersonic motion where $u_q \rightarrow 1$ and $v_q \rightarrow 0$, the correction to the dissipation rate is then given by

$$\dot{\varepsilon}' = -\frac{\pi g_{ab}^2}{\hbar} \sum_{\mathbf{p},\mathbf{p}'} \sum_n [N(\mathbf{p}) - N(\mathbf{p}')] \delta(\hbar\omega n - \varepsilon_{\mathbf{p}'} + \varepsilon_{\mathbf{p}}) \left| \frac{\omega}{2\pi} \int_0^{2\pi/\omega} e^{i(\mathbf{p}-\mathbf{p}')\cdot\mathbf{r}(t)} dt \right|^2 \hbar\omega n, \quad (5.70)$$

where, as before, $N(\mathbf{p}) = (\exp[\varepsilon_{\mathbf{p}}/(k_B T)] - 1)^{-1}$ is the mean number of thermal Bogoliubov excitations with momentum $\hbar\mathbf{p}$ present in the superfluid.

In order to cool the system to the ground state we already require $\hbar\omega \gg k_B T$, which has been shown to be a reasonable experimental condition in section 5.4.3. In this case, the thermally generated excitations with momentum $\hbar\mathbf{p}$ will have a much smaller energy than the scattered excitations, which have momentum $\hbar\mathbf{p}'$. Also, $\varepsilon_{\mathbf{p}'} > \hbar\omega \gg k_B T$ and $N(\mathbf{p}') \approx 0$. Thus,

$$\begin{aligned}\dot{\varepsilon}' &\approx -\frac{\pi g_{ab}^2}{\hbar} \sum_{\mathbf{p}, \mathbf{p}'} \sum_n N(\mathbf{p}) \delta(\hbar\omega n - \varepsilon_{\mathbf{p}'}) \left| \frac{\omega}{2\pi} \int_0^{2\pi/\omega} e^{i(\mathbf{p}') \cdot \mathbf{r}(t)} dt \right|^2 \hbar\omega n, \\ &= \frac{\dot{\varepsilon}}{2\rho_0} \frac{1}{2\pi^2} \int_0^\infty p^2 dp N(\mathbf{p}).\end{aligned}\quad (5.71)$$

This result is proportional to the density of thermal excitations and essentially describes the classical friction due to scattering of thermal excitations by the moving particle.

If $k_B T \ll m_b u^2/2$, then $\varepsilon_{\mathbf{p}} \approx \hbar u p$. The additional damping is then given in terms of the rate $\dot{\varepsilon}$ in (5.52) by

$$\dot{\varepsilon}' = \frac{\dot{\varepsilon} \zeta(3)}{2\pi^2 \rho_0 (\hbar u)^3} (k_B T)^3, \quad (5.72)$$

where $\zeta(x)$ denotes the Riemann Zeta function. Note that because the wavenumber of phonons in this regime is of the order of $k_B T/(\hbar u)$, this result is proportional to the density of thermal phonons, ρ_{phonons} . Thus the additional damping term is equal to that in (5.52), but with the numerical coefficient modified, and the density of the condensate ρ_0 replaced by the density of thermal phonons, ρ_{phonons} . This term will always be small, as in this regime $T < T_c$, the critical temperature of the Bose gas, so $\rho_0 \gg \rho_{\text{phonons}}$.

If $k_B T \gg m_b u^2/2$, then $\varepsilon_{\mathbf{p}} \approx \hbar^2 p^2/(2m_b)$. The rate of additional damping is then

$$\dot{\varepsilon}' = \frac{\dot{\varepsilon} \zeta(3/2) m_b^{3/2}}{4\sqrt{2} \pi^{3/2} \rho_0 \hbar^3} (k_B T)^{3/2}. \quad (5.73)$$

For a uniform Bose gas the critical temperature for Bose condensation can be expressed as [35]

$$k_B T_c = \frac{2\pi \hbar^2 \rho_t^{2/3}}{m_b [\zeta(3/2)]^{2/3}}, \quad (5.74)$$

where $\rho_t = \rho_0 + \rho_n$ is the total density, and ρ_n is the density of the normal component, so that we can rewrite (5.73) as

$$\dot{\varepsilon}' = \frac{\dot{\varepsilon} \rho_t}{2\rho_0} \left(\frac{T}{T_c} \right)^{3/2} = \frac{\dot{\varepsilon} \rho_n}{2\rho_0}, \quad (5.75)$$

where we have used the well known result $\rho_n = \rho_t (T/T_c)^{3/2}$ [35]. Thus, this result has the same form as the damping rate obtained in (5.52), but the condensate density is replaced by the density of the normal component, and the numerical coefficient is decreased by a factor of 2. Again, at small temperatures compared with the critical temperature, $T \ll T_c$, when $\rho_n \ll \rho_0$, the contribution from this term will be small.

The same calculation can be performed for the subsonic case. In this regime, the contribution from the terms involving $\hat{a}_{\mathbf{p}} \hat{a}_{\mathbf{p}'}$ and $\hat{a}_{\mathbf{p}}^\dagger \hat{a}_{\mathbf{p}'}^\dagger$ is small, because the double summation

over \mathbf{p} and \mathbf{p}' is restricted by energy conservation such that $|\varepsilon_p + \varepsilon_{p'}| = \hbar\omega n$, and in the subsonic case, this quantity is always small. With respect to the subsonic energy dissipation rate in (5.54), $\dot{\varepsilon}$, we obtain

$$\dot{\varepsilon}' \approx -\frac{\pi^2 \dot{\varepsilon}}{480 \rho_0 m_b u^5 \hbar^3} (k_B T)^4. \quad (5.76)$$

Note that as $\hbar\omega n \ll m_b u^2/2$, this expression is derived considering only the case where $k_B T \ll m_b u^2/2$. It can be shown that in the limit $k_B T \ll m u^2/2$ that the density of the normal component ρ_n is given by [35]

$$\rho_n = \frac{2\pi^2 (k_B T)^4}{45 m_b \hbar^3 u^5}, \quad (5.77)$$

so that we can write (5.76) as

$$\dot{\varepsilon}' \approx -\frac{3\dot{\varepsilon}\rho_n}{64\rho_0}. \quad (5.78)$$

Again, this result is a modification of the zero-temperature damping result, with the condensate density replaced by the density of the normal component and the numerical coefficient decreased. In the limit $T \ll T_c$, as with the supersonic results, this result will be small, as $\rho_n \ll \rho_0$.

Bibliography

- [1] See, for example, *Experimental Quantum Computation and Information*, Proceedings of the International School of Physics “Enrico Fermi”, Course CXLVIII (IOS Press, Amsterdam, 2002).
- [2] S. Kuhr, W. Alt, D. Schrader, M. Müller, V. Gomer, and D. Meschede, *Science* **293**, 278 (2001); N. Schlosser, G. Reymond, I. Protsenko, and P. Grangier, *Nature (London)* **411**, 1024 (2001).
- [3] M. Greiner, O. Mandel, T. W. Hänsch and I. Bloch *Nature (London)* **415**, 39 (2002); M. Greiner, O. Mandel, T. Esslinger, T.W. Hänsch and I. Bloch, *Nature (London)* **419** 51 (2002).
- [4] R. Folman, P. Krüger, J. Schmiedmayer, J. H. Denschlag, and C. Henkel, *Adv. At. Mol. Opt. Phys.* **48**, 263 (2002); R. Dumke, M. Volk, T. Müther, F. B. J. Buchkremer, G. Birkl, and W. Ertmer, *Phys. Rev. Lett.* **89**, 097903 (2002); W. Hänsel, J. Reichel, P. Hommelhoff, and T. W. Hänsch, *Phys. Rev. Lett.* **86**, 608 (2001).
- [5] See, for example, H. J. Metcalf and P. van der Straten, *Laser Cooling and Trapping*, (Springer, New York, 1999).
- [6] For a review, see Insight section, *Nature (London)* **416** (2002).
- [7] I. H. Deutsch and P. S. Jessen, *Phys. Rev. A* **57**, 1972 (1998).
- [8] D. Jaksch, C. Bruder, J. I. Cirac, C. W. Gardiner, and P. Zoller, *Phys. Rev. Lett.* **81**, 3108 (1998).

- [9] O. Mandel, M. Greiner, A. Widera, T. Rom, T. W. Hänsch, and I. Bloch, *Phys. Rev. Lett.* **91**, 010407 (2003).
- [10] C. Fort, F. S. Cataliotti, L. Fallani, F. Ferlaino, P. Maddaloni, and M. Inguscio, *Phys. Rev. Lett.* **90**, 140405 (2003).
- [11] O. Morsch, J. H. Müller, D. Ciampini, M. Cristiani, P. B. Blakie, C. J. Williams, P. S. Julienne, and E. Arimondo, *Phys. Rev. A* **67**, 031603(R) (2003).
- [12] T. Calarco, H.-J. Briegel, D. Jaksch, J.I. Cirac, and P. Zoller, *Fortschr. Phys.* **48**, 945 (2000).
- [13] G. K. Brennen, C. M. Caves, P. S. Jessen, and I. H. Deutsch, *Phys. Rev. Lett.* **82**, 1060 (1999).
- [14] R. Raussendorf and H. J. Briegel, *Phys. Rev. Lett.* **86**, 5188 (2001).
- [15] J. Mompart, K. Eckert, W. Ertmer, G. Birkl, and M. Lewenstein, *Phys. Rev. Lett.* **90**, 147901 (2003).
- [16] E. Charron, E. Tiesinga, F. Mies, and C. Williams, *Phys. Rev. Lett.* **88**, 077901 (2002).
- [17] H. Rohde, S. T. Gulde, C. F. Roos, P. A. Barton, D. Leibfried, J. Eschner, F. Schmidt-Kaler, and R. Blatt, *J. Opt. B: Quantum Semiclassical Opt.* **3**, S34 (2001).
- [18] D. Leibfried, B. DeMarco, V. Meyer, M. Rowe, A. Ben-Kish, M. Barrett, J. Britton, J. Hughes, W. M. Itano, B. M. Jelenkovic, C. Langer, D. Lucas, T. Rosenband, and D. J. Wineland, *J. Phys. B* **36**, 599 (2003); B.B. Blinov, L. Deslauriers, P. Lee, M.J. Madsen, R. Miller, and C. Monroe, *Phys. Rev. A* **65**, 040304(R) (2002).
- [19] C. J. Myatt, E. A. Burt, R. W. Ghrist, E. A. Cornell, and C. E. Wieman, *Phys. Rev. Lett.* **78**, 586 (1997); B. DeMarco and D. S. Jin, *Science* **285**, 1703 (1999).
- [20] I. Bloch, M. Greiner, O. Mandel, T. W. Hänsch, and T. Esslinger, *Phys. Rev. A* **64**, 021402 (2001).
- [21] F. Schreck, G. Ferrari, K. L. Corwin, J. Cubizolles, L. Khaykovich, M.-O. Mewes, and C. Salomon, *Phys. Rev. A* **64**, 011402 (2001); A. G. Truscott, K. E. Strecker, W. I. McAlexander, G. B. Partridge, and R. G. Hulet, *Science* **291**, 2570 (2001).
- [22] For a review on ultracold collisions, see J. Weiner, V. S. Bagnato, S. Zilio, and P. S. Julienne, *Rev. Mod. Phys.* **71**, 1 (1999).
- [23] E. Tiesinga, B. J. Verhaar, and H. T. C. Stoof, *Phys. Rev. A* **47**, 4114 (1993).
- [24] L.-M. Duan, A. Sørensen, J. I. Cirac, and P. Zoller, *Phys. Rev. Lett.* **85**, 3991 (2000).
- [25] A. Sørensen, L.-M. Duan, J. I. Cirac and P. Zoller, *Nature (London)* **409**, 63 (2001).
- [26] E. M. Lifshitz and L. P. Pitaevskii, *Statistical Physics, Part 2*, (Pergamon Press, Oxford, 1980).

-
- [27] See, for example D. Pines and P. Nozières, *The Theory of Quantum Liquids*, (Benjamin, New York, 1966), Vol. I.
- [28] See, for example, C. W. Gardiner, *Handbook of Stochastic Methods*, 2nd Ed. (Springer-Verlag, Berlin, 1985).
- [29] A. B. Migdal, *Qualitative Methods in Quantum Theory*, (W. A. Benjamin, Massachusetts, 1977).
- [30] E. H. Lieb and W. Liniger, Phys. Rev. **130**, 1605 (1963); E. H. Lieb, Phys. Rev. **130**, 1616 (1963).
- [31] F. D. M. Haldane, Phys. Rev. Lett. **47**, 1840 (1981).
- [32] M. Olshanii, Phys. Rev. Lett. **81**, 938 (1998); D. S. Petrov, G. V. Shlyapnikov and J. T. M. Walraven, Phys. Rev. Lett. **85**, 3745 (2000).
- [33] S. T. Beliaev, Zh. Eksp. Teor. Fiz. **34**, 433 (1958) [Sov. Phys. JETP **7**, 299 (1958)].
- [34] See, for example, D. F. Walls and G. J. Milburn, *Quantum Optics*, (Springer-Verlag, Berlin, 1994).
- [35] C. J. Pethick and H. Smith, *Bose-Einstein Condensation in Dilute Gases*, (Cambridge University Press, Cambridge, 2002).
- [36] G. E. Astracharchik and L. P. Pitaevski, e-print cond-mat/0307247 [Phys. Rev. A **70**, 013608 (2004)].

CHAPTER 6

PUBLICATION

Fault-Tolerant Dissipative Preparation of Atomic Quantum Registers with Fermions[†]

Accepted for publication in Phys. Rev. A

A. Griessner^{1,2}, A. J. Daley^{1,2}, D. Jaksch³, and P. Zoller^{1,2}

1) *Institute for Quantum Optics and Quantum Information of the Austrian Academy of Sciences, A-6020 Innsbruck, Austria*

2) *Institute for Theoretical Physics, University of Innsbruck, A-6020 Innsbruck, Austria*

3) *Clarendon Laboratory, University of Oxford, Parks Road, Oxford OX1 3PU, U.K.*

We propose a fault tolerant loading scheme to produce an array of fermions in an optical lattice of the high fidelity required for applications in quantum information processing and the modelling of strongly correlated systems. A cold reservoir of Fermions plays a dual role as a source of atoms to be loaded into the lattice via a Raman process and as a heat bath for sympathetic cooling of lattice atoms. Atoms are initially transferred into an excited motional state in each lattice site, and then decay to the motional ground state, creating particle-hole pairs in the reservoir. Atoms transferred into the ground motional level are no longer coupled back to the reservoir, and doubly occupied sites in the motional ground state are prevented by Pauli blocking. This scheme has strong conceptual connections with optical pumping, and can be extended to load high-fidelity patterns of atoms.

6.1 Introduction

High-precision control of cold atoms in optical lattices has found many potential applications in recent years, especially in the implementation of quantum information processing and the

[†]The author of the present thesis acted primarily in an advisory role throughout this work, discussing the concepts, calculation methods, and scientific conclusions with AG, who performed most of the primary calculations.

modelling of strongly correlated condensed matter systems [1]. These applications have been fuelled by experimental techniques which enable engineering of lattice models with sensitive control over lattice parameters [2–4], independent control for different internal spin states [5], and control of interactions between atoms via Feshbach resonances [6, 7].

For high precision applications, initial state preparation will play a key role in addition to such control of Hamiltonian parameters [8]. Quantum computing applications generally require an initial register with exactly one atom per lattice site [9], and observation of interesting effects in strongly correlated systems often requires the initial spatial patterns of atoms or states with precisely chosen filling factors [10].

The first step in preparation of such states is often adiabatically increasing the lattice potential, making use of repulsive onsite interactions for bosons [11] or Pauli blocking for fermions [12] to load essentially one atom on each lattice site. However, experimental imperfections will generally lead to non-negligible errors in the resulting states. This can be improved upon by coherently filtering a state with a filling factor initially greater than one [8, 13], or potentially by schemes involving individual addressing and precise measurement of the occupation in individual lattice sites [14, 15]. Whilst these methods can, in principle, produce high fidelity initial states, each of them relies either on the perfect experimental implementation of a single-shot coherent process or on perfect measurements to avoid defects in the final state. In this article we propose a *fault-tolerant* loading scheme in which the state being prepared always improves in time. The key idea is the addition of a dissipative element to the loading process, in contrast to previous schemes, which rely on coherent transfer or perfect measurements. As we will see below, this dissipative element plays a similar role in our scheme to that of spontaneous emissions in optical pumping.

Motivated by advances in experiments with cold fermions [16–24], our scheme is designed to produce a regular patterned array of fermions in an optical lattice. Fermions have a natural advantage in initialising atomic qubit registers because Pauli-blocking prevents doubly-occupied sites, and most of the techniques illustrated using bosons in quantum computing proposals apply equally to fermions. Fermionic species are also of special interest in the simulation of condensed matter systems [25].

The setup for our scheme is illustrated in Fig. 6.1. Atoms in an internal state $|b\rangle$ do not couple to the lattice lasers, and form a cold Fermi reservoir, which will play the dual role of a source for atoms to transfer into the lattice, and a bath for cooling lattice atoms. Atoms in the reservoir are coupled into an excited motional level in the lattice (in internal state $|a\rangle$) via a coherent laser-induced Raman process (Fig. 6.1a) [26]. These atoms are then cooled sympathetically by the reservoir atoms via collisional interactions, and will decay to the motional ground state together with creation of a particle-hole pair in the reservoir (Fig. 6.1b). This is analogous to the sympathetic cooling process previously presented for a bosonic reservoir in [27]. Double occupancy in the ground state is prevented by Pauli blocking (Fig. 6.1b), and atoms in the ground state are not coupled back to the reservoir because the Raman process is far off resonance, so the occupation of the lowest motional level always increases in time. Additional atoms remaining in excited states at the end of the process can then be removed by a careful adiabatic detuning and switching off of the coupling lasers (Fig. 6.1c).

Such dissipative transfer of atoms into a desired dark state is strongly reminiscent of optical pumping, in which atoms are excited by a laser, and undergo spontaneous emissions

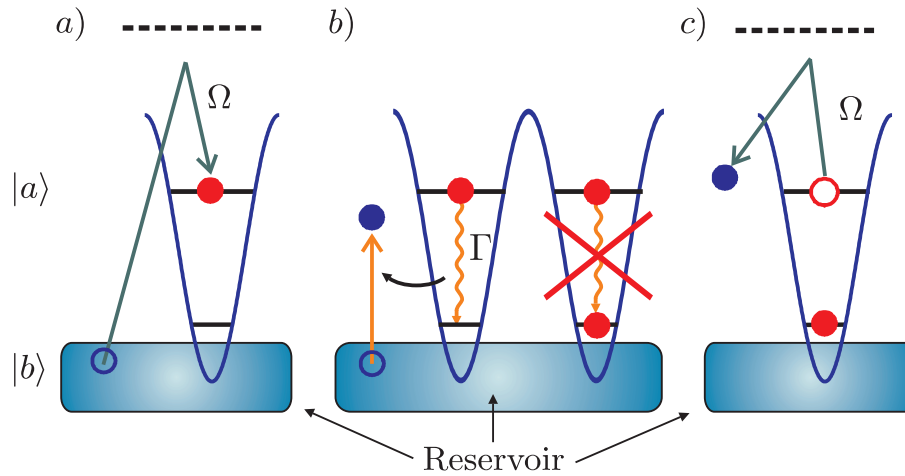


Figure 6.1. *Laser-assisted dissipative loading of fermions in an optical lattice: (a) Atoms are coupled from an external reservoir (in internal state $|b\rangle$) into an excited motional state in the lattice (internal state $|a\rangle$) via a Raman process; (b) These atoms are cooled to the ground motional level via collisional interaction with the reservoir atoms, and doubly-occupied sites in the ground level are prevented by Pauli blocking; (c) Remaining atoms in the excited motional levels are removed by carefully detuning the Raman coupling above the Fermi Energy.*

into a desired state which does not couple to the laser field. The net result of this is to transfer entropy from the atomic system into the “reservoir” (the vacuum modes of the radiation field) in order to produce a single pure electronic state from an initial mixed state. Here the creation of an excitation in the reservoir replaces the spontaneous emission event, placing the atom in a state where it is not coupled by the Raman process, and leading to the production of our final pure state, namely a high fidelity array of one atom in each lattice site (or a pattern of occupied and unoccupied sites).

We note, in addition, that the purely coherent laser-assisted loading could be used as a stand-alone technique to load the lattice, and could produce high fidelity states if used iteratively, together with cooling of the Fermi reservoir. Such cooling would fill holes produced in the previous loading step, so that Pauli blocking would prevent a net transfer of atoms from the lattice to the reservoir, thus ensuring that the filling factor in the lattice is improved in each step.

The detailed analysis of this dissipative loading process is divided into two parts. Coherent laser-assisted loading of atoms into the entire lattice in a single addressed motional band is discussed in section 6.2, and the dissipative transfer of atoms to the lowest motional band is analysed in section 6.3. The combination of these two elements into the overall scheme is then detailed in section 6.4.

6.2 Laser-Assisted Loading

We begin by studying the coupling of the atoms forming the reservoir into the optical lattice via a Raman process, as shown in Fig. 6.2. The atoms in the Reservoir are in an internal state $|b\rangle$, which does not couple to the lasers producing the optical lattice. They form a Fermi gas containing N atoms with a density $n_{3D} = N/V$ in a volume V , with Fermi energy ($\hbar = 1$) $\epsilon_F = (6\pi^2 n_{3D})^{2/3} / 2m$, where m is the mass of the atoms. The internal state $|b\rangle$ is coupled to a different internal state $|a\rangle$, which is trapped by a deep three dimensional optical lattice potential $V_a(\mathbf{x})$ via a Raman transition.

Our goal is to couple atoms b into the lattice and to achieve an average occupation of fermions close to one in all lattice sites in one chosen motional band, without coupling to other motional levels. This should be achieved on a time scale where no atoms are allowed to tunnel between different lattice sites and no loss of atoms occurs due, e.g., to spontaneous emission events leading to additional internal states or to inelastic three body collisions, where two atoms in the reservoir collide with an atom in the lattice and form a molecule. We note that the latter process is strongly suppressed for fermions due to a mechanism related to Pauli blocking [28], which is also responsible for the greatly increased lifetime observed for Fermionic dimers in a two-species mixture [29].

6.2.1 The Model

The total Hamiltonian of this system is given by

$$H = H_a + H_b + H_{RC}, \quad (6.1)$$

where the Hamiltonians for the atoms a in the optical lattice and for the atoms b forming the reservoir are

$$H_a = \int d^3x \hat{\psi}_a^\dagger(\mathbf{x}) \left(-\frac{\nabla^2}{2m} + V_a(\mathbf{x}) \right) \hat{\psi}_a(\mathbf{x}), \quad (6.2)$$

and

$$H_b = \int d^3x \hat{\psi}_b^\dagger(\mathbf{x}) \left(-\frac{\nabla^2}{2m} \right) \hat{\psi}_b(\mathbf{x}), \quad (6.3)$$

respectively, in which the anticommuting field operators $\hat{\psi}_i^\dagger(\mathbf{x})$ create a fermion in the internal state $i \in \{a, b\}$ at the position \mathbf{x} .

The two internal states are coupled via a Raman process described by the Hamiltonian

$$H_{RC} = \int d^3x \left[\frac{\Omega}{2} \left(\hat{\psi}_b^\dagger(\mathbf{x}) \hat{\psi}_a(\mathbf{x}) + \text{h.c.} \right) + \Delta \hat{\psi}_a^\dagger(\mathbf{x}) \hat{\psi}_a(\mathbf{x}) \right], \quad (6.4)$$

with the Raman detuning Δ and the effective (two photon) Rabi frequency Ω , where we have assumed running waves with the same wave vectors for two lasers producing the Raman coupling.

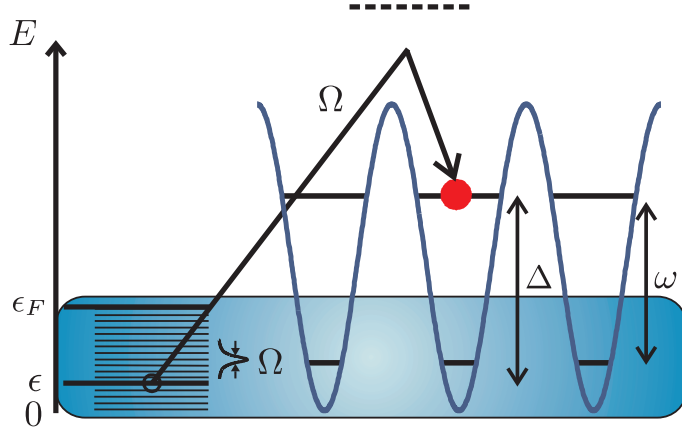


Figure 6.2. Reservoir atoms with energy ϵ are resonantly coupled to the first excited Bloch band of the lattice via a Raman laser with two photon Rabi frequency Ω . The resonant energy ϵ is experimentally tunable via the Raman detuning, and the energy separation of the two Bloch bands is denoted by ω . All frequencies and energies are plotted in arbitrary units with $\hbar = 1$.

We expand the field operators for the free fermions in the reservoir as plane waves and the field operators for the lattice atoms in terms of Wannier functions,

$$\begin{aligned}\hat{\psi}_b(\mathbf{x}) &= \frac{1}{\sqrt{V}} \sum_{\mathbf{k}} e^{i\mathbf{k}\mathbf{x}} b_{\mathbf{k}}, \\ \hat{\psi}_a(\mathbf{x}) &= \sum_{\alpha, \mathbf{n}} w_{\mathbf{n}}(\mathbf{x} - \mathbf{x}_{\alpha}) a_{\alpha, \mathbf{n}},\end{aligned}\quad (6.5)$$

where, $b_{\mathbf{k}}^{\dagger}$ creates a reservoir atom with momentum \mathbf{k} , $a_{\alpha, \mathbf{n}}^{\dagger}$ is the creation operator for an atom in lattice site α and motional state with $\mathbf{n} = (n_x, n_y, n_z)$ in the deep three dimensional optical lattice, for which $w_{\mathbf{n}}(\mathbf{x} - \mathbf{x}_{\alpha})$, denotes the corresponding Wannier function.

Inserting into Eqs. (6.2)-(6.4) we obtain

$$\begin{aligned}H_b &= \sum_{\mathbf{k}} \epsilon_{\mathbf{k}} b_{\mathbf{k}}^{\dagger} b_{\mathbf{k}}, \\ H_a &= \sum_{\alpha, \mathbf{n}} (\omega_{\mathbf{n}} + \Delta) a_{\alpha, \mathbf{n}}^{\dagger} a_{\alpha, \mathbf{n}}, \\ H_{RC} &= \frac{\Omega}{2} \sum_{\mathbf{k}, \alpha, \mathbf{n}} \left(R_{\mathbf{k}, \mathbf{n}} e^{-i\mathbf{k}\mathbf{x}_{\alpha}} b_{\mathbf{k}}^{\dagger} a_{\alpha, \mathbf{n}} + \text{h.c.} \right),\end{aligned}\quad (6.6)$$

where the single particle energy of a reservoir atom with momentum \mathbf{k} is $\epsilon_{\mathbf{k}} = |\mathbf{k}|^2/2m$ and the energy of a lattice atom in the motional state \mathbf{n} is given by

$$\omega_{\mathbf{n}} = \int d^3x w_{\mathbf{n}}(\mathbf{x}) \left(-\frac{\nabla^2}{2m} + V_a(\mathbf{x}) \right) w_{\mathbf{n}}(\mathbf{x}).\quad (6.7)$$

As we are dealing with very deep optical lattices, tunneling between different lattice sites is strongly suppressed and has thus been neglected. The Raman coupling parameter $R_{\mathbf{k},\mathbf{n}}$ can be written as

$$R_{\mathbf{k},\mathbf{n}} = \frac{1}{\sqrt{V}} \int d^3x e^{-i\mathbf{k}\mathbf{x}} w_{\mathbf{n}}(\mathbf{x}). \quad (6.8)$$

For our deep optical lattices without tunneling between different sites, the periodic lattice is equivalent to an array of independent microtraps, where each individual trap is well approximated by a harmonic oscillator. The Wannier functions $w_{\mathbf{n}}(\mathbf{x} - \mathbf{x}_{\alpha})$ can then be approximated by harmonic oscillator eigenfunctions $\phi_{\mathbf{n}}(\mathbf{x} - \mathbf{x}_{\alpha})$ of the \mathbf{n} -th oscillator level in lattice site α . This approximation allows us to calculate the coupling parameters $R_{\mathbf{k},\mathbf{n}}$ from the Fermi reservoir to the optical lattice explicitly. For an isotropic three dimensional lattice (where the frequency ω of each oscillator is given by $\omega \approx \omega_n - \omega_{n-1}$ and $n \equiv (n_x + n_y + n_z)$) the couplings to the lowest and first three (degenerate) excited motional states are given by

$$\begin{aligned} R_{\mathbf{k},0} &= \frac{1}{\sqrt{V}} \pi^{3/4} (8a_0^3)^{1/2} e^{-\mathbf{k}^2 a_0^2/2}, \\ R_{\mathbf{k},1_{x,y,z}} &= \sqrt{2} a_0 i \mathbf{k}_{x,y,z} R_{\mathbf{k},0}, \end{aligned} \quad (6.9)$$

where $a_0 = \sqrt{1/m\omega}$ denotes the size of the harmonic oscillator ground state, and the index x, y, z labels the coupling to the three degenerate states of the first excited oscillator level.

The characteristics of the coherent loading procedure strongly depend on the interplay between the (experimentally adjustable) parameters: the detuning Δ and two photon Rabi frequency Ω of the lasers producing the Raman coupling, the Fermi energy ϵ_F and the separation ω of the oscillator levels. The Raman detuning can be adjusted to address different states in the Fermi sea and different motional states in the lattice. In the following we write $\Delta = -5\omega/2 + \epsilon$ to indicate the resonant coupling of reservoir atoms with energy ϵ to the $n = 1$ motional states of each lattice site. We note that it is straightforward to address other motional states in the lattice (e.g. to directly load the lowest level) by adjusting the detuning Δ . However, as we will later use the transfer of the atoms from the reservoir to the lattice as a first step of an indirect loading of the lowest motional states as described in the introduction, we choose the transfer to the first excited motional state here. To be able to selectively fill the first excited oscillator levels, the conditions $(\epsilon_F - \epsilon) \ll \omega$ and $\epsilon \ll \omega$ (and consequently $\epsilon_F \ll \omega$) have to be fulfilled, in order to avoid unwanted coupling to higher excited and to the lowest motional state, respectively.

6.2.2 The Fast and Slow Loading Regimes

The physics of the loading process allows us to identify two different loading limits: (1) the “fast loading regime”, where

$$\Omega \gg \omega, \epsilon_F, \quad (6.10)$$

and (2) the “slow regime”, where

$$\Omega \ll \omega, \epsilon_F. \quad (6.11)$$

Below we will see that our goal to selectively fill a certain motional state without coupling to other states can only be achieved in the slow loading regime, but to obtain more insight into the physics of the loading dynamics it is instructive to discuss both regimes.

In the fast loading regime, where the Rabi frequency Ω is the largest frequency scale in the system, the loading is performed in a very short time $T \sim \pi/\Omega \ll a_0/v_F$, with $v_F = \sqrt{2\epsilon_F/M}$ the Fermi velocity, where atoms in the Fermi reservoir do not move significantly during the loading on a lengthscale given by the size a_0 of the harmonic oscillator ground state. The Wannier modes in the lattice then couple to localized reservoir fermions at each site, and thus the dynamics for different sites decouple. Given there is at least one fermion in the reservoir per size a_0 of the ground state in each lattice site during the loading, i.e., given the density of the reservoir atoms

$$n_{3D} \gtrsim 1/a_0^3, \quad (6.12)$$

each $n = 1$ motional state in each lattice site can be filled with at least one atom from the reservoir by applying a π -pulse $\Omega T = \pi$. For an optical lattice with $\omega/2\pi \sim 50\text{kHz}$ the required densities of the Fermi gas are $n_{3D} \gtrsim 3 \times 10^{15}\text{cm}^{-3}$ for ^{40}K and for deeper lattices the required densities are even higher. The condition (6.12) for the density of the reservoir can be expressed in terms of energies as

$$\epsilon_F \geq (6\pi^2/\sqrt{2})^{2/3}\omega. \quad (6.13)$$

This inequality violates the condition $\epsilon_F \ll \omega$, which is necessary to be able to selectively address individual motional states. Consequently, unwanted population will be transferred to additional motional states in this loading limit, which would have to be carefully removed after the loading process.

In the slow loading regime, where condition (6.11) is fulfilled, the atoms in the Fermi reservoir are no longer frozen during the loading process, but are allowed to move with respect to the lattice during the loading. This is now performed in a time $T \gg \lambda/2v_F$, where $\lambda/2$ is the lattice spacing. Consequently, the density condition (6.12) can be relaxed to

$$n_{3D} \left(\frac{\lambda}{2}\right)^3 \gtrsim 1, \quad (6.14)$$

i.e., we only need one atom in the reservoir per lattice site to be able to efficiently fill the lattice. For typical experimental parameters $\lambda \sim 800\text{nm}$ for ^{40}K this results in the condition $n_{3D} \gtrsim 10^{13}\text{cm}^{-3}$, which has already been achieved in current experiments (e.g. [30]). The density condition (6.14) expressed in terms of energies now reads

$$\epsilon_F \gtrsim \left(\frac{6}{\pi}\right)^{2/3} \omega_R, \quad (6.15)$$

with $\omega_R = 2\pi^2/m\lambda^2$ the recoil frequency. As $\omega_R \ll \omega$ for a deep optical lattice, the condition $\epsilon_F \ll \omega$ can be fulfilled in this loading limit, and as $\Omega \ll \omega$, individual motional states in each site can be addressed. In the following we will investigate these two extreme limits and the intermediate regime in detail.

6.2.3 Analysis of the Loading Regimes

Fast Loading Regime

In this regime, where the motion of the atoms in the reservoir is frozen on the scale a_0 during the transfer, the physics is essentially an on-site coupling and transfer. We thus find it useful to expand the modes in the reservoir in terms of localized Wannier functions corresponding to the lattice. Such an expansion of the reservoir modes arises naturally from the definition of the matrix elements $R_{\mathbf{k},\mathbf{n}}e^{-i\mathbf{k}\mathbf{x}_\alpha}$ (Eq. (6.8)) and allows us to write

$$H_{\text{RC}} = \frac{\Omega}{2} \sum_{\alpha,\mathbf{n}} \left(B_{\alpha,\mathbf{n}}^\dagger a_{\alpha,\mathbf{n}} + \text{h.c.} \right), \quad (6.16)$$

where $B_{\alpha,\mathbf{n}} = \sum_{\mathbf{k}} R_{\mathbf{k},\mathbf{n}} b_{\mathbf{k}} e^{-i\mathbf{k}\mathbf{x}_\alpha}$ is the mode corresponding to the Wannier function $w_{\mathbf{n}}(\mathbf{x} - \mathbf{x}_\alpha)$. Note that these collective modes fulfill

$$\{B_{\alpha,\mathbf{n}}, B_{\beta,\mathbf{m}}^\dagger\} = \delta_{\alpha,\beta} \delta_{\mathbf{n},\mathbf{m}}, \quad (6.17)$$

(where δ denotes the Kronecker Delta), i.e., modes corresponding to different lattice sites or to different motional states are orthogonal. Furthermore, in the fast regime we can neglect the first two terms H_a and H_b in the Hamiltonian (6.1) due to the condition Eq. (6.10) during the loading time $T \sim \pi/\Omega$ and the total Hamiltonian can be approximated by $H \approx H_{\text{RC}}$. The sites thus decouple, and the loading process at each site proceeds independently, but with the same Rabi frequency Ω for the coupling.

We are interested in the time evolution of the matrix elements of the single particle density matrix, i.e., $\langle a_{\alpha,\mathbf{n}}^\dagger a_{\beta,\mathbf{m}} \rangle$, $\langle a_{\alpha,\mathbf{n}}^\dagger B_{\beta,\mathbf{m}} \rangle$ and $\langle B_{\alpha,\mathbf{n}}^\dagger B_{\beta,\mathbf{m}} \rangle$. In the fast loading regime, where $H \approx H_{\text{RC}}$, the respective matrix elements can be calculated analytically from the Schrödinger equation with the Hamiltonian Eq. (6.16), and we find for states, where $\Omega/2 \gg |(n-1)\omega|$, i.e., $t \lesssim T \ll a_0/v_F$

$$\langle a_{\alpha,\mathbf{n}}^\dagger a_{\beta,\mathbf{m}}(t) \rangle = \delta_{\alpha,\beta} \delta_{\mathbf{n},\mathbf{m}} \sin^2 \frac{\Omega}{2} t, \quad (6.18)$$

and

$$\langle B_{\alpha,\mathbf{n}}^\dagger B_{\beta,\mathbf{m}}(t) \rangle = \delta_{\alpha,\beta} \delta_{\mathbf{n},\mathbf{m}} \cos^2 \frac{\Omega}{2} t, \quad (6.19)$$

for the time evolution of the occupation of the modes in the lattice and in the Fermi sea, respectively. These expressions assume that the lattice modes are initially empty and the corresponding modes in the Fermi sea are initially filled. If the Fermi sea is initially filled up to ϵ_F , then this assumption is fulfilled for any α and \mathbf{n} for which that each mode $B_{\alpha,\mathbf{n}}$ contains contributions only from states with energy below ϵ_F . Thus, in the fast loading regime the occupation in the lowest and first excited motional state undergoes Rabi-oscillations at a Rabi frequency Ω , and provided the density is sufficiently high, the lattice can be efficiently filled by applying a π -pulse,

$$\Omega T \sim \pi, \quad (6.20)$$

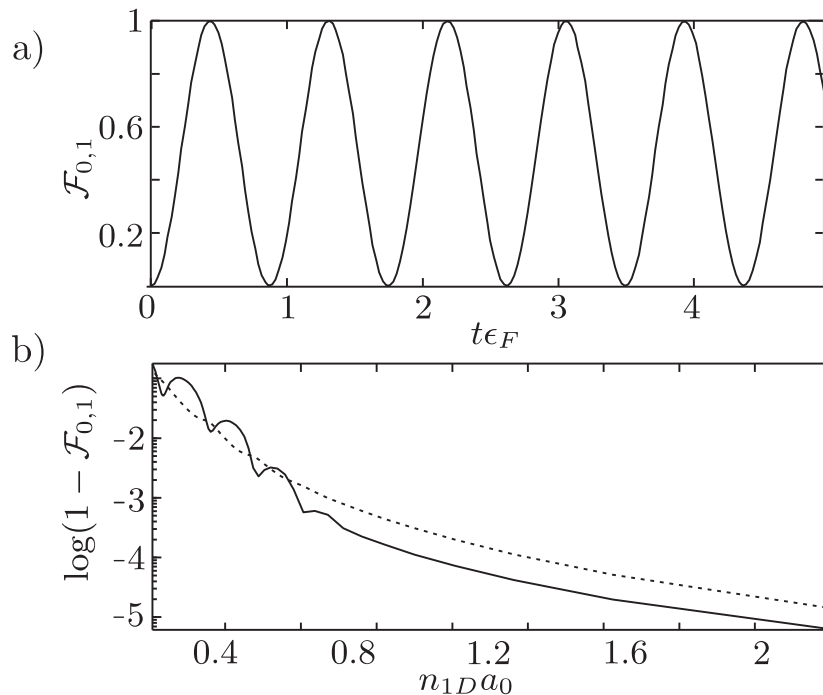


Figure 6.3. Numerical results in the fast loading limit. (a) The time evolution of the occupation of the lowest ($n = 0$) and first excited motional ($n = 1$) levels against time in dimensionless units. Note that these lines are indistinguishable. (b) $1 - \mathcal{F}_n(t = \pi/\Omega)$ after applying a π -pulse, for the lowest ($n = 0$, dotted line) and the first excited ($n = 1$, solid line) motional state, as a function of the dimensionless density $n_{1D}a_0$. Parameters used: $N=201$ particles in the Fermi sea, $M=5$ lattice sites, $\Omega = 17.8\epsilon_F$, $\Delta = -3\omega/2$ and in (a) $\omega = 0.1 \epsilon_F$, whereas in (b) ω is varied.

with loading time T . Atoms will also be coupled to other motional states in the lattice with the resulting filling factors depending on the density of the reservoir gas and the actual value of the Rabi frequency Ω .

To model the full loading dynamics we use numerical simulations of the dynamics generated by the Hamiltonian (6.1). In these simulations we only consider the lowest two motional states for simplicity, but all results are easily extended to more motional states. Also, the simulations are one dimensional, which means that the excited oscillator state with $n = 1$ is no longer degenerate. Because couplings to motional excitations in different spatial directions are independent, such simulations are representative for loading into each of the three 3D modes.

In Fig. 6.3a we show the results of our numerical simulations of the complete system described by the Hamiltonian Eq. (6.1) in the fast loading limit. In the upper and lower part

we plot the fidelity of the lowest and first excited Bloch band,

$$\mathcal{F}_m(t) \equiv \sum_{\alpha} \frac{\langle a_{\alpha,m}^{\dagger} a_{\alpha,m}(t) \rangle}{M}, \quad (6.21)$$

with M the number of lattice sites, as a function of time in dimensionless units $t\epsilon_F$. We refer to this quantity as a fidelity for the final state, because \mathcal{F}_0 gives the average filling factor in the lowest band, and thus the probability that we obtain exactly one fermion per site in the lowest band. The numerical results are in excellent agreement with the analytical calculations (Eq. (6.18)), as we find oscillations of the fidelity in both Bloch bands between zero and $\mathcal{F}_m(t) \gtrsim 1 - 10^{-4}$ occur with a Rabi frequency Ω . In Fig. 6.3b we analyze the scaling of the fidelity in the two bands with the dimensionless density $n_{3D}a_0^3$ (i.e., with $n_{1D}a_0 = \sqrt{2\epsilon_F/\omega}/\pi$ in our one dimensional simulations, with n_{1D} the one dimensional density of the reservoir gas). As expected, the fidelity after a π pulse, i.e., $\mathcal{F}_m(t = \pi/\Omega)$ increases with the density, and high fidelity states can be achieved for large densities $n_{1D}a_0 \gtrsim 1$. In this and all numerical simulations below we have checked that the results are independent of the quantization volume, which is much smaller than in a real experiment, due to the comparably small number of particles in the simulations.

In Fig. 6.4 we show how the loading dynamics change when approaching the intermediate regime from the fast limit, i.e. the scaling of the fidelity with the Rabi frequency Ω . In Fig. 6.4a we show the qualitative behaviour of the loading dynamics for typical parameters, in Fig. 6.4b the scaling of the fidelity $\mathcal{F}_m(t = \pi/\Omega)$, $m = 0, 1$ is shown as a function of the Rabi frequency. These numerical simulations show that the Bloch bands still cannot be individually addressed, and the fidelity becomes worse if the Rabi frequency is decreased.

Thus, our chosen motional state can, in principle, be efficiently filled in this regime on sufficiently fast timescales. However, the requirements on the density are difficult to achieve experimentally, and occupation in other motional states cannot be avoided. As a result in this regime we obtain no significant advantage over traditional loading mechanisms such as adiabatically turning on the lattice. In the next section we will investigate the slow loading regime. In this limit these problems do not exist and we are able to selectively load a single energy level efficiently.

Slow Loading Regime

In this regime, transport is significant during the loading, and the system dynamics are described by the complete Hamiltonian (6.1). As the reservoir atoms move between Wannier modes during the loading process, it is now more convenient to directly use the momentum representation Eq. (6.6) to express the coupling Hamiltonian.

From Eq. (6.6) one can see that each lattice site α and each motional state \mathbf{n} is coupled to many momentum modes $b_{\mathbf{k}}$ in the reservoir. However, as $\Omega \ll \epsilon_F$, effectively only a subset of momentum modes with energies centered around the resonant frequency $\epsilon = \Delta + 3\omega/2$ is coupled to the lattice, whereas the remaining states are far detuned and the transfer is suppressed. The width of this effective coupling range depends on both the Rabi frequency Ω and the matrix elements $R_{\mathbf{k},\mathbf{n}}$, and an upper bound for the width of this range is given by the Rabi frequency Ω .

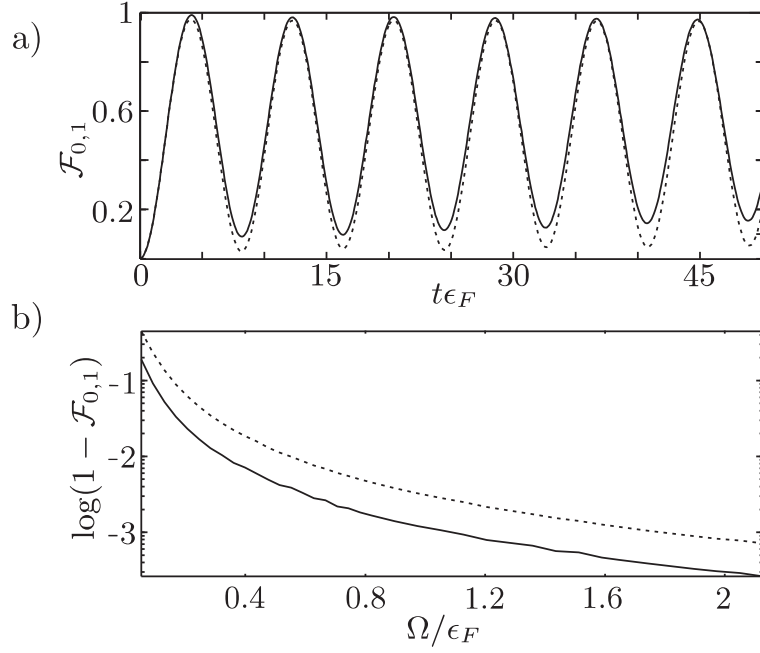


Figure 6.4. Numerical results for Ω approaching an intermediate regime from the fast loading limit. (a) The time evolution of the occupation of the lowest ($n = 0$, dotted line) and first excited ($n = 1$, solid line) motional state against time in dimensionless units, again for $N = 101$, $M = 5$ and for a typical set of parameters $\Omega = 0.72\epsilon_F$, $\Delta = -3\omega/2$ and $n_{1D}a_0 \sim 2$. (b) The occupation number for the lowest ($n = 0$, dotted line) and first excited ($n = 1$, solid line) after applying a π -pulse versus the dimensionless Rabi frequency Ω .

It is convenient to rewrite the coupling Hamiltonian of Eq. (6.6) as

$$H_{RC} = \sum_{\mathbf{k}, \mathbf{n}} \left[R_{\mathbf{k}, \mathbf{n}} b_{\mathbf{k}}^\dagger \left(\sum_{\alpha} e^{-i\mathbf{k}\mathbf{x}_{\alpha}} a_{\alpha, \mathbf{n}} \right) + \text{h.c.} \right], \quad (6.22)$$

from which we can see that each momentum mode in the reservoir couples to a collective mode $\sum_{\alpha} e^{i\varphi_{\mathbf{k}, \alpha}} a_{\alpha, \mathbf{n}}$ in the lattice. To fill the lattice it is necessary that the range of states in the reservoir couples to at least M orthogonal collective modes in the lattice. Writing the phase as

$$\mathbf{k}\mathbf{x}_{\alpha} = \pi \sqrt{\frac{\epsilon_F}{\omega_R}} \left(\frac{\mathbf{k}}{k_F} \frac{\mathbf{x}_{\alpha}}{\lambda/2} \right), \quad (6.23)$$

we see that it is necessary to couple a range of states with width of at least $k_F \sqrt{\omega_R/\epsilon_F}$ in momentum space to the lattice to fill M lattice sites. In the slow regime, where $\Omega \ll \epsilon_F$ and furthermore $\omega_R \lesssim \epsilon_F$ (from the density condition (6.15), the recoil frequency will typically exceed the Rabi frequency, i.e., $\Omega < \omega_R$). As only states within a range $\epsilon \pm \Omega$ are coupled to the lattice, the lattice cannot be filled efficiently for a constant ϵ .

Thus to achieve a high population in the desired motional state of each lattice site we must sweep the resonant frequency ϵ through a range of at least ω_R , scanning through many modes. Such a procedure also has the advantage that as we only couple to a narrow range in the Fermi sea at any one time, the reverse process of transferring particles from the lattice to the Fermi sea will be suppressed by Pauli blocking. In our numerical simulations we linearly sweep the detuning from $\epsilon = 0$ to $\epsilon = \epsilon_F$ in a loading time T .

We are interested in the time evolution of the matrix elements $\langle a_{\alpha,n}^\dagger a_{\beta,m} \rangle$, $\langle a_{\alpha,n}^\dagger b_{\mathbf{k}} \rangle$, and $\langle b_{\mathbf{k}}^\dagger b_{\mathbf{k}'} \rangle$ of the single particle density matrix. For a system described by a quadratic Hamiltonian the equations of motion for the second order correlation functions can be obtained from the (linear) Heisenberg equations (see Appendix 6.A). As the system is described by the quadratic Hamiltonian (6.1) and (6.6), the linear Heisenberg equations for the operators $a_{\alpha,n}$ and $b_{\mathbf{k}}$ have the simple form (again only considering the lowest two motional states in a one dimensional system)

$$\begin{aligned} \dot{a}_{\alpha,1} &= -i\frac{\Omega}{2} \sum_{\mathbf{q}} R_{\mathbf{q},1}^* e^{i\mathbf{k}\mathbf{x}_\alpha} b_{\mathbf{q}} - i\epsilon a_{\alpha,1}, \\ \dot{b}_{\mathbf{k}} &= -i\frac{\Omega}{2} \sum_{\mu,n} R_{\mathbf{k},n} e^{-i\mathbf{k}\mathbf{x}_\mu} a_{\mu,n} - i\epsilon_{\mathbf{k}} b_{\mathbf{k}}, \\ \dot{a}_{\alpha,0} &= -i\frac{\Omega}{2} \sum_{\mathbf{q}} R_{\mathbf{q},0}^* e^{i\mathbf{k}\mathbf{x}_\mu} b_{\mathbf{q}} + i(\omega - \epsilon) a_{\alpha,0}, \end{aligned} \quad (6.24)$$

which can be used to efficiently calculate the time evolution of the desired functions numerically. Note that in an isotropic three dimensional lattice again all three degenerate $n = 1$ states will be loaded by sweeping the resonant frequency ϵ through the Fermi sea. In practice it is also possible to selectively load only a single atom in each lattice site by shifting two excited motional states out of resonance, choosing an anisotropic lattice with significantly higher oscillator frequencies in two dimensions.

In Fig. 6.5a we show numerical results for the time evolution of the occupation number in the first (upper plot) and in the lowest (lower plot) Bloch band as a function of time in dimensionless units. Here, Ω is slowly switched on to reduce the additional holes introduced in the Fermi sea by coupling atoms into states above ϵ_F . This is an example of many possible optimisations to produce high filling, and we find the final $\mathcal{F}_1 > 0.99$, in a time of the order of 10 milliseconds (with $\omega \sim 2\pi \times 100$ kHz). In Fig. 6.5b the occupation of the two motional levels after a loading sweep is plotted as a function of the sweep time T . These results are not optimised (Ω is held constant, and we sweep ϵ from $\epsilon_F \rightarrow 0$), but still produce fidelities $\mathcal{F}_1 > 0.95$ on a timescale of a few milliseconds, and we see that the average filling factor increases with the loading time.

It is important to note that whilst high fidelities can be obtained by optimising the parameters of the sweep, it is not necessary to achieve high filling during this sweep in order to produce high fidelities for the overall loading scheme. In the full scheme with decay of atoms to the ground motional state included, the upper band need never be completely filled at any one time, and removal of atoms via the decay process will lead to further atoms being coupled into the lattice in the upper motional band.

Due to the condition $\Omega \ll \omega$, unwanted coupling to other Bloch bands can be avoided in this regime, by choosing $\epsilon \ll \omega$ (c.f. Fig. 6.2), as the coupling is then sufficiently far detuned

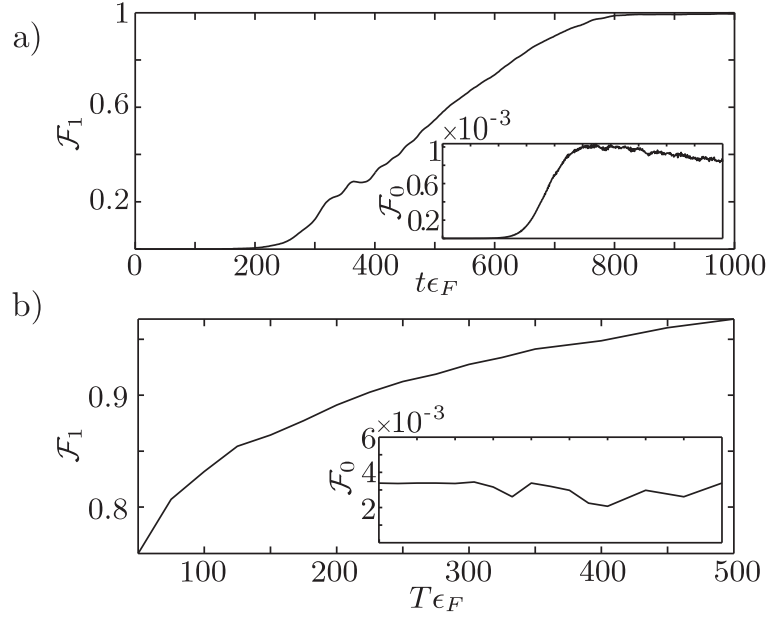


Figure 6.5. Numerical simulation of the loading dynamics in the “slow loading” limit. (a) Occupation of the lowest and first excited motional bands as a function of time, showing attainment of a high fidelity in the excited band. The resonant frequency ϵ is swept from $\epsilon_F \rightarrow 0$, and Ω is ramped from 0 to $0.45\epsilon_F$, reaching that value at $t\epsilon_F = 500$. Parameters used: $N = 81$ particles in the Fermi sea, $M = 5$ lattice sites, $\omega = 5\epsilon_F$ and $n_{1D}\lambda/2 = 3.4$. (b) The final occupation number after a loading sweep with constant Ω , and ϵ ramped from $\epsilon_F \rightarrow 0$, versus the dimensionless sweep time $\epsilon_F T$. Parameters used: $N = 81$, $M = 5$, $\Omega = 0.9\epsilon_F$ and $\omega = 10\epsilon_F$ and $n_{1D}\lambda/2 = 1.7$.

as demonstrated in the lower two plots of Fig. 6.5. The scaling of the unwanted coupling to the lower band is shown in Fig. 6.6a, where we plot the occupation of the two Bloch bands after a linear sweep with $\epsilon_F T = 300$ against the ratio ω/ϵ_F .

In Fig. 6.6b we show the numerical results when approaching the intermediate regime, i.e., the scaling of the occupation of the two bands after the linear sweep with the Rabi frequency. We find that also here high occupation of the first Bloch band can be achieved, but by increasing the Rabi frequency the unwanted coupling to the lower band also increases, as can be seen in the lower plot of the figure.

In summary, in the “slow loading” regime high fidelity loading of the $n = 1$ motional level can be achieved on timescales much shorter than those on which atoms are lost from the lattice by sweeping the resonant coupling frequency ϵ through the Fermi sea. This loading mechanism gives us the significant advantage over simple loading techniques such as adiabatically increasing the lattice depth that we can address a particular energy level in the lattice, whilst not coupling to levels that are sufficiently far detuned. This property can also be used to load patterns of atoms, because if a superlattice is applied, then the energy of certain lattice sites can be shifted out of resonance with the Raman process, so that no atoms are

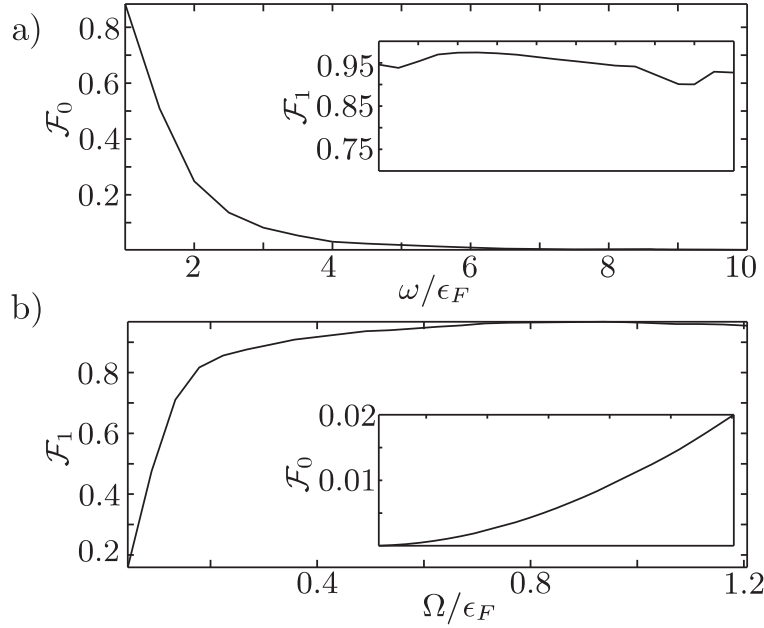


Figure 6.6. In (a) we show the occupation of the lowest and first excited Bloch band after a linear loading sweep from $\epsilon = \epsilon_F \rightarrow 0$ with $\epsilon_F T = 300$ versus the band separation ω in dimensionless units. Part (b) shows the loading dynamics approaching an intermediate regime from the slow regime: We plot the occupation of the lowest and first excited Bloch band after a linear loading sweep, with $\epsilon_F T = 300$ against Ω . Parameters used: $N=81$ particles in the Fermi Sea, $M=5$ lattice sites and $n_{1D}\lambda/2 = 1.7$, in (a) $\Omega = 0.9\epsilon_F$ and in (b) $\omega = 10\epsilon_F$.

coupled into these sites.

In the next section we will discuss the cooling of atoms in higher motional levels to the ground state, which removes the atoms from the motional state being coupled from the reservoir. Together with Pauli blocking of modes in the lattice, this allows us to make the overall loading process fault-tolerant. As an additional remark, though, we note that this laser-assisted loading of a selected energy level in the lattice could be used as a stand-alone technique to load the lattice, e.g., coupling atoms directly into the ground motional state. (In order to load an excited motional state in this manner, interaction of atoms in the lattice and atoms in the reservoir must be made very small on the timescale of the loading process, e.g., by using a Feshbach resonance, in order to avoid decay of the atoms into the ground state). This process on its own is not as robust as the procedure we obtain by including a dissipative element in the loading scheme, which will be discussed in the next section. However, reasonably high fidelities could still be obtained with this method alone, especially if the method was applied iteratively, cooling the Fermi reservoir between each two steps. Net transfer of atoms already in the lattice back to the reservoir would be prevented in each step by Pauli blocking in the filled Fermi sea. Note again that as with the full dissipative loading scheme, a single sweep would also not need to completely fill the upper band. The

dissipative element discussed in the next section allows for the production of an arbitrarily high-fidelity state without the requirement of iteratively cooling the Fermi reservoir.

6.3 Dissipative Transfer: Cooling Atoms to the Lowest Band

The second stage of the loading process is cooling atoms in an excited motional state to the ground state via interaction with the reservoir gas. This is closely related to the cooling process with a bosonic reservoir in [27]. The external gas here plays the role of an effective $T = 0$ heat bath for the lattice atoms, and ground state cooling is achieved on timescales much shorter than atoms are lost from the lattice.

We consider the coupling of lattice atoms a via a collisional interaction to the atoms b in the reservoir so that the system is described by the Hamiltonian

$$H = H_a + H_b + H_{\text{int}}, \quad (6.25)$$

where the collisional interaction, H_{int} , between two fermions is the usual density-density interaction

$$H_{\text{int}} = g \int d^3x \hat{\psi}_a^\dagger(\mathbf{x}) \hat{\psi}_a(\mathbf{x}) \hat{\psi}_b^\dagger(\mathbf{x}) \hat{\psi}_b(\mathbf{x}), \quad (6.26)$$

with $g = 4\pi a_s/m$ and a_s the s -wave scattering length. Expanding the field operators as described in the previous section we obtain

$$H_{\text{int}} = \sum_{\substack{\mathbf{k}, \mathbf{k}' \\ \alpha, \mathbf{n}, \mathbf{n}'}} g_{\alpha, \mathbf{n}, \mathbf{n}'}^{\mathbf{k}, \mathbf{k}'} b_{\mathbf{k}}^\dagger b_{\mathbf{k}'} a_{\alpha, \mathbf{n}}^\dagger a_{\alpha, \mathbf{n}'}, \quad (6.27)$$

which is local in each lattice site because of the small overlap between Wannier functions for neighboring sites in a deep lattice, with

$$g_{\alpha, \mathbf{n}, \mathbf{n}'}^{\mathbf{k}, \mathbf{k}'} = \frac{g}{V} e^{i\mathbf{x}_\alpha(\mathbf{k}' - \mathbf{k})} \int d^3x e^{i\mathbf{x}(\mathbf{k}' - \mathbf{k})} w_{\mathbf{n}}(\mathbf{x}) w_{\mathbf{n}'}(\mathbf{x}). \quad (6.28)$$

Each $g_{\alpha, \mathbf{n}, \mathbf{n}'}^{\mathbf{k}, \mathbf{k}'}$ describes a scattering process in which a particle-hole pair is created in the reservoir by scattering an atom from momentum state $\mathbf{k} \rightarrow \mathbf{k}'$, combined with the transition of an atom at site α from motional state $\mathbf{n} \rightarrow \mathbf{n}'$.

If the transition in the lattice is from a higher energy mode to a lower energy mode, this corresponds to a cooling transition, whereas the reverse process constitutes heating. As the initial temperature of the reservoir $k_B T \ll \epsilon_F \ll \omega$, the heating processes will be, at least initially, insignificant, as few reservoir atoms will exist with sufficient energy to excite an atom in the lattice. If the number of atoms in the reservoir is large compared to the number of sites in the lattice ($N \gg M$), then the rate of heating processes due to interaction with previously excited atoms will be small compared to cooling processes due to interaction with atoms remaining below the Fermi energy ϵ_F . Because the cooling processes in different lattice sites couple to different modes, and therefore are incoherent, the reservoir can then be treated throughout the process approximately as a $T = 0$ bath.

This can be further enhanced in two ways. Firstly, in an experiment in which the reservoir gas is confined in a weak harmonic trap, particles with sufficiently large energies can be allowed to escape from the trap. The large separation of the Bloch band ω , and corresponding excitation energy will then cause many excited reservoir atoms to leave the trap, providing effective evaporative cooling during the process. Secondly, the lattice depth could be modulated during the experiment, so that the excitation energy changes, decreasing the probability that atoms are heated by previously excited reservoir atoms.

The cooling dynamics are then described in the Born-Markov approximation by a Master equation for the reduced density operator ρ for the atoms in the lattice. If we consider coupling of atoms from the first excited motional levels $\mathbf{n} \in \{(1, 0, 0), (0, 1, 0), (0, 0, 1)\}$ to the ground state, the resulting master equation (derived in Appendix 6.B) is

$$\dot{\rho} = \sum_{\alpha, \beta, \mathbf{n}} \frac{\Gamma_{\alpha, \beta, \mathbf{n}}}{2} \left(2A_{\alpha, \mathbf{n}} \rho A_{\beta, \mathbf{n}}^\dagger - A_{\alpha, \mathbf{n}}^\dagger A_{\beta, \mathbf{n}} \rho - \rho A_{\alpha, \mathbf{n}}^\dagger A_{\beta, \mathbf{n}} \right), \quad (6.29)$$

with

$$\Gamma_{\alpha, \beta, \mathbf{n}} = 2\pi \sum_{\substack{\mathbf{k}, \mathbf{k}' \\ k' > k}} g_{\alpha, 1, 0}^{\mathbf{k}, \mathbf{k}'} g_{\beta, 1, 0}^{\mathbf{k}, \mathbf{k}'} * \delta(\omega - \epsilon_{\mathbf{k}} + \epsilon_{\mathbf{k}'}) \approx \frac{g^2 n_{3D} m}{\pi a_0 \sqrt{2}} \frac{2}{3e} \delta_{\alpha, \beta}. \quad (6.30)$$

Here, the jump operator $A_{\alpha, \mathbf{n}} = a_{\alpha, 0}^\dagger a_{\alpha, \mathbf{n}}$ describes the cooling of a lattice atom in site α from the first excited motional level \mathbf{n} to the ground state. These results are obtained by calculating the integral over momenta in the Fermi sea to lowest order in ϵ_F/ω .

The approximation in the second line of Eq. (6.30), in which neglect off diagonal terms $\alpha \neq \beta$ amounts to the approximation that the coherence length of the Fermi reservoir is much shorter than the lattice spacing. This is true provided that the wavelength of the emitted particle excitation, $\sqrt{2\pi^2/(m\omega)}$, is much shorter than the lattice spacing, i.e., $\omega_R/\omega \ll 1$. This is consistent with the previous approximation that the lattice is so deep that we can neglect tunnelling between neighbouring sites. This can be seen directly when these off-diagonal terms are calculated, as for large ω_R/ω they decay (to lowest order in $\epsilon_F \ll \omega$) as

$$\Gamma_{\alpha, \beta, \mathbf{n}} \sim \frac{\sin(\pi \sqrt{\omega/\omega_R} |\alpha - \beta|)}{\pi \sqrt{\omega/\omega_R} |\alpha - \beta|}. \quad (6.31)$$

This effect is analogous to the spontaneous emission of two excited atoms which are separated spatially by more than one wavelength of the photons they emit. In this case, the atoms can be treated as coupling to two independent reservoirs, and effects of super- and sub-radiance do not play a role.

For typical experimental values $n_{3D} \sim 10^{14} \text{cm}^{-3}$ and $a_s = 174 a_B$, for ^{40}K as given in [30], with the Bohr radius a_B and a deep optical lattice with $\omega/2\pi \sim 100 \text{kHz}$, we find a decay rate $\Gamma/2\pi \sim 3.6 \text{kHz}$. Thus, cooling can again be achieved on sufficiently short time scales, as this rate is much faster than typical loss rates of the lattice atoms. For example, we can estimate the rate of the three-body loss processes described in section 6.2 to be of the order of ten seconds [28]. Note that this value of the decay rate can be made even larger e.g. by tuning the scattering length a_s via a Feshbach resonance, as $\Gamma \propto a_s^2$, by increasing the density of the external gas or by increasing the lattice depth.

In summary we have shown that for a cold reservoir gas with sufficiently many atoms fast ground state cooling of lattice atoms can be achieved with the dissipative coupling of the lattice to the reservoir. The necessary experimental parameters have already been achieved in real experiments, and the cooling rates are tunable via the scattering length and the density of the reservoir gas.

6.4 Combined Process

The combination of the cooling process with laser-assisted loading in the limit $\Omega \ll \omega, \epsilon_F$ will give a final high-fidelity state in the lowest motional level. The primary role of the dissipative element is to transfer atoms into a state in which they are not coupled back to the Fermi reservoir, which is made possible because of the selective addressing of the $n = 1$ motional levels in this regime. Multiple occupation of a single site in the lowest motional state is forbidden due to Pauli-blocking, and thus the lowest motional state is monotonically filled, with the filling factor and hence the fidelity of the state being prepared always improving in time. Again, patterns of atoms may be loaded in the lowest state by using a superlattice to shift the energy of the $n = 1$ motional level out of resonance with the Raman process in particular sites, preventing atoms from being coupled from the Fermi reservoir into those sites. This energy shift will also further suppress tunnelling of atoms from neighbouring sites.

If the laser-assisted loading and the cooling are carried out separately, each being performed after the other in iterative steps, then from the analysis of sections 6.2 and 6.3 we see that an arbitrarily high fidelity final state can be obtained. This *pulsed* scheme gives us an upper bound on the timescale for loading a state of given fidelity, which corresponds to the combination of the two individual timescales for laser-assisted loading and cooling. Provided that the number of atoms in the reservoir is much larger than the number of lattice sites to be filled ($N \gg M$), and the Markov approximation made in describing the cooling dynamics is valid, then there will be no adverse effects arising from the loading and cooling processes sharing the same reservoir. Thus, we can combine the two processes into a *continuous* scheme, which in practice will proceed much faster, as the continuous evacuation of the excited band due to cooling will also speed up the loading process.

At the end of the loading process we must still ensure that the finite occupation of the excited motional levels is properly removed. This can be achieved by detuning the resonant frequency for the Raman coupling above the Fermi energy after the loading sweep, coupling the remaining atoms to empty states above the Fermi sea, and then switching off the coupling adiabatically.

The dynamics of the pulsed process are already well understood from the analysis of sections 6.2 and 6.3. To illustrate the dynamics of the combined continuous process, we again perform numerical simulations, in which we compute the matrix elements of the reduced system density operator. The dynamics of the total system including both the laser coupling and the collisional interaction between the optical lattice and the Fermi reservoir are described by the full Hamiltonian

$$H = H_a + H_b + H_{\text{RC}} + H_{\text{int}}, \quad (6.32)$$

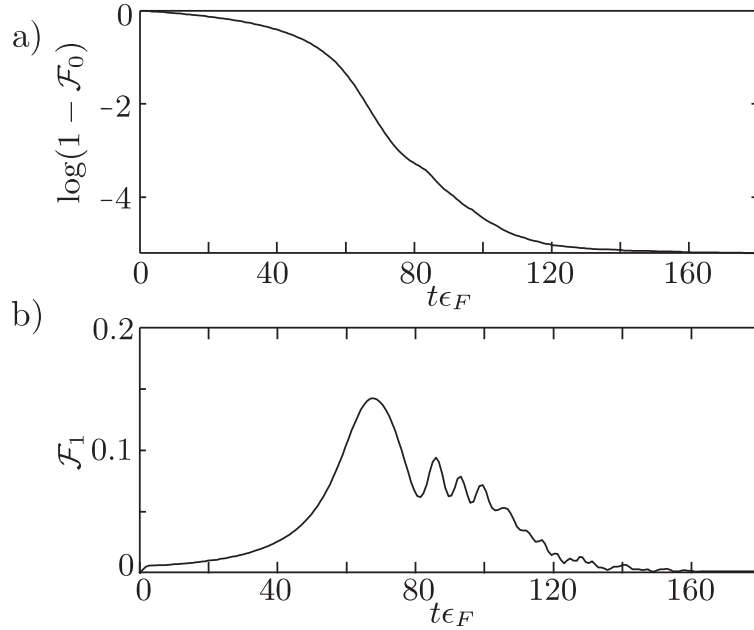


Figure 6.7. *The occupation of (a) the lowest ($n = 0$) and (b) first excited ($n = 1$) motional level for the continuous combination of coherent loading in the slow regime and dissipative cooling. The resonant frequency is swept from $\epsilon = 0$ to $\epsilon = 4\epsilon_F$ and the Raman coupling is switched off adiabatically. Parameters used: $N = 101$, $M = 5$, $\Omega/2 = 0.45\epsilon_F$, $n_{1D}\lambda/2 = 1.4$, $\omega = 10\epsilon_F$ and $\Gamma = 0.1\epsilon_F$.*

and in the Markov approximation with respect to the cooling process, the matrix elements of the system density operator can now be calculated from the Master equation (6.29) as shown in Appendix 6.C. In order to obtain a closed set of differential equations which can be integrated numerically, we use an approximation based on Wick's theorem to factorize fourth order correlation functions into second order correlation functions (see appendix 6.C) [31].

In Fig. 6.7 we plot the time evolution of the occupation of the two motional levels in the continuous regime as a function of time. In Fig. 6.7a we see that we indeed achieve a high occupation of the lowest motional level from the combination of laser-assisted coupling to the excited motional level in the regime $\Omega \ll \omega, \epsilon_F$ and cooling to the ground state. For the typical values given in the figure caption, the loading time T for a state with $\mathcal{F}_0 \sim 1 - 10^{-4}$ is again on the order of a few milliseconds. This required loading time can be further decreased by tuning Γ via the density of the external gas or the strength of the collisional interaction between atoms in the lattice and atoms in the reservoir.

From Fig. 6.7b we see that as we fill the lower motional level, the filling in the upper level is depleted, and as we continue to tune the lasers so that this level is coupled to states in the reservoir above the Fermi energy ϵ_F , the remaining population in this level is removed.

As a final remark we note that such a procedure could, in principle, also be applied to bosons. However, without Pauli blocking to prevent double-occupation of the ground motional level, we rely on the onsite collisional shift U to make the Raman coupling of an

atom from the reservoir into an excited state off-resonant if an atom already exists in the ground motional state. Second order processes occurring at a rate $\sim \Omega\Gamma/U$ can still create double occupation, so we require $\Omega, \Gamma \ll U$, and the advantage of true fault tolerance is not present as it is for fermions.

6.5 Summary

In conclusion, we have shown that the combination of laser-assisted loading of atoms into an excited motional state and the cooling of atoms from this motional state to the ground level gives a fault-tolerant loading scheme to produce high fidelity registers of fermions in an optical lattices with one atom per lattice site. Application of a superlattice allows this to be extended to generalised patterns of atoms, and all of these processes can be completed on timescales much faster than those on which atoms can be lost from the lattice. The advantage of this scheme is that the dissipative transitions in the lattice, similar to optical pumping, gives us a process in which the fidelity of the final state (in the lowest motional level) improves monotonically in time.

Acknowledgments

The authors would like to thank Peter Rabl and members of R. Grimm's group for helpful discussions. AG thanks the Clarendon Laboratory and DJ thanks the Institute for Quantum Optics and Quantum Information of the Austrian Academy of Sciences for hospitality during the development of this work. Work in Innsbruck is supported by the Austrian Science Foundation, EU Networks, OLAQUI, and the Institute for Quantum Information. DJ is supported by EPSRC through the QIP IRC (www.qipirc.org) (GR/S82176/01) and the project EP/C51933/1.

6.A Derivation of the Heisenberg Equations for Coherent Loading

Consider a system, which is described by a Hamiltonian quadratic in a set of operators $\vec{\mathcal{O}} = (\mathcal{O}_1, \mathcal{O}_2, \dots, \mathcal{O}_d)$. Then the Heisenberg equations of motion can be written as

$$\dot{\vec{\mathcal{O}}}(t) = M\vec{\mathcal{O}}(t), \quad (6.33)$$

with a matrix M , and formal solution $\vec{\mathcal{O}}(t) = U\vec{\mathcal{O}}(0)$ with $U = \exp(Mt)$. By choosing the initial conditions $\mathcal{O}_j(0) = \delta_{j,\alpha}$ we can construct the full time evolution matrix $U(t)$ by solving Eqs. (6.33), as

$$U_{i,\alpha}(t) \equiv \sum_j U_{i,j}(t)\mathcal{O}_j(0) = \mathcal{O}_i(t). \quad (6.34)$$

The time evolution of the second order correlation functions is then easily calculated as

$$\langle \mathcal{O}_i^\dagger \mathcal{O}_j(t) \rangle = \left\langle \sum_{\alpha, \beta} U_{i,j}^*(t) U_{j,\beta}(t) \mathcal{O}_\alpha^\dagger \mathcal{O}_\beta(0) \right\rangle. \quad (6.35)$$

6.B Derivation of the Master Equation

In the interaction picture, and after making the Born-Markov approximation, the master equation for the reduced density operator ρ of a system which interacts with a heat bath via an interaction Hamiltonian H_{int} can be written as (see e.g. [32])

$$\dot{\rho}(t) = - \int_0^t d\tau \text{Tr}_B \left\{ \left[H_{\text{int}}(t), [H_{\text{int}}(t - \tau), \rho(t) \otimes \rho_B] \right] \right\}. \quad (6.36)$$

Here, ρ_B is the bath density operator, and Tr_B denotes the trace over the bath, which is represented by the cold Fermi reservoir in our setup. The interaction between the Fermi reservoir and the optical lattice system is given by the Hamiltonian (6.27), and in the interaction picture with respect to the internal dynamics in the lattice and in the Fermi reservoir,

$$H_{\text{int}}(t) = \sum_{\substack{\mathbf{k}, \mathbf{k}' \\ \alpha, \mathbf{n}, \mathbf{n}'}} g_{\alpha, \mathbf{n}, \mathbf{n}'}^{\mathbf{k}, \mathbf{k}'} b_{\mathbf{k}}^\dagger b_{\mathbf{k}'} a_{\alpha, \mathbf{n}}^\dagger a_{\alpha, \mathbf{n}'} e^{-i(\epsilon_{\mathbf{k}} - \epsilon_{\mathbf{k}'} + \omega(n - n'))t}. \quad (6.37)$$

As the number of atoms in the reservoir exceeds the number of lattice sites, $N \gg M$, and as in addition the bath has temperature $T \sim 0$, the reservoir will approximately remain in its ground state, i.e., the filled Fermi sea throughout the cooling process, and the bath correlation functions are approximately given by

$$\langle b_{\mathbf{k}_1}^\dagger b_{\mathbf{k}'_1} b_{\mathbf{k}_2}^\dagger b_{\mathbf{k}'_2} \rangle \approx \delta_{\mathbf{k}_1, \mathbf{k}'_1} \delta_{\mathbf{k}_2, \mathbf{k}'_2} + \delta_{\mathbf{k}_1, \mathbf{k}'_2} \delta_{\mathbf{k}'_1, \mathbf{k}_2}, \quad (6.38)$$

where $\langle \cdot \rangle = \text{Tr}_B \{ \cdot \rho_B \}$.

For t much larger than the correlation time in the bath we can let the upper limit of the integral in Eq. (6.36) go to ∞ , and writing $\int_0^\infty e^{i(\epsilon_{\mathbf{k}} - \epsilon_{\mathbf{k}'} + \omega(n - n'))\tau} \rightarrow \delta(\epsilon_{\mathbf{k}} - \epsilon_{\mathbf{k}'} + \omega(n - n'))$, we find

$$\dot{\rho} = \sum_{\alpha, \beta, \mathbf{n}} \frac{\Gamma_{\alpha, \beta, \mathbf{n}}}{2} \left(2A_{\alpha, \mathbf{n}} \rho A_{\beta, \mathbf{n}}^\dagger - A_{\alpha, \mathbf{n}}^\dagger A_{\beta, \mathbf{n}} \rho - \rho A_{\alpha, \mathbf{n}}^\dagger A_{\beta, \mathbf{n}} \right), \quad (6.39)$$

with the jump operator $A_{\alpha, \mathbf{n}} = a_{\alpha, 0}^\dagger a_{\alpha, \mathbf{n}}$,

$$\Gamma_{\alpha, \beta, \mathbf{n}} = 2\pi \sum_{\substack{\mathbf{k}, \mathbf{k}' \\ k' > k}} g_{\alpha, 1, 0}^{\mathbf{k}, \mathbf{k}'} g_{\beta, 1, 0}^{\mathbf{k}, \mathbf{k}'} \delta(\omega - \epsilon_{\mathbf{k}} + \epsilon_{\mathbf{k}'}), \quad (6.40)$$

and where we note that $\sum_{\mathbf{k}, \mathbf{k}'} g_{\alpha, \mathbf{n}, 0}^{\mathbf{k}, \mathbf{k}'} g_{\alpha, \mathbf{n}', 0}^{\mathbf{k}, \mathbf{k}'} = 0$ for $\mathbf{n} \neq \mathbf{n}'$. The rate $\Gamma_{\alpha, \beta, \mathbf{n}}$ rapidly decays with $|\alpha - \beta|$, and for each of the three degenerate excited states $\mathbf{n} \in \{(1, 0, 0), (0, 1, 0), (0, 0, 1)\}$,

the slowest rate of this decay is found in the direction of \mathbf{n} . In the harmonic oscillator approximation we find (for the direction with the slowest decay)

$$\Gamma_{\alpha,\beta} \sim \frac{g^2 n_{3D} m}{\pi a_0 \sqrt{2}} \frac{2}{3e} F\left(\pi \sqrt{\frac{\omega}{\omega_R}} |\alpha - \beta|\right), \quad (6.41)$$

to first order in ϵ_F/ω , with the function

$$F(\xi) = 3 \frac{2\xi \cos \xi + (\xi^2 - 2) \sin \xi}{\xi^3}. \quad (6.42)$$

For large ξ this result simplifies to the sinc function in Eq. (6.31). For a deep optical lattice where $\omega \gg \omega_R$, $F\left(\pi \sqrt{\frac{\omega}{\omega_R}} |\alpha - \beta|\right) \approx \delta_{\alpha,\beta}$, and we end up with a standard quantum optical master equation (see e.g. [32]), describing the decay of an excited lattice atom from each of the three degenerate $n = 1$ states to the $n = 0$ level at a rate Γ .

6.C Equations of motion for Combined Dynamics

The time evolution of the expectation value of an arbitrary system operator $\hat{\mathcal{O}}$ can be calculated from the master equation (6.29) and Eq. (6.30) as

$$\langle \dot{\mathcal{O}} \rangle = i \langle [H_{\text{sys}}, \hat{\mathcal{O}}] \rangle + \frac{\Gamma}{2} \sum_{\alpha,\mathbf{n}} \left(2 \langle A_{\alpha,\mathbf{n}}^\dagger \hat{\mathcal{O}} A_{\alpha,\mathbf{n}} \rangle - \langle \{ \hat{\mathcal{O}}, A_{\alpha,\mathbf{n}}^\dagger A_{\alpha,\mathbf{n}} \} \rangle \right), \quad (6.43)$$

where $H_{\text{sys}} = H_a + H_b + H_{\text{RC}}$ and $\Gamma \equiv \Gamma_{\alpha,\alpha,1}$. We are interested in the time evolution of the matrix elements of the single particle density matrix, which can be calculated from Eq. (6.43)

as

$$\begin{aligned}
\frac{d}{dt}\langle a_{\alpha,0}^\dagger a_{\beta,0} \rangle &= i\frac{\Omega}{2} \sum_{\mathbf{q}} \left(R_{\mathbf{q},\alpha,0} \langle b_{\mathbf{q}}^\dagger a_{\beta,0} \rangle - R_{\mathbf{q},\beta,0}^* \langle a_{\alpha,0}^\dagger b_{\mathbf{q}} \rangle \right) \\
&\quad + \frac{\Gamma}{2} \left(2\langle a_{\alpha,1}^\dagger a_{\alpha,1} \rangle \delta_{\alpha,\beta} - \langle a_{\alpha,1}^\dagger a_{\alpha,0}^\dagger a_{\beta,0} a_{\alpha,1} \rangle - \langle a_{\beta,1}^\dagger a_{\alpha,0}^\dagger a_{\beta,0} a_{\beta,1} \rangle \right) \\
\frac{d}{dt}\langle a_{\alpha,1}^\dagger a_{\beta,1} \rangle &= i\frac{\Omega}{2} \sum_{\mathbf{q}} \left(R_{\mathbf{q},\alpha,1} \langle b_{\mathbf{q}}^\dagger a_{\beta,1} \rangle - R_{\mathbf{q},\beta,1}^* \langle a_{\alpha,1}^\dagger b_{\mathbf{q}} \rangle \right) \\
&\quad - \frac{\Gamma}{2} \left(2\langle a_{\alpha,1}^\dagger a_{\beta,1} \rangle - \langle a_{\alpha,1}^\dagger a_{\beta,0}^\dagger a_{\beta,0} a_{\beta,1} \rangle - \langle a_{\alpha,1}^\dagger a_{\alpha,0}^\dagger a_{\alpha,0} a_{\beta,1} \rangle \right) \\
\frac{d}{dt}\langle a_{\alpha,1}^\dagger a_{\beta,0} \rangle &= i(\omega - \epsilon) \langle a_{\alpha,1}^\dagger a_{\beta,0} \rangle + i\frac{\Omega}{2} \sum_{\mathbf{q}} \left(R_{\mathbf{q},\alpha,1} \langle b_{\mathbf{q}}^\dagger a_{\beta,0} \rangle - R_{\mathbf{q},\beta,0}^* \langle a_{\alpha,1}^\dagger b_{\mathbf{q}} \rangle \right) \\
&\quad + \frac{\Gamma}{2} \left(-\langle a_{\alpha,1}^\dagger a_{\beta,0} \rangle - \langle a_{\alpha,1}^\dagger a_{\beta,1}^\dagger a_{\beta,1} a_{\beta,0} \rangle - \langle a_{\alpha,1}^\dagger a_{\alpha,0}^\dagger a_{\alpha,0} a_{\beta,0} \rangle \right) \\
\frac{d}{dt}\langle a_{\alpha,1}^\dagger b_{\mathbf{k}} \rangle &= i(\epsilon - \epsilon_{\mathbf{k}}) \langle a_{\alpha,1}^\dagger b_{\mathbf{k}} \rangle + i\frac{\Omega}{2} \left(\sum_{\mathbf{q}} R_{\mathbf{q},\alpha,1} \langle b_{\mathbf{q}}^\dagger b_{\mathbf{k}} \rangle - \sum_{\mu} R_{\mathbf{k},\mu,1} \langle a_{\alpha,1}^\dagger a_{\mu,1} \rangle \right) \\
&\quad - \frac{\Gamma}{2} \left(\langle a_{\alpha,1}^\dagger b_{\mathbf{k}} \rangle + \langle a_{\alpha,1}^\dagger a_{\alpha,0}^\dagger a_{\alpha,0} b_{\mathbf{k}} \rangle \right) \\
\frac{d}{dt}\langle a_{\alpha,0}^\dagger b_{\mathbf{k}} \rangle &= i(\epsilon - \epsilon_{\mathbf{k}} - \omega) \langle a_{\alpha,0}^\dagger b_{\mathbf{k}} \rangle + i\frac{\Omega}{2} \left(\sum_{\mathbf{q}} R_{\mathbf{q},\alpha,0} \langle b_{\mathbf{q}}^\dagger b_{\mathbf{k}} \rangle - \sum_{\mu} R_{\mathbf{k},\mu,0} \langle a_{\alpha,0}^\dagger a_{\mu,0} \rangle \right) \\
&\quad - \frac{\Gamma}{2} \langle a_{\alpha,1}^\dagger a_{\alpha,0}^\dagger b_{\mathbf{k}} a_{\alpha,1} \rangle \\
\frac{d}{dt}\langle b_{\mathbf{k}}^\dagger b_{\mathbf{k}'} \rangle &= i(\epsilon_{\mathbf{k}} - \epsilon_{\mathbf{k}'} - \omega) \langle b_{\mathbf{k}}^\dagger b_{\mathbf{k}'} \rangle + i\frac{\Omega}{2} \sum_{\mu,n} \left(-R_{\mathbf{k},\mu,n} \langle b_{\mathbf{k}}^\dagger a_{\mu,n} \rangle - R_{\mathbf{k},\mu,n}^* \langle a_{\mu,n}^\dagger b_{\mathbf{k}'} \rangle \right).
\end{aligned} \tag{6.44}$$

A closed set of equations can be obtained from Eqs. (6.44) by using Wick's theorem to factorize fourth order correlation functions into products of second order correlation functions according to

$$\langle \hat{c}_1 \hat{c}_2 \hat{c}_4 \hat{c}_4 \rangle = \langle \hat{c}_1 \hat{c}_2 \rangle \langle \hat{c}_3 \hat{c}_4 \rangle - \langle \hat{c}_1 \hat{c}_3 \rangle \langle \hat{c}_2 \hat{c}_4 \rangle + \langle \hat{c}_1 \hat{c}_4 \rangle \langle \hat{c}_2 \hat{c}_3 \rangle,$$

for fermionic operators $\hat{c}_i \in \{a_{\alpha,n}^\dagger, a_{\alpha,n}, b_{\mathbf{k}}^\dagger, b_{\mathbf{k}}\}$ (see e.g. [33]).

Bibliography

- [1] For a review see D. Jaksch and P. Zoller, *Annals of Physics* **315**, 52 (2005), and references therein.
- [2] M. Greiner, O. Mandel, T. W. Hänsch and I. Bloch *Nature* **415**, 39 (2002); M. Greiner, O. Mandel, T. Esslinger, T.W. Hänsch and I. Bloch, *Nature* **419** 51 (2002).
- [3] T. Stöferle, H. Moritz, C. Schori, M. Köhl, and T. Esslinger, *Phys. Rev. Lett.* **92** 130403 (2004).

- [4] B. Paredes, A. Widera, V. Murg, O. Mandel, S. Fölling, I. Cirac, G. V. Shlyapnikov, T. W. Hänsch, and I. Bloch, *Nature* **429**, 277 (2004).
- [5] O. Mandel, M. Greiner, A. Widera, T. Rom, T. W. Hänsch, and I. Bloch, *Phys. Rev. Lett.* **91**, 010407 (2003).
- [6] E. L. Bolda, E. Tiesinga, and P. S. Julienne, *Phys. Rev. A* **66**, 013403; E. A. Donley, N. R. Claussen, S. T. Thompson, and C. E. Wieman, *Nature* **417**, 529 (2002); T. Loftus, C. A. Regal, C. Ticknor, J. L. Bohn, and D. S. Jin, *Phys. Rev. Lett.* **88**, 173201 (2002).
- [7] M. Theis, G. Thalhammer, K. Winkler, M. Hellwig, G. Ruff, R. Grimm, J. Hecker Denschlag, *Phys. Rev. Lett.* **93**, 123001 (2004).
- [8] P. Rabl, A. J. Daley, P. O. Fedichev, J. I. Cirac, and P. Zoller, *Phys. Rev. Lett.* **91**, 110403 (2003).
- [9] I.H. Deutsch, G.K. Brennen, and P.S. Jessen, *Fortschritte der Physik* **48**, 925 (2000).
- [10] For example see L. Santos, M. A. Baranov, J. I. Cirac, H.-U. Everts, H. Fehrmann, and M. Lewenstein, *Phys. Rev. Lett.* **93** 030601 (2004).
- [11] D. Jaksch, C. Bruder, J. I. Cirac, C. W. Gardiner, and P. Zoller, *Phys. Rev. Lett.* **81**, 3108 (1998).
- [12] L. Viverit, C. Menotti, T. Calarco, A. Smerzi, *Phys. Rev. Lett.* **93**, 110401 (2004).
- [13] K. G. H. Vollbrecht, E. Solano, and J. I. Cirac, *Phys. Rev. Lett.* **93**, 220502 (2004).
- [14] G. K. Brennen, G. Pupillo, A. M. Rey, C. W. Clark, and C. J. Williams, *J. Phys. B* **38**, 1687 (2005).
- [15] D. S. Weiss, J. Vala, A. V. Thapliyal, S. Myrgren, U. Vazirani, and K. B. Whaley, *Phys. Rev. A* **70**, 040302(R) (2004).
- [16] B. DeMarco and D. S. Jin, *Science* **285**, 1703 (1999).
- [17] S. Jochim, M. Bartenstein, A. Altmeyer, G. Hendl, S. Riedl, C. Chin, J. Hecker Denschlag, and R. Grimm, *Science* **302**, 2101 (2003).
- [18] M. Greiner, C. A. Regal, and D. S. Jin, *Nature* **426**, 537 (2003).
- [19] M. W. Zwierlein, C. A. Stan, C. H. Schunck, S. M. F. Raupach, A. J. Kerman, and W. Ketterle, *Phys. Rev. Lett.* **92**, 120403 (2004).
- [20] G. Roati, F. Riboli, G. Modugno, and M. Inguscio, *Phys. Rev. Lett.* **89**, 150403 (2002).
- [21] M. Köhl, H. Moritz, T. Stöferle, K. Günter, and T. Esslinger, *Phys. Rev. Lett.* **94**, 080403 (2005).
- [22] T. Bourdel, L. Khaykovich, J. Cubizolles, J. Zhang, F. Chevy, M. Teichmann, L. Tarruell, S. J. J. M. F. Kokkelmans, and C. Salomon, *Phys. Rev. Lett.* **93**, 050401 (2004).
- [23] K. E. Strecker, G. B. Partridge, and R. G. Hulet, *Phys. Rev. Lett.* **91**, 080406 (2003).

- [24] J. Kinast, S. L. Hemmer, M. E. Gehm, A. Turlapov, and J. E. Thomas, Phys. Rev. Lett. **92**, 150402 (2004).
- [25] W. Hofstetter, J. I. Cirac, P. Zoller, E. Demler, and M. D. Lukin, Phys. Rev. Lett. **89**, 220407 (2002).
- [26] B. Mohring, M. Bienert, F. Haug, G. Morigi, W. P. Schleich, and M. G. Raizen, Phys. Rev. A **71**, 053601 (2005); R. B. Diener, B. Wu, M. G. Raizen, and Q. Niu, Phys. Rev. Lett **89**, 070401 (2002).
- [27] A. J. Daley, P. O. Fedichev, and P. Zoller Phys. Rev. A **69**, 022306 (2004).
- [28] D. S. Petrov, Phys. Rev. A **67**, 010703(R) (2003).
- [29] J. Cubizolles, T. Bourdel, S. J. J. M. F. Kokkelmans, G. V. Shlyapnikov and C. Salomon, Phys. Rev. Lett. **91**, 240401 (2003).
- [30] C. A. Regal and D. S. Jin, Phys. Rev. Lett. **90**, 230404 (2003).
- [31] This problem could, in principle, be treated exactly using new methods for simulation of dissipative 1D systems, as discussed in M. Zwolak and G. Vidal, Phys. Rev. Lett. **93**, 207205 (2004); F. Verstraete, J. J. Garcia-Ripoll, and J. I. Cirac, Phys. Rev. Lett. **93**, 207204 (2004).
- [32] C. W. Gardiner and P. Zoller, Quantum Noise, Springer (2000).
- [33] Y. Castin, cond-mat/0407118 (2004).

Part III

Exact Time-Dependent Simulation of Many Atoms in 1D Optical Lattices

CHAPTER 7

EXACT CALCULATIONS FOR 1D MANY-BODY SYSTEMS USING VIDAL'S ALGORITHM

7.1 Time-Dependent Calculations for 1D Systems

The simulation of many-body quantum systems beyond very small sizes is, in general, a very difficult task due to the number of parameters required to represent the associated Hilbert space. This can be clearly seen in the case of the lattice models describing the dynamics of atoms in optical lattices. For the Hubbard model with M lattice sites, N_{\uparrow} spin-up fermions, and N_{\downarrow} spin-down fermions, the dimension of the associated Hilbert space is

$$W_H(M, N_{\uparrow}, N_{\downarrow}) = \frac{(M!)^2}{(M - N_{\uparrow})!N_{\uparrow}!(M - N_{\downarrow})!N_{\downarrow}!}, \quad (7.1)$$

and for the Bose-Hubbard Model with M lattice sites and N Bosons, the corresponding Hilbert space has dimension¹

$$W_{BH}(M, N) = \frac{(M + N - 1)!}{(M - 1)!N!}. \quad (7.2)$$

For example, typical systems with 12 lattice sites and 12 particles result in $W_H(12, 6, 6) = 853\,776$, and $W_{BH}(12, 12) = 1\,352\,078$. To treat systems of this size, large sparse matrices must be used to represent the Hamiltonian, and long computing times can be expected, dependent somewhat on the available hardware. For yet larger systems, these values become completely prohibitive. For example, with 16 particles in 16 lattice sites, $W_H(16, 8, 8) = 165\,636\,900$, and $W_{BH}(16, 16) = 300\,540\,195$.

Over the past fifteen years, there have been many algorithmic developments that have made possible the calculation of ground states of 1D many-body systems without needing to store coefficients of the entire Hilbert space. This is primarily achieved either by sampling in Quantum Monte-Carlo methods, or by careful reduction of the Hilbert space to those basis states that contribute significantly to the ground state, as is performed in Density Matrix

¹The dimension of the Hilbert space for the Bose-Hubbard model arises in combinatorics from sampling N sites (on which to place the atoms) from M sites with replacement.

Renormalisation Group (DMRG) methods. Both methods have been extremely successful in computing ground states of large 1D systems, and in a series of major advances over the past two years, algorithms of the latter type have been successfully generalised to time-dependent studies of 1D systems.

DMRG methods, which were first invented by White in 1992 [1], are extensively reviewed in [2]. Essentially, the algorithms were originally designed to find the ground state of a large 1D system based on the principle of growing the size of the system, whilst at each point in the growth forming a new reduced basis for the Hilbert space, retaining only those states considered to be the most significant. Beginning in 2002, there were several attempts to generalise basic DMRG methods to time dependent calculations. Initially these involved performing DMRG calculations to find the ground states for various Hamiltonian parameters, and using these calculations to pre-determine a truncated Hilbert space on which time evolution could be calculated (for more information see 9.2). The major step forward from this, first made by Vidal in 2003 [3] was to produce a method in which the truncated Hilbert space was modified at each time step so that the representation of the state satisfied some criteria of optimality. This method effectively provides near-exact integration of the many body Schrödinger equation in 1D on an adaptively decimated Hilbert space, under the restriction that the Hamiltonian couples at most neighbouring sites, and provided that the state as it evolves can always be represented with a sufficiently small number of retained basis states (such states are referred to as “slightly entangled”, which will be explained in section 7.2). Vidal’s Algorithm [often referred to as the Time Evolving Block Decimation Algorithm (TEBD)] has been generalised to the treatment of master equations for dissipative systems and systems at finite temperatures [4], as have similar methods proposed by Verstrate and Cirac [5]. These latter methods use a different criteria for what constitutes the optimal representation of the states, and have also been generalised to systems with periodic boundary conditions and to 2D systems [6].

The method we used to perform time-dependent simulations of lattice models relevant for describing atoms in optical lattice is based on Vidal’s original algorithm, which will be discussed in detail in the remainder of this chapter. We have significantly optimised the algorithm by enforcing the intrinsic conservation of particle number in the Hamiltonians we simulate, and this is presented, together with some example results from the method in chapter 8. The relationship between DMRG and Vidal’s algorithm was first made explicit in two articles [7], which had the effects both of making Vidal’s TEBD algorithm available to a large section of the DMRG community, and making clear the possibility for standard optimisations from DMRG methods to be implemented in Vidal’s original algorithm. The enforcement of particle number conservation is one of the most important examples of this. One of these articles was co-authored by the author of this thesis, and this article is presented in chapter 9.

7.2 Vidal’s State Representation

In order for Vidal’s algorithm to be applied to a particular system, the Hilbert space of that system must be expressed as the product of a series of local Hilbert spaces, i.e., each state

$|\psi\rangle$ can be written as the sum

$$|\psi\rangle = \sum_{i_1, i_2, \dots, i_M=1}^S c_{i_1 i_2 \dots i_M} |i_1\rangle \otimes |i_2\rangle \otimes \dots \otimes |i_M\rangle, \quad (7.3)$$

where $\{|i_i\rangle\}_i$ are the basis states in the local Hilbert space at site i , and for simplicity of notation, we assume that the dimension of the local Hilbert spaces, S , is a constant.

For example, the Hilbert space for a spin chain is a product of local Hilbert spaces of dimension $S = 2$ corresponding to each spin, with basis states $|\uparrow\rangle$ and $|\downarrow\rangle$. Similarly, the Hilbert space for a Hubbard model with two species can be expressed as a product over the local Hilbert spaces corresponding to the occupation of each lattice site, which each have dimension $S = 4$ (the possible states are $|0\rangle$, $|\uparrow\rangle$, $|\downarrow\rangle$, and $|\uparrow\downarrow\rangle$).

The key to the algorithm is then to represent this state as a convenient decomposition into a series of tensors, usually defined in terms of the Schmidt decomposition.

7.2.1 Schmidt Decompositions

For any given state ψ of a bipartite system, decomposed into subsystems A and B , there always exists a decomposition of the form

$$|\psi\rangle = \sum_{\alpha=1}^{\chi_A} \lambda_{\alpha} |\phi_{\alpha}^{[A]}\rangle |\phi_{\alpha}^{[B]}\rangle, \quad (7.4)$$

where $|\phi_{\alpha}^{[A]}\rangle$ are states forming a particular orthonormal basis for A and $|\phi_{\alpha}^{[B]}\rangle$ are states forming a particular orthonormal basis for B . This is called the Schmidt decomposition, and the Schmidt coefficients λ_{α} satisfy $\sum_{\alpha} |\lambda_{\alpha}|^2 = 1$ and

$$\langle \phi_{\alpha}^{[A]} | \psi \rangle = \lambda_{\alpha} |\phi_{\alpha}^{[B]}\rangle. \quad (7.5)$$

The Schmidt coefficients are related to the eigenvalues of the reduced density matrices for each half of the system, $\rho_A = \text{Tr}_B(|\psi\rangle\langle\psi|)$ and $\rho_B = \text{Tr}_A(|\psi\rangle\langle\psi|)$, where Tr denotes the trace, with

$$\rho_A |\phi_{\alpha}^{[A]}\rangle = |\lambda_{\alpha}|^2 |\phi_{\alpha}^{[A]}\rangle \quad (7.6)$$

and

$$\rho_B |\phi_{\alpha}^{[B]}\rangle = |\lambda_{\alpha}|^2 |\phi_{\alpha}^{[B]}\rangle. \quad (7.7)$$

The Schmidt rank, χ_A , is used in quantum information theory as a measure of entanglement for pure states [8]. Larger values of χ_A correspond to more highly entangled subsystems A and B , and when $\chi_A = 1$, the Schmidt decomposition shows that the system is in a product state.

That this decomposition exists for all states of all finite-dimensional bipartite systems, can be derived directly from the singular value decomposition of matrices in linear algebra. If we write a general state of the bipartite system as

$$|\psi\rangle = \sum_{i,j} c_{i,j} |i\rangle_A |j\rangle_B, \quad (7.8)$$

where we have chosen any arbitrary orthonormal bases for A and B , $|i\rangle_A$ and $|j\rangle_B$ respectively, then we obtain a matrix of complex coefficients $c_{i,j}$.

Now, if $C = c_{i,j}$ is an $m \times n$ matrix (i.e., A and B have dimensionalities m and n), then we know from linear algebra that C has a singular value decomposition (see, for example [8]). That is, there exist an $m \times m$ unitary matrix $U \equiv u_{i,j}$, an $n \times n$ unitary matrix $V \equiv v_{i,j}$, and a matrix $D \equiv d_{i,j}$ of size $m \times n$ for which only the diagonal elements are non-zero, such that $C = UDV$. If we thus expand $c_{i,j}$ in terms of these quantities, we obtain,

$$\begin{aligned} |\psi\rangle &= \sum_k d_{k,k} \sum_i u_{i,k} |i\rangle_A \sum_j v_{k,j} |j\rangle_B \\ &= \sum_k \lambda_k |\phi_k^{[A]}\rangle |\phi_k^{[B]}\rangle, \end{aligned} \quad (7.9)$$

where we have identified $\lambda_k = d_{k,k}$, $|\phi_k^{[A]}\rangle = \sum_i u_{i,k} |i\rangle_A$, and $|\phi_k^{[B]}\rangle = \sum_j v_{k,j} |j\rangle_B$. Note that the unitarity of U and V guarantees the orthonormality of $\{|\phi_k^{[A]}\rangle\}$ and $\{|\phi_k^{[B]}\rangle\}$.

7.2.2 The State Decomposition

We then choose to decompose the coefficients $c_{i_1 i_2 \dots i_M}$ from Eq. 7.3 as

$$c_{i_1 i_2 \dots i_M} = \sum_{\alpha_1, \dots, \alpha_{M-1}}^{\chi} \Gamma_{\alpha_1}^{[1] i_1} \lambda_{\alpha_1}^{[1]} \Gamma_{\alpha_1 \alpha_2}^{[2] i_2} \lambda_{\alpha_2}^{[2]} \Gamma_{\alpha_2 \alpha_3}^{[3] i_3} \dots \Gamma_{\alpha_{M-1}}^{[M] i_M}, \quad (7.10)$$

where the Γ and λ tensors are chosen so that when a bipartite splitting is made between any two local Hilbert spaces in the chain, e.g., site l and $l+1$, then $\lambda_{\alpha}^{[l]}$ contains the coefficients of the related Schmidt decomposition,

$$|\psi\rangle = \sum_{\alpha_l=1}^{\chi_l} \lambda_{\alpha_l}^{[l]} |\phi_{\alpha_l}^{[1\dots l]}\rangle |\phi_{\alpha_l}^{[l+1\dots M]}\rangle, \quad (7.11)$$

and the sum over the remaining Γ and λ tensors produces the Schmidt eigenvectors as

$$|\phi_{\alpha}^{[1\dots l]}\rangle = \sum_{\alpha_1, \dots, \alpha_{l-1}}^{\chi_l} \Gamma_{\alpha_1}^{[1] i_1} \lambda_{\alpha_1}^{[1]} \Gamma_{\alpha_1 \alpha_2}^{[2] i_2} \lambda_{\alpha_2}^{[2]} \Gamma_{\alpha_2 \alpha_3}^{[3] i_3} \dots \Gamma_{\alpha_{l-1} \alpha_l}^{[l] i_l} |i_1\rangle \otimes \dots \otimes |i_l\rangle, \quad (7.12)$$

and

$$|\phi_{\alpha}^{[l+1\dots M]}\rangle = \sum_{\alpha_{l+1}, \dots, \alpha_{M-1}}^{\chi_l} \Gamma_{\alpha_l \alpha_{l+1}}^{[l+1] i_{l+1}} \lambda_{\alpha_{l+1}}^{[l+1]} \Gamma_{\alpha_{l+1} \alpha_{l+2}}^{[l+2] i_{l+2}} \dots \Gamma_{\alpha_{M-1}}^{[M] i_M} |i_{l+1}\rangle \otimes \dots \otimes |i_M\rangle, \quad (7.13)$$

It is shown in section 9.4 that this representation is a matrix product state (the definition and properties of which are discussed in section 9.3), and thus equivalent to the representations used in standard DMRG methods.

It is straightforward to show by construction that any state of the form in Eq. 7.3 can be written in this way. We begin by writing the Schmidt Decomposition between sites 1 and 2,

$$\begin{aligned} |\psi\rangle &= \sum_{\alpha_1} \lambda_{\alpha_1}^{[1]} |\phi_{\alpha_1}^{[1]}\rangle |\phi_{\alpha_1}^{[2\dots M]}\rangle, \\ &= \sum_{\alpha_1, i_1} \Gamma_{\alpha_1}^{[1]i_1} \lambda_{\alpha_1}^{[1]} |i_1\rangle |\phi_{\alpha_1}^{[2\dots M]}\rangle, \end{aligned} \quad (7.14)$$

where we have expanded $|\phi_{\alpha_1}^{[1]}\rangle$ in the local basis for site 1. We now expand $|\phi_{\alpha_1}^{[2\dots M]}\rangle$ in the local basis for site 2 in the chain,

$$|\phi_{\alpha_1}^{[2\dots M]}\rangle = \sum_{i_2} |i_2\rangle |\zeta_{i_2\alpha_1}^{[3\dots M]}\rangle, \quad (7.15)$$

where $|\zeta_{i_2\alpha_1}^{[3\dots M]}\rangle$ is some unnormalised vector that exists on the space formed by the product of local Hilbert spaces for sites 3 to N . We choose to write these vectors in terms of the basis for local spaces 3 to N given by the Schmidt eigenvectors for the bipartite splitting between local spaces 2 and 3, and in terms of the corresponding Schmidt eigenvalues, i.e.,

$$|\zeta_{i_2\alpha_1}^{[3\dots M]}\rangle = \sum_{\alpha_2} \Gamma_{\alpha_1\alpha_2}^{[2]i_2} \lambda_{\alpha_2}^{[2]} |\phi_{\alpha_2}^{[3\dots M]}\rangle. \quad (7.16)$$

Substituting Eqs. 7.16 and 7.15 into Eq. 7.14, we then obtain

$$|\psi\rangle = \sum_{\alpha_1, \alpha_1, i_1, i_2} \Gamma_{\alpha_1}^{[1]i_1} \lambda_{\alpha_1}^{[1]} \Gamma_{\alpha_1\alpha_2}^{[2]i_2} \lambda_{\alpha_2}^{[2]} |i_1\rangle |i_2\rangle |\phi_{\alpha_2}^{[3\dots M]}\rangle. \quad (7.17)$$

From here we can iterate the steps in Eqs. 7.15 and 7.16 in order to construct the representation in Eq. 7.10. The identity Eq. 7.13 is then correct by construction, and Eq. 7.12 can be checked using Eq. 7.5.

7.2.3 Use and Validity of Truncated Decompositions

In Eq. 7.10, we have replaced the original S^N coefficients with $\sim (S\chi^2 + \chi)M$ coefficients, where $\chi = \max(\chi_l)$. However, for a general state, $\chi \sim \exp(M)$, and so we have neither lost nor gained anything by writing this decomposition. The key to the success of this representation is that we find for many states, especially the low energy states of 1D systems, that the Schmidt coefficients ordered from highest to lowest decrease approximately exponentially as a function of their index. This allows us to truncate the decomposition at a relatively small value of χ whilst not significantly changing the state (the inner product between the states is essentially unity). The widespread success in the use of DMRG techniques to compute ground states of 1D lattice and spin models using matrix product states [2] demonstrates the common occurrence of states for which a decomposition truncated at a particular value of χ provides an accurate representation for the state.

The relationship between the Schmidt decomposition and measures of entanglement in quantum information theory [8] means that states for which the truncation can be such states are often referred to as ‘‘slightly entangled’’ [3]. This relationship can be further quantified,

and has been very successful in justifying the success of this representation for certain classes of 1D models, and equally at explaining the difficulties encountered in using DMRG methods for large systems at critical points in 1D and more generally in higher dimensions [9].

In quantum information theory, both amount of information in a system and the entanglement between two subsystems can be quantified via the von Neumann entropy, which is the same for subsystems A and B ,

$$\mathcal{S}(A) = -\text{Tr}[\rho_A \log_2 \rho_A] = -\sum_{\alpha=1}^{\chi} \lambda_{\alpha}^2 \log_2 \lambda_{\alpha}^2. \quad (7.18)$$

This value provides a theoretical lower bound on how many qubits are required to express the information in subsystem A (or B), and thus a lower bound on the states required to express that information, $\chi \geq 2^{\mathcal{S}_A}$. It has been shown that for certain classes of systems in 1D, that as the length L of the system grows, the von Neumann entropy saturates, at a value depending on the correlation length [9]. In contrast, the von Neumann entropy diverges logarithmically for 1D systems at a critical point, and diverges as $\mathcal{S}_A(L) \propto L^{d-1}$ in dimension $d > 1$. Thus, we expect that in the thermodynamic limit ($L \rightarrow \infty$), the ground state of 1D systems away from critical points can be represented with a finite value of χ , whereas states at criticality will require a χ that diverges polynomially in L , and in higher dimensions will diverge exponentially as $\chi \propto 2^{L^{d-1}}$ when $L \rightarrow \infty$.

Whilst these theoretical results are useful guides and give good agreement with the general behaviour observed for DMRG methods, it is clearly possible to simulate finite systems, even in higher dimensions, for sufficiently small L . Whether a particular truncation is valid must still be determined numerically, especially when truncations are being performed during the time evolution of a state. The best test in this regard is to run simulations multiple times with different values of χ to ensure convergence of the representation, although the sum of the eigenvalues thrown away in each truncation is also a useful indicator as to what extent the truncated representations have changed the state (see section 7.4.1).

7.3 Vidal's TEBD Algorithm

The other major advantage of this decomposition is that it can be efficiently updated when operators are applied that act either on a single local Hilbert space, or on the local Hilbert spaces of two neighbouring sites. In each of these cases, only the Γ tensors corresponding to the spaces that are acted upon need to be updated. This can be seen simply by considering the Schmidt decompositions taken to the left and to the right of the sites that are acted upon. For example, if an operator acts on local space of site l , then from the Schmidt decomposition taken between local spaces $l-1$ and l , we see that the tensors $\Gamma^{[j]}$ and $\lambda^{[j]}$ with $j < l$ are not altered, as the Schmidt eigenvectors on spaces $1 \dots (l-1)$ are not changed by the operation. Similarly, from the Schmidt decomposition taken between local spaces l and $l+1$, we see that the tensors $\Gamma^{[j]}$ and $\lambda^{[j]}$ with $j > l$ are not altered, as the Schmidt eigenvectors on spaces $l+1 \dots M$ are not changed by the operation.

7.3.1 Single-Site Operations

In the case of an operation $U = \sum_{i_l, j_l} U_{j_l}^{i_l} |i_l\rangle\langle j_l|$ on a single local space, at site l , we need only update $\Gamma^{[l]}$, and the new state is given by

$$\Gamma_{\alpha_{l-1}\alpha_l}^{[l]i_l} = \sum_{j_l=1}^S U_{j_l}^{i_l} \Gamma_{\alpha_{l-1}\alpha_l}^{[l]j_l}. \quad (7.19)$$

This operation can be performed in the order of $\chi^2 S^2$ operations.

7.3.2 Two-Site Operations

For an operation on two neighbouring sites, l and $l+1$, we must apply the operator $V = \sum V_{kl}^{ij} |i_l j_{l+1}\rangle\langle k_l l_{l+1}|$ to update the tensors $\Gamma^{[l]}$, $\Gamma^{[l+1]}$, and $\lambda^{[l]}$. In order to apply the operator, we express the state in terms of the Schmidt eigenvectors to the left of the two sites,

$$|\alpha\rangle = |\phi_\alpha^{[1\dots(l-1)]}\rangle, \quad (7.20)$$

and to the right of the two sites,

$$|\gamma\rangle = |\phi_\gamma^{[(l+2)\dots M]}\rangle, \quad (7.21)$$

as

$$|\psi\rangle = \sum_{\alpha, \beta, \gamma=1}^{\chi} \sum_{i, j=1}^S \lambda_\alpha^{[l-1]} \Gamma_{\alpha\beta}^{[l]i} \lambda_\beta^{[l]} \Gamma_{\beta\gamma}^{[l+1]j} \lambda_\gamma^{[l+1]} |\alpha i j \gamma\rangle, \quad (7.22)$$

where we have dropped the tensor product symbols in $|\alpha i j \gamma\rangle \equiv |\alpha\rangle \otimes |i\rangle_l \otimes |j\rangle_{l+1} \otimes |\gamma\rangle$. We can then apply the operator V to write

$$|\psi'\rangle = \sum_{\alpha, \gamma=1}^{\chi} \sum_{i, j=1}^S \Theta_{\alpha\gamma}^{ij} |\alpha i j \gamma\rangle, \quad (7.23)$$

with

$$\Theta_{\alpha\gamma}^{ij} = \sum_{\beta=1}^{\chi} \sum_{k, l=1}^S V_{kl}^{ij} \lambda_\alpha^{[l-1]} \Gamma_{\alpha\beta}^{[l]k} \lambda_\beta^{[l]} \Gamma_{\beta\gamma}^{[l+1]l} \lambda_\gamma^{[l+1]} |\alpha i j \gamma\rangle. \quad (7.24)$$

This gives us a total of $\chi^2 S^2$ basis states for the operation, which must then be reduced to χ^2 states afterwards, by performing a Schmidt decomposition between sites l and $l+1$ and retaining only the basis states corresponding to the χ largest coefficients. In this way, we adapt the truncated Hilbert space that we use to represent the final state. In practice, we do this by diagonalising the reduced density matrix

$$\begin{aligned} \rho^{[1\dots l]} &= \text{Tr}_{(l+1)\dots M} |\psi'\rangle\langle\psi'| \\ &= \sum_{j, j', \gamma, \gamma'} \left[\sum_{\alpha, i} \Theta_{\alpha\gamma}^{ij} (\Theta_{\alpha\gamma'}^{ij'})^* \right] |j\gamma\rangle\langle j'\gamma'|, \end{aligned} \quad (7.25)$$

in order to find the new Schmidt coefficients $\lambda_\beta^{[l]}$ and eigenstates

$$|\phi_\beta^{[(l+1)\dots M]}\rangle = \sum_{j,\gamma} \Gamma_{\beta\gamma}^{\prime[l+1]j} \lambda_\gamma^{[l+1]} |j\gamma\rangle, \quad (7.26)$$

from which we can compute the new tensor $\Gamma_{\beta\gamma}^{\prime[l+1]j}$. The eigenstates $|\phi_\beta^{[1\dots l]}\rangle$ and the remaining tensor $\Gamma_{\alpha\beta}^{\prime[l]i}$ can then be found from

$$\begin{aligned} \lambda_\beta^{[l]} |\phi_\beta^{\prime[1\dots l]}\rangle &= \langle \phi_\beta^{[(l+1)\dots M]} | \psi' \rangle \\ &= \sum_{i,j,\alpha,\gamma} \left\{ \left[(\Gamma_{\beta\gamma}^{\prime[l+1]j})^* \Theta_{\alpha\gamma}^{ij} \right] / \lambda_\alpha^{[l-1]} \right\} |\alpha i\rangle \end{aligned} \quad (7.27)$$

$$= \sum_{i,\alpha} \Gamma_{\alpha\beta}^{\prime[l]i} |\alpha i\rangle. \quad (7.28)$$

For sufficiently large χ , this procedure is limited by the time required to diagonalise $\rho^{[1\dots l]}$, which requires $\sim \chi^3 S^3$ operations.

7.3.3 Coherent Time Evolution of a State

Using this method, we can simulate a range of Hamiltonian time evolutions provided that the Hamiltonian describing the system can be written in the form

$$\hat{H} = \sum_i \hat{H}_{i,i+1}, \quad (7.29)$$

where $\hat{H}_{i,i+1}$ are operators that act only on the local Hilbert space for sites i and $i+1$ of the system. We can rewrite this sum as

$$\hat{H} = \sum_{i \text{ odd}} \hat{H}_{i,i+1} + \sum_{i \text{ even}} \hat{H}_{i,i+1} = \hat{F} + \hat{G}, \quad (7.30)$$

where all of the terms in the sum for \hat{F} commute with one another, as do those in the sum that gives \hat{G} .

We then perform a Suzuki-Trotter decomposition [10] of the time evolution operator for a short time δt ,

$$e^{-i\hat{H}\delta t} = e^{-i\hat{F}\delta t} e^{-i\hat{G}\delta t} + \mathcal{O}(\delta t). \quad (7.31)$$

This allows us to apply the time evolution in sequence to pairs of neighbouring sites using the algorithm in section 7.3.2, whilst incurring an error proportional to the size of the timestep δt . This error can be made smaller by applying a second order expansion,

$$e^{-i\hat{H}\delta t} = e^{-i\hat{F}\delta t/2} e^{-i\hat{G}\delta t} e^{-i\hat{F}\delta t/2} + \mathcal{O}[(\delta t)^2], \quad (7.32)$$

or higher order expansions (see [10, 11]).

7.3.4 Finding Initial States

Where the desired initial state for a time evolution is easily expressed as a product state of sites, this state can easily be written directly with all $\lambda_\alpha^{[l]} = \delta_{\alpha,1}$ where $\delta_{\alpha,1}$ denotes the Kronecker delta. However, this is generally not the case, and we would like to instead produce the ground state, $|\psi_0\rangle$ of some Hamiltonian \hat{H}_0 as our initial configuration. Possible methods then include computing $|\psi_0\rangle$ using DMRG methods and using the resulting state to write the initial decomposition for the present algorithm; or beginning with a product state which is the ground state of a particular Hamiltonian, \hat{H}_P , and finding a smooth interpolation between \hat{H}_P and \hat{H}_0 so that $|\psi_0\rangle$ may be found by an adiabatic time evolution beginning with the ground state of \hat{H}_P .

In practice, the technique we mostly use is to simulate a time evolution in imaginary time with Hamiltonian \hat{H}_0 , i.e., we find the ground state as

$$|\psi_0\rangle = \lim_{t \rightarrow \infty} \frac{\exp(-H_0 t) |\psi_p\rangle}{\|\exp(-H_0 t) |\psi_p\rangle\|}, \quad (7.33)$$

where $|\psi_p\rangle$ is some initial product state with $\langle \psi_p | \psi_0 \rangle \neq 0$. This procedure is straight-forward to implement, and requires that the time step δt from section 7.3.3 be replaced by an imaginary value, and that the Θ tensor from section 7.3.2 be explicitly normalised in the code. However, there are two important comments to be made about its practical implementation and interpretation

Imaginary Time Evolution: Non-conservation of good quantum numbers

Unless the code is adapted so that good quantum numbers, such as total particle number in the Bose Hubbard model, are explicitly conserved (see chapter 8), numerical noise in the diagonalisation process can introduce small contributions from states that do not have the same value of these “good” quantum numbers as the initial state. This is despite the fact that these values should be conserved if they are conserved when the Hamiltonian is applied to the state. In a real time evolution this is not normally a problem, as the linear nature of the time evolution means that these states do not significantly contribute to the dynamics. However, for an imaginary time evolution this is not the case and the relative weight of these states can increase exponentially if they have lower energy expectation values than the initial state. Thus, in an imaginary time evolution for the Bose-Hubbard model, the total particle number will change in time, and must be chosen by adding a chemical potential term, $-\mu \sum_i \hat{n}_i$ to the Hamiltonian. The resulting state is normally a superposition of states with different total particle numbers, although we find that the variance in total particle number (which depends strongly on the initial condition) is very narrow, e.g., much narrower than that expected for a Bose Hubbard model described in the Grand Canonical Ensemble [12].

Imaginary Time Evolution: Orthogonalisation

High-order Trotter decompositions often used in real time evolution must not be used during imaginary time evolutions, unless the sets of Schmidt eigenstates that are assumed to

be orthogonal during the two site operation in section 7.3.2 are explicitly orthogonalised and normalised afterwards. This is because the non-unitary operations being applied here cause many parts of the representation that initially corresponding to Schmidt eigenstates to become non-orthogonal. This is in contrast to the case of real time evolution, where the unitarity of the operations ensures that all orthonormal sets of states to which the operation is applied remain orthonormal. The simplest method to overcome this requirement, ensuring that all necessary sets of eigenstates remain orthonormal, is to carefully apply the imaginary time evolution operators in sweeps forwards and backwards through the system, with the order $(1, 2), (2, 3), \dots, (l-1, l), (l-1, l), (l-2, l-1), \dots, (1, 2)$.

The potential problem here arises because the two-site operation in section 7.3.2 assumes that when we apply an operator to the sites l and $l+1$, the states $\{|\phi_\alpha^{[1\dots l-1]}\rangle\}$ and $\{|\phi_\gamma^{[l+2\dots M]}\rangle\}$ are always orthogonal, but it only explicitly orthogonalises the states $\{|\phi_\beta^{[1\dots l]}\rangle\}$ and $\{|\phi_\beta^{[l+1\dots M]}\rangle\}$ during the operation. If the operation applied is unitary, then all other initially orthogonal sets of eigenstates will remain orthogonal. However, in imaginary time evolution, any set of Schmidt eigenstates corresponding to the part of the system on which the operator is acting will, in general, become non-orthogonal. For example, amongst other sets of Schmidt eigenstates, we apply the operation to $\{|\phi_\alpha^{[1\dots l+1]}\rangle\}$, because these states exist on a basis containing the local Hilbert spaces of sites l and $l+1$. If we perform a second-order Trotter decomposition, and, e.g., apply the next operation to sites $l+2$ and $l+3$, then we assume during the operation that the states $\{|\phi_\alpha^{[1\dots l+1]}\rangle\}$ are orthonormal, which is no longer the case. However, if we perform the next operation instead on sites $l+1$ and $l+2$ then we require only that $\{|\phi_\alpha^{[1\dots l]}\rangle\}$ and $\{|\phi_\gamma^{[l+3\dots M]}\rangle\}$ are orthonormal. This condition is satisfied for $\{|\phi_\alpha^{[1\dots l]}\rangle\}$ because these are orthogonalised by the original operation on sites l and $l+1$, and for $\{|\phi_\gamma^{[l+3\dots M]}\rangle\}$ because the previous operation did not change these states, and therefore we have orthogonality from the original state. This situation recurs as we sweep forwards, and again as we sweep back through the system. Many sets of states become non-orthogonal, but the sets of states that we assume at any point to be orthogonal are either made so by the previous step, or were made so during the previous sweep in the opposite direction. This provides a simple work-around for the problem of maintaining orthonormality.

At the end of the imaginary time evolution the representation can be restored to a completely orthonormal representation by applying any unitary operator (e.g., the identity) with the same forwards-and-back sweep.

Imaginary Time Evolution: Testing the Ground State

The quality of ground states obtained can be tested by performing a real time evolution with the same Hamiltonian, and testing the change in the state as a function of time. We find that for ground states of the Bose-Hubbard Hamiltonian found by imaginary time evolution we normally observe $|\langle\psi_0(0)|\psi_0(t)\rangle|^2 > 1 - 10^{-7}$ for $t \sim 5J$. This value could probably be improved upon by optimising the imaginary time evolution sweeps, e.g., by carefully decreasing the timestep δt as the state converges to the ground state, in order to reduce the Trotter error in each step.

7.4 Implementation of the Algorithm

Our code was originally written for MATLAB² as a C MEX interface program, and has since been rewritten as stand-alone C-code. Typical runtimes of the current code, which is optimised for particle number conservation in the Bose-Hubbard model, with parameters $\chi = 50$, $M = 50$, $S = 5$ are of the order of several hours for 20000 timesteps. Comparable performance was previously achievable with an unoptimised code with $\chi < 10$ (see chapter 8 for more details on the optimisation of the code by making use of number conservation).

7.4.1 Choosing simulation parameters

As was already mentioned in section 7.2.2, it is always important to test the convergence of the results with increasing χ . A useful indicator of convergence is the sum of the eigenvalues discarded after each diagonalisation, $\sum_{\alpha > \chi} \lambda_{\alpha}^2$. Where comparisons with exact calculations are possible for small systems, $M \sim 10$, we find that if the maximum value of this sum is less than $\sim 10^{-9}$, then even when inner products between states are being computed there is little error introduced over ~ 20000 timesteps. Under most circumstances, many calculated quantities will be reasonably accurate even if the sum of discarded Schmidt coefficients $\sim 10^{-6}$. However, it is not possible to be sure of correct results in this case without substantially increasing χ and explicitly testing for convergence of the quantities being calculated.

For Bosons on an optical lattice the states in the local Hilbert space correspond to the number of particles on the site, and we must also choose the dimension S of the local Hilbert space to be large enough to accommodate as many particles as are present in the states we observe. Here, we test the occupation of the highest number state as an indicator of the convergence with S . In some problems we also allow S to be a function of the site number, for example in the treatment of the Single Atom Transistor (see Part III of this thesis), where we consider the existence of a molecular state on one site which does not exist on others. Allowing such a variable dimension dramatically reduces the simulation time, which when χ is sufficiently large that the diagonalisation step of the matrix defined in Eq. 7.25 is the slowest step, scales (for unoptimised implementations of the algorithm) as $\chi^3 \sum_l S_l^3$.

Bibliography

- [1] S. R. White, Phys. Rev. Lett. **69**, 2863 (1992); S. R. White, Phys. Rev. B **48**, 10345 (1993).
- [2] U. Schollwöck, Rev. Mod. Phys., **77**, 259 (2005).
- [3] G. Vidal, Phys. Rev. Lett. **91**, 147902 (2003); G. Vidal, Phys. Rev. Lett. **93**, 040502 (2004).
- [4] M. Zwolak and G. Vidal, Phys. Rev. Lett. **93**, 207205 (2004).
- [5] F. Verstraete, J. J. Garcia-Ripoll, and J. I. Cirac, Phys. Rev. Lett. **93**, 207204 (2004).

²MATLAB[®] is a registered trademark of The Mathworks, Inc.

- [6] F. Verstraete, and J. I. Cirac, cond-mat/0407066.
- [7] A. J. Daley, C. Kollath, U. Schollwöck, G. Vidal, J. Stat. Mech.: Theor. Exp. P04005 (2004); S.R. White and A.E. Feiguin, Phys. Rev. Lett. **93**, 076401 (2004).
- [8] M. A. Nielsen and I. L. Chuang, *Quantum Computation and quantum communication*, Cambridge University Press, 2000.
- [9] See, [2] and references therein, and also F. Verstraete, J.I. Cirac, cond-mat/0505140; F. Verstraete, D. Porras, and J. I. Cirac, Phys. Rev. Lett. **93**, 227205 (2004).
- [10] M. Suzuki, Phys. Lett. A **146**, 6 (1990); M. Suzuki J. Math. Phys. **32**, 2 (1991).
- [11] For higher order expansions see also A. T. Sornborger and E. D. Stewart, quant-ph/9809009.
- [12] This result has also been observed in simulations performed in Oxford, S. Clark and D. Jaksch, private communication.

CHAPTER 8

EXTENSIONS TO THE METHOD AND SHORT EXAMPLES

Vidal's Algorithm is particularly suited to treating systems of atoms in optical lattices in 1D. Whilst exact methods on full Hilbert spaces cannot access more than $M \sim 10$ sites, we can generally reach size scales on the order of $M \sim 50 - 100$, which compares with typical experimental size scales, $M \sim 100$ sites. The ability to perform these calculations is even more important given that many analytical techniques, especially the use of mean field theories are known to often work poorly in 1D. Using Vidal's algorithm we have the means not only to test predictions from analytical theories, but also to go beyond them and make exact quantitative predictions of quantities that can be measured in experiments, even in regimes that cannot be described analytically.

In this chapter two important additions to Vidal's original scheme are presented. The first is the method used to calculate correlation functions, and the second is a scheme to greatly optimise the simulation code by properly taking conserved quantities into consideration. At the end of the chapter two short examples are presented, demonstrating the types of results that can be calculated for the Bose-Hubbard model using this algorithm.

8.1 Calculating Correlation Functions

Correlation functions of the form $\langle \tilde{\psi} | \hat{A}_k \hat{B}_l | \psi \rangle$, where $\hat{A}_k \equiv A_{j_k}^{i_k}$ and $\hat{B}_l \equiv A_{j_l}^{i_l}$ act only on the local Hilbert spaces in sites k and l respectively, can easily be computed with of the order of $MS\chi^4$ operations. In fact, provided the operations \hat{A} and \hat{B} act only on single sites, one can also calculate a single instance of a higher order correlation function in the following way at no additional computational cost. In each case, the calculation of the correlation function reduces to the sum over four dimensional tensors G_m , which can each be computed from the tensors $\tilde{\Gamma}^{[m]}$, $\Gamma^{[m]}$, $\tilde{\lambda}^{[m]}$, and $\lambda^{[m]}$, with tensors G_k and G_l being defined from the values of

$\Gamma^{[k]}$ and $\Gamma^{[l]}$ after the operations \hat{A}_k and \hat{B}_l have been applied. Specifically, we see that

$$\begin{aligned}
\langle \tilde{\psi} | \hat{A}_k \hat{B}_l | \psi \rangle &= \sum_{i_1 \dots i_M} \left(\sum_{\beta_1, \dots, \beta_{M-1}} \tilde{\Gamma}_{\beta_1}^{[1] i_1} \tilde{\lambda}_{\beta_1}^{[1]} \tilde{\Gamma}_{\beta_1 \beta_2}^{[2] i_2} \dots \tilde{\Gamma}_{\beta_{M-1}}^{[M] i_M} \right)^* \\
&\times \left(\sum_{\alpha_1, \dots, \alpha_{M-1}} \Gamma_{\alpha_1}^{[1] i_1} \lambda_{\alpha_1}^{[1]} \dots \sum_{j_k} A_{j_k}^{i_k} \Gamma_{\alpha_{k-1} \alpha_k}^{[k] j_k} \dots \sum_{j_l} B_{j_l}^{i_l} \Gamma_{\alpha_{l-1} \alpha_l}^{[l] j_l} \dots \Gamma_{\alpha_{M-1}}^{[M] i_M} \right) \\
&= \sum_{\beta_1, \dots, \beta_{M-1}} \sum_{\alpha_1, \dots, \alpha_{M-1}} \left(\sum_{i_1} \tilde{\lambda}_{\beta_1}^{[1]} \tilde{\Gamma}_{\beta_1}^{*[1] i_1} \Gamma_{\alpha_1}^{[1] i_1} \lambda_{\alpha_1}^{[1]} \right) \left(\sum_{i_2} \tilde{\lambda}_{\beta_2}^{[2]} \tilde{\Gamma}_{\beta_1 \beta_2}^{*[2] i_2} \Gamma_{\alpha_1 \alpha_2}^{[2] i_2} \lambda_{\alpha_2}^{[2]} \right) \\
&\times \left(\sum_{i_3} \tilde{\lambda}_{\beta_3}^{[3]} \tilde{\Gamma}_{\beta_2 \beta_3}^{*[3] i_3} \Gamma_{\alpha_2 \alpha_3}^{[3] i_3} \lambda_{\alpha_3}^{[3]} \right) \dots \left[\sum_{i_k} \tilde{\lambda}_{\beta_k}^{[k]} \tilde{\Gamma}_{\beta_{k-1} \beta_k}^{*[k] i_k} \left(\sum_{j_k} A_{j_k}^{i_k} \Gamma_{\alpha_{k-1} \alpha_k}^{[k] j_k} \right) \lambda_{\alpha_k}^{[k]} \right] \dots \\
&\times \dots \left[\sum_{i_l} \tilde{\lambda}_{\beta_l}^{[l]} \tilde{\Gamma}_{\beta_{l-1} \beta_l}^{*[l] i_l} \left(\sum_{j_l} B_{j_l}^{i_l} \Gamma_{\alpha_{l-1} \alpha_l}^{[l] j_l} \right) \lambda_{\alpha_l}^{[l]} \right] \dots \left(\sum_{i_M} \tilde{\Gamma}_{\beta_{M-1}}^{*[M] i_M} \Gamma_{\alpha_{M-1}}^{[M] i_M} \right) \\
&= (G_1)_{\beta_1 \alpha_1} (G_2)_{\beta_2 \alpha_2}^{\beta_1 \alpha_1} (G_3)_{\beta_3 \alpha_3}^{\beta_2 \alpha_2} \dots (G_k)_{\beta_k \alpha_k}^{\beta_{k-1} \alpha_{k-1}} \dots (G_l)_{\beta_l \alpha_l}^{\beta_{l-1} \alpha_{l-1}} \dots (G_M)^{\beta_{M-1} \alpha_{M-1}},
\end{aligned} \tag{8.1}$$

with

$$\begin{aligned}
(G_1)_{\beta_1 \alpha_1} &= \left(\sum_{i_1} \tilde{\lambda}_{\beta_1}^{[1]} \tilde{\Gamma}_{\beta_1}^{*[1] i_1} \Gamma_{\alpha_1}^{[1] i_1} \lambda_{\alpha_1}^{[1]} \right) \\
(G_2)_{\beta_2 \alpha_2}^{\beta_1 \alpha_1} &= \left(\sum_{i_2} \tilde{\lambda}_{\beta_2}^{[2]} \tilde{\Gamma}_{\beta_1 \beta_2}^{*[2] i_2} \Gamma_{\alpha_1 \alpha_2}^{[2] i_2} \lambda_{\alpha_2}^{[2]} \right) \\
&\vdots \\
(G_k)_{\beta_k \alpha_k}^{\beta_{k-1} \alpha_{k-1}} &= \left[\sum_{i_k} \tilde{\lambda}_{\beta_k}^{[k]} \tilde{\Gamma}_{\beta_{k-1} \beta_k}^{*[k] i_k} \left(\sum_{j_k} A_{j_k}^{i_k} \Gamma_{\alpha_{k-1} \alpha_k}^{[k] j_k} \right) \lambda_{\alpha_k}^{[k]} \right] \\
&\vdots \\
(G_M)^{\beta_{M-1} \alpha_{M-1}} &= \left(\sum_{i_M} \tilde{\Gamma}_{\beta_{M-1}}^{*[M] i_M} \Gamma_{\alpha_{M-1}}^{[M] i_M} \right),
\end{aligned} \tag{8.2}$$

and where in the last line of Eq. 8.1 we have omitted the summation symbols for α_m and β_m . Note that, in principle, more complicated operations can also be performed on the state $|\psi\rangle$ before calculating the sum, and thus more complex correlation functions could be computed. For example the application of an operation acting on two neighbouring sites could be performed as discussed in section 7.3.2.

Two special cases of Eq. 8.1 are the inner product for two states, $\langle \tilde{\psi} | \psi \rangle$, and the calculation of simple correlation functions, e.g., the elements of the single particle density matrix for the

Bose-Hubbard model, $\langle \psi | \hat{b}_i^\dagger \hat{b}_j | \psi \rangle$. Where the two states $|\psi\rangle$ and $|\tilde{\psi}\rangle$ are the same, there is no need to perform the entire sum in Eq. 8.1. Instead, the orthonormality of Schmidt eigenstates in the representation means that the calculation can be simplified because parts of the representation are unchanged by the application of the operator $\hat{A}_k \hat{B}_l$. In particular (assuming $k \leq l$), all $\Gamma^{[i]}$ for $i < k$ or $i > l$ and all $\lambda^{[i]}$ are unchanged, and as a result the sum simplifies to

$$\langle \psi | \hat{A}_k \hat{B}_l | \psi \rangle = |\lambda_{\beta_{k-1}}^{[k-1]}|^2 (G_k)_{\beta_k \alpha_k}^{\beta_{k-1} \beta_{k-1}} \dots (G_l)_{\beta_l \beta_l}^{\beta_{l-1} \alpha_{l-1}}. \quad (8.3)$$

8.2 Conserved Quantities and Vidal's Algorithm

The algorithm can be substantially optimised by taking into account the existence of conserved quantities, or “good quantum numbers” for the Hamiltonian describing the time evolution being computed. This optimisation is well known in implementations of DMRG methods [1], and its implementation here was adapted after the equivalence of matrix product state representations in DMRG and Vidal's Algorithm were demonstrated (see [2], and chapter 9 of this thesis). Whilst many similar symmetries can be dealt with in the manner described here (e.g., the total magnetisation in spin systems), the implementation is presented here for conservation of total particle number, as arises in the Bose-Hubbard model.

In the Bose-Hubbard model the states in each local Hilbert spaces, $|i\rangle_l$, each correspond to a particular number of particles on the site (l). We denote this number $N_L(i)$. Then, given a system with a fixed total particle number, \mathcal{N} , let us assume that the initial Schmidt eigenvectors, $|\alpha\rangle \equiv |\phi_\alpha^{[1\dots l]}\rangle$ and $|\gamma\rangle \equiv |\phi_\gamma^{[l+1\dots M]}\rangle$ each are states of fixed total particle number, $N_S(\alpha)$ and $N_S(\gamma)$. This can clearly be chosen in the initial state, and we will show that these vectors still correspond to some particular total particle number after a two-site operation (see section 7.3.2 for details of this operation). We then keep track of those numbers and use them to divide the problem into smaller parts as shown below.

After the application of the time-evolution or imaginary time evolution operator (both of which are number conserving), the state as expressed in Eq. 7.23 reads

$$|\psi'\rangle = \sum_{\alpha, \gamma=1}^{\chi} \sum_{i, j=1}^S \Theta_{\alpha\gamma}^{ij} |\alpha i j \gamma\rangle.$$

Because we know that any state $|\alpha i j \gamma\rangle$ contributing to $|\psi'\rangle$ must satisfy $\mathcal{N} = N_S(\alpha) + N_L(i) + N_L(j) + N_S(\gamma)$, the tensor $\Theta_{\alpha\gamma}^{ij}$ is non-zero only when this sum is satisfied. In practice, we form tables of valid combinations of i and j given the values of $N_S(\alpha)$ and $N_S(\gamma)$ (this can also be used to optimise the construction of $\Theta_{\alpha\gamma}^{ij}$). Then, when we form the reduced density matrix, Eq. 7.25,

$$\rho^{[1\dots l]} = \sum_{j, j', \gamma, \gamma'} \left[\sum_{\alpha, i} \Theta_{\alpha\gamma}^{ij} (\Theta_{\alpha\gamma'}^{ij'})^* \right] |j\gamma\rangle \langle j'\gamma'|,$$

we see that the only non-zero values are those where $N_L(j') + N_S(\gamma') = N_L(j) + N_S(\gamma)$, thus leading (when the states are appropriately ordered) to a block-diagonal matrix with each block corresponding to a fixed particle number, $N_R = N_L(j) + N_S(\gamma)$.

Instead of diagonalising the whole matrix $\rho^{[1\dots l]}$ we instead diagonalise the blocks separately, as matrices $\rho_{N_R}^{[1\dots l]}$, each corresponding to a fixed total particle number for the “right hand side” of the system, sites $\{l+1, \dots, M\}$. The resulting eigenvectors then also each correspond to states with fixed number of particles, and we choose the eigenvectors corresponding to the largest eigenvalues taken over $\rho_{N_R}^{[1\dots l]}$ for all N_R to be the new eigenstates $|\phi_\beta^{[(l+1)\dots M]}\rangle$. When the corresponding Schmidt eigenstates for the “left hand side” of the system, sites $\{1, \dots, l\}$ are found, their particle numbers must also be fixed so that $N_S(\phi_\beta^{[(l+1)\dots M]}) + N_S(\phi_\beta^{[1\dots l]}) = \mathcal{N}$. Thus, the new Schmidt eigenvectors all correspond to fixed particle numbers, and the process can be repeated in subsequent two-site operations.

The major gain from this optimisation occurs because the matrices $\rho_{N_R}^{[1\dots l]}$ that we must diagonalise are much smaller than the full reduced density matrix $\rho^{[1\dots l]}$. Not only is the algorithm then faster for a fixed χ than the unoptimised algorithm, but the computation time no longer scales as $S^3\chi^3$ (a scaling which arose from the diagonalisation of $\rho^{[1\dots l]}$). For fixed $S \sim 5$, we find that the computation time scales approximately as $\sim \chi^2$, on top of a speed increase of more than an order of magnitude for fixed $\chi = 10$.

8.3 Example: Superfluid and Mott Insulator Ground states in 1D

A simple demonstration of the capabilities of the imaginary time evolution routine is computation of ground states for the Bose-Hubbard model with different trapping potentials. This model, as discussed in chapter 2 is given in terms of bosonic creation and annihilation operators \hat{b}_i^\dagger and \hat{b}_i for particles on site i as

$$\hat{H} = -J \sum_{\langle i,j \rangle} \hat{b}_i^\dagger \hat{b}_j + \frac{U}{2} \sum_i \hat{n}_i(\hat{n}_i - 1) + \sum_i \epsilon_i \hat{n}_i,$$

where $\langle i, j \rangle$ denotes a sum over all combinations of neighbouring sites, and $\hat{n}_i = \hat{b}_i^\dagger \hat{b}_i$. Ground states of this and other models serve as the initial states in our time-dependent calculations, and provide important information about the system in their own right. In this section we present example calculations of these ground states, represented by the computed values of the single particle density matrix, $\langle \hat{b}_i^\dagger \hat{b}_j \rangle$. The diagonal entries of this matrix are $\langle \hat{n}_i \rangle$, the onsite densities, and the off-diagonal elements represent correlations between different sites.

8.3.1 Box Trap

Fig. 8.1 shows the single particle density matrix for a typical superfluid ground state of the Bose-Hubbard model in a box trap ($\epsilon_i = 0$). In this case, we have computed the ground state for $N = 60$ particles in $M = 60$ lattice sites with $U/J = 1$. The superfluid state is characterised by strong off-diagonal correlations, representative of the off-diagonal quasi-long range order found in this system. These off-diagonal correlations give rise to maxima and minima that are observed experimentally in interference patterns when atoms are released from the lattice [3]. In contrast, for the same calculation in the Mott Insulator regime (with

$U/J = 20$), which is shown in Fig. 8.2, we see that the off diagonal correlations decay rapidly (in fact exponentially) with the separation between lattice sites.

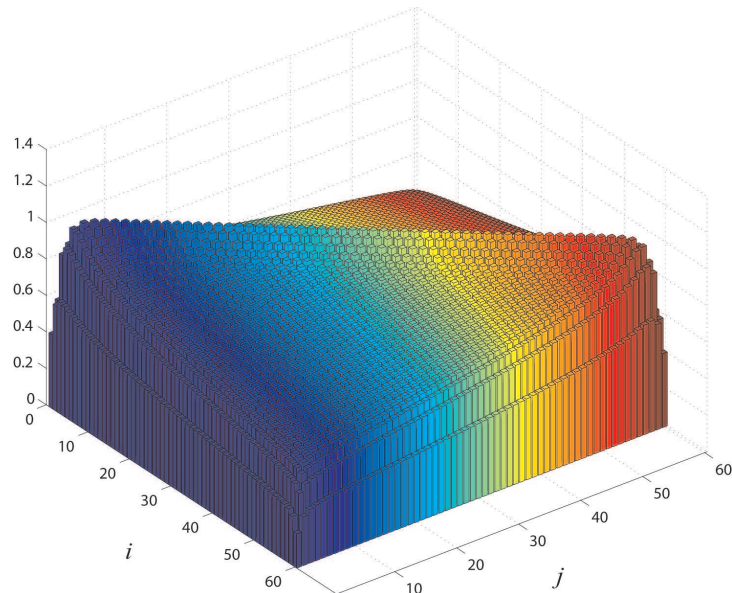


Figure 8.1. Single particle density matrix, $\langle \hat{b}_i^\dagger \hat{b}_j \rangle$, for the superfluid ground state of the 1D Bose-Hubbard model with $N = M = 60$, $U/J = 1$, $\epsilon_i = 0$.

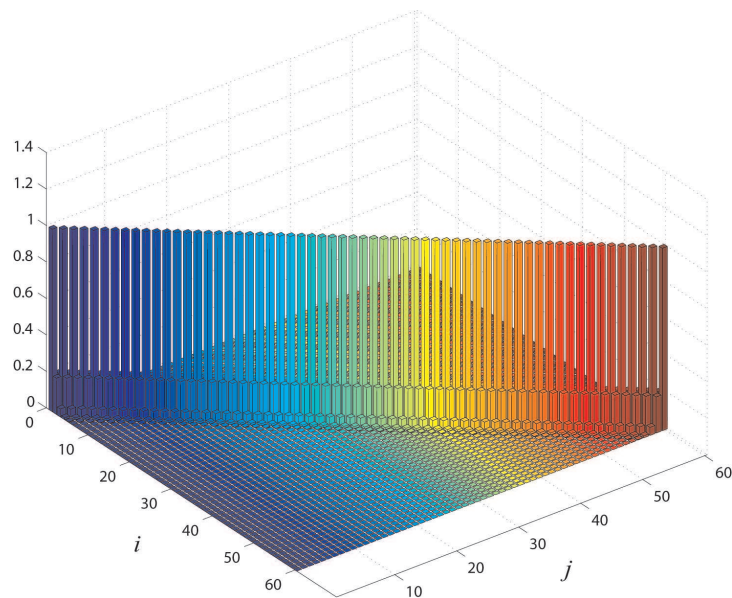


Figure 8.2. Single particle density matrix, $\langle \hat{b}_i^\dagger \hat{b}_j \rangle$, for the MI ground state of the 1D Bose-Hubbard model with $N = M = 60$, $U/J = 20$, $\epsilon_i = 0$.

8.3.2 Harmonic Trap

The ground states of the system in a Harmonic trap look considerably different, and depend strongly on the number of particles found in the system. In Figs. 8.3, 8.4, and 8.5, the single particle density matrix is shown for $N = 20$, $N = 35$, and $N = 50$ particles respectively, in a harmonic trap with $\epsilon_i/J = 0.1(i - i_0)^2$, and $U/J = 20$. For 20 particles, we observe a standard Mott Insulator state for the average filling factor $n = 1$, with correlations decaying exponentially as a function of the lattice site separation. In the outermost occupied sites we observe a small decrease in the number of atoms and a small increase in off-diagonal elements of the single particle density matrix, indicating that a small superfluid component exists at the very edge of the trapped gas. For 35 particles, this same behaviour is observed, except that there is now also a clear region in the middle of the trap with a superfluid component sitting on top of the Mott Insulator core. For 50 particles, we see clearly from Fig. 8.5 yet another step in this progression, with a Mott Insulator state with $n = 2$ in the centre of the trap, flanked by superfluid regions, then a Mott Insulator phase with $n = 1$, and finally a small superfluid region at the edge. This behaviour can be explained in terms of the Grand Canonical Ensemble phase diagram (Fig. 2.5) if we make a local density approximation, and approximate a local chemical potential $\mu_i \approx \mu - \epsilon_i$. We then see that as we move from the centre of the trap to the outside, the effective chemical potential decreases, and for a fixed J/U we pass through phases corresponding to different Mott lobes in the phase diagram, and to the superfluid regions in between.

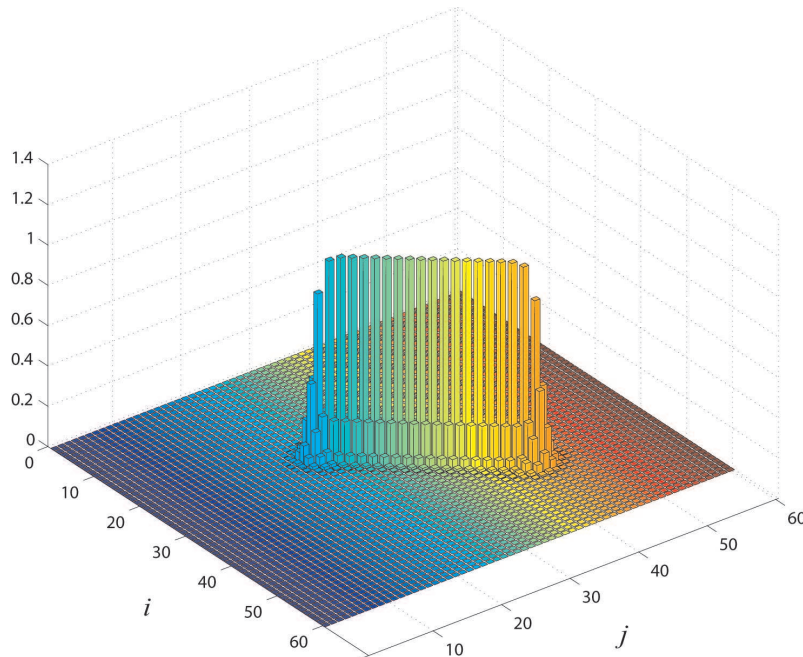


Figure 8.3. Single particle density matrix, $\langle \hat{b}_i^\dagger \hat{b}_j \rangle$, for the ground state of the 1D Bose-Hubbard model with $N = 20$ particles, $U/J = 20$, $\epsilon_i/J = 0.1(i - i_0)^2$.

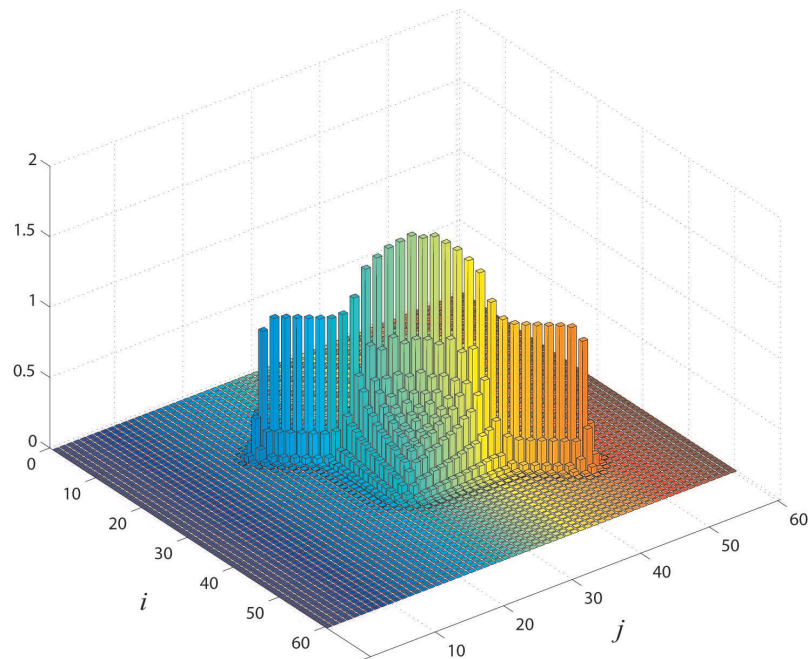


Figure 8.4. Single particle density matrix, $\langle \hat{b}_i^\dagger \hat{b}_j \rangle$, for the ground state of the 1D Bose-Hubbard model with $N = 35$ particles, $U/J = 20$, $\epsilon_i/J = 0.1(i - i_0)^2$.

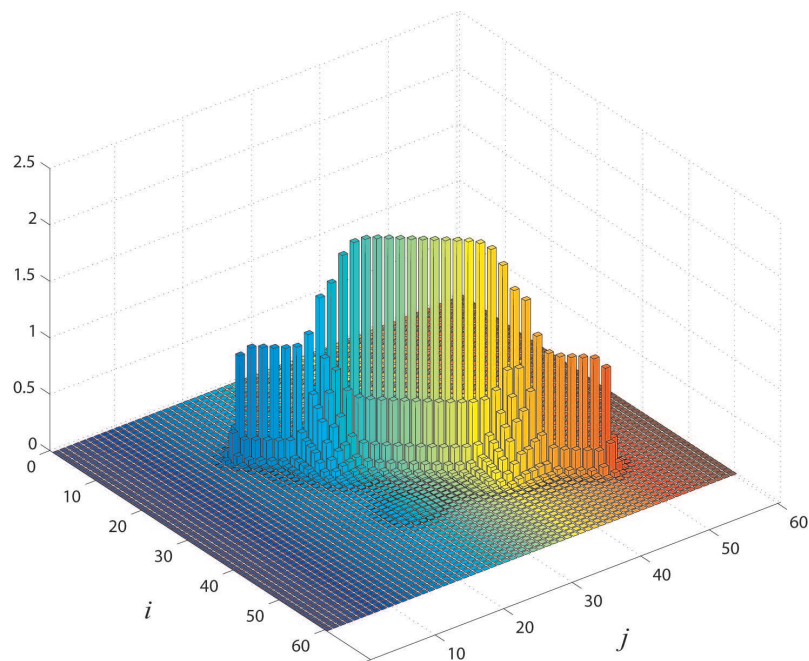


Figure 8.5. Single particle density matrix, $\langle \hat{b}_i^\dagger \hat{b}_j \rangle$, for the ground state of the 1D Bose-Hubbard model with $N = 50$ particles, $U/J = 20$, $\epsilon_i/J = 0.1(i - i_0)^2$.

8.4 Time Dependence of the MI-Superfluid Transition

The study of the properties of phase transitions for finite system is one of the more interesting possibilities presented by time-dependent many body calculations. Here we present an example from the Superfluid-Mott Insulator transition, the dynamics of which were analysed in some detail by Clark and Jaksch [4]. Here we present results of dynamical calculations in which we begin in the Mott Insulator ground state for $U/J = 10$ at $t = 0$, and ramp linearly in a time $t_R/2$ to $U/J = 1$, and then back to $U/J = 10$ at $t = t_R$. In Fig. 8.6 we present the time dependent overlap between the time evolving state $|\psi(t)\rangle$ and the initial Mott Insulator state $|\psi(0)\rangle$,

$$F(t) = |\langle\psi(0)|\psi(t)\rangle|^2. \quad (8.4)$$

This quantity is interesting because it gives the most stringent possible accuracy test both for the computed state and for whether the system returns to the initial state after passing the phase transition twice. From Fig. 8.6a we see that we obtain excellent agreement with the calculation for a small system, with $M = N = 6$, and observe that for slow sweeps we essentially return to the exactly the initial state. When we perform the calculation for $M = N = 20$, Fig. 8.6, we observe that much slower ramp speeds are required to return the state adiabatically to $|\psi(0)\rangle$ at $t = t_R$. This occurs because the energy separation of the ground state and lowest excited states decreases substantially as the system size is increased.

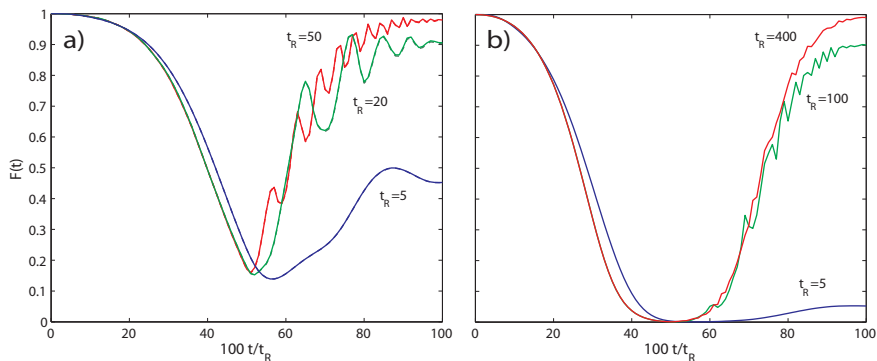


Figure 8.6. *Plots of $F(t) = |\langle\psi(0)|\psi(t)\rangle|^2$ as U/J is ramped across the MI-Superfluid transition with $U/J = 10 \rightarrow 1$ as a linear ramp in time $t_R/2$, and $U/J = 1 \rightarrow 10$ in time $t_R/2$. These results are for a Bose Hubbard model with $\epsilon_i = 0$, and (a) $M = N = 6$, (b) $M = N = 20$. The dashed lines in (a) are exact calculations using the full Hilbert space.*

Bibliography

- [1] U. Schollwöck, Rev. Mod. Phys., **77**, 259 (2005).
- [2] A. J. Daley, C. Kollath, U. Schollwöck, G. Vidal, J. Stat. Mech.: Theor. Exp. P04005 (2004); S.R. White and A.E. Feiguin, Phys. Rev. Lett. **93**, 076401 (2004).

-
- [3] M. Greiner, O. Mandel, T. W. Hänsch and I. Bloch *Nature* **415**, 39 (2002); M. Greiner, O. Mandel, T. Esslinger, T.W. Hänsch and I. Bloch, *Nature* **419** 51 (2002); V.A. Kashurnikov, N.V. Prokof'ev, B.V. Svistunov, cond-mat/0202510.
- [4] S.R. Clark and D. Jaksch, *Phys. Rev. A* **70**, 043612 (2004)

CHAPTER 9

PUBLICATION

Time-dependent density-matrix renormalization-group using adaptive effective Hilbert spaces[†]

J. Stat. Mech.: Theor. Exp. P04005 (2004)

A J Daley^{1,2}, C Kollath³, U. Schollwöck⁴, and G Vidal⁵

- 1) *Institute for Quantum Optics and Quantum Information of the Austrian Academy of Sciences, A-6020 Innsbruck, Austria*
- 2) *Institute for Theoretical Physics, University of Innsbruck, A-6020 Innsbruck, Austria*
- 3) *Department für Physik, Ludwig-Maximilians-Universität München, D-80333 Munich, Germany*
- 4) *Institut für Theoretische Physik C, RWTH Aachen, D-52056 Aachen, Germany*
- 5) *Institute for Quantum Information, California Institute of Technology, Pasadena, CA 91125, USA*

An algorithm for the simulation of the evolution of slightly entangled quantum states has been recently proposed as a tool to study time-dependent phenomena in one-dimensional quantum systems. Its key feature is a time-evolving block-decimation (TEBD) procedure to identify and dynamically update the relevant, conveniently small subregion of the otherwise exponentially large Hilbert space. Potential applications of the TEBD algorithm are the simulation of time-dependent Hamiltonians, transport in quantum systems far from equilibrium and dissipative quantum mechanics. In this paper we translate the TEBD algorithm into the language of matrix product states in order to both highlight and exploit its resemblances to the widely used density-matrix renormalization-group (DMRG) algorithms. The TEBD algorithm, being based on updating a matrix product state in time, is very accessible to the DMRG community and it can be enhanced by

[†]The primary contribution of the author of the present thesis to this work was the explicit expression of the TEBD algorithm in Matrix Product state notation (sections 9.3 and 9.4), which formed the basis of the implementation. The example calculations were carried out by other coauthors, with the author of the present thesis acting as a discussion partner.

using well-known DMRG techniques, for instance in the event of good quantum numbers. More importantly, we show how it can be simply incorporated into existing DMRG implementations to produce a remarkably effective and versatile “adaptive time-dependent DMRG” variant, that we also test and compare to previous proposals.

9.1 Introduction

Over many decades the description of the physical properties of low-dimensional strongly correlated quantum systems has been one of the major tasks in theoretical condensed matter physics. Generically, this task is complicated by the strong quantum fluctuations present in such systems which are usually modelled by minimal-model Hubbard or Heisenberg-style Hamiltonians. Despite the apparent simplicity of these Hamiltonians, few analytically exact solutions are available and most analytical approximations remain uncontrolled. Hence, numerical approaches have always been of particular interest, among them exact diagonalization and quantum Monte Carlo.

Decisive progress in the description of the low-energy equilibrium properties of one-dimensional strongly correlated quantum Hamiltonians was achieved by the invention of the density-matrix renormalization-group (DMRG) [1, 2]. It is concerned with the iterative decimation of the Hilbert space of a growing quantum system such that some quantum state, say the ground state, is approximated in that restricted space with a maximum of overlap with the true state. Let the quantum state of a one-dimensional system be

$$|\psi\rangle = \sum_i \sum_j \psi_{ij} |i\rangle |j\rangle, \quad (9.1)$$

where we consider a partition of the system into two blocks S and E, and where $\{|i\rangle\}$ and $\{|j\rangle\}$ are orthonormal bases of S and E respectively. Then the DMRG decimation procedure consists of projecting $|\psi\rangle$ on the Hilbert spaces for S and E spanned by the M eigenvectors $|w_\alpha^S\rangle$ and $|w_\alpha^E\rangle$ corresponding to the largest eigenvalues λ_α^2 of the reduced density matrices

$$\hat{\rho}_S = \text{Tr}_E |\psi\rangle \langle \psi| \quad \hat{\rho}_E = \text{Tr}_S |\psi\rangle \langle \psi|, \quad (9.2)$$

such that $\hat{\rho}_S |w_\alpha^S\rangle = \lambda_\alpha^2 |w_\alpha^S\rangle$ and $\hat{\rho}_E |w_\alpha^E\rangle = \lambda_\alpha^2 |w_\alpha^E\rangle$. That both density matrices have the same eigenvalue spectrum is reflected in the guaranteed existence of the so-called Schmidt decomposition of the wave function [3],

$$|\psi\rangle = \sum_\alpha \lambda_\alpha |w_\alpha^S\rangle |w_\alpha^E\rangle, \quad \lambda_\alpha \geq 0, \quad (9.3)$$

where the number of positive λ_α is bounded by the dimension of the smaller of the bases of S and E.

Recently [4–9], the ability of the DMRG decimation procedure to preserve the entanglement of $|\psi\rangle$ between S and E has been studied in the context of quantum information science [3, 10]. This blooming field of research, bridging between quantum physics, computer science and information theory, offers a novel conceptual framework for the study of quantum many-body systems [3–17]. New insights into old quantum many-body problems can be

gained from the perspective of quantum information science, mainly through its eagerness to characterize quantum correlations. As an example, a better understanding of the reasons of the breakdown of the DMRG in two-dimensional systems has been obtained in terms of the growth of bipartite entanglement in such systems [7, 9].

More specifically, in quantum information the entanglement of $|\psi\rangle$ between S and E is quantified by the von Neumann entropy of $\hat{\rho}_S$ (equivalently, of $\hat{\rho}_E$),

$$\mathcal{S}(\hat{\rho}_S) = - \sum \lambda_\alpha^2 \log_2 \lambda_\alpha^2, \quad (9.4)$$

a quantity that imposes a useful (information theoretical) bound $M \geq 2^{\mathcal{S}}$ on the minimal number M of states to be kept during the DMRG decimation process if the truncated state is to be similar to $|\psi\rangle$. On the other hand, arguments from field theory imply that, at zero temperature, strongly correlated quantum systems are in some sense only slightly entangled in $d = 1$ dimensions but significantly more entangled in $d > 1$ dimensions: In particular, in $d = 1$ a block corresponding to l sites of a gapped infinite-length chain has an entropy \mathcal{S}_l that stays finite even in the thermodynamical limit $l \rightarrow \infty$, while at criticality \mathcal{S}_l only grows logarithmically with l . It is this saturation or, at most, moderate growth of \mathcal{S}_l that ultimately accounts for the success of DMRG in $d = 1$. Instead, in the general d -dimensional case the entropy of bipartite entanglement for a block of linear dimension l scales as $\mathcal{S}_l \sim l^{d-1}$. Thus, in $d = 2$ dimensions the DMRG algorithm should keep a number M of states that grows exponentially with l , and the simulation becomes inefficient for large l (while still feasible for small l).

While DMRG has yielded an enormous wealth of information on the static and dynamic equilibrium properties of one-dimensional systems [18, 19] and is arguably the most powerful method in the field, only few attempts have been made so far to determine the time evolution of the states of such systems, notably in a seminal paper by Cazalilla and Marston [20]. This question is of relevance in the context of the time-dependent Hamiltonians realized e.g. in cold atoms in optical lattices [21, 22], in systems far from equilibrium in quantum transport, or in dissipative quantum mechanics. However, in another example of how quantum information science can contribute to the study of quantum many-body physics, one of us (G.V.) has recently developed an algorithm for the simulation of slightly entangled quantum computations [23] that can be used to simulate time evolutions of one-dimensional systems [17].

This new algorithm, henceforth referred to as the time-evolving block decimation (TEBD) algorithm, considers a small, dynamically updated subspace of the blocks S and E in Eq. (9.3) to efficiently represent the state of the system, as we will review in detail below. It was originally developed in order to show that a large amount of entanglement is necessary in quantum computations, the rationale there being quite simple: any *quantum* evolution (e.g. a quantum computation) involving only a “sufficiently restricted” amount of entanglement can be efficiently simulated in a *classical* computer using the TEBD algorithm; therefore, from an algorithmical point of view, any such quantum evolution is not more powerful than a classical computation.

Regardless of the implications for computer science, the above connection between the amount of entanglement and the complexity of simulating quantum systems is of obvious practical interest in condensed matter physics since, for instance, in $d = 1$ dimensions the

entanglement of most quantum systems happens to be “sufficiently restricted” precisely in the sense required for the TEBD algorithm to yield an efficient simulation. In particular, the algorithm has already been implemented and tested successfully on spin chains[17], the Bose-Hubbard model and single-atom transistors[24] and dissipative systems at finite temperature [25].

A primary aim of this paper is to reexpress the TEBD algorithm in a language more familiar to the DMRG community than the one originally used in Refs. [17, 23], which made substantial use of the quantum information parlance. This turns out to be a rewarding task since, as we show, the conceptual and formal similarities between the TEBD and DMRG are extensive. Both algorithms search for an approximation to the true wave function within a restricted class of wave functions, which can be identified as matrix product states [26], and had also been previously proposed under the name of finitely-correlated states[27]. Arguably, the big advantage of the TEBD algorithm relies on its flexibility to flow in time through the submanifold of matrix product states. Instead of considering time evolutions within some restricted subspace according to a fixed, projected, effective Hamiltonian, the TEBD algorithm updates a matrix product state in time using the bare Hamiltonian directly. Thus, in a sense, it is the Schrödinger equation that decides, at each time step, which are the relevant eigenvectors for S and E in Eq. (9.3), as opposed to having to select them from some relatively small, pre-selected subspace.

A second goal of this paper is to show how the two algorithms can be integrated. The TEBD algorithm can be improved by considering well-known DMRG techniques, such as the handling of good quantum numbers. But most importantly, we will describe how the TEBD simulation algorithm can be incorporated into preexisting, quite widely used DMRG implementations, the so-called finite-system algorithm[2] using White’s prediction algorithm[28]. The net result is an extremely powerful “adaptive time-dependent DMRG” algorithm, that we test and compare against previous proposals.

The outline of this paper is as follows: In Section 9.2, we discuss the problems currently encountered in applying DMRG to the calculation of explicitly time-dependent quantum states. Section 9.3 reviews the common language of matrix product states. We then express both the TEBD simulation algorithm (Sec. 9.4) and DMRG (Sec. 9.5) in this language, revealing where both methods coincide, where they differ and how they can be combined. In Section 9.6, we then formulate the modifications to introduce the TEBD algorithm into standard DMRG to obtain the adaptive time-dependent DMRG, and Section 9.7 discusses an example application, concerning the quantum phase transition between a superfluid and a Mott-insulating state in a Bose-Hubbard model. To conclude, we discuss in Section 9.8 the potential of the new DMRG variant.

9.2 Simulation of time-dependent quantum phenomena using DMRG

The first attempt to simulate the time evolution of quantum states using DMRG is due to Cazalilla and Marston [20]. After applying a standard DMRG calculation using the Hamiltonian $\hat{H}(t = 0)$ to obtain the ground state of the system at $t = 0$, $|\psi_0\rangle$, the time-

dependent Schrödinger equation is numerically integrated forward in time, building an effective $\hat{H}_{\text{eff}}(t) = \hat{H}_{\text{eff}}(0) + \hat{V}_{\text{eff}}(t)$, where $\hat{H}_{\text{eff}}(0)$ is taken as the Hamiltonian approximating $\hat{H}(0)$ in the truncated Hilbert space generated by DMRG. $\hat{V}_{\text{eff}}(t)$ as an approximation to $\hat{V}(t)$ is built using the representations of operators in the block bases obtained in the standard DMRG calculation of the $t = 0$ state. $\hat{V}(t)$ contains the changes in the Hamiltonian with respect to the starting Hamiltonian: $\hat{H}(t) = \hat{H}_0 + \hat{V}(t)$. The (effective) time-dependent Schrödinger equation reads

$$i \frac{\partial}{\partial t} |\psi(t)\rangle = [\hat{H}_{\text{eff}} - E_0 + \hat{V}_{\text{eff}}(t)] |\psi(t)\rangle, \quad (9.5)$$

where the time-dependence of the ground state resulting of $\hat{H}(0)$ has been transformed away. If the evolution of the ground state is looked for, the initial condition is obviously to take $|\psi(0)\rangle = |\psi_0\rangle$ obtained by the preliminary DMRG run. Forward integration can be carried out by step-size adaptive methods such as the Runge-Kutta integration based on the infinitesimal time evolution operator

$$|\psi(t + \delta t)\rangle = (1 - i\hat{H}(t)\delta t) |\psi(t)\rangle, \quad (9.6)$$

where we drop the subscript denoting that we are dealing with effective Hamiltonians only. The algorithm used was a fourth-order adaptive size Runge-Kutta algorithm [29].

Sources of errors in this approach are twofold, due to the approximations involved in numerically carrying out the time evolution, and to the fact that all operators live on a truncated Hilbert space.

For the systems studied we have obtained a conceptually simple improvement concerning the time evolution by replacing the explicitly non-unitary time-evolution of Eq. (9.6) by the unitary Crank-Nicholson time evolution

$$|\psi(t + \delta t)\rangle = \frac{1 - i\hat{H}(t)\delta t/2}{1 + i\hat{H}(t)\delta t/2} |\psi(t)\rangle. \quad (9.7)$$

To implement the Crank-Nicholson time evolution efficiently we have used a (non-Hermitian) biconjugate gradient method to calculate the denominator of Eq. (9.7). In fact, this modification ensures higher precision of correlators, and the occurrence of asymmetries with respect to reflection in the results decreased.

It should be noted, however, that for the Crank-Nicholson approach only lowest-order expansions of the time evolution operator $\exp(-i\hat{H}\delta t)$ have been taken; we have not pursued feasible higher-order expansions.

As a testbed for time-dependent DMRG methods we use throughout this paper the time-dependent Bose-Hubbard Hamiltonian,

$$\hat{H}_{BH}(t) = -J \sum_{i=1}^{L-1} b_{i+1}^\dagger b_i + b_i^\dagger b_{i+1} + \frac{U(t)}{2} \sum_{i=1}^L n_i(n_i - 1), \quad (9.8)$$

where the (repulsive) onsite interaction $U > 0$ is taken to be time-dependent. This model exhibits for commensurate filling a Kosterlitz-Thouless-like quantum phase transition from a superfluid phase for $u < u_c$ (with $u = U/J$) to a Mott-insulating phase for $u > u_c$. We

have studied a Bose-Hubbard model with $L = 8$ and open boundary conditions, total particle number $N = 8$, $J = 1$, and instantaneous switching from $U_1 = 2$ in the superfluid phase to $U_2 = 40$ in the Mott phase at $t = 0$. We consider the nearest-neighbor correlation, a robust numerical quantity, between sites 2 and 3. Up to 8 bosons per site (i.e. $N_{\text{site}} = 9$ states per site) were allowed to avoid cut-off effects in the bosonic occupation number in all calculations in this Section. All times in this paper are measured in units of \hbar/J or $1/J$, setting $\hbar \equiv 1$. Comparing Runge-Kutta and Crank-Nicholson (with time steps of $\delta t = 5 \times 10^{-5}$) we found the latter to be numerically preferable; all static time-dependent DMRG calculations have been carried out using the latter approach.

However, Hilbert space truncation is at the origin of more severe approximations. The key assumption underlying the approach of Cazalilla and Marston is that the effective static Hilbert space created in the preliminary DMRG run is sufficiently large that $|\psi(t)\rangle$ can be well approximated within that Hilbert space for all times, such that

$$\epsilon(t) = 1 - |\langle \psi(t) | \psi_{\text{exact}}(t) \rangle| \quad (9.9)$$

remains small as t grows. This, in general, will only be true for relatively short times. A variety of modifications that should extend the reach of the static Hilbert space in time can be imagined. They typically rest on the DMRG practice of “targeting” several states: to construct the reduced density matrix used to determine the relevant Hilbert space states, one may carry out a partial trace over a mixture of a small number of states such that the truncated Hilbert space is constructed so that all of those states are optimally approximated in the DMRG sense:

$$\hat{\rho}_S = \text{Tr}_E |\psi\rangle\langle\psi| \rightarrow \hat{\rho}_S = \text{Tr}_E \sum_i \alpha_i |\psi_i\rangle\langle\psi_i|. \quad (9.10)$$

A simple choice uses the targeting of $\hat{H}^n |\psi_0\rangle$, for n less than 10 or so, approximating the short-time evolution, which we have found to substantially improve the quality of results for non-adiabatic switching of Hamiltonian parameters in time: convergence in M is faster and more consistent with the new DMRG method (see below).

Similarly, we have found that for adiabatic changes of Hamiltonian parameters results improve if one targets the ground states of both the initial and final Hamiltonian. These approaches are conceptually very similar to targeting not only $|\psi_0\rangle$, but also $\hat{O}|\psi_0\rangle$ and some $\hat{H}^n \hat{O}|\psi_0\rangle$, $n = 1, 2, 3, \dots$ in Lanczos vector dynamics DMRG[30, 31], or real and imaginary part of $(\hat{H} - \omega - E_0 + i\eta)^{-1} \hat{O}|\psi_0\rangle$ in correction vector dynamics DMRG[31, 32] to calculate Green’s functions

$$\langle \psi_0 | \hat{O}^\dagger \frac{1}{H - \omega - E_0 + i\eta} \hat{O} | \psi_0 \rangle. \quad (9.11)$$

To illustrate the previous approaches, we show results for the parameters of the Bose-Hubbard model discussed above. Time evolution is calculated in the Crank-Nicholson approach using a stepwidth $\delta t = 5 \cdot 10^{-5}$ in time units of \hbar/J targeting (i) just the superfluid ground state $|\psi_0\rangle$ for $U_1 = 2$ (Fig. 9.1), (ii) in addition to (i) also the Mott-insulating ground state $|\psi'_0\rangle$ for $U_2 = 40$ and $\hat{H}(t > 0)|\psi_0\rangle$ (Fig. 9.2), (iii) in addition to (i) and (ii) also $\hat{H}(t > 0)^2|\psi_0\rangle$ and $\hat{H}(t > 0)^3|\psi_0\rangle$ (Fig. 9.3).

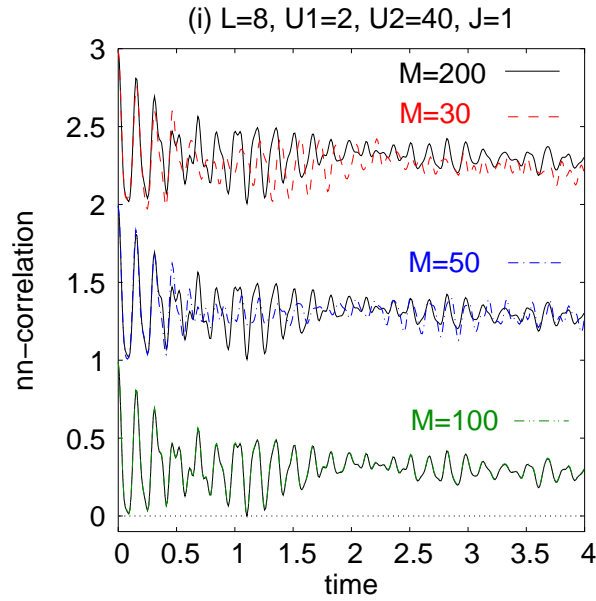


Figure 9.1. *Time evolution of the real part of the nearest-neighbor correlations in a Bose-Hubard model with instantaneous change of interaction strength at $t = 0$: superfluid state targeting only. The different curves for different M are shifted.*

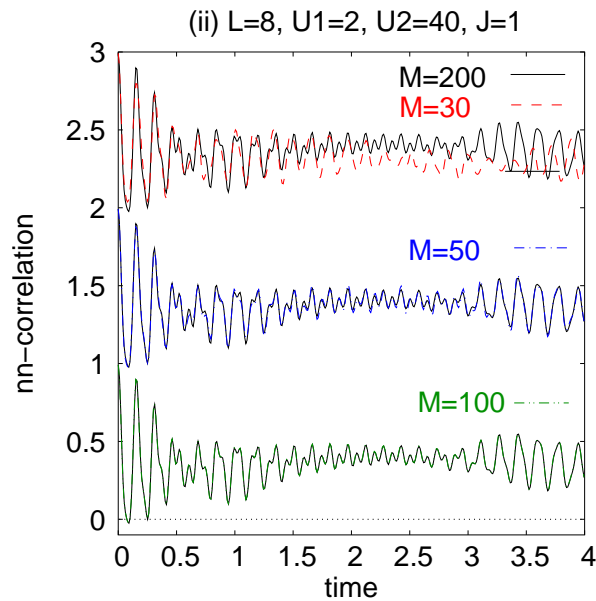


Figure 9.2. *Time evolution of the real part of the nearest-neighbor correlations in a Bose-Hubard model with instantaneous change of interaction strength at $t = 0$: targeting of the initial superfluid ground state, Mott insulating ground state and one time-evolution step. The different curves for different M are shifted.*

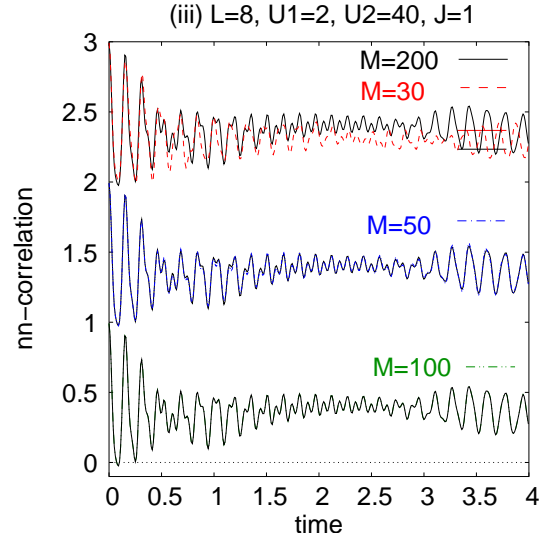


Figure 9.3. Time evolution of the real part of the nearest-neighbor correlations in a Bose-Hubbard model with instantaneous change of interaction strength at $t = 0$: targeting of the initial superfluid ground state, Mott insulating ground state and three time-evolution steps. The different curves for different M are shifted.

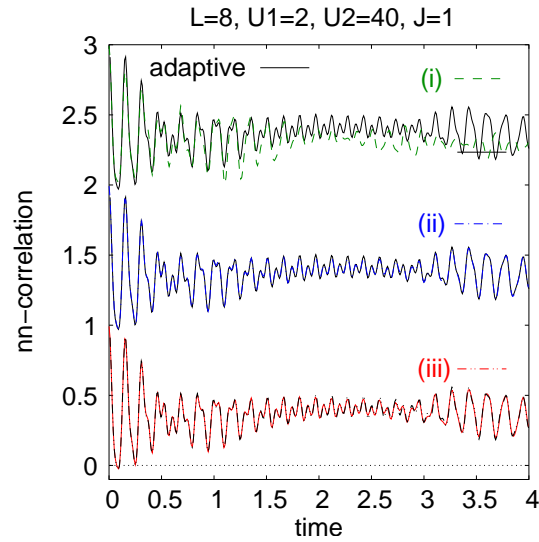


Figure 9.4. Comparison of the three $M = 200$ Crank-Nicholson calculations to adaptive time-dependent DMRG at $M = 50$: we target (i) just the superfluid ground state $|\psi_0\rangle$ for $U_1 = 2$ (Fig. 9.1), (ii) in addition to (i) also the Mott-insulating ground state $|\psi'_0\rangle$ for $U_2 = 40$ and $\hat{H}(t > 0)|\psi_0\rangle$ (Fig. 9.2), (iii) in addition to (i) and (ii) also $\hat{H}(t > 0)^2|\psi_0\rangle$ and $\hat{H}(t > 0)^3|\psi_0\rangle$. The different curves are shifted.

We have used up to $M = 200$ states to obtain converged results (meaning that we could observe no difference between the results for $M = 100$ and $M = 200$) for $t \leq 4$, corresponding to roughly 25 oscillations. The results for the cases (ii) and (iii) are almost converged for $M = 50$, whereas (i) shows still crude deviations.

A remarkable observation can be made if one compares the three $M = 200$ curves (Fig. 9.4), which by standard DMRG procedure (and for lack of a better criterion) would be considered the final, converged outcome, both amongst each other or to the result of the new adaptive time-dependent DMRG algorithm which we are going to discuss below: result (i) is clearly *not* quantitatively correct beyond very short times, whereas result (ii) agrees very well with the new algorithm, and result (iii) agrees almost (beside some small deviations at $t \approx 3$) with result (ii) and the new algorithm. Therefore we see that for case (i) the criterion of convergence in M does not give a good control to determine if the obtained results are correct. This raises as well doubts about the reliability of this criterion for cases (ii) and (iii).

A more elaborate, but also much more time-consuming improvement still within the framework of a static Hilbert space was proposed by Luo, Xiang and Wang [33, 34]. Additional to the ground state they target a finite number of quantum states at various discrete times using a bootstrap procedure starting from the time evolution of smaller systems that are iteratively grown to the desired final size.

The observation that even relatively robust numerical quantities such as nearest-neighbor correlations can be qualitatively and quantitatively improved by the additional targeting of states which merely share some fundamental characteristics with the true quantum state (as we will never reach the Mott-insulating ground state) or characterize only the very short-term time evolution indicates that it would be highly desirable to have a modified DMRG algorithm which, for each time t , selects Hilbert spaces of dimension M such that $|\psi(t)\rangle$ is represented optimally in the DMRG sense, thus attaining at *all* times the typical DMRG precision for M retained states. The presentation of such an algorithm is the purpose of the following sections.

9.3 Matrix product states

As both the TEBD simulation algorithm and DMRG can be neatly expressed in the language of matrix product states, let us briefly review the properties of these states also known as finitely-correlated states [26, 27].

We begin by considering a one-dimensional system of size L , divided up into sites which each have a local Hilbert space, \mathcal{H}_i . For simplicity we take the same dimension N_{site} at all sites. In such a system a product state may be expressed as

$$|\sigma\rangle = |\sigma_1\rangle \otimes |\sigma_2\rangle \otimes \dots \otimes |\sigma_L\rangle, \quad (9.12)$$

where $|\sigma_i\rangle$ denotes the local state on site i . We can express a general state of the whole system as

$$\begin{aligned} |\psi\rangle &= \sum_{\sigma_1, \dots, \sigma_L} \psi_{\sigma_1, \dots, \sigma_L} |\sigma_1\rangle \otimes |\sigma_2\rangle \otimes \dots \otimes |\sigma_L\rangle \\ &\equiv \sum_{\sigma} \psi_{\sigma} |\sigma\rangle. \end{aligned} \quad (9.13)$$

This general state exists in the Hilbert space $\mathcal{H} = \prod_{i=1}^L \mathcal{H}_i$, with dimension $(N_{\text{site}})^L$.

A matrix product state is now formed by only using a specific set of expansion coefficients $\psi_{\boldsymbol{\sigma}}$. Let us construct this set in the following. To do this we define operators $\hat{A}_i[\sigma_i]$ which correspond to a local basis state $|\sigma_i\rangle$ at site i of the original system, but which act on auxiliary spaces of dimension M , i.e.,

$$\hat{A}_i[\sigma_i] = \sum_{\alpha, \beta} A_{\alpha\beta}^i[\sigma_i] |\alpha\rangle \langle \beta|, \quad (9.14)$$

where $|\alpha\rangle$ and $|\beta\rangle$ are orthonormal basis states in auxiliary spaces. For visualization, we imagine the auxiliary state spaces to be located on the bonds next to site i . If we label the bond linking sites i and $i+1$ by i , then we say that the states $|\beta\rangle$ live on bond i and the states $|\alpha\rangle$ on bond $i-1$. The operators $\hat{A}_i[\sigma_i]$ hence act as transfer operators past site i depending on the local state on site i . On the first and last site, which will need special attention later, this picture involves bonds 0 and L to the left of site 1 and to the right of site L respectively. While these bonds have no physical meaning for open boundary conditions, they are identical and link sites 1 and L as one physical bond for periodic boundary conditions. There is no a priori significance to be attached to the states in the auxiliary state spaces.

In general, operators corresponding to different sites can be different. If this is the case the resulting matrix product state to be introduced is referred to as a position dependent matrix product state. We also impose the condition

$$\sum_{\sigma_i} \hat{A}_i[\sigma_i] \hat{A}_i^\dagger[\sigma_i] = \mathcal{I}, \quad (9.15)$$

which we will see to be related to orthonormality properties of bases later. An unnormalized matrix product state in a form that will be found useful for Hamiltonians with open boundary conditions is now defined as

$$|\tilde{\psi}\rangle = \sum_{\boldsymbol{\sigma}} \left(\langle \phi_L | \prod_{i=1}^L \hat{A}_i[\sigma_i] | \phi_R \rangle \right) |\boldsymbol{\sigma}\rangle, \quad (9.16)$$

where $|\phi_L\rangle$ and $|\phi_R\rangle$ are the left and right boundary states in the auxiliary spaces on bonds 0 and L . They act on the product of the operators \hat{A}_i to produce scalar coefficients

$$\psi_{\boldsymbol{\sigma}} = \langle \phi_L | \prod_{i=1}^L \hat{A}_i[\sigma_i] | \phi_R \rangle \quad (9.17)$$

for the expansion of $|\tilde{\psi}\rangle$.

Several remarks are in order. It should be emphasized that the set of states obeying Eq. (9.16) is an (arbitrarily constructed) submanifold of the full boundary-condition independent Hilbert space of the quantum many-body problem on L sites that is hoped to yield good approximations to the true quantum states for Hamiltonians with open boundary conditions. If the dimension M of the auxiliary spaces is made sufficiently large then any general state of the system can, in principle, be represented exactly in this form (provided that $|\phi_L\rangle$ and $|\phi_R\rangle$ are chosen appropriately), simply because the $O(N_{\text{site}} L M^2)$ degrees of freedom to choose the expansion coefficients will exceed N_{site}^L . This is, of course, purely academic. The practical

relevance of the matrix product states even for computationally manageable values of M is shown by the success of DMRG, which is known [35, 36] to produce matrix product states of auxiliary state space dimension M , in determining energies and correlators at very high precision for moderate values of M . In fact, some very important quantum states in one dimension, such as the valence-bond-solid (VBS) ground state of the Affleck-Kennedy-Lieb-Tasaki (AKLT) model [37–39], can be described exactly by matrix product states using very small M ($M = 2$ for the AKLT model).

Let us now formulate a Schmidt decomposition for matrix product states which can be done very easily. An unnormalized state $|\tilde{\psi}\rangle$ of the matrix-product form of Eq. (9.16) with auxiliary space dimension M can be written as

$$|\tilde{\psi}\rangle = \sum_{\alpha=1}^M |\tilde{w}_\alpha^S\rangle |\tilde{w}_\alpha^E\rangle, \quad (9.18)$$

where we have arbitrarily cut the chain into S on the left and E on the right with

$$|\tilde{w}_\alpha^S\rangle = \sum_{\{\sigma^S\}} \left[\langle \phi_L | \prod_{i \in S} \hat{A}_i[\sigma_i] | \alpha \rangle \right] |\sigma^S\rangle, \quad (9.19)$$

and similarly $|\tilde{w}_\alpha^E\rangle$, where $\{|\alpha\rangle\}$ are the states spanning the auxiliary state space on the cut bond. Normalizing the states $|\tilde{\psi}\rangle$, $|\tilde{w}_\alpha^S\rangle$ and $|\tilde{w}_\alpha^E\rangle$ we obtain the representation

$$|\psi\rangle = \sum_{\alpha=1}^M \lambda_\alpha |w_\alpha^S\rangle |w_\alpha^E\rangle \quad (9.20)$$

where in λ_α the factors resulting from the normalization are absorbed. The relationship to reduced density matrices is as detailed in Sec. 9.1.

9.4 TEBD Simulation Algorithm

Let us now express the TEBD simulation algorithm in the language of the previous section. In the original exposition of the algorithm [23], one starts from a representation of a quantum state where the coefficients for the states are decomposed as a product of tensors,

$$\psi_{\sigma_1, \dots, \sigma_L} = \sum_{\alpha_1, \dots, \alpha_{L-1}} \Gamma_{\alpha_1}^{[1]\sigma_1} \lambda_{\alpha_1}^{[1]} \Gamma_{\alpha_1 \alpha_2}^{[2]\sigma_2} \lambda_{\alpha_2}^{[2]} \Gamma_{\alpha_2 \alpha_3}^{[3]\sigma_3} \dots \Gamma_{\alpha_{L-1}}^{[L]\sigma_L}. \quad (9.21)$$

It is of no immediate concern to us how the Γ and λ tensors are constructed explicitly for a given physical situation. Let us assume that they have been determined such that they approximate the true wave function close to the optimum obtainable within the class of wave functions having such coefficients; this is indeed possible as will be discussed below. There are, in fact, two ways of doing it, within the framework of DMRG (see below), or by a continuous imaginary time evolution from some simple product state, as discussed in Ref. [17].

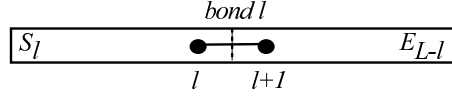


Figure 9.5. *Bipartitioning by cutting bond l between sites l and $l + 1$.*

Let us once again attempt a visualization; the (diagonal) tensors $\lambda^{[i]}$, $i = 1, \dots, L - 1$ are associated with the bonds i , whereas $\Gamma^{[i]}$, $i = 2, \dots, L - 1$ links (transfers) from bond i to bond $i - 1$ across site i . Note that at the boundaries ($i = 1, L$) the structure of the Γ is different, a point of importance in the following. The sums run over M states $|\alpha_i\rangle$ living in auxiliary state spaces on bond i . A priori, these states have no physical meaning here.

The Γ and λ tensors are constructed such that for an arbitrary cut of the system into a part S_l of length l and a part E_{L-l} of length $L - l$ at bond l , the Schmidt decomposition for this bipartite splitting reads

$$|\psi\rangle = \sum_{\alpha_l} \lambda_{\alpha_l}^{[l]} |w_{\alpha_l}^{S_l}\rangle |w_{\alpha_l}^{E_{L-l}}\rangle, \quad (9.22)$$

with

$$|w_{\alpha_l}^{S_l}\rangle = \sum_{\alpha_1, \dots, \alpha_{l-1}} \sum_{\sigma_1, \dots, \sigma_l} \Gamma_{\alpha_1}^{[1]\sigma_1} \lambda_{\alpha_1}^{[1]} \dots \Gamma_{\alpha_{l-1}\alpha_l}^{[l]\sigma_l} |\sigma_1\rangle \otimes \dots \otimes |\sigma_l\rangle, \quad (9.23)$$

and

$$|w_{\alpha_l}^{E_{L-l}}\rangle = \sum_{\alpha_l, \dots, \alpha_{L-1}} \sum_{\sigma_{l+1}, \dots, \sigma_L} \Gamma_{\alpha_l\alpha_{l+1}}^{[l+1]\sigma_{l+1}} \lambda_{\alpha_{l+1}}^{[l+1]} \dots \Gamma_{\alpha_{L-1}}^{[L]\sigma_L} |\sigma_{l+1}\rangle \otimes \dots \otimes |\sigma_L\rangle, \quad (9.24)$$

where $|\psi\rangle$ is normalized and the sets of $\{|w_{\alpha_l}^{S_l}\rangle\}$ and $\{|w_{\alpha_l}^{E_{L-l}}\rangle\}$ are orthonormal. This implies, for example, that

$$\sum_{\alpha_l} (\lambda_{\alpha_l}^{[l]})^2 = 1. \quad (9.25)$$

We can see that (leaving aside normalization considerations for the moment) this representation may be expressed as a matrix product state if we choose for $\hat{A}_i[\sigma_i] = \sum_{\alpha, \beta} A_{\alpha\beta}^i[\sigma_i] |\alpha\rangle \langle \beta|$

$$A_{\alpha\beta}^i[\sigma_i] = \Gamma_{\alpha\beta}^{[i]\sigma_i} \lambda_{\beta}^{[i]}, \quad (9.26)$$

except for $i = 1$, where we choose

$$A_{\alpha\beta}^1[\sigma_1] = f_{\alpha} \Gamma_{\beta}^{[1]\sigma_1} \lambda_{\beta}^{[1]}, \quad (9.27)$$

and for $i = L$, where we choose

$$A_{\alpha\beta}^L[\sigma_L] = \Gamma_{\alpha}^{[L]\sigma_L} g_{\beta}. \quad (9.28)$$

The vectors f_{α} and g_{β} are normalised vectors which must be chosen in conjunction with the boundary states $|\phi_L\rangle$ and $|\phi_R\rangle$ so as to produce the expansion (9.21) from this choice of the \hat{A}_i . Specifically, we require

$$|\phi_L\rangle = \sum_{\alpha} f_{\alpha} |\alpha\rangle \quad (9.29)$$

$$|\phi_R\rangle = \sum_{\beta} g_{\beta}^* |\beta\rangle, \quad (9.30)$$

where $|\alpha\rangle$ and $|\beta\rangle$ are the states forming the same orthonormal basis in the auxiliary spaces on bonds 0 and L used to express $A_{\alpha\beta}^i$. In typical implementations of the algorithm it is common to take $f_\alpha = g_\alpha = \delta_{\alpha,1}$. Throughout the rest of the article we take this as the definition for g_α and f_α , as this allows us to treat the operators on the boundary identically to the other operators for the purposes of the simulation protocol. For the same reason we define a vector $\lambda_\alpha^{[0]} = \delta_{\alpha,1}$.

In the above expression we have grouped Γ and λ such that the λ reside on the *right* of the two bonds linked by Γ . There is another valid choice for the \hat{A}_i , which will produce identical states in the original system, and essentially the same procedure for the algorithm. If we set

$$\tilde{A}_{\alpha\beta}^i[\sigma_i] = \lambda_\alpha^{[i-1]} \Gamma_{\alpha\beta}^{[i]\sigma_i}, \quad (9.31)$$

except for $i = 1$, where we choose

$$\tilde{A}_{\alpha\beta}^1[\sigma_1] = f_\alpha \Gamma_\beta^{[1]\sigma_1}, \quad (9.32)$$

and for $i = L$, where we choose

$$\tilde{A}_{\alpha\beta}^L[\sigma_L] = \lambda_\alpha^{[L-1]} \Gamma_\alpha^{[L]\sigma_L} g_\beta, \quad (9.33)$$

then the same choice of boundary states produces the correct coefficients. Here we have grouped Γ and λ such that the λ reside on the *left* of the two bonds linked by Γ . It is also important to note that any valid choice of f_α and g_β that produces the expansion (9.21) specifically *excludes* the use of periodic boundary conditions. While generalizations are feasible, they lead to a much more complicated formulation of the TEBD simulation algorithm and will not be pursued here.

To conclude the identification of states, let us consider normalization issues. The condition (9.15) is indeed fulfilled for our choice of $A_i[\sigma_i]$, because we have from (9.24) for a splitting at l that

$$\begin{aligned} |w_{\alpha_{l-1}}^{E_{L-(l-1)}}\rangle &= \sum_{\alpha_l \sigma_l} \Gamma_{\alpha_{l-1} \alpha_l}^{[l]\sigma_l} \lambda_{\alpha_l}^{[l]} |\sigma_l\rangle \otimes |w_{\alpha_l}^{E_{L-l}}\rangle \\ &= \sum_{\alpha_l \sigma_l} A_{\alpha_{l-1} \alpha_l}^l[\sigma_l] |\sigma_l\rangle \otimes |w_{\alpha_l}^{E_{L-l}}\rangle, \end{aligned} \quad (9.34)$$

so that from the orthonormality of the sets of states $\{|w_\alpha^{E_{L-(l-1)}}\}_{\alpha=1}^M$, $\{|\sigma_l\rangle\}_{\sigma_l=1}^{N_{\text{site}}}$ and $\{|w_\gamma^{E_{L-l}}\}_{\gamma=1}^M$,

$$\begin{aligned} \sum_{\sigma_l} \hat{A}_l[\sigma_l] \hat{A}_l^\dagger[\sigma_l] &= \sum_{\alpha\beta\gamma} \sum_{\sigma_l} A_{\alpha\gamma}^l[\sigma_l] (A_{\beta\gamma}^l[\sigma_l])^* |\alpha\rangle \langle \beta| \\ &= \sum_{\alpha\beta} \langle w_\beta^{E_{L-(l-1)}} | w_\alpha^{E_{L-(l-1)}} \rangle |\alpha\rangle \langle \beta| \\ &= \sum_{\alpha\beta} \delta_{\alpha\beta} |\alpha\rangle \langle \beta| = \mathcal{I}. \end{aligned} \quad (9.35)$$

Let us now consider the time evolution for a typical (possibly time-dependent) Hamiltonian in strongly correlated systems that contains only short-ranged interactions, for simplicity only

nearest-neighbor interactions here:

$$\hat{H} = \sum_{i \text{ odd}} \hat{F}_{i,i+1} + \sum_{j \text{ even}} \hat{G}_{j,j+1}, \quad (9.36)$$

$F_{i,i+1}$ and $G_{j,j+1}$ are the local Hamiltonians on the odd bonds linking i and $i+1$, and the even bonds linking j and $j+1$. While all F and G terms commute among each other, F and G terms do in general not commute if they share one site. Then the time evolution operator may be approximately represented by a (first order) Trotter expansion as

$$e^{-i\hat{H}\delta t} = \prod_{i \text{ odd}} e^{-i\hat{F}_{i,i+1}\delta t} \prod_{j \text{ even}} e^{-i\hat{G}_{j,j+1}\delta t} + \mathcal{O}(\delta t^2), \quad (9.37)$$

and the time evolution of the state can be computed by repeated application of the two-site time evolution operators $\exp(-i\hat{G}_{j,j+1}\delta t)$ and $\exp(-i\hat{F}_{i,i+1}\delta t)$. This is a well-known procedure in particular in Quantum Monte Carlo[40] where it serves to carry out imaginary time evolutions (checkerboard decomposition).

The TEBD simulation algorithm now runs as follows[17, 23]:

1. Perform the following two steps for all even bonds (order does not matter):
 - (i) Apply $\exp(-i\hat{G}_{l,l+1}\delta t)$ to $|\psi(t)\rangle$. For each local time update, a new wave function is obtained. The number of degrees of freedom on the ‘‘active’’ bond thereby increases, as will be detailed below.
 - (ii) Carry out a Schmidt decomposition cutting this bond and retain as in DMRG only those M degrees of freedom with the highest weight in the decomposition.
2. Repeat this two-step procedure for all *odd* bonds, applying $\exp(-i\hat{F}_{l,l+1}\delta t)$.
3. This completes one Trotter time step. One may now evaluate expectation values at selected time steps, and continues the algorithm from step 1.

Let us now consider the computational details.

(i) Consider a local time evolution operator acting on bond l , i.e. sites l and $l+1$, for a state $|\psi\rangle$. The Schmidt decomposition of $|\psi\rangle$ after partitioning by cutting bond l reads

$$|\psi\rangle = \sum_{\alpha_l=1}^M \lambda_{\alpha_l}^{[l]} |w_{\alpha_l}^S\rangle |w_{\alpha_l}^{E_{L-l}}\rangle. \quad (9.38)$$

Using Eqs. (9.23), (9.24) and (9.34), we find

$$|\psi\rangle = \sum_{\alpha_{l-1}\alpha_l\alpha_{l+1}} \sum_{\sigma_l\sigma_{l+1}} \lambda_{\alpha_{l-1}}^{[l-1]} A_{\alpha_{l-1}\alpha_l}^l[\sigma_l] A_{\alpha_l\alpha_{l+1}}^{l+1}[\sigma_{l+1}] |w_{\alpha_{l-1}}^{S_{l-1}}\rangle |\sigma_l\rangle |\sigma_{l+1}\rangle |w_{\alpha_{l+1}}^{E_{L-(l+1)}}\rangle. \quad (9.39)$$

We note, that if we identify $|w_{\alpha_{l-1}}^{S_{l-1}}\rangle$ and $|w_{\alpha_{l+1}}^{E_{L-(l+1)}}\rangle$ with DMRG system and environment block states $|w_{m_{l-1}}^S\rangle$ and $|w_{m_{l+1}}^E\rangle$, we have a typical DMRG state for two blocks and two sites

$$|\psi\rangle = \sum_{m_{l-1}} \sum_{\sigma_l} \sum_{\sigma_{l+1}} \sum_{m_{l+1}} \psi_{m_{l-1}\sigma_l\sigma_{l+1}m_{l+1}} |w_{m_{l-1}}^S\rangle |\sigma_l\rangle |\sigma_{l+1}\rangle |w_{m_{l+1}}^E\rangle \quad (9.40)$$

with

$$\psi_{m_{l-1}\sigma_l\sigma_{l+1}m_{l+1}} = \sum_{\alpha_l} \lambda_{m_{l-1}}^{[l-1]} A_{m_{l-1}\alpha_l}^l [\sigma_l] A_{\alpha_l m_{l+1}}^{l+1} [\sigma_{l+1}]. \quad (9.41)$$

The local time evolution operator on site $l, l+1$ can be expanded as

$$\hat{U}_{l,l+1} = \sum_{\sigma_l\sigma_{l+1}} \sum_{\sigma'_l\sigma'_{l+1}} U_{\sigma_l\sigma_{l+1}}^{\sigma'_l\sigma'_{l+1}} |\sigma'_l\sigma'_{l+1}\rangle \langle \sigma_l\sigma_{l+1}| \quad (9.42)$$

and generates $|\psi'\rangle = \hat{U}_{l,l+1}|\psi\rangle$, where

$$\begin{aligned} |\psi'\rangle &= \sum_{\alpha_{l-1}\alpha_l\alpha_{l+1}} \sum_{\sigma_l\sigma_{l+1}} \sum_{\sigma'_l\sigma'_{l+1}} \\ &\lambda_{\alpha_{l-1}}^{[l-1]} A_{\alpha_{l-1}\alpha_l}^l [\sigma'_l] A_{\alpha_l\alpha_{l+1}}^{l+1} [\sigma'_{l+1}] U_{\sigma'_l\sigma'_{l+1}}^{\sigma_l\sigma_{l+1}} |w_{\alpha_{l-1}}^{S_{l-1}}\rangle |\sigma_l\rangle |\sigma_{l+1}\rangle |w_{\alpha_{l+1}}^{E_{L-(l+1)}}\rangle. \end{aligned}$$

This can also be written as

$$|\psi'\rangle = \sum_{\alpha_{l-1}\alpha_{l+1}} \sum_{\sigma_l\sigma_{l+1}} \Theta_{\alpha_{l-1}\alpha_{l+1}}^{\sigma_l\sigma_{l+1}} |w_{\alpha_{l-1}}^{S_{l-1}}\rangle |\sigma_l\rangle |\sigma_{l+1}\rangle |w_{\alpha_{l+1}}^{E_{L-(l+1)}}\rangle, \quad (9.43)$$

where

$$\Theta_{\alpha_{l-1}\alpha_{l+1}}^{\sigma_l\sigma_{l+1}} = \lambda_{\alpha_{l-1}}^{[l-1]} \sum_{\alpha_l} A_{\alpha_{l-1}\alpha_l}^l [\sigma'_l] A_{\alpha_l\alpha_{l+1}}^{l+1} [\sigma'_{l+1}] U_{\sigma'_l\sigma'_{l+1}}^{\sigma_l\sigma_{l+1}}. \quad (9.44)$$

(ii) Now a *new* Schmidt decomposition identical to that in DMRG can be carried out for $|\psi'\rangle$: cutting once again bond l , there are now MN_{site} states in each part of the system, leading to

$$|\psi'\rangle = \sum_{\alpha_l=1}^{MN_{\text{site}}} \tilde{\lambda}_{\alpha_l}^{[l]} |\tilde{w}_{\alpha_l}^{S_l}\rangle |\tilde{w}_{\alpha_l}^{E_{L-l}}\rangle. \quad (9.45)$$

In general the states and coefficients of the decomposition will have changed compared to the decomposition (9.38) previous to the time evolution, and hence they are *adaptive*. We indicate this by introducing a tilde for these states and coefficients. As in DMRG, if there are more than M non-zero eigenvalues, we now choose the M eigenvectors corresponding to the largest $\tilde{\lambda}_{\alpha_l}^{[l]}$ to use in these expressions. The error in the final state produced as a result is proportional to the sum of the magnitudes of the discarded eigenvalues. After normalization, to allow for the discarded weight, the state reads

$$|\psi'\rangle = \sum_{\alpha_l=1}^M \lambda_{\alpha_l}^{[l]} |w_{\alpha_l}^{S_l}\rangle |w_{\alpha_l}^{E_{L-l}}\rangle. \quad (9.46)$$

Note again that the states and coefficients in this superposition are in general different from those in Eq. (9.38); we have now dropped the tildes again, as this superposition will be the starting point for the next time evolution (state adaption) step. As is done in DMRG, to obtain the Schmidt decomposition reduced density matrices are formed, e.g.

$$\begin{aligned} \hat{\rho}_E &= \text{Tr}_S |\psi'\rangle \langle \psi'| \\ &= \sum_{\sigma_{l+1}\sigma'_{l+1}\alpha_{l+1}\alpha'_{l+1}} |\sigma_{l+1}\rangle |w_{\alpha_{l+1}}\rangle \langle w_{\alpha'_{l+1}}| \langle \sigma'_{l+1}| \left(\sum_{\alpha_{l-1}\sigma_l} \Theta_{\alpha_{l-1}\alpha_{l+1}}^{\sigma_l\sigma_{l+1}} (\Theta_{\alpha_{l-1}\alpha'_{l+1}}^{\sigma_l\sigma'_{l+1}})^* \right) \end{aligned} \quad (9.47)$$



Figure 9.6. Typical two-block two-site setup of DMRG as used here.

If we now diagonalise $\hat{\rho}_E$, we can read off the new values of $A_{\alpha_l \alpha_{l+1}}^{l+1}[\sigma_{l+1}]$ because the eigenvectors $|w_{\alpha_l}^{E_{L-l}}\rangle$ obey

$$|w_{\alpha_l}^{E_{L-l}}\rangle = \sum_{\sigma_{l+1} \alpha_{l+1}} A_{\alpha_l \alpha_{l+1}}^{l+1}[\sigma_{l+1}] |\sigma_{l+1}\rangle |w_{\alpha_{l+1}}^{E_{L-(l+1)}}\rangle. \quad (9.48)$$

We also obtain the eigenvalues, $(\lambda_{\alpha_l}^{[l]})^2$. Due to the asymmetric grouping of Γ and λ into A discussed above, a short calculation shows that the new values for $A_{\alpha_{l-1} \alpha_l}^l[\sigma_l]$ can be read off from the slightly more complicated expression

$$\lambda_{\alpha_l}^{[l]} |w_{\alpha_l}^{S_l}\rangle = \sum_{\alpha_{l-1} \sigma_l} \lambda_{\alpha_{l-1}}^{[l-1]} A_{\alpha_{l-1} \alpha_l}^l[\sigma_l] |w_{\alpha_{l-1}}^{S_{l-1}}\rangle |\sigma_l\rangle. \quad (9.49)$$

The states $|w_{\alpha_l}^{S_l}\rangle$ are the normalized eigenvectors of $\hat{\rho}_S$ formed in analogy to $\hat{\rho}_E$.

The key point about the TEBD simulation algorithm is that a DMRG-style truncation to keep the most relevant density matrix eigenstates (or the maximum amount of entanglement) is carried out *at each time step*. This is in contrast with time-dependent DMRG methods up to now, where the basis states were chosen before the time evolution, and did not “adapt” to optimally represent the final state.

9.5 DMRG and matrix-product states

Typical normalized DMRG states for the combination of two blocks S and E and two single sites (Fig. 9.6) have the form

$$|\psi\rangle = \sum_{m_{l-1}} \sum_{\sigma_l} \sum_{\sigma_{l+1}} \sum_{m_{l+1}} \psi_{m_{l-1} \sigma_l \sigma_{l+1} m_{l+1}} |w_{m_{l-1}}^S\rangle |\sigma_l\rangle |\sigma_{l+1}\rangle |w_{m_{l+1}}^E\rangle \quad (9.50)$$

which can be Schmidt decomposed as

$$|\psi\rangle = \sum_{m_l} \lambda_{m_l}^{[l]} |w_{m_l}^S\rangle |w_{m_l}^E\rangle. \quad (9.51)$$

It has been known for a long time[35, 36] that a DMRG calculation retaining M block states produces $M \times M$ matrix-product states for $|\psi\rangle$. Consider the reduced basis transformation to obtain the states of DMRG block S that terminates on bond l from those of the block terminating on bond $l-1$ and those on a single site l ,

$$\langle w_{m_{l-1}}^S \sigma_l | w_{m_l}^S \rangle \equiv A_{m_{l-1} m_l}^l[\sigma_l], \quad (9.52)$$

such that

$$|w_{m_l}^S\rangle = \sum_{m_{l-1}\sigma_l} A_{m_{l-1}m_l}^l[\sigma_l]|w_{m_{l-1}}^S\rangle \otimes |\sigma_l\rangle. \quad (9.53)$$

The reduced basis transformation matrices $A_l[\sigma_l]$ automatically obey Eq. (9.15), which here ensures that $\{|w_{m_l}^S\rangle\}$ is an orthonormal set provided $\{|w_{m_{l-1}}^S\rangle\}$ is one, too. We may now use Eq. (9.53) for a backward recursion to express $|w_{m_{l-1}}^S\rangle$ via $|w_{m_{l-2}}^S\rangle$ and so forth. There is a complication as the number of block states for very short blocks is less than M . For simplicity, we assume that M is chosen such that we have exactly $N_{\text{site}}^{\tilde{N}} = M$. If we stop the recursion at the shortest block of size \tilde{N} that has M states we obtain

$$|w_{m_l}^S\rangle = \sum_{m_{\tilde{N}+1}\dots m_{l-1}} \sum_{\sigma_1\dots\sigma_l} A_{m_{\tilde{N}}m_{\tilde{N}+1}}^{\tilde{N}+1}[\sigma_{\tilde{N}+1}] \dots A_{m_{l-1}m_l}^l[\sigma_l]|\sigma_1\dots\sigma_l\rangle,$$

where we have boundary-site states on the first \tilde{N} sites indexed by $m_{\tilde{N}} \equiv \{\sigma_1\dots\sigma_{\tilde{N}}\}$.

Similarly, for the DMRG block E we have

$$\langle w_{m_{l+1}}^E \sigma_{l+1} | w_{m_l}^E \rangle \equiv A_{m_l m_{l+1}}^{l+1}[\sigma_{l+1}], \quad (9.54)$$

such that (again having \tilde{N} boundary sites) a recursion gives

$$|w_{m_l}^E\rangle = \sum_{m_{l+1}\dots m_{L-\tilde{N}}} \sum_{\sigma_{l+1}\dots\sigma_L} A_{m_l m_{l+1}}^{l+1}[\sigma_{l+1}] \dots A_{m_{L-\tilde{N}} m_{L-\tilde{N}}}^{L-\tilde{N}}[\sigma_{L-\tilde{N}}]|\sigma_{l+1}\dots\sigma_L\rangle, \quad (9.55)$$

with boundary-site states on the last \tilde{N} sites indexed by $m_{L-\tilde{N}} \equiv \{\sigma_{L-\tilde{N}+1}\dots\sigma_L\}$.

A comparison with Eqs. (9.16), (9.18) and (9.19) shows that DMRG generates position-dependent $M \times M$ matrix-product states as block states for a reduced Hilbert space of M states; the auxiliary state space to a bond is given by the Hilbert space of the block at whose end the bond sits. This physical meaning attached to the auxiliary state spaces and the fact that for the shortest block the states can be labeled by good quantum numbers (if available) ensures through (9.52) and (9.54) that they carry good quantum numbers for *all* block sizes. The big advantage is that using good quantum numbers allows us to exclude a large amount of wave function coefficients as being 0, drastically speeding up all calculations by at least one, and often two orders of magnitude. Moreover, as is well known, DMRG can be easily adapted to periodic boundary conditions, which is in principle also possible for the TEBD algorithm but cumbersome to implement. Fermionic degrees of freedom also present no specific problem, and in particular, there exists no negative sign problem of the kind that is present in Quantum Monte Carlo methods.

The effect of the finite-system DMRG algorithm[2] is now to shift the two free sites through the chain, growing and shrinking the blocks S and E as illustrated in Fig. 9.7. At each step, the ground state is redetermined and a new Schmidt decomposition carried out in which the system is cut between the two free sites, leading to a new truncation and new reduced basis transformations (2 matrices A adjacent to this bond). It is thus a sequence of *local* optimization steps of the wave function oriented towards an optimal representation of the ground state. Typically, after some ‘‘sweeps’’ of the free sites from left to right and back, physical quantities evaluated for this state converge. While comparison of DMRG results to

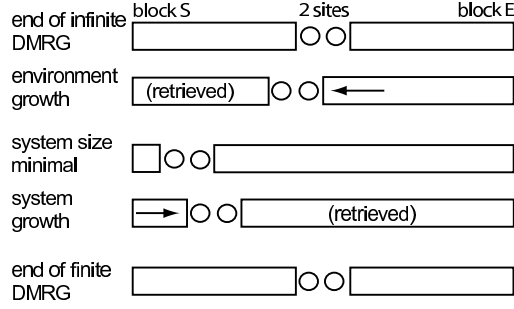


Figure 9.7. *Finite-system DMRG algorithm. Block growth and shrinkage. For the adaptive time-dependent DMRG, replace ground state optimization by local time evolution.*

exact results shows that one often comes extremely close to an optimal representation within the matrix state space (which justifies the usage of the DMRG algorithm to obtain them), it has been pointed out and numerically demonstrated[36, 41] that finite-system DMRG results can be further improved and better matrix product states be produced by switching, after convergence is reached, from the $S\bullet\bullet E$ scheme (with two free sites) to an $S\bullet E$ scheme and to carry out some more sweeps. This point is not pursued further here, it just serves to illustrate that finite-system DMRG for all practical purposes comes close to an optimal matrix product state, while not strictly reaching the optimum.

As the actual decomposition and truncation procedure in DMRG and the TEBD simulation algorithm are identical, our proposal is to use the finite-system algorithm to carry out the sequence of local time evolutions (instead of, or after, optimizing the ground state), thus constructing by Schmidt decomposition and truncation new block states best adapted to a state at any given point in the time evolution (hence adaptive block states) as in the TEBD algorithm, while maintaining the computational efficiency of DMRG. To do this, one needs not only all reduced basis transformations, but also the wave function $|\psi\rangle$ in a two-block two-site configuration such that the bond that is currently updated consists of the two free sites. This implies that $|\psi\rangle$ has to be transformed between different configurations. In finite-system DMRG such a transformation, which was first implemented by White[28] (“state prediction”) is routinely used to predict the outcome of large sparse matrix diagonalizations, which no longer occur during time evolution. Here, it merely serves as a basis transformation. We will outline the calculation for shifting the active bond by one site to the left.

Starting from

$$|\psi\rangle = \sum_{m_{i-1}^S} \sum_{\sigma_i} \sum_{\sigma_{i+1}} \sum_{m_{i+1}^E} \psi_{m_{i-1}^S \sigma_i \sigma_{i+1} m_{i+1}^E} |w_{m_{i-1}}^S\rangle |\sigma_i\rangle |\sigma_{i+1}\rangle |w_{m_{i+1}}^E\rangle, \quad (9.56)$$

one inserts the identity $\sum_{m_i^E} |w_{m_i}^E\rangle \langle w_{m_i}^E|$ obtained from the Schmidt decomposition (i.e. density matrix diagonalization) to obtain

$$|\psi\rangle = \sum_{m_{i-1}^S} \sum_{\sigma_i} \sum_{m_i^E} \psi_{m_{i-1}^S \sigma_i m_i^E} |w_{m_{i-1}}^S\rangle |\sigma_i\rangle |w_{m_i}^E\rangle, \quad (9.57)$$

where

$$\psi_{m_{l-1}^S \sigma_l m_l^E} = \sum_{m_{l+1}^E} \sum_{\sigma_{l+1}} \psi_{m_{l-1}^S \sigma_l \sigma_{l+1} m_{l+1}^E} A_{m_l m_{l+1}}^{l+1} [\sigma_{l+1}]. \quad (9.58)$$

After inserting in a second step the identity $\sum_{m_{l-2}^S \sigma_{l-1}} |w_{m_{l-2}^S \sigma_{l-1}}^S\rangle \langle w_{m_{l-2}^S \sigma_{l-1}}^S|$, one ends up with the wave function in the shifted bond representation:

$$|\psi\rangle = \sum_{m_{l-2}^S} \sum_{\sigma_{l-1}} \sum_{\sigma_l} \sum_{m_l^E} \psi_{m_{l-2}^S \sigma_{l-1} \sigma_l m_l^E} |w_{m_{l-2}^S}^S\rangle |\sigma_{l-1}\rangle |\sigma_l\rangle |w_{m_l^E}^E\rangle, \quad (9.59)$$

where

$$\psi_{m_{l-2}^S \sigma_{l-1} \sigma_l m_l^E} = \sum_{m_{l-1}^S} \psi_{m_{l-1}^S \sigma_l m_l^E} A_{m_{l-2} m_{l-1}}^{l-1} [\sigma_{l-1}]. \quad (9.60)$$

9.6 Adaptive time-dependent DMRG

The adaptive time-dependent DMRG algorithm which incorporates the TEBD simulation algorithm in the DMRG framework is now set up as follows (details on the finite-system algorithm can be found in Ref. [2]):

0. Set up a conventional finite-system DMRG algorithm with state prediction using the Hamiltonian at time $t = 0$, $\hat{H}(0)$, to determine the ground state of some system of length L using effective block Hilbert spaces of dimension M . At the end of this stage of the algorithm, we have for blocks of all sizes l reduced orthonormal bases spanned by states $|m_l\rangle$, which are characterized by good quantum numbers. Also, we have all reduced basis transformations, corresponding to the matrices A .
1. For each Trotter time step, use the finite-system DMRG algorithm to run one sweep with the following modifications:
 - i) For each even bond apply the local time evolution \hat{U} at the bond formed by the free sites to $|\psi\rangle$. This is a very fast operation compared to determining the ground state, which is usually done instead in the finite-system algorithm.
 - ii) As always, perform a DMRG truncation at each step of the finite-system algorithm, hence $O(L)$ times.
 - (iii) Use White's prediction method to shift the free sites by one.
2. In the reverse direction, apply step (i) to all odd bonds.
3. As in standard finite-system DMRG evaluate operators when desired at the end of some time steps. Note that there is no need to generate these operators at all those time steps where no operator evaluation is desired, which will, due to the small Trotter time step, be the overwhelming majority of steps.

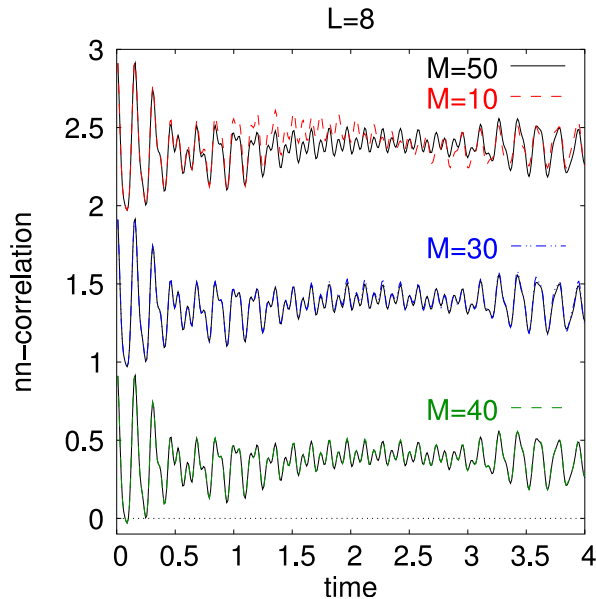


Figure 9.8. *Time evolution of the real part of nearest-neighbor correlations in a Bose-Hubbard model with instantaneous change of interaction strength using the adaptive time-dependent DMRG. The different curves for different M are shifted (parameters as in section 9.2).*

The calculation time of adaptive time-dependent DMRG scales linearly in L , as opposed to the static time-dependent DMRG which does not depend on L . The diagonalization of the density matrices (Schmidt decomposition) scales as $N_{\text{site}}^3 M^3$; the preparation of the local time evolution operator as N_{site}^6 , but this may have to be done only rarely e.g. for discontinuous changes of interaction parameters. Carrying out the local time evolution scales as $N_{\text{site}}^4 M^2$; the basis transformation scales as $N_{\text{site}}^2 M^3$. As $M \gg N_{\text{site}}$ typically, the algorithm is of order $O(LN_{\text{site}}^3 M^3)$ at each time step.

9.7 Case study: time-dependent Bose-Hubbard model

In this section we present some results of calculations on the Bose-Hubbard Hamiltonian introduced in section 9.2 which have been carried out, using modest computational resources and an unoptimized code (this concerns in particular the operations on complex matrices and vectors). In the following, Trotter time steps down to $\delta t = 5 \times 10^{-4}$ in units of \hbar/J were chosen. It is also important to note that in contrast to the DMRG calculations shown earlier for conventional time-dependent DMRG up to $N_{\text{site}} = 14$ states per site were used as a local site basis for all calculations in this Section.

Comparing the results of the adaptive time-dependent DMRG for the Bose-Hubbard model with the parameters chosen as in section 9.2 with the static time-dependent DMRG we find that the convergence in M is much faster, for the nearest neighbor correlations it sets in at about $M = 40$ (Fig. 9.8) compared to $M = 100$ for the static method (Fig. 9.3).

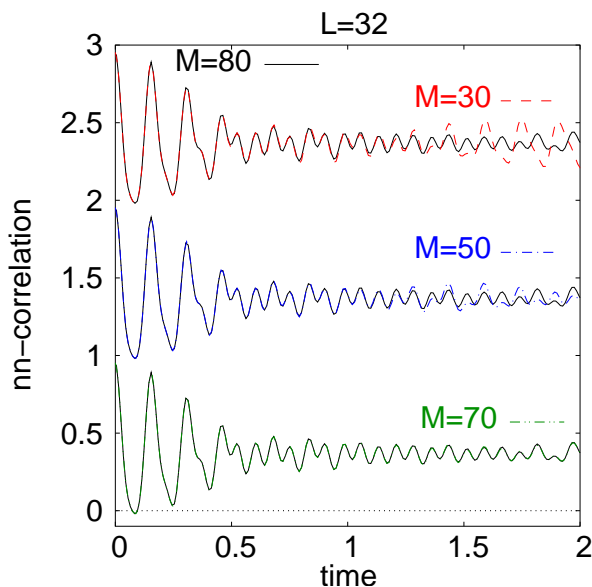


Figure 9.9. *Time evolution of the real part of nearest-neighbor correlations in a Bose-Hubbard model with instantaneous change of interaction strength using the adaptive time-dependent DMRG but for a larger system $L = 32$ with $N = 32$ bosons. The different curves for different M are shifted, comparing $M = 30, 50, 70$ to $M = 80$ respectively.*

This faster convergence in M enables us to study larger systems than with static time-dependent DMRG (Fig. 9.9). In the $L = 32$ system considered here, we encountered severe convergence problems using static time-dependent DMRG. By contrast, in the new approach convergence sets in for M well below 100, which is easily accessible numerically. Let us remark that the number M of states which have to be kept does certainly vary with the exact parameters chosen, depending if the state can be approximated well by matrix product states of a low dimension. At least in the case studied here, we found that this dependency is quite weak. We expect (also from studying the time evolution of density matrix spectra) that the model dependence of M is roughly similar as in the static case.

Similar observations are made both for local occupancy (a simpler quantity than nearest-neighbor correlations) and longer-ranged correlations (where we expect less precision). Moving back to the parameter set of section 9.2, we find as expected that the result for the local occupancy (Fig. 9.10) is converged for the same M leading to convergence in the nearest-neighbor correlations. In contrast, if we consider the correlation $\langle b^\dagger b \rangle$ between sites further apart from each other the numerical results converge more slowly under an increase of M than the almost local quantities. This can be seen in Fig. 9.11 where the results for $M = 40$ and $M = 50$ still differ a bit for times larger than $t \approx 2\hbar/J$.

The controlling feature of DMRG is the density matrix formed at each DMRG step – the decay of the density-matrix eigenvalue spectrum and the truncated weight (i.e. the sum of all eigenvalues whose eigenvectors are not retained in the block bases) control its precision. In the discarded weight for the Bose-Hubbard model of section 9.2 shown in Fig. 9.12, we can observe that the discarded weight shrinks drastically, going from $M = 20$ to $M = 50$. This

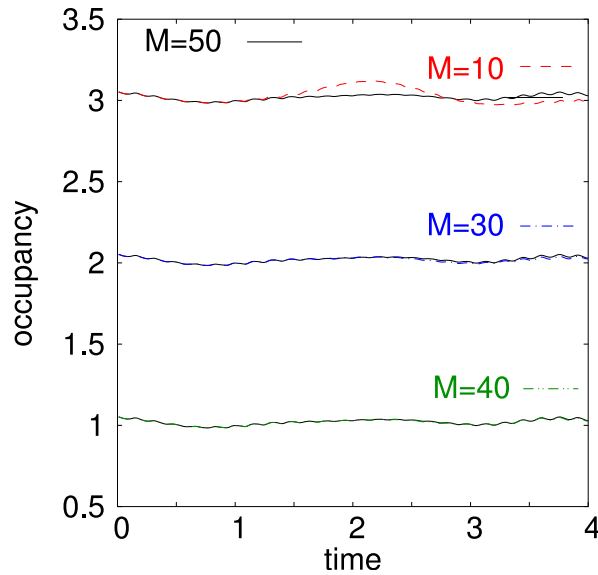


Figure 9.10. *Time evolution of the occupancy of the second site. Parameters as used in section 9.2 ($L = 8$, $N = 8$). The different curves for different M are shifted.*

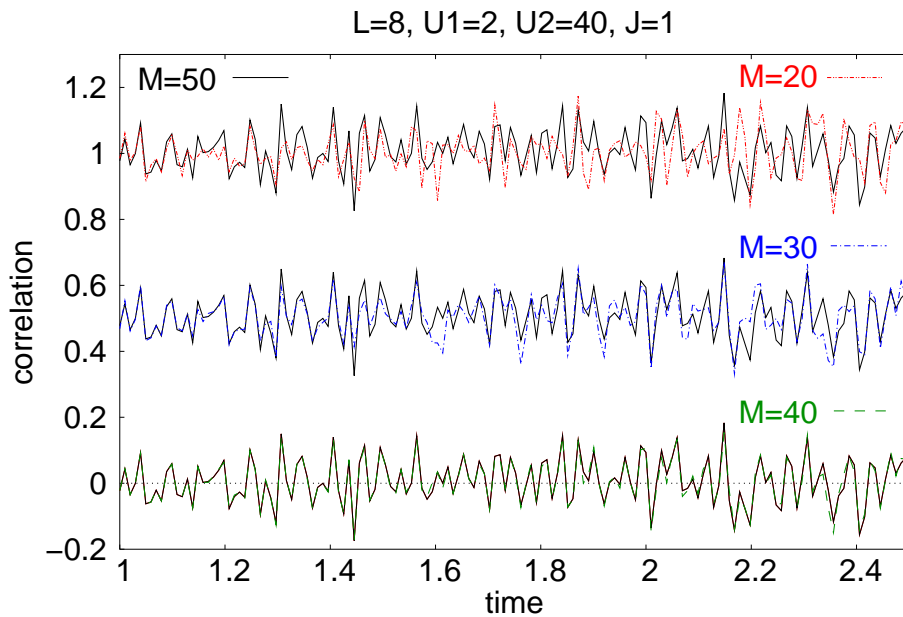


Figure 9.11. *Time evolution of the real part of the correlation between site 2 and 7. Parameters as used in section 9.2 with $N = 8$ particles. The different curves for different M are shifted. Note that the plot starts at $t = 1$ (parameters were changed at $t = 0$).*

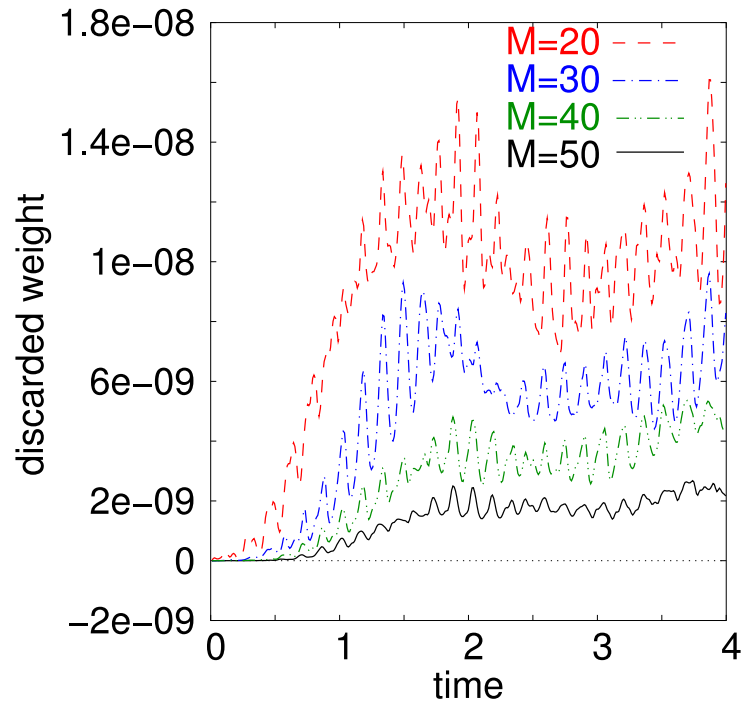


Figure 9.12. *Discarded weight for different values of M . Parameters chosen as in section 9.2.*

supports the idea that the system shows a fast convergence in M . Even more importantly, the discarded weight grows in time, as the state that was originally a ground state at $t < 0$ decays into a superposition of many eigenstates of the system at $t > 0$. However, in particular for larger M , it stays remarkably small throughout the simulation, indicating that adaptive time-dependent DMRG tracks the time-evolving state with high precision. Moving to the detailed spectrum of the density matrix (shown in Fig. 9.13 for the left density matrix when the chain is symmetrically decomposed into S and E), the corresponding distribution of the eigenvalues can be seen to be approximately exponential. In agreement with the increasing truncation error, one also observes that the decay becomes less steep as time grows. Yet, we still find a comparatively fast decay of the eigenvalue spectrum at all times, necessary to ensure the applicability of TEBD and adaptive time-dependent DMRG respectively.

Note for all results shown that the unusually large number of states per site ($N_{\text{site}} = 14$) which would not occur in Hubbard or Heisenberg models could there be translated directly into longer chains or larger state spaces (larger M) for the same computational effort, given that the algorithm is $O(LN_{\text{site}}^3 M^3)$. In that sense, we have been discussing an algorithmically hard case, but in fermionic models DMRG experience tells us that M has to be taken much larger in fermionic systems. For the fermionic Hubbard model, with $N_{\text{site}} = 4$, more than $M = 300$ is feasible with the unoptimized code, and much higher M values would be possible if optimizations were carried out. This should be enough to have quantitatively reliable time-evolutions for fermionic chains, while of course not reaching the extreme precision one is used to in DMRG for the static case. As the algorithmic cost is dominated by $(N_{\text{site}}M)^3$, the product $N_{\text{site}}M$ is an important quantity to look at: while current TEBD implementations

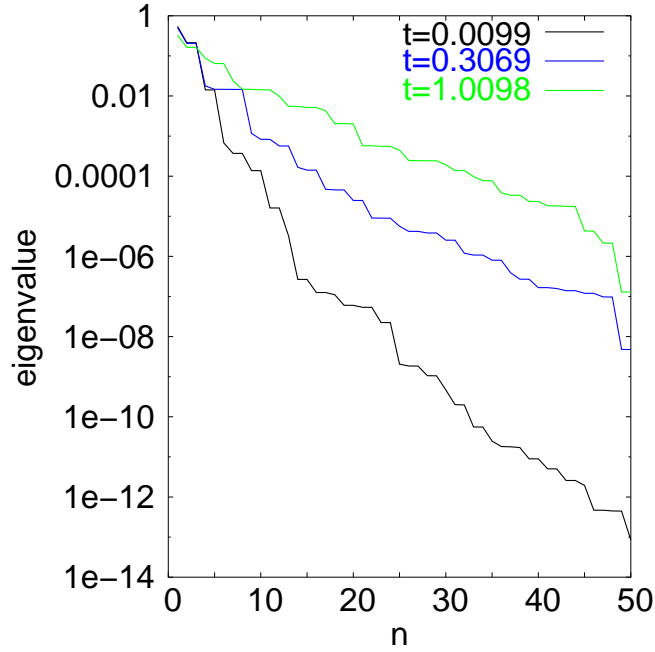


Figure 9.13. *Eigenvalue spectrum of the left reduced density matrix at different times for a symmetric S/E decomposition. Parameters chosen as in section 9.2, $M = 50$ states retained.*

range at 100 or less, adaptive time-dependent DMRG using good quantum numbers runs at the order of 1000 (and more).

Let us conclude this section by pointing out that at least one improvement can be incorporated almost trivially into this most simple version of adaptive time-dependent DMRG. Since we have used a first-order Trotter decomposition, we expect that for fixed M results of measurements at a fixed time converge linearly with respect to the time step δt chosen, as the error per time step scales as δt^2 , but the number of time steps needed to reach the fixed time grows as δt^{-1} . In other words, the Trotter error is inversely proportional to the calculation time spent. This can indeed be observed in results such as presented in Fig. 9.14.

It is very easily and at hardly any algorithmic cost that a second order Trotter decomposition can be implemented, leading to errors of order δt^2 . The second order Trotter decomposition reads[40]

$$e^{-i\hat{H}\delta t} = e^{-i\hat{H}_{odd}\delta t/2} e^{-i\hat{H}_{even}\delta t} e^{-i\hat{H}_{odd}\delta t/2}, \quad (9.61)$$

where we have grouped all local Hamiltonians on odd and even bonds into \hat{H}_{odd} and \hat{H}_{even} respectively. At first sight this seems to indicate that at each Trotter time step three (instead of two) moves (“zips”) through the chain have to be carried out. However, in many applications at the end of most time steps, the Hamiltonian does not change, such that for almost all time steps, we can contract the second $e^{-i\hat{H}_{odd}\delta t/2}$ from the previous and the first $e^{-i\hat{H}_{odd}\delta t/2}$ from the current time step to a standard $e^{-i\hat{H}_{odd}\delta t}$ time step. Hence, we incur

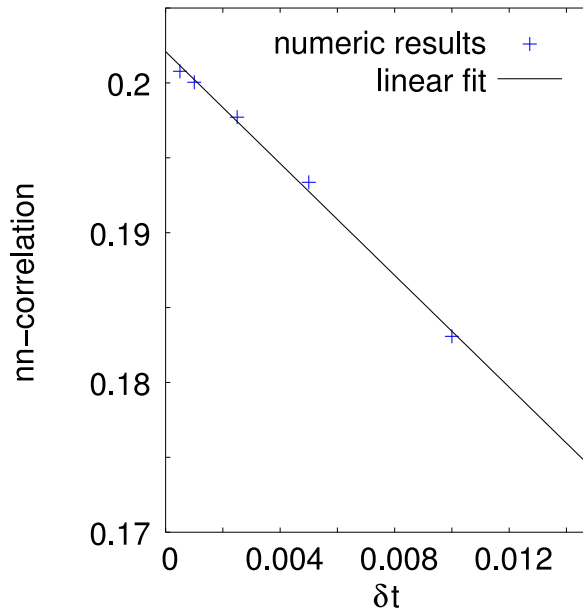


Figure 9.14. *Convergence in the Trotter time of the real part of the nearest-neighbor correlations between site 2 and 3 in a Bose-Hubbard model with instantaneous change with the parameters chosen as in section 9.2 at a fixed time.*

almost no algorithmic cost. This is also standard practice in Quantum Monte Carlo [44]; following QMC, second order Trotter evolution is set up as follows:

1. Start with a half-time step $e^{-i\hat{H}_{odd}\delta t/2}$.
2. Carry out successive time steps $e^{-i\hat{H}_{even}\delta t}$ and $e^{-i\hat{H}_{odd}\delta t}$.
3. At measuring times, measure expectation values after a $e^{-i\hat{H}_{odd}\delta t}$ time step, and again after a time step $e^{-i\hat{H}_{even}\delta t}$, and form the average of the two values as the outcome of the measurement.
4. At times when the Hamiltonian changes, do not contract two half-time steps into one time step.

In this way, additional algorithmic cost is only incurred at the (in many applications rare) times when the Hamiltonian changes while strongly reducing the Trotter decomposition error. Even more precise, but now at an algorithmic cost of factor 5 over the first or second-order decompositions, would be the usage of fourth-order Trotter decompositions (leading to 15 zips through the chain per time step, of which 5, however, can typically be eliminated)[42, 43].

9.8 Conclusion

The TEBD algorithm for the simulation of slightly entangled quantum systems, such as quantum spin chains and other one-dimensional quantum systems, was originally developed

in order to establish a link between the computational potential of quantum systems and their degree of entanglement, and serves therefore as a good example of how concepts and tools from quantum information science can influence other areas of research, in this case quantum many-body physics.

While exporting ideas from one field of knowledge to another may appear as an exciting and often fruitful enterprise, differences in language and background between researchers in so far separated fields can also often become a serious obstacle to the proper propagation and full assimilation of such ideas. In this paper we have translated the TEBD algorithm into the language of matrix product states. This language is a natural choice to express the DMRG algorithm – which, for over a decade, has dominated the simulation of one-dimensional quantum many-body systems. In this way, we have made the TEBD algorithm fully accessible to the DMRG community. On the other hand, this translation has made evident that the TEBD and the DMRG algorithms have a number of common features, a fact that can be exploited.

We have demonstrated that a very straightforward modification of existing finite-system DMRG codes to incorporate the TEBD leads to a new adaptive time-dependent DMRG algorithm. Even without attempting to reach the computationally most efficient incorporation of the TEBD algorithm into DMRG implementations, the resulting code seems to perform systematically better than static time-dependent DMRG codes at very reasonable numerical cost, converging for much smaller state spaces, as they change in time to track the actual state of the system. On the other hand, while it presents no new conceptual idea, the new code is also significantly more efficient than existing embodiments of the TEBD, for instance thanks to the way DMRG handles good quantum numbers. While we have considered bosons as an example, as in standard DMRG fermionic and spin systems present no additional difficulties. Various simple further improvements are feasible, and we think that adaptive time-dependent DMRG can be applied not only to problems with explicitly time-dependent Hamiltonians, but also to problems where the quantum state changes strongly in time, such as in systems where the initial quantum state is far from equilibrium. The method should thus also be of great use in the fields of transport and driven dissipative quantum systems.

Acknowledgments. US and GV would wish to thank the Institute of Theoretical Physics at the University of Innsbruck, where this work was initiated, for its hospitality. CK is supported by the Studienstiftung des Deutschen Volkes and DFG grant DE 730/3-1. The work in Innsbruck is supported by EU networks and the Institute for Quantum Information. GV acknowledges support from the US National Science Foundation under Grant No. EIA-0086038. US acknowledges support by The Young Academy at the Berlin-Brandenburg Academy of Sciences and the Leopoldina Society. We also thank Peter Zoller, Dieter Jaksch, Hans Briegel, Willi Zwerger, Ignacio Cirac, Juanjo Garcia-Ripoll, Miguel Cazalilla, Brad Marston, Jan von Delft and Matthias Troyer for discussions.

Note added in proof. After submission of this work, we became aware of closely related work by White and Feiguin[45].

References

Bibliography

- [1] White S R 1992 *Phys. Rev. Lett.* **69** 2863
- [2] White S R 1993 *Phys. Rev. B* **48** 10345
- [3] Nielsen M A and Chuang I L 2000 *Quantum Computation and quantum communication* Cambridge University Press
- [4] Osborne T J and Nielsen M A 2002 *Quant. Inf. Proc.* **1** 45 (Osborne T J and Nielsen M A *Preprint* quant-ph/0109024)
- [5] Dawson C M and Nielsen M A *Preprint* quant-ph/0401061 [Phys. Rev. A **69**, 052316 (2004)]
- [6] Haselgroeve H L, Nielsen M A and Osborne T J 2003 *Preprint* quant-ph/0308083 [Phys. Rev. A **69**, 032303 (2004)]
- [7] Vidal G, Latorre J I, Rico E and Kitaev A 2003 *Phys. Rev. Lett.* **90** 227902
- [8] Gaite J 2003 *Preprint* quant-ph/0301120
- [9] Latorre J I, Rico E and Vidal G 2003 *Preprint* quant-ph/0304098 [Quant. Inf. and Comp. **4**, 48 (2004)]
- [10] Bennett C H and DiVincenzo D P 2000 *Nature* **404** 247
- [11] Osborne T J and Nielsen M A 2002 *Phys. Rev. A* **66** 032110
- [12] Osterloh A, Amico L, Falci G and Fazio R 2002 *Nature* **416** 608
- [13] Legeza O 2003 *Phys. Rev. B* **68** 195116
- [14] Legeza O 2004 *Preprint* cond-mat/0401136
- [15] Verstraete F, Popp M, Cirac J I 2004 *Phys. Rev. Lett.* **92** 027901
- [16] Verstraete F, Martin-Delgado M A and Cirac J I 2004 *Phys. Rev. Lett.* **92** 087201
- [17] Vidal G 2003 *Preprint* quant-ph/0310089 [Phys. Rev. Lett. **93**, 040502 (2004)]
- [18] Peschel I, Wang X, Kaulke M and Hallberg K (eds.) 1999 *Density-Matrix Renormalization* Springer
- [19] Schollwöck U 2004 *Rev. Mod. Phys.* submitted
- [20] Cazalilla M A and Marston J B 2002 *Phys. Rev. Lett.* **88** 256403
- [21] Greiner M, Mandel O, Esslinger T, Hänsch T W and Bloch I 2002 *Nature* **415** 39
- [22] Stöferle H *et al.* 2003 *Preprint* cond-mat/0312440 [Phys. Rev. Lett. **92**, 130403 (2004)]

- [23] Vidal G 2003 *Phys. Rev. Lett.* **91** 147902
- [24] Jaksch D and Zoller P 2004 *in preparation*
- [25] Zwolak M and Vidal G 2004 *in preparation*
- [26] Klümper A, Schadschneider A and Zittartz J 1993 *Europhys. Lett.* **24** 293
- [27] Fannes M, Nachtergaele B and Werner R F 1992 *Comm. Math. Phys.* **144** 3
- [28] White S R 1996 *Phys. Rev. Lett.* **77** 3633
- [29] Press W H *et al.* 1992 *Numerical Recipes in C: The Art of Scientific Computing* Cambridge University Press
- [30] Hallberg K 1995 *Phys. Rev. B* **52** 9827
- [31] Kühner T D and White S R 1999 *Phys. Rev. B* **60** 335
- [32] Jeckelmann E 2002 *Phys. Rev. B* **66** 045114
- [33] Luo H G, Xiang T and Wang X Q 2003 *Phys. Rev. Lett.* **91** 049701
- [34] Cazalilla M A and Marston J B 2003 *Phys. Rev. Lett.* **91** 049702
- [35] Östlund S and Rommer S 1995 *Phys. Rev. Lett.* **75** 19
- [36] Dukelsky J, Martín-Delgado M A, Nishino T and Sierra G 1998 *Europhys. Lett.* **43** 457
- [37] Affleck I, Kennedy T, Lieb E H and Tasaki H 1987 *Phys. Rev. Lett.* **59** 799
- [38] Affleck I, Kennedy T, Lieb E H and Tasaki H 1988 *Comm. Math. Phys.* **115** 477
- [39] Fannes M, Nachtergaele B and Werner R F 1989 *Europhys. Lett.* **10** 643
- [40] Suzuki M 1976 *Prog. Theor. Phys.* **56** 1454
- [41] Takasaki H, Hikihara T and Nishino T 1999 *J. Phys. Soc. Jpn.* **68** 1537
- [42] Yoshida H 1990 *Phys. Lett. A* **150** 262
- [43] Krech M, Bunker A and Landau D P 1998 *Comp. Phys. Comm.* **111** 1
- [44] Assaad F F and Würtz D 1991 *Phys. Rev. B* **44** 2681
- [45] White S R 2004 *Preprint* cond-mat/0403310 [Phys. Rev. Lett. **93**, 076401 (2004)]

Part IV

A Single Atom Transistor in a 1D Optical Lattice

CHAPTER 10

THE SINGLE ATOM TRANSISTOR: INTRODUCTION

The Single Atom Transistor setup consists of a single spin-1/2 impurity atom, localised at a particular lattice site in a 1D setup and *probe* atoms which are mobile along the axis of the lattice, and initially situated to one side of the impurity. It is so named because interactions between the single localised impurity and the probe atoms can be engineered so that the transport of the probe atoms is switched based on the state of the impurity atom. In one state the impurity acts as a single atom mirror, blocking transport for the probe atoms, and in the other it is transparent to the flow of probes. Thus, the state of the impurity atom is “amplified” in the sense of becoming entangled with the (potentially macroscopic) state of the probe atoms, measurements on which can then be used as a single-shot Quantum Non-Demolition readout of the impurity’s spin.

The primary interest in this system is two-fold. Firstly, recent experimental advances with 1D lattices [1–3] and controlled coupling of two atoms into molecular states via magnetic [4] and optical [5] Feshbach resonances make such a system experimentally feasible. This would allow the study of the properties of this system, including the QND measurements it facilitates and interesting macroscopic superpositions it produces. Secondly, and equally as experimentally measurable, the transport properties of this system for weak coupling between the impurity and the probes, where the current passing the impurity is non-zero, can be highly sensitive to interactions between the probe atoms. Many-body effects become especially important in this system because the coherence times are very long, and because the probe atoms can be made strongly or weakly interacting depending on the initial density and lattice parameters. These many-body effects can be studied using the numerical methods described in part II of this thesis, where the dynamics of the system can be exactly computed in regimes which have proved otherwise inaccessible via analytical methods.

In the publication in chapter 11 the original introduction to the Single Atom Transistor is given, detailing its basic properties for single probe atoms and for many fermionic probe atoms, and giving some examples of the many body results for Bosonic probe atoms that we can calculate for this system using time-dependent numerical simulations. These results include the current of atoms passing the impurity as a function of time, and various properties of an initial Mott Insulator state as it is allowed to “melt” through the impurity site, forming a quasi-condensate.

Chapter 12 provides more information on the application of the time-dependent numerical methods to the SAT system. In particular, the time dependence of currents through the SAT

is discussed in greater detail as a result of more recent data, which is made accessible by the optimisation of the numerical method for fixed total particle number (as presented in chapter 8). Many more numerical results are then presented, both for initial configurations in which the cloud of probe atoms has zero mean momentum, and in the regime where the initial cloud of probe atoms is accelerated towards the impurity atom. The quantitative results produced in this chapter should be measurable in experiments, and give a good example of interesting many-body physics that is made accessible by the numerical methods discussed in part II.

Bibliography

- [1] T. Stöferle, H. Moritz, C. Schori, M. Köhl, and T. Esslinger, *Phys. Rev. Lett.* **92**, 130403 (2004);
- [2] B. Paredes, A. Widera, V. Murg, O. Mandel, S. Fölling, I. Cirac, G. V. Shlyapnikov, T. W. Hänsch, and I. Bloch, *Nature* **429**, 277 (2004).
- [3] C. D. Fertig, K. M. O'Hara, J. H. Huckans, S. L. Rolston, W. D. Phillips, and J. V. Porto, *Phys. Rev. Lett.* **94**, 120403 (2005)
- [4] E. L. Bolda, E. Tiesinga, and P. S. Julienne, *Phys. Rev. A* **66**, 013403; E. A. Donley, N. R. Claussen, S. T. Thompson, and C. E. Wieman, *Nature* **417**, 529 (2002); T. Loftus, C. A. Regal, C. Ticknor, J. L. Bohn, and D. S. Jin, *Phys. Rev. Lett.* **88**, 173201 (2002).
- [5] M. Theis, G. Thalhammer, K. Winkler, M. Hellwig, G. Ruff, R. Grimm, J. Hecker Denschlag, *Phys. Rev. Lett.* **93**, 123001 (2004).

CHAPTER 11

PUBLICATION

A Single Atom Transistor in a 1D Optical Lattice[†]

Phys. Rev. Lett. **93**, 140408 (2004)

A. Micheli^{1,2}, A. J. Daley^{1,2}, D. Jaksch³, and P. Zoller^{1,2}

1) *Institute for Quantum Optics and Quantum Information of the Austrian Academy of Sciences, A-6020 Innsbruck, Austria*

2) *Institute for Theoretical Physics, University of Innsbruck, A-6020 Innsbruck, Austria*

3) *Clarendon Laboratory, University of Oxford, Parks Road, Oxford OX1 3PU, U.K.*

We propose a scheme utilising a quantum interference phenomenon to switch the transport of atoms in a 1D optical lattice through a site containing an impurity atom. The impurity represents a qubit which in one spin state is transparent to the probe atoms, but in the other acts as a single atom mirror. This allows a single-shot quantum non-demolition measurement of the qubit spin.

Coupling of a spin 1/2 system to Bosonic and Fermionic modes is one of the fundamental building blocks of quantum optics and solid state physics. Motivated by the recent progress with cold atoms in 1D [1], we consider a spin 1/2 atomic impurity which is used to switch the transport of either a 1D Bose-Einstein Condensate (BEC) or a 1D degenerate Fermi gas initially situated to one side of the impurity. In one spin state the impurity is transparent to the probe atoms, whilst in the other it acts as single atom mirror, prohibiting transport via a quantum interference mechanism reminiscent of electromagnetically induced transparency (EIT) [2] (Fig. 11.1a). Observation of the atomic current passing the impurity can then be used as a quantum non-demolition (QND) measurement [3] of its internal state, which can be seen to encode a qubit, $|\psi_q\rangle = \alpha|\uparrow\rangle + \beta|\downarrow\rangle$. If a macroscopic number of atoms pass the impurity,

[†]The primary contribution of the author of the present thesis to this publication was the numerical calculation of results for Tonks gases, although he also acted as a discussion partner on all other aspects of the work.

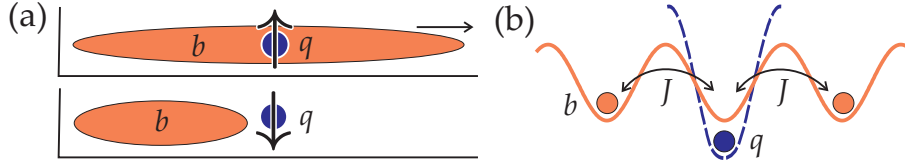


Figure 11.1. (a) A spin $1/2$ impurity used as a switch: in one spin state it is transparent to the probe atoms, but in the other it acts as a single atom mirror. (b) Implementation of the SAT as a separately trapped impurity q with probe atoms b in an optical lattice.

then the system will be in a macroscopic superposition, $|\Psi(t)\rangle = \alpha|\uparrow\rangle|\phi_\uparrow(t)\rangle + \beta|\downarrow\rangle|\phi_\downarrow(t)\rangle$, which can form the basis for a single shot readout of the qubit spin. Here, $|\phi_\sigma(t)\rangle$ denotes the state of the probe atoms after evolution to time t , given that the qubit is in state σ (Fig. 11.1a). In view of the analogy between state amplification via this type of blocking mechanism and readout with single electron transistors (SET) used in solid state systems [4], we refer to this setup as a Single Atom Transistor (SAT).

We propose the implementation of a SAT using cold atoms in 1D optical lattices [5–8]. We consider probe atoms b to be loaded in the lattice to the left of a site containing the impurity atom, which is trapped by a separate (e.g., spin-dependent [8]) potential (Fig. 11.1b). The passage of b atoms past the impurity q is then governed by the spin-dependent effective collisional interaction $\hat{H}_{\text{int}} = \sum_\sigma U_{\text{eff},\sigma} \hat{b}_0^\dagger \hat{b}_0 \hat{q}_\sigma^\dagger \hat{q}_\sigma$. By making use of a quantum interference mechanism, we engineer complete blocking (effectively $U_{\text{eff}} \rightarrow \infty$) for one spin state and complete transmission ($U_{\text{eff}} \rightarrow 0$) for the other. Below we first consider the detailed scattering processes involved in the transport of a single particle through the SAT, and then generalise this to interacting many-particle systems including a 1D Tonks gas.

The quantum interference mechanism needed to engineer U_{eff} can be produced using an optical or magnetic Feshbach resonance [9]. For the optical case a Raman laser drives a transition on the impurity site, 0, from the atomic state $\hat{b}_0^\dagger \hat{q}_\sigma^\dagger |\text{vac}\rangle$ via an off-resonant excited molecular state to a bound molecular state back in the lowest electronic manifold $\hat{m}_\sigma^\dagger |\text{vac}\rangle$ (Fig. 11.2a). We denote the effective two-photon Rabi frequency and detuning by Ω_σ and Δ_σ respectively. For the magnetic case, the Hamiltonian will have the same form, but with Ω_σ the coupling between open and closed channels and Δ_σ the magnetic field detuning [9]. The Hamiltonian for our system is then given ($\hbar \equiv 1$) by $\hat{H} = \hat{H}_b + \hat{H}_0$, with

$$\begin{aligned}
 \hat{H}_b &= -J \sum_{\langle ij \rangle} \hat{b}_i^\dagger \hat{b}_j + \frac{1}{2} U_{bb} \sum_j \hat{b}_j^\dagger \hat{b}_j (\hat{b}_j^\dagger \hat{b}_j - 1) \\
 \hat{H}_0 &= \sum_\sigma \left[\Omega_\sigma (\hat{m}_\sigma^\dagger \hat{q}_\sigma \hat{b}_0 + \text{H.c.}) + \Delta_\sigma \hat{m}_\sigma^\dagger \hat{m}_\sigma \right] \\
 &\quad + \sum_\sigma \left[U_{qb,\sigma} \hat{b}_0^\dagger \hat{q}_\sigma^\dagger \hat{q}_\sigma \hat{b}_0 + U_{bm,\sigma} \hat{b}_0^\dagger \hat{m}_\sigma^\dagger \hat{m}_\sigma \hat{b}_0 \right], \tag{11.1}
 \end{aligned}$$

where the operators \hat{b} obey the standard commutation (anti-commutation) relations for Bosons (Fermions). \hat{H}_b gives a Hubbard Hamiltonian for the b atoms with tunnelling matrix

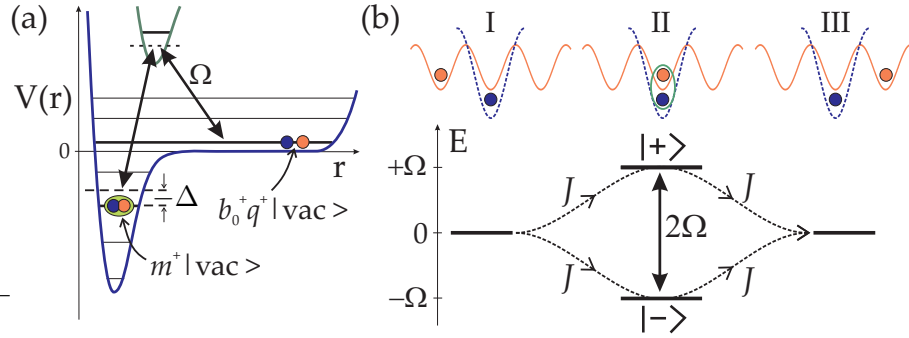


Figure 11.2. (a) The optical Feshbach setup couples the atomic state $\hat{b}_0^\dagger \hat{q}_\sigma^\dagger |\text{vac}\rangle$ (in a particular motional state quantised by the trap) to a molecular bound state of the Born-Oppenheimer potential, $\hat{m}_\sigma^\dagger |\text{vac}\rangle$, with effective Rabi frequency Ω_σ and detuning Δ_σ . (b) A single atom passes the impurity (I \rightarrow III) via the two dressed states (II), $|+\rangle = \hat{b}_0^\dagger \hat{q}_\sigma^\dagger |\text{vac}\rangle + \hat{m}_\sigma^\dagger |\text{vac}\rangle$ and $|-\rangle = \hat{b}_0^\dagger \hat{q}_\sigma^\dagger |\text{vac}\rangle - \hat{m}_\sigma^\dagger |\text{vac}\rangle$ and quantum interference gives rise to an effective tunnelling rate $J_{\text{eff},\sigma}$.

elements J giving rise to a single Bloch band with dispersion relation $\varepsilon(k) = -2J \cos ka$ (a is the lattice spacing), and collisional interactions (which are non-zero only for Bosons) given by $U_{bb} = 4\pi\hbar^2 a_{bb} \int d^3\mathbf{x} |w_j(\mathbf{x})|^4 / m_b$, where $w_j(\mathbf{x})$ is the Wannier-function for a particle localized on site j , a_{bb} is the scattering length for b atoms and m_b is their mass. \hat{H}_0 describes the additional dynamics due to the impurity on site 0, where atoms b and q are converted to a molecular state with effective Rabi frequency Ω_σ and detuning Δ_σ , and the last two terms describe background interactions, $U_{\alpha\beta,\sigma}$ for two particles $\alpha, \beta \in \{q, b, m\}$, which are typically weak. This model is valid for $U_{\alpha\beta}, J, \Omega, \Delta \ll \omega$, where ω is the energy separation between Bloch bands. Because the dynamics for the two spin channels q_σ can be treated independently, in the following we will consider a single spin channel, and drop the subscript σ .

For off-resonant laser driving ($\Omega \ll |\Delta|$), the Feshbach resonance enhances the interaction between b and q atoms, giving the familiar result $U_{\text{eff}} = U_{qb} - \Omega^2/\Delta$. However, for resonant driving ($\Delta = 0$) the physical mechanism changes, and the effective tunnelling J_{eff} of an atom b past the impurity (Fig. 11.2b, I \rightarrow III) is blocked by quantum interference. On the impurity site, laser driving mixes the states $\hat{b}_0^\dagger \hat{q}_\sigma^\dagger |\text{vac}\rangle$ and $\hat{m}_\sigma^\dagger |\text{vac}\rangle$, forming two dressed states with energies $\varepsilon_\pm = (U_{qb})/2 \pm (U_{qb}^2/4 + \Omega^2)^{1/2}$ (Fig. 11.2b, II). The two resulting paths for a particle of energy ε destructively interfere so that for large $\Omega \gg J$ and $U_{qb} = 0$, $J_{\text{eff}} = -J^2/(\varepsilon + \Omega) - J^2/(\varepsilon - \Omega) \rightarrow 0$. This is analogous to the interference effect underlying EIT [2], and is equivalent to having an effective interaction $U_{\text{eff}} \rightarrow \infty$. In addition, if we choose $\Delta = \Omega^2/U_{qb}$, the paths constructively interfere, screening the background interactions to produce perfect transmission ($U_{\text{eff}} \rightarrow 0$).

For a more detailed analysis, we solve the Lippmann-Schwinger equation exactly for scattering from the impurity of an atom b with incident momentum $k > 0$ in the lowest Bloch-band. The resulting forwards and backwards scattering amplitudes, $f^{(\pm)}(k)$ respectively,

are

$$f^{(\pm)}(k) = \left[1 + \left(\frac{iaU_{\text{eff}}(k)}{v(k)} \right)^{\pm 1} \right]^{-1}, \quad (11.2)$$

where the energy dependent interaction $U_{\text{eff}} = U_{qb} + \Omega^2/(\varepsilon(k) - \Delta)$ and the phase-velocity $v(k) = \partial\varepsilon/\partial k = 2Ja \sin ka$. The corresponding transmission probabilities, $T(k) = |f^{(+)}(k)|^2$, are plotted in Fig. 11.3a as a function of $\varepsilon(k)$ for various Ω and Δ . For $\Omega \sim J$, these are Fano-profiles with complete reflection at $\varepsilon(k) = \Delta$ and complete transmission at $\varepsilon(k) = \Delta - \Omega^2/U_{qb}$. The SAT thus acts as an energy filter, which is widely tunable via the laser strength and detuning used in the optical Feshbach setup. For $\Omega > 4J$, T is approximately independent of k , and we recover the previous result, i.e., that transport can be completely blocked or permitted by appropriate selection of Δ . Note that this mechanism survives when higher energy Bloch bands are included, and is resistant to loss processes, which are discussed below.

We now consider the full many-body dynamics of N probe atoms b initially prepared in the ground state in a trap (box) of M lattice sites on the left side of the impurity q . We are then interested in the expectation value of the steady state coherent current $\hat{I} = d\hat{N}_R/dt$ (where $\hat{N}_R = \sum_{j>0} \hat{b}_j^\dagger \hat{b}_j$ is the number of particles on the right side of the impurity, see Fig. 11.3b), which depends on the laser parameters, the initial filling factor on the left of the impurity, $n = N/M$, and, for Bosons, the interaction strength, U_{bb} . We first consider the case of a dilute or noninteracting gas, before treating both interacting Bosons, and non-interacting Fermions with arbitrary n .

For a dilute noninteracting Bose quasi-condensate ($n \ll 1, U_{bb} = 0$), or for any very dilute gas, (where the momentum distribution is very narrow), the behaviour is very similar to that of a single particle. If the gas is quickly accelerated to a finite momentum k , e.g., by briefly tilting the lattice, then the atoms will coherently tunnel through the impurity according to the scattering amplitudes $f^{(\pm)}(k)$. The resulting current $I \propto N |f^{(+)}(k)|^2 v(k)$, where $v(k)$ is the velocity of a Bloch-wave with momentum k .

For a Fermi gas the equations of motion are linear and may be solved exactly provided $U_{bm} = U_{qb}$. Scattering from the impurity then occurs independently for each particle in the initial Fermi sea, with scattering amplitudes $f^{(\pm)}(k)$ for $k \leq k_F$, where the Fermi momentum $k_F = \pi n/a$. After a short transient period, on the order of the inverse tunnelling rate $1/J$, the system establishes a roughly constant flux of particles through the impurity (Fig. 11.3b), with a time-averaged current for resonant driving $\Delta = 0$ given by

$$\begin{aligned} I_0 &= \frac{1}{\pi a} \int_{-2J}^{-2J+\varepsilon_F} d\varepsilon f(\varepsilon) T(\varepsilon) v(\varepsilon) \\ &= \frac{J}{\pi} \left[V - \frac{G_+ \arctan \frac{VG_-}{G_+^2 - V} + G_- \operatorname{arctanh} \frac{VG_+}{G_-^2 + V}}{(G_+^2 + G_-^2)/(G_+ G_-)} \right], \end{aligned} \quad (11.3)$$

with ε_F the Fermi Energy in the initial state, $f(\varepsilon)$ the density of states per site (left of the impurity), $2G_\pm^2 \equiv (1 + \Omega^4/4J^4)^{1/2} \pm 1$ and $V \equiv \varepsilon_F/2J = 2 \sin^2(n\pi/2)$.

For a Tonks gas of strongly interacting Bosons ($U_{bb}/J \gg 1$ with $n \leq 1$) we expect to observe similar behaviour to that observed for Fermions. In this limit, double occupation

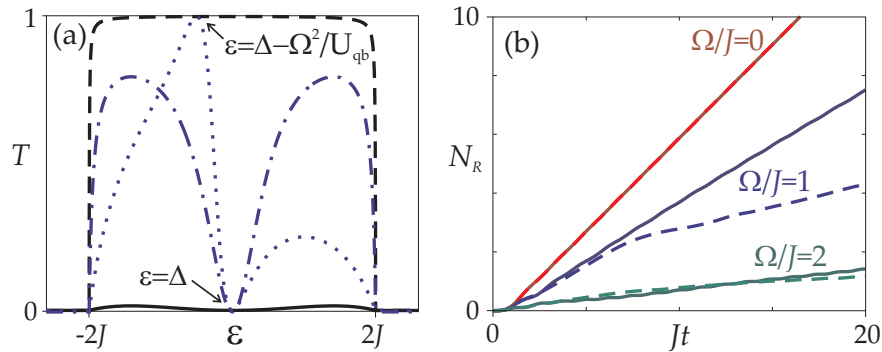


Figure 11.3. (a) SAT transmission coefficients $T \equiv |f^{(+)}|^2$ for a particle b as a function of its energy $\varepsilon(k)$ for $\Omega/J = 4, \Delta = 0, U_{qb}/J = 0$ (solid line), $\Omega/J = 8, \Delta/J = 4, U_{qb}/J = 2$ (dashed line), $\Omega/J = 1, \Delta = 0, U_{qb}/J = 2$ (dotted), and $\Omega/J = 1, \Delta = 0, U_{qb}/J = 0$ (dash-dot). (b) The number of particles to the right of the impurity, $N_R(t)$, from exact numerical calculations for Bosons in the limit $U_{bb}/J \rightarrow \infty$ (dashed lines) and Fermions (solid lines) in a 1D Mott Insulator state with $n = 1$, for $\Delta = 0, \Omega/J = 0, 1, 2$.

of a site can be neglected, and the behaviour can be mapped onto Fermionic particles via a Jordan-Wigner transformation (JWT) [10]. The Hamiltonian is then the same up to a nonlinear phase factor $\Omega \rightarrow \Omega(-1)^{\hat{N}_R}$, which essentially causes Ω to change sign when a particle passes the impurity. The contribution of this phase factor should be small for weak coupling, $\Omega \ll J$, and also for strong coupling, where no particles will tunnel through the impurity, i.e., $N_R \simeq 0$.

For the general case of many Bosons we perform exact numerical integration of the time dependent Schrödinger equation for the Hamiltonian (11.1) using Vidal’s algorithm for “slightly entangled quantum states” [11]. This algorithm selects adaptively a decimated Hilbert space on which a state is represented, by retaining at each time step only those basis states that carry the greatest weight in Schmidt decompositions taken from every possible bipartite splitting of the system into two contiguous parts. A sufficiently large decimated Hilbert space is then selected so that the results of the simulations are essentially exact. For each set of parameters we first prepared the initial state via an imaginary time evolution which found the ground state for atoms in a box trap on the left of the impurity. Then, considering initially a single impurity atom q on the site 0 and unoccupied sites to the right of that site, we calculated the time evolution of the system until it had reached a quasi-steady state behaviour. In the simulations we obtained the behavior at finite repulsion U_{bb} , and tested the effects of the nonlinear phase factor $(-1)^{\hat{N}_R}$ for strongly interacting Bosons, $U_{bb} \rightarrow \infty$.

In Fig. 11.3b we plot the number of particles on the right of the impurity $N_R(t)$ for Fermions and for Bosons with $U_{bb}/J \rightarrow \infty$, starting from a Mott Insulator (MI) state with $n = 1$, for $\Delta = 0, \Omega/J = 0, 1, 2$. For $\Omega = 0$ the results for Bosons and Fermions are identical, whilst for $\Omega/J = 1, 2$, we observe an initial period for the Bosons in which the current is similar to that for the Fermionic systems, after which the Bosons settle into a steady state with a significantly smaller current. The initial transient period for the Bosons incorporates

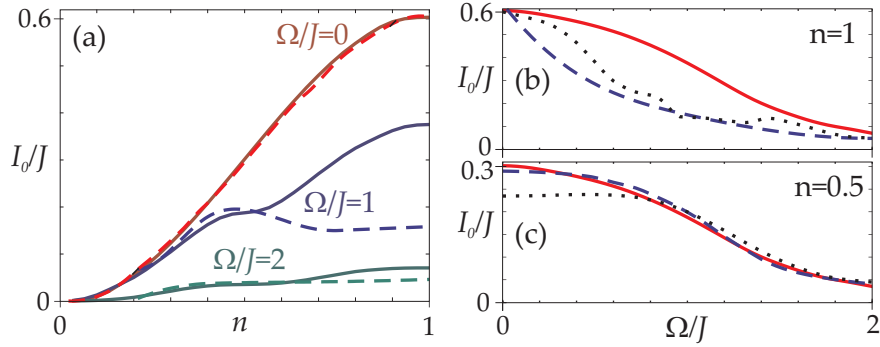


Figure 11.4. (a) The steady state current of b atoms through the impurity as function of the initial filling factor n for $\Delta = 0$ and $\Omega/J = 0, 1, 2$. The solid lines show the analytic result I_0 for Fermions, whereas the dashed lines show the exact numerical result for hard-core Bosons with $U_{bb}/J \rightarrow \infty$. For $\Omega = 0$ these results are indistinguishable. (b, c) The steady state current as function of the Rabi-frequency Ω/J on resonance $\Delta = 0$ for (b) unit filling and (c) half filling. The solid lines show the analytic result for Fermions, whereas the dashed (dotted) lines give numerical results for Bosons with $U_{bb}/J = 20$ ($U_{bb}/J = 4$).

the settling to steady state of firstly the molecule dynamics, and secondly the momentum distribution on the right of the impurity. These transients are suppressed if Ω is ramped slowly to its final value from a large value $\Omega > 4J$.

The dependence of the steady state current on the initial filling factor n is depicted in Fig. 11.4a for resonant driving with $\Omega/J = 0, 1, 2$. For $\Omega = U_{qb} = U_{bm} = 0$, the current $I_0 = 2J \sin^2(n\pi/2)/\pi$ is identical for Fermions and hard-core Bosons ($U_{bb} \rightarrow \infty$), as we expect from the exact correspondence given in this limit by the JWT. For Fermions with weak, resonant laser driving, the main features of the Fano profile (Fig. 11.3a) are observed in correspondence with the integral in (11.3). For example, a plateau in $I_0(n)$ is observed near $n = \arccos(-\Delta/2J)/\pi = 1/2$, as the Fermi Energy is raised past $\varepsilon \sim \Delta = 0$, which corresponds to the zero of the transmission probability $T(\varepsilon)$. Good agreement is also observed with the result for Bosons in this limit with $n < 1/2$, whilst for larger n Bosons are blocked better, with a factor of 2 – 3 in the steady state currents.

The enhanced blocking for Bosons is also seen in Fig. 11.4b showing the steady state current against Ω for resonant driving and $n = 1$. It is clear from these figures together that this difference is a feature of the regime $n > 1/2$, $\Omega \sim J$, which is directly linked to the phase factor of $(-1)^{N_R}$ arising in the JWT. As Ω is increased and fewer particles pass the impurity, the results for Fermions and Bosons again converge as expected. For small Ω there are small differences between Bosons with finite $U_{bb}/J = 4$ and $U_{bb}/J \rightarrow \infty$, with currents always lower than the equivalent fermionic current, owing largely to the smaller mean squared momentum in the initial state. For large driving, $\Omega \gg 4J$ the basic interference process is extremely efficient for Bosons and Fermions, and we observe complete blocking or transmission by quantum interference for the proper choice of Δ .

In Fig. 11.5 we investigate the time evolution of 30 hard-core Bosons ($U_{bb} \rightarrow \infty$) in an initial MI state, which are released through a SAT which is switched at $t = 0$. For $\Omega = 0$, we see that as the gas expands the momentum distribution becomes peaked as a quasi-condensate is formed with $k = \pi/2a$, which consists of a coherent superposition of particles propagating to the right and holes propagating to the left as the MI state melts [6]. This mode grows outwards from the edge of the initial distribution, and contains at its peak $\sim \sqrt{N}$ particles, as is expected for such dynamically formed quasi-condensates in a 1D lattice [12]. In contrast, for $\Omega/J = 0.5$, the momentum distribution is broader, and the quasi-condensate mode contains many fewer particles. The mode also consists of distinct branches, holes in the melting MI propagating to the left and particles to the right, which are initially coherent, but become decoupled at $t \sim 12/J$. For larger Ω this behaviour becomes more pronounced, and for $\Omega > 4J$, the MI state essentially remains unchanged.

The melting of a MI in this way can be used as the basis for a convenient single-shot measurement of the spin state of q . If q is in a superposition of spin states, only one of which will permit transport of the b atoms, then after some propagation time, the system will be in a macroscopic superposition of distinct quantum phases (MI and quasi-condensates). These are distinguishable because if the b atoms are released from the lattice, the quasi-condensate will produce an interference pattern, whereas the MI state will not. The visibility of the resulting pattern can thus be used to measure the qubit spin.

A remarkable feature of the SAT is its resistance to both two- and three-body loss processes on the impurity site. Spontaneous emissions from the off-resonant excited molecular state in the case of an optical Feshbach resonance amount to a two-body loss process at a rate $\sim \gamma_{2B}$ in the states $|+\rangle$ and $|-\rangle$. These small rates are further suppressed in the blocking regime $J, \gamma_{2B} \ll \Omega$, with the resulting decoherence rate $\gamma_{\text{dec}} \propto J^2 \gamma_{2B} n / \Omega^2$, with n the mean site occupation of the b atoms. Collisions of atoms b with molecules m [13] are strongly suppressed in the Tonks gas regime, as well as for Fermions. For a weakly interacting Bose gas the corresponding three-body loss rate, γ_{3B} , is again strongly suppressed in the blocking regime ($J, \gamma_{3B} \ll \Omega$) with $\gamma_{\text{dec}} \propto J^4 \gamma_{3B} n^2 / \Omega^4$.

Parallels may be drawn between the SAT and other systems coupled to fermionic and bosonic modes. These include the QND-readout of a single photon in cavity-quantum electrodynamics [14], electron counting statistics [15], and the transport of electrons past impurities such as quantum dots [16] (although there particles are normally initially present on both sides of the impurity). However, the long decoherence times for atoms in optical lattices imply coherent transport over longer timescales than is observed in these other systems, which are inherently dissipative. In addition, blocking and/or energy filtering by one or more SATs could be applied as tools in the study of Bose and Fermi gases in a 1D lattice.

Work in Innsbruck is supported by the Austrian Science Foundation, EU Networks and the Institute for Quantum Information. DJ is supported by the IRC on quantum information processing.

Bibliography

- [1] T. Stöferle *et al.*, Phys. Rev. Lett. **92**, 130403 (2004); B. Paredes *et al.*, Nature **429**, 277 (2004).

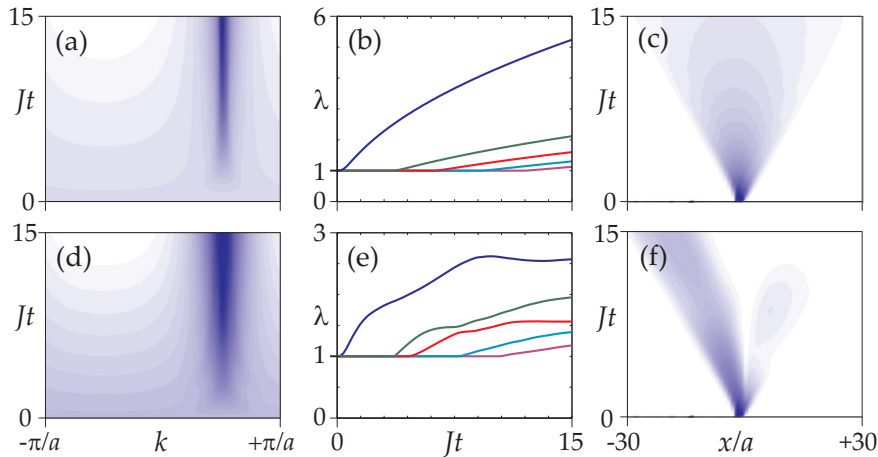


Figure 11.5. *Exact numerical results showing the propagation of $N = 30$ hardcore Bosons in an initial MI state ($n = 1$) through a SAT with (a-c) $\Omega = 0$ and (d-f) $\Omega = 0.5J$, with $\Delta = U_{qb} = U_{bm} = 0$. The plot shows (a,d) the momentum distribution, (b,e) the five largest eigenvalues, λ_m , of the single particle density matrix, $\langle \hat{b}_i^\dagger \hat{b}_j \rangle$ and (c,f) the spatial density of the largest eigenmode (the quasi-condensate) as a function of time. Darker colours represent higher values.*

- [2] M. Lukin, *Rev. Mod. Phys.* **75**, 457 (2003).
- [3] V. B. Braginsky and F. Y. Khalili, *Quantum Measurement*, (Cambridge University Press, UK, 1992).
- [4] See, for example, G. Johansson et al., cond-mat/0210163.
- [5] D. Jaksch *et al.*, *Phys. Rev. Lett.* **81**, 3108 (1998).
- [6] D. Jaksch *et al.*, *Phys. Rev. Lett.* **89**, 040402 (2002).
- [7] M. Greiner, O. Mandel, T. W. Hänsch and I. Bloch, *Nature* **415**, 39 (2002); M. Greiner *et al.*, *ibid* **419** 51 (2002).
- [8] O. Mandel *et al.*, *Phys. Rev. Lett.* **91**, 010407 (2003).
- [9] E. L. Bolda, E. Tiesinga, and P. S. Julienne, *Phys. Rev. A* **66**, 013403 (2002); For an optical Feshbach resonance, see M. Theis *et al.*, *Phys. Rev. Lett.* **93**, 123001 (2004).
- [10] See, for example, S. Sachdev, *Quantum Phase Transitions*, (Cambridge University Press, UK, 1999).
- [11] G. Vidal, *Phys. Rev. Lett.* **91**, 147902 (2003).
- [12] M. Rigol and A. Muramatsu, cond-mat/0403387 [*Phys. Rev. Lett.* **93**, 230404 (2004)].
- [13] D. Petrov, cond-mat/0404036.
- [14] G. Nogues *et al.*, *Nature* **400**, 239 (1999).

-
- [15] L. S. Levitov, in *Quantum Noise in Mesoscopic Physics*, Ed. Y. V. Nazarov (Kluwer Academic Publishers, Dordrecht, 2002).
- [16] See, for example, M. A. Cazalilla and J. B. Marston, *Phys. Rev. Lett.* **88**, 256403 (2002).

CHAPTER 12

PUBLICATION

Numerical Analysis of Coherent Many-Body Currents in a Single Atom Transistor[†]

Preprint quant-ph/0506256

A. J. Daley^{1,2}, S. R. Clark³, D. Jaksch³, and P. Zoller^{1,2}

1) *Institute for Quantum Optics and Quantum Information of the Austrian Academy of Sciences, A-6020 Innsbruck, Austria*

2) *Institute for Theoretical Physics, University of Innsbruck, A-6020 Innsbruck, Austria*

3) *Clarendon Laboratory, University of Oxford, Parks Road, Oxford OX1 3PU, U.K.*

We study the dynamics of many atoms in the recently proposed Single Atom Transistor setup [A. Micheli, A. J. Daley, D. Jaksch, and P. Zoller, Phys. Rev. Lett. **93**, 140408 (2004)] using recently developed numerical methods. In this setup, a localised spin 1/2 impurity is used to switch the transport of atoms in a 1D optical lattice: in one state the impurity is transparent to probe atoms, but in the other acts as a single atom mirror. We calculate time-dependent currents for bosons passing the impurity atom, and find interesting many body effects. These include substantially different transport properties for bosons in the strongly interacting (Tonks) regime when compared with fermions, and an unexpected decrease in the current when weakly interacting probe atoms are initially accelerated to a non-zero mean momentum. We also provide more insight into the application of our numerical methods to this system, and discuss open questions about the currents approached by the system on long timescales.

12.1 Introduction

The recently proposed Single Atom Transistor (SAT) setup [1] provides new opportunities to experimentally examine the coupling of a spin-1/2 system with bosonic and fermionic modes.

[†]The author of the present thesis performed the calculations for Fermions, for the Tonks gas and for zero coupling to the impurity atom in this article, and collaborated with SRC and DJ on the remaining calculations.

Such couplings form fundamental building blocks in several areas of physics. For example, atoms passing through a cavity can allow the quantum non-demolition (QND) readout of single-photon states in quantum optics [2], and in solid state physics, such systems occur in Single Electron Transistors [3], in studies of electron counting statistics [4] and in the transport of electrons past impurities such as quantum dots [5].

In the SAT setup, which was motivated by the significant experimental advances made recently with cold atoms in 1D [6–8], a single spin-1/2 impurity atom, q , is used to switch the transport of a gas of cold atoms in a 1D optical lattice (Fig. 12.1). The impurity atom, which can encode a qubit on two internal spin states, is transparent to a gas of probe atoms in one spin state (the “on” state), but acts as a single atom mirror in the other (the “off” state), prohibiting transport via a quantum interference mechanism (Fig. 12.1). Observation of probe atoms that are initially situated to one side of the impurity, and which can constitute either a 1D degenerate Bose or Fermi gas, can then be used as a QND measurement [9] of the qubit state of the impurity atom $|\psi_q\rangle = \alpha|\uparrow\rangle + \beta|\downarrow\rangle$ [1] (see Fig. 12.1).

The long coherence times associated with atoms in optical lattices allow many-body effects to contribute coherently to the transport properties over longer timescales than is observed in other systems where bosonic and fermionic modes couple to a spin 1/2 system. This produces novel physics in which the current of atoms passing the impurity, especially in a regime of weak coupling between probe atoms and impurity, is sensitive to interactions between the probe atoms [1]. These effects could be directly observed in experiments, for example, via measurements of the density of probe atoms on each site of the impurity atom as a function of time.

In this article we present a detailed numerical analysis of these currents, making use of recently developed numerical methods [10] to calculate the dynamics of the bosonic probe atoms by directly integrating the many-body Schrödinger equation in 1D on an adaptively truncated Hilbert space. When these currents are compared to analytical calculations of transmission coefficients for single particles passing the impurity atom and the related currents for a non-interacting 1D Fermi gas, significant interaction effects are observed, as first discussed in Ref. [1]. Here we provide new insight into the time dependence of these currents, and what conclusions can be drawn from our numerical results on different timescales. We then calculate the initial currents for atoms at zero temperature diffusing past the impurity (where the initial mean momentum of the 1D gas, $\langle\hat{k}\rangle_{t=0} = 0$, with \hat{k} is the operator corresponding to the quasi-momentum in the lowest Bloch band and t the time), and explore the effects observed for different interaction strengths of bosonic probe atoms. We then also investigate the currents for fermions and bosons when the probe atoms are initially kicked ($\langle\hat{k}\rangle_{t=0} \neq 0$). This study is complementary to the analytical study of the SAT that is given in recent article by Micheli et al. [11].

In section 12.2 we discuss the basic physics of the SAT, and give a summary of the dynamics found in [1] for single particles and non-interacting fermions. Then we present in detail the numerical techniques that we use to compute the exact time evolution of the many-body 1D system. The time-dependence of the resulting currents is discussed in section 12.3, followed by a presentation of the values of the initial steady state currents, both in the diffusive ($\langle\hat{k}\rangle_{t=0} = 0$) and kicked ($\langle\hat{k}\rangle_{t=0} \neq 0$) regimes. The conclusions are then summarised in section 12.4.

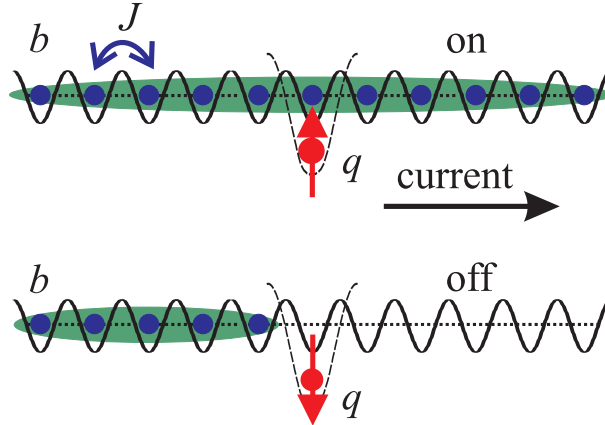


Figure 12.1. A Single Atom Transistor (SAT) in a 1D optical lattice: A single spin-1/2 impurity atom q separately trapped at a particular lattice site is transparent to probe atoms b in one state (“on”), but in the other acts as a single atom mirror (“off”). The probe atoms can either diffuse past the impurity site with mean initial momentum $\langle \hat{k} \rangle_{t=0} = 0$ or can be accelerated to a finite initial momentum $\langle \hat{k} \rangle_{t=0} \neq 0$ by a kick of strength p_k .

12.2 Overview

12.2.1 The Single Atom Transistor

The System

As described in section 12.1, we consider probe atoms b , which are loaded into an optical lattice [12–15] with strong confinement in two dimensions, so that the atoms are restricted to move along a lattice in 1D. The probe atoms are initially situated to the left of a site containing an impurity atom q , which is trapped independently (by a species or spin-dependent [16] potential), fixing it to a particular site while the probe atoms are free to move. In order to produce the “on” and “off” states of the SAT, we must appropriately engineer the effective spin-dependent interaction between the probe atoms and the impurity, $H_{\text{int}} = \sum_{\sigma} U_{\text{eff},\sigma} \hat{b}_0^{\dagger} \hat{b}_0 \hat{q}_{\sigma}^{\dagger} \hat{q}_{\sigma}$. Here, \hat{b}_i^{\dagger} and \hat{q}^{\dagger} are second-quantised creation operators for the b and q atoms respectively, obeying the standard commutation (anti-commutation) relations for bosons (fermions) and the site index i is chosen so that the impurity is on site $i = 0$. These interactions can be controlled using either a magnetic [17, 18] or optical [19] Feshbach resonance. For simplicity we discuss the case of an optical Feshbach resonance, depicted in Fig. 12.2. Here, lasers are used to drive a transition from the atomic state $\hat{b}_0^{\dagger} \hat{q}_{\sigma}^{\dagger} |\text{vac}\rangle$ via an off-resonant excited molecular state to a bound molecular state back in the lowest electronic manifold $\hat{m}_{\sigma}^{\dagger} |\text{vac}\rangle$ on the impurity site, $i = 0$ (see Fig. 12.2). The two-photon Rabi frequency for this process is denoted Ω_{σ} and the Raman detuning Δ_{σ} , and throughout this article we use units with $\hbar = 1$.

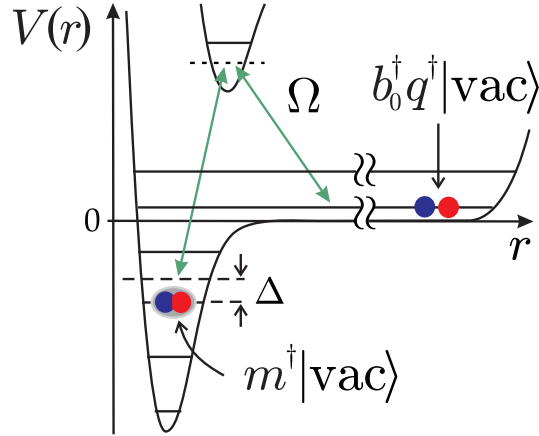


Figure 12.2. An optical Feshbach resonance for a single spin channel ($\Omega = \Omega_\sigma$, $\Delta = \Delta_\sigma$): One probe atom and the impurity atom, in an atomic state $b_0^\dagger q^\dagger |\text{vac}\rangle$ which is quantised by the trapping potential of the lattice site, are coupled by an optical Feshbach setup to a bound molecular state, $m^\dagger |\text{vac}\rangle$, of the Born-Oppenheimer potential, $V(r)$ (note that here the Born-Oppenheimer potential is modified by the trapping potential of the lattice site [17]). The coupling has the effective two-photon Rabi frequency Ω , and detuning Δ .

Single Atoms

We consider initially a single probe atom passing the impurity. If the coupling to the molecular state is far off resonance ($\Omega_\sigma \ll |\Delta_\sigma|$), the effect of the Feshbach resonance is to modify the interaction between the b and q atoms in the familiar manner, with $U_{\text{eff}} = U_{qb} + \Omega_\sigma^2/\Delta_\sigma$. This can be used to screen the background interaction between these atoms, U_{qb} , so that the “on” state of the SAT ($U_{\text{eff}} = 0$) can be produced by choosing $\Delta_\uparrow = -\Omega_\uparrow^2/U_{qb}$.

If the coupling is resonant ($\Delta_\downarrow = 0$), then the physical mechanism is different, and the passage of a probe atom b past the impurity is blocked by quantum interference. The mixing of the unbound atomic state and the molecular state on the impurity site produces two dressed states

$$\frac{1}{\sqrt{2}} \left(\hat{b}_0^\dagger \hat{q}_\downarrow^\dagger |\text{vac}\rangle \pm m_\downarrow^\dagger |\text{vac}\rangle \right), \quad (12.1)$$

with energies

$$\varepsilon_\pm = \frac{U_{qb}}{2} \pm \left(\frac{U_{qb}^2}{4} + \Omega_\downarrow^2 \right)^{1/2}. \quad (12.2)$$

The two resulting paths for a particle of energy ε then destructively interfere so that when $\Omega_\downarrow \gg J$, where J is the normal tunneling amplitude between neighbouring lattice sites, and $U_{qb} = 0$, the effective tunnelling amplitude past the impurity (see Fig. 12.3) is

$$J_{\text{eff}} = \left(-\frac{J^2}{\varepsilon + \Omega_\downarrow} - \frac{J^2}{\varepsilon - \Omega_\downarrow} \right) \rightarrow 0. \quad (12.3)$$

This is reminiscent of the interference effect which underlies Electromagnetically Induced Transparency [20], and corresponds to the effective interaction $U_{\text{eff}} \rightarrow \infty$ required for the “off” state of the SAT.

In Refs. [1, 11], the Lippmann-Schwinger equation is solved exactly for scattering from the impurity of an atom b with incident momentum $k > 0$ in the lowest Bloch-band, where the energy of the particle $\varepsilon(k) = -2J \cos(ka)$, with a the lattice spacing. The resulting transmission probabilities $T(p)$ are in the form of Fano Profiles [21]. For $\Omega_\sigma \sim J$ these have a minimum corresponding to complete reflection for $\varepsilon(k) = -\Delta_\sigma$ and complete transmission for $\varepsilon(k) = -\Delta_\sigma - \Omega_\sigma^2/U_{qb}$. For $\Omega_\sigma > 4J$, the transmission coefficients are approximately independent of k , and so complete transparency of the impurity atom is obtained for $\Delta_\sigma = -\Omega_\sigma^2/U_{qb}$ and complete blocking of the incident atoms for $\Delta = 0$.

Many Atoms

The treatment of this system for many atoms is similar to the single atom case, but the motion of the probe atoms in the lattice, except on the impurity site, is governed by a (Bose-) Hubbard Hamiltonian [13]. As the two spin channels for the impurity atom, q can be treated independently, we will consider only a single spin channel q_σ , and drop the subscript in the notation throughout the remainder of the article [1]. The Hamiltonian for the system is then given (with $\hbar \equiv 1$) by $\hat{H} = \hat{H}_b + \hat{H}_0$, with

$$\begin{aligned}\hat{H}_b &= -J \sum_{\langle ij \rangle} \hat{b}_i^\dagger \hat{b}_j + \frac{1}{2} U_{bb} \sum_j \hat{b}_j^\dagger \hat{b}_j (\hat{b}_j^\dagger \hat{b}_j - 1), \\ \hat{H}_0 &= \Omega (\hat{m}^\dagger \hat{q} \hat{b}_0 + \text{h.c.}) - \Delta \hat{m}^\dagger \hat{m} + U_{qb} \hat{b}_0^\dagger \hat{q} \hat{b}_0 + U_{bm} \hat{b}_0^\dagger \hat{m}^\dagger \hat{m} \hat{b}_0.\end{aligned}\quad (12.4)$$

Here, H_b gives a Hubbard Hamiltonian for the b atoms with tunnelling matrix elements J , and collisional interactions U_{bb} . For fermions, $U_{bb} = 0$, whereas for bosons $U_{bb} = 4\pi\hbar^2 a_{bb} \int d^3\mathbf{x} |\mathbf{w}_j(\mathbf{x})|^4 / m_b$, with $\mathbf{w}_j(\mathbf{x})$ the Wannier-function on site j , and a_{bb} and m_b the scattering length and mass of b atoms respectively. H_0 describes the dynamics in the presence of the impurity on site 0, where atoms b and q are converted to a molecular state with effective Rabi frequency Ω and detuning Δ , and the final two terms describe background interactions, $U_{\alpha\beta}$ for two particles $\alpha, \beta \in \{q, b, m\}$, which are typically weak and will be neglected in our treatment. This single-band model is valid in the limit for $U_{\alpha\beta}, J, \Omega, \Delta \ll \omega$, where ω is the energy separation between Bloch bands, an inequality which is fulfilled in current experiments. The robustness of the SAT with respect to loss processes is discussed in [1].

In the rest of this article, we will study the current of atoms past the impurity site that develops as a function of time, and how this current depends on the interaction between probe atoms and on interactions between the probe atoms and the impurity.

12.2.2 Atomic Currents through the SAT

To analyse the case of many atoms passing the impurity site, we consider the probe atoms b to be prepared initially to the left of the impurity, in a ground state corresponding to a

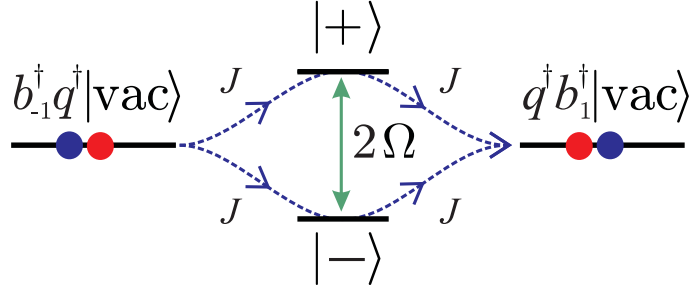


Figure 12.3. *The sequence as (left) a probe atom approaches the impurity site and is located on site $i = -1$, (centre) the probe atom is on the impurity site, $i = 0$, and (right) the probe atom has tunneled past the impurity and is located on site $i = 1$. Quantum interference in this process because the two dressed states on the impurity site, $|\pm\rangle = (\hat{b}_0^\dagger \hat{q}_\sigma^\dagger |\text{vac}\rangle \pm m_\sigma^\dagger |\text{vac}\rangle) / \sqrt{2}$ give rise to two separate paths with equal and opposite amplitude.*

1D box potential. The current of atoms passing the impurity is $I(t) = d\hat{N}_R/dt$, where N_R is the mean number of atoms to the right of the impurity, $N_R = \langle \sum_{j>0} \hat{b}_j^\dagger \hat{b}_j \rangle$. For a sufficiently large number of atoms in the initial cloud, this current is generally found to rapidly settle into an initial steady state current, I_{ss} , on relatively short timescales ($tJ \sim 1$) (see section 12.3.1 for further discussion of steady state currents for bosons).

For a non-interacting Fermi gas at zero temperature, the currents can be calculated exactly when $U_{bm} = U_{qb}$, as the equations of motion are linear. Scattering from the impurity occurs independently for each particle in the initial Fermi sea, and after a short transient period of the order of the inverse tunnelling rate $1/J$, a steady state current I_{ss} is established. This can be calculated either by integrating the single-particle transmission probabilities [1, 11] or by direct numerical integration of the Heisenberg equations.

For a non-interacting and very dilute Bose gas, the situation will be identical to considering a single particle. However, for higher densities, many-boson effects become important, and additionally for non-zero interactions the situation becomes even more complicated. In the limit $U_{bb}/J \rightarrow \infty$ in 1D (the Tonks gas regime) it is usually possible to replace the bosonic operators $\hat{b}_i, \hat{b}_i^\dagger$ by fermionic operators $\hat{f}_i, \hat{f}_i^\dagger$ using a Jordan-Wigner transformation [22]. However, in this case the resulting Hamiltonian,

$$\begin{aligned} \hat{H} = & -J \sum_{\langle ij \rangle} \hat{f}_i^\dagger \hat{f}_j - \Delta \hat{m}^\dagger \hat{m} + (-1)^{\hat{N}_L} \Omega \left(\hat{m}^\dagger \hat{q} \hat{f}_0 + \text{h.c.} \right) \\ & + U_{qb} \hat{f}_0^\dagger \hat{q}^\dagger \hat{q} \hat{f}_0 + U_{bm} \hat{f}_0^\dagger \hat{m}^\dagger \hat{m} \hat{f}_0, \end{aligned} \quad (12.5)$$

contains a nonlinear phase factor resulting from the coupling on the impurity site, $(-1)^{\hat{N}_L}$, where $\hat{N}_L = \sum_{j<0} \hat{f}_j^\dagger \hat{f}_j$ is the operator for the number of atoms to the left of the impurity site. For $\Omega = 0$, the boson currents are exactly the same as the currents for noninteracting fermions as $\langle \hat{b}_i^\dagger \hat{b}_i \rangle = \langle \hat{f}_i^\dagger \hat{f}_i \rangle$. For finite Ω it is not clear what role the phase factor will play in determining the system dynamics, although for sufficiently large $\Omega \gg J$ we again expect very little current to pass the impurity.

Thus, for the intermediate regime $\Omega \sim J$, and for the case of finite interaction strength U/J there are no known analytical solutions for the currents. For this reason, we specifically study these regimes in this paper, using near-exact numerical methods.

12.2.3 Time-Dependent Numerical Algorithm for 1D Many-Body Systems

The algorithm that we use to compute the time evolution of our many body system for bosonic probe atoms was originally proposed by Vidal [10]. This method allows near-exact integration of the many body Schrödinger equation in 1D by an adaptive decimation of the Hilbert space, provided that the Hamiltonian couples nearest-neighbour sites only and that the resulting states are only “slightly entangled” (this will be explained in more detail below). Recently both this algorithm [23], and similar methods proposed by Verstrate and Cirac [24] have been generalised to the treatment of master equations for dissipative systems and systems at finite temperature, and progress has been made applying the latter method to 2D systems [25].

In 1D, these methods rely on a decomposition of the many-body wavefunction into a matrix product representation of the type used in Density Matrix Renormalisation Group (DMRG) calculations [26], which had previously been widely applied to find the ground state in 1D systems. The time dependent algorithms have now been incorporated within DMRG codes [27], and also been used to study the coherent dynamics of a variety of systems [28]. In our case, we write the coefficients of the wavefunction expanded in terms of local Hilbert spaces of dimension S ,

$$|\Psi\rangle = \sum_{i_1 i_2 \dots i_M=1}^S c_{i_1 i_2 \dots i_M} |i_1\rangle \otimes |i_2\rangle \otimes \dots \otimes |i_M\rangle, \quad (12.6)$$

as a product of tensors

$$c_{i_1 i_2 \dots i_M} = \sum_{\alpha_1 \dots \alpha_{M-1}}^{\chi} \Gamma_{\alpha_1}^{[1] i_1} \lambda_{\alpha_1}^{[1]} \Gamma_{\alpha_1 \alpha_2}^{[2] i_2} \lambda_{\alpha_2}^{[2]} \Gamma_{\alpha_3 \alpha_4}^{[2] i_2} \dots \Gamma_{\alpha_{M-1}}^{[M] i_M}. \quad (12.7)$$

These are chosen so that the tensor $\lambda_{\alpha}^{[l]}$ specifies the coefficients of the Schmidt decomposition [29] for the bipartite splitting of the system at site l ,

$$|\psi\rangle = \sum_{\alpha=1}^{\chi_l} \lambda_{\alpha}^{[l]} |\phi_{\alpha}^{[1 \dots l]}\rangle |\phi_{\alpha}^{[l+1 \dots M]}\rangle, \quad (12.8)$$

where χ_l is the Schmidt rank, and the sum over remaining tensors specify the Schmidt eigenstates, $|\phi_{\alpha}^{[1 \dots l]}\rangle$ and $|\phi_{\alpha}^{[l+1 \dots M]}\rangle$. The key to the method is two-fold. Firstly, for many states corresponding to a low-energy in 1D systems we find that the Schmidt coefficients $\lambda_{\alpha}^{[l]}$, ordered in decreasing magnitude, decay rapidly as a function of their index α (this is what we mean by the state being “slightly entangled”) [10]. Thus the representation can be truncated at relatively small χ and still provide an inner product of almost unity with the exact state of the system $|\Psi\rangle$. Secondly, when an operator acts on the local Hilbert state of two neighbouring sites, the representation can be efficiently updated by changing the Γ tensors corresponding to those two sites, a number of operations that scales as $\chi^3 S^3$ for

sufficiently large χ [10]. Thus, we represent the state on a systematically truncated Hilbert space, which changes adaptively as we perform operations on the state.

In order to simulate the time evolution of a state, we perform a Suzuki-Trotter decomposition [30] of the time evolution operator $\exp(-i\hat{H}t)$, which is applied to each pair of sites individually in small timesteps δt . Initial states can also be found using an imaginary time evolution, i.e., the repeated application of the operator $\exp(-\hat{H}\delta t)$, together with renormalisation of the state.

In this paper, results are not only produced using the original algorithm as presented in [10], but also using an optimised version in which the Schmidt eigenstates are forced to correspond to fixed numbers of particles. This allows us to make use of the total number conservation in the Hamiltonian to substantially increase the speed of the code, and also improve the scaling with χ and S . With this number conserving code we are able to compute results with much higher values of χ , however we also find that for insufficiently large χ , the results from this code become rapidly unphysical, in contrast to the original code (see section 12.3.1).

In implementations of this method we vary the value of χ to check that the point at which the representation is being truncated does not affect the final results. A useful indicator for convergence of the method is the sum of the Schmidt coefficients discarded in each time step, although in practice the convergence of calculated quantities (such as the single particle density matrix, $\langle \hat{b}_i^\dagger \hat{b}_j \rangle$) are normally used. This is also discussed further in section 12.3.1

For bosons on an optical lattice we must also choose the dimension S of the local Hilbert space, which corresponds to one more than the maximum number of atoms allowed on one lattice site. For simulation of the SAT, we allow a variable dimension of the local Hilbert space S_l , as we must consider the state of the molecule on the impurity site in addition to the probe atoms. Allowing such a variable dimension dramatically reduces the simulation time, which scales as $\chi^3 \sum_l S_l^3$ when $\chi \gg S$, and scales proportional to S^4 when χ is small. For a Bose gas with finite U/J we usually take $S_l = 6$ away from the impurity site, and $S_0 = 12$ on the impurity site, whereas simulations of a Tonks gas can be performed with $S_l = 2$ away from the impurity site and $S_0 = 4$ on the impurity site.

12.3 Numerical Results

In section 12.3.1 we discuss the time dependence of the current for bosons and the applicability of our numerical methods in different regimes. We establish the existence of an initial steady state current, I_{SS} that appears on a timescale $tJ \sim 1$, and discuss the observation of a second steady state current I_0 , observed in some cases on a timescale $tJ \sim 10$. In sections 12.3.2 and 12.3.3 we then present our numerical results for I_{SS} for the case where the initial cloud diffuses past the impurity site, and the case where the initial cloud is kicked respectively.

We are primarily interested in the behaviour of the current through the SAT when it is used in the ‘‘off’’ state, i.e., we choose $\Delta = 0$. To enhance clarity of the results, we also choose $U_{bq} = U_{bm} = 0$.

In each case, we considered an initial cloud of between $N = 1$ and $N = 30$ atoms, confined

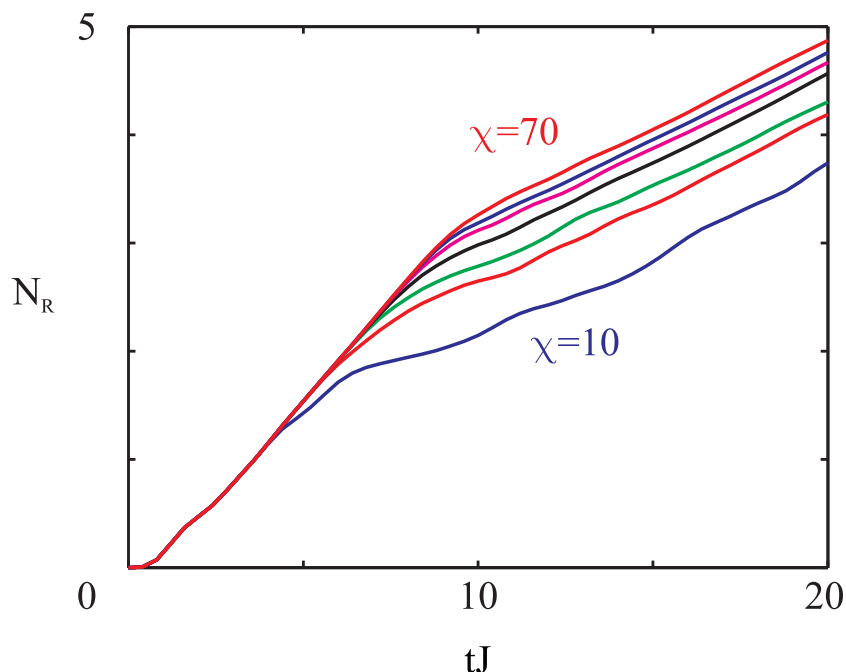


Figure 12.4. The number of atoms to the right of the impurity site, N_R as a function of dimensionless time tJ for a Bose gas in the Tonks limit ($U_{bb}/J \rightarrow \infty$) with $\Omega/J = 1$, $n = N/M = 1$, and varying number of states retained in the method, $\chi = 10, 20, 30, 40, 50, 60, 70$ (lines from bottom to top). These results are from the original simulation method.

on $M = 30$ lattice sites situated immediately to the left of the impurity site. The initial state used corresponds to the ground state, $|\phi_0\rangle$ of a Bose-Hubbard model with a box trap.

Our total grid for the time evolution consisted of 61 lattice sites, with the 30 rightmost sites initially unoccupied, and the results we present are, except for very small systems, independent of the size of the initial cloud and of the grid size. Fermionic results are derived from exact integration of the Heisenberg equations of motion, whereas bosonic results are near-exact simulations as described in section 12.2.3.

12.3.1 Time Dependence of the current for bosonic probe atoms

The mean number of probe atoms on the right of the impurity, N_R is plotted as a function of time, t , in Fig. 12.4 for a Tonks gas ($U/J \rightarrow \infty$) with $\Omega/J = 1$ and initial state of density $n = N/M = 1$. These results were calculated with the original simulation algorithm, and it is clear from the figure that the current settles into an initial steady state value I_{SS} on the timescale $tJ \sim 1$. However, as is typical for bosonic probe atoms with $n > 0.5$, there exists a knee in the curve at a time $t_{\text{knee}}(\chi)$, leading to a new and final steady state current, which we will denote I_0 . The time $t_{\text{knee}}(\chi)$ depends on the initial density, n , and coupling, Ω , and as can be seen from this figure, we require a high value of χ to find the exact time.

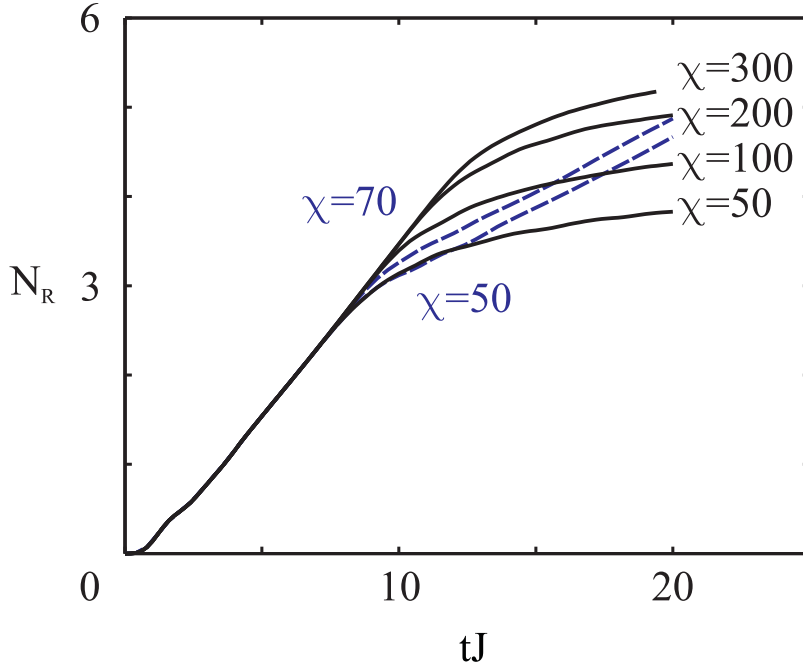


Figure 12.5. *The number of atoms to the right of the impurity site, N_R as a function of dimensionless time tJ for a Bose gas in the Tonks limit ($U_{bb}/J \rightarrow \infty$) with $\Omega/J = 1$, $n = N/M = 1$. This plot shows a comparison of results from the original method (dashed lines, $\chi = 50, 70$, c.f. Fig. 12.4), and from the number conserving method (solid lines, $\chi = 50, 100, 200, 300$).*

For $n = 1, \Omega/J = 1$, $t_{\text{knee}}(\chi)$ appears to converge to a value between $tJ = 9$ and $tJ = 12$ as χ is increased. It is clear that significant level of correlation, or entanglement between the left and right hand side of the system (in the sense of the number of significant Schmidt eigenvalues for a bipartite splitting) are involved in determining the dynamics leading to the knee. However, the actual value of the steady state current I_0 appears to converge for much lower values of χ and there is essentially no change in this result from $\chi = 10$ to $\chi = 70$.

The interpretation of these results is more complex when they are compared with similar results from the new, number conserving version of our code. In Fig. 12.5 we observe that the behaviour diverges at the same value of $t_{\text{knee}}(\chi)$, and even for $\chi = 300$, the value of $t_{\text{knee}}(\chi)$ has only shifted a little further from where it was observed for $\chi = 70$ with the original version of the code. This confirms that the dynamics on this timescale are dominated by the significant level of correlation, or entanglement between the left and right hand side of the system.

In contrast to the steady state current I_0 obtained using the original code, though, the current in the number conserving simulations rapidly approaches 0, even for $\chi = 300$. As can be seen from the dotted line in Fig. 12.6, this behaviour occurs when the maximum sum of squares of the Schmidt coefficients being discarded in each timestep, $\varepsilon_\lambda = \sum_{\beta > \chi} \lambda_\beta^2$, reaches a steady value on the order of 10^{-7} , indicating that the simulation results from the number

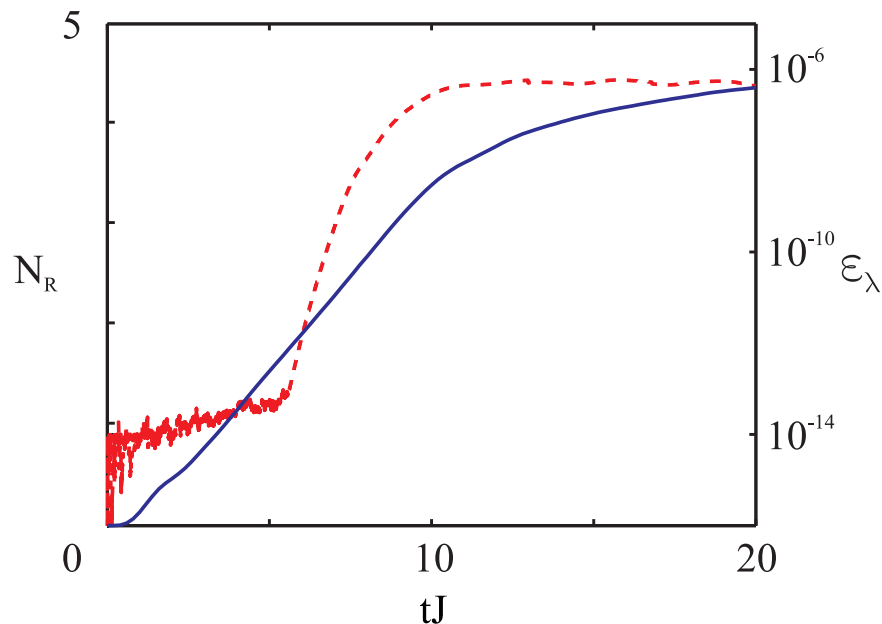


Figure 12.6. Comparison as a function of dimensionless time tJ of the number of atoms to the right of the impurity site, N_R , (solid line), and the sum of squares of the discarded Schmidt eigenvalues, $\varepsilon_\lambda = \sum_{\beta > \chi} \lambda_\beta^2$ (dashed line). These results are taken from the number conserving simulation method with $\chi = 100$, for a Bose gas in the Tonks limit ($U_{bb}/J \rightarrow \infty$) with $\Omega/J = 1$, $n = N/M = 1$.

conserving code are probably not valid for $t > t_{\text{knee}}$. Indeed, we observe the same behaviour from the new simulation code with $\Omega = 0$, where we know from Eq. 12.5 that the time dependent current $I(t)$ is equal to that for fermions, and should not decrease in this manner (see currents for fermions in Ref. [1]). Interestingly, the original code, which produces the steady state currents I_0 at finite Ω reproduces the known result at $\Omega = 0$ exactly even for small values of χ , with a steady state current I_{SS} and no knee.

Our conclusions from these results are as follows:

(i) We know that up to t_{knee} our simulation results are exact, as they are unchanged in the linear region with current I_{SS} for $\chi = 20 \rightarrow 300$. As this regime lasts at least until $tJ \sim 10$, these results would be observable in an experimental implementation of the SAT.

(ii) As an impractically large value of χ would be required to reproduce the results exactly on long timescales, we can not be certain what the final behaviour will be for $t > t_{\text{knee}}(\chi = 300)$. This depends on clearly interesting phenomena that arise from strong correlations between the left and right sides of the impurity site, and could include settling to a final steady state current I_0 . These effects would also be observable in an experiment.

The expected final steady state values I_0 are already discussed in Ref. [1], and so in the remainder of this article we investigate the initial steady state currents I_{SS} in various parameter regimes.

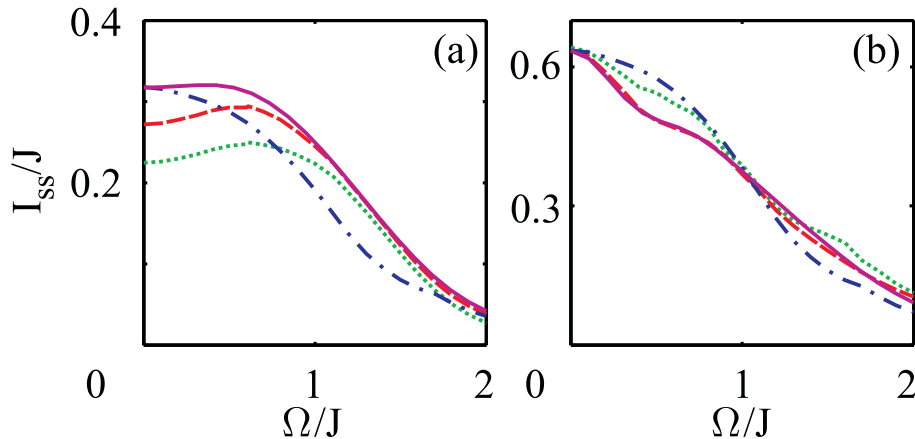


Figure 12.7. Steady state currents through the SAT I_{SS} as a function of the coupling between probe atoms and the impurity, Ω/J . These plots show the comparison of a Bose gas with different interaction strengths $U/J = 4$ (dotted line), $U/J = 10$ (dashed) and $U/J \rightarrow \infty$ (solid), and a Fermi gas (dash-dot), with (a) $n = 1/2$ and (b) $n = 1$. In both cases, $\Delta = U_{qb} = U_{bm} = 0$.

12.3.2 Diffusive evolution, with initial mean momentum ($\langle \hat{k} \rangle_{t=0} = 0$)

We first consider the motion of atoms past the impurity site in the diffusive regime, where the initial state at $t = 0$ is the ground state of a Bose-Hubbard model on $M = 30$ lattice sites in a box trap.

Dependence of the current on impurity-probe coupling, Ω

In Fig. 12.7 we show the initial steady state current I_{SS} as a function of Ω/J for fermionic probe atoms, and for bosonic probe atoms with $U_{bb}/J = 4, 10, \infty$ and $\Delta = 0$. All of these results decrease as expected with increasing Ω/J , and even for a relatively small $\Omega = 2J$ the current is minimal in each case. At half filling (Fig. 12.7a), the results for the Tonks gas are identical to the Fermi results for $\Omega = 0$, but become substantially different as Ω increases, with the currents in this regime greater for the bosons. At weaker interactions the currents are smaller than the Tonks result at all Ω , but for $\Omega/J > 1$ the currents for $U/J = 4$ are larger than for a non-interacting Fermi gas. The variation in the currents for different interaction strengths of bosons appears to be due to the broader initial momentum distributions that occur at larger U/J . At unit filling (Fig. 12.7b), I_{SS} is less dependent on the interaction strength, with all of the bosonic results very close to one another, currents becoming larger than that for fermions when $\Omega/J > 1$.

Dependence of the current on interaction strength, U/J

The dependence of the initial steady state current I_{SS} on the interaction strength for bosons is depicted more clearly in Fig. 12.8, both at unit filling, $n = 1$, and half filling, $n = 1/2$ for

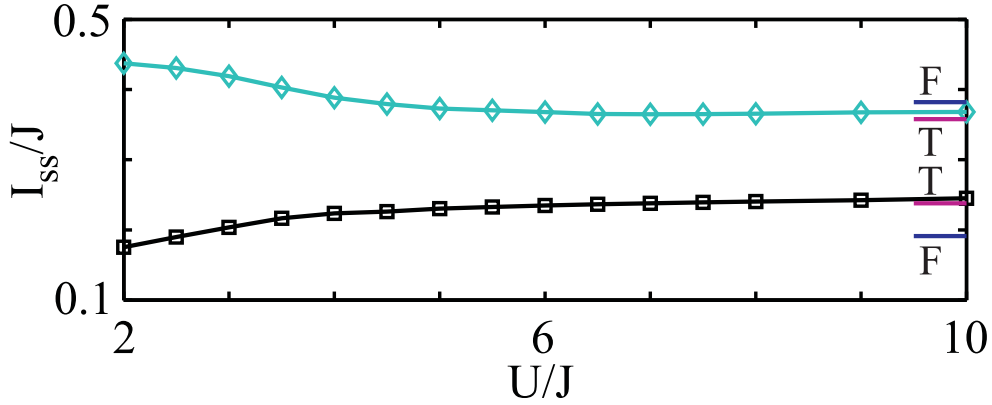


Figure 12.8. Steady state currents through the SAT I_{ss} as a function of the interaction strength U/J for bosonic probe atoms initially at half-filling, $n = 1/2$ (squares) and at unit filling, $n = 1$ (diamonds) with $\Omega/J = 1$. The equivalent results for the Tonks gas ($U/J \rightarrow \infty$) and fermions are marked on the right hand side of the plot. $\Delta = U_{qb} = U_{bm} = 0$.

$\Omega = J$. At half filling the current increases with increasing U/J , which is due to the broader initial momentum distribution produced by the higher interaction energies. In contrast, at higher densities (here $n = 1$), the probe atoms are blocked better by the SAT for higher interaction strengths, and I_{ss} decreases. The key principle here is that bosons appear to be better blocked when they approach the impurity individually. For high densities this is achieved when large interaction strengths eliminate the higher occupancies of all lattice site including the impurity site. For weaker interactions the bosons can swamp the transistor, with one atom being bound to the impurity, whilst other probe atoms tunnel onto and past the impurity site.

This effect is seen in Fig. 12.9, where the molecular occupation and average probe atom occupation on the impurity site are shown for (a) $U/J = 4$ and (b) $U/J = 10$. We see that as n increases, the molecular occupation becomes rapidly higher for $U/J = 10$ than for $U/J = 4$, despite the larger occupation of probe atoms on the impurity site for $U/J = 4$. This indicates that for $U/J = 10$ atoms arrive individually at the impurity site, where they are coupled with the impurity atom into a molecular state, and their transport is efficiently blocked. For $U/J = 4$, more than one atom enters the impurity site at once, leading to a larger average probe atom occupation on the impurity site, but a comparatively small molecular occupation.

It is important to note, however, that even when $U/J = 4$, the resulting currents are only slightly larger than they are for non-interacting fermions. At higher interaction strengths we then see an even stronger suppression of the steady state current for dense, strongly interacting bosons. As Ω increases, both the molecular occupation and probe atom occupation on the impurity site decrease (Fig. 12.9) as the probability of even a single atom tunnelling onto the impurity site becomes small. For $\Omega > 2J$ the blocking mechanism of the SAT functions extremely well even in the regime where the probe atoms are dense and weakly interacting.

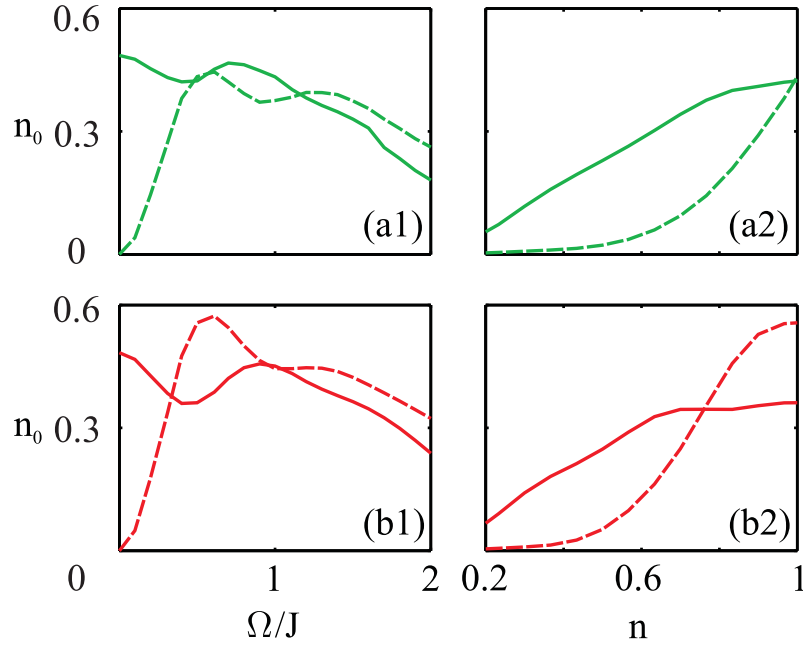


Figure 12.9. Plot showing the average steady state occupation of the molecular state (dashed lines) and the average steady state atomic occupation of the impurity site (solid lines) for (a) $U/J = 4$ and (b) $U/J = 10$, as a function of (a, b 1) Ω/J with $n = 1$ and (a, b 2) n with $\Omega/J = 0.5$. In all cases, $\Delta = U_{qb} = U_{bm} = 0$, and calculations were performed for $M = 30$.

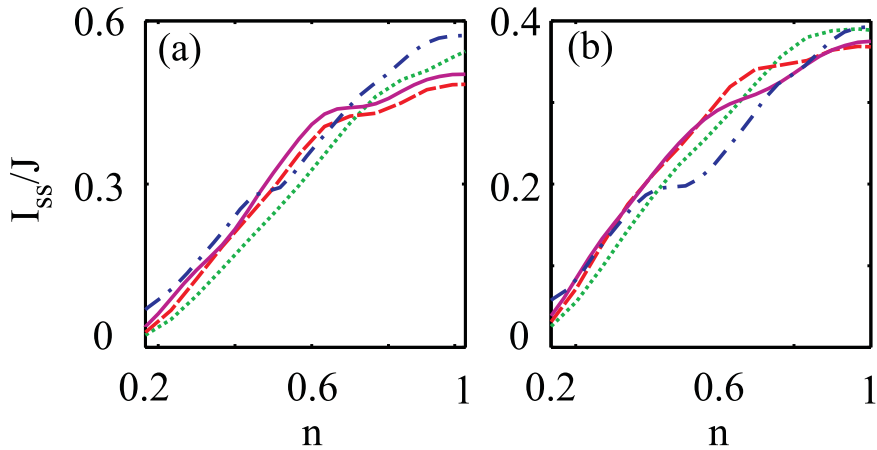


Figure 12.10. Steady state currents through the SAT I_{ss} as a function of the initial density of atoms $n = N/M$. These plots show the comparison of a Bose gas with different interaction strengths $U/J = 4$ (dotted line), $U/J = 10$ (dashed) and $U/J \rightarrow \infty$ (solid), and a Fermi gas (dash-dot), with (a) $\Omega/J = 0.5$ and (b) $\Omega/J = 1$. In both cases, $\Delta = U_{qb} = U_{bm} = 0$.

Dependence of the current on initial density, n

In Fig. 12.10 we show the dependence of the initial steady state current, I_{SS} on the initial filling factor n with (a) $\Omega/J = 0.5$ and (b) $\Omega/J = 1$. In both cases, the currents for bosons of different interaction strengths are very similar, with the variations following the patterns discussed in the preceding section. These results also agree well with the results for fermions at small n and for $n \sim 1$, but the plateau observed in fermionic currents near $n \sim 0.5$ does not occur in the currents for bosons. For fermions, this plateau arises from the transmission profile of the SAT as a function of incoming momentum [1], and occurs when the Fermi momentum is raised past the minimum in this transmission profile. For interacting bosons, this correspondence between the momentum distribution of the gas and the transmission profile is destroyed by many-body effects, and we see instead a smooth increase in the current. This results in the bosonic currents being substantially larger than those for fermions near half filling when $\Omega \sim 1$ (as was previously observed in Fig. 12.7a).

12.3.3 Kicked evolution, with initial mean momentum ($\langle \hat{k} \rangle_{t=0} \neq 0$)

In this section we consider an initial state with a non-zero initial momentum, which is obtained, e.g., by briefly tilting the lattice on a timescale much shorter than that corresponding to dynamics of atoms in the lattice. If the tilt is linear, the resulting state will be given by

$$|\phi(t=0)\rangle = \sum_j \exp(ip_k j \hat{b}_j^\dagger \hat{b}_j) |\phi_0\rangle, \quad (12.9)$$

where $|\phi_0\rangle$ is the initial many-body ground state, and the quantity p_k is determined by the magnitude and duration of the tilt. The effect of this tilt is to translate the ground state in the periodic quasimomentum space by a momentum p_k . The final mean momentum $\langle k \rangle$ then depends both on the value p_k and the properties of the initial momentum distribution.

Dependence of the current on kick strength p_k

In the case of fermions, the dependence of the current on q for different filling factors $n = N/M$ and Ω can be clearly understood in terms of the SAT transmission profile (see [11]). In Fig. 12.11a we see the current I_{ss} as a function of p_k with $\Omega = 0$. The currents are each peaked at $p_k = \pi/2$, where the resulting mean velocity of the probe atoms is the largest. For $N/M = 1$, the whole Bloch band is filled, and the momentum distribution is not changed by the application of the kick, i.e., $\langle \hat{k} \rangle_{t=0} = 0$. In Fig. 12.11b the same results are shown, but with $\Omega/J = 1$. Here we see that for small filling factors, a minimum appears at $p_k = \pi/2$, corresponding to the minimum in the transmission profile of the SAT for this incident momentum [1, 11]. At higher filling factors, this feature of the transmission profile for $\Omega/J = 1$ is not sufficiently broad to overcome the increase current due to higher mean velocities in the initial cloud, and the peak at $p_k = \pi/2$ reappears. The currents here are, of course, reduced in comparison with those for $\Omega = 0$.

Whilst for all p_k the currents with no coupling to the impurity atom, i.e., $\Omega = 0$, are the same for the Tonks gas as for fermions (Fig. 12.11a), the currents for finite interaction

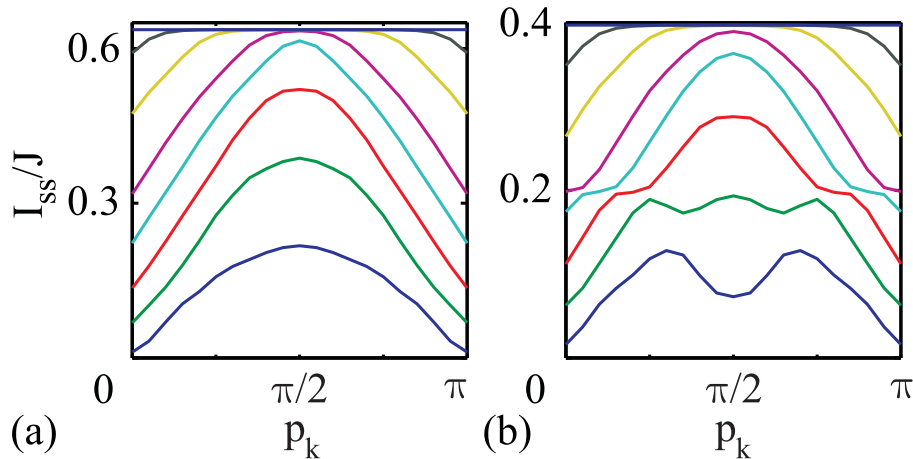


Figure 12.11. Steady state currents I_{SS} through the SAT for fermions as a function of the kick parameter p_k , for (a) $\Omega = 0$ and (b) $\Omega/J = 1$. In each plot the lines from bottom to top sequentially correspond to filling of $N = 3, 6, 9, 12, 15, 20, 25, 30$ particles initially on $M = 30$ lattice sites. Note that the scales are different for (a) and (b), and also that the results in (a) are exactly the same as those for a Tonks gas of bosons. In both cases, $\Delta = U_{qb} = U_{bm} = 0$.

strengths are found to be remarkably different. In Fig. 12.12 these rates are plotted for $U/J = 4, 7, 10$ for $N = 5, 15, 30$ particles initially situated on $M = 30$ sites. For the very dilute system with $N = 5$ (Fig. 12.12a) we see a peak similar to that observed for fermions which is independent of the interaction strength. Here the currents are essentially those for non-interacting particles, and the currents determined by the initial momentum distribution. For $N = 15$ (Fig. 12.12b) we observe the surprising result that the current is peaked at a lower value than is observed for fermions or for the Tonks gas. We have observed this peak consistently for such cases of finite interaction, and note that as U/J increases, the peak moves back towards $p_k = \pi/2$ as the currents converge to the Tonks gas results. As N is further increased, the peak continues to move left, and for $N = 30$ (Fig. 12.12c) we see a monotonically decreasing current as p_k increases. As U/J increases these values tend towards the p_k independent result observed for the Tonks gas. These results are surprising, but the trends in the behaviour are clear, and they should be directly verifiable in experiments, even without the presence of the impurity atom.

For non-zero coupling to the impurity atom, the currents as a function of p_k are shown in Fig. 12.13. Again we notice that the current for bosons with finite interaction strength is peaked at much lower values of p_k than the fermionic currents and that peaks of all of the bosonic currents, including the Tonks currents, as significantly larger than the fermionic currents at half filling, as was observed for diffusive results ($p_k = 0$). The most remarkable feature of these plots is that despite a significant reduction in the current, the basic dependence on p_k is very similar to the $\Omega = 0$ results.

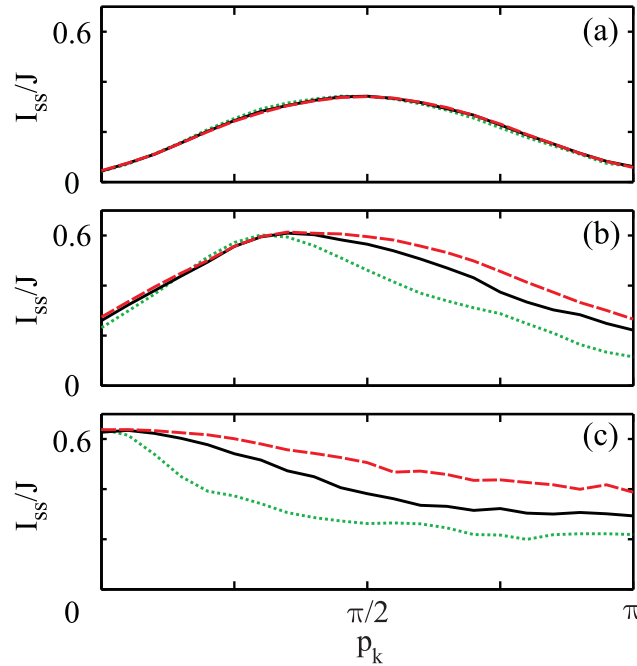


Figure 12.12. *Steady state currents with coupling to the SAT, $\Omega = 0$, I_{SS} as a function of the kick parameter p_k for varying interaction strengths, $U/J = 4$ (dotted), $U/J = 7$ (solid), and $U/J = 10$ (dashed), for (a) $N = 5$, (b) $N = 15$ and (c) $N = 30$ particles initially situated on $M = 30$ lattice sites. In all cases, $\Delta = U_{qb} = U_{bm} = 0$.*

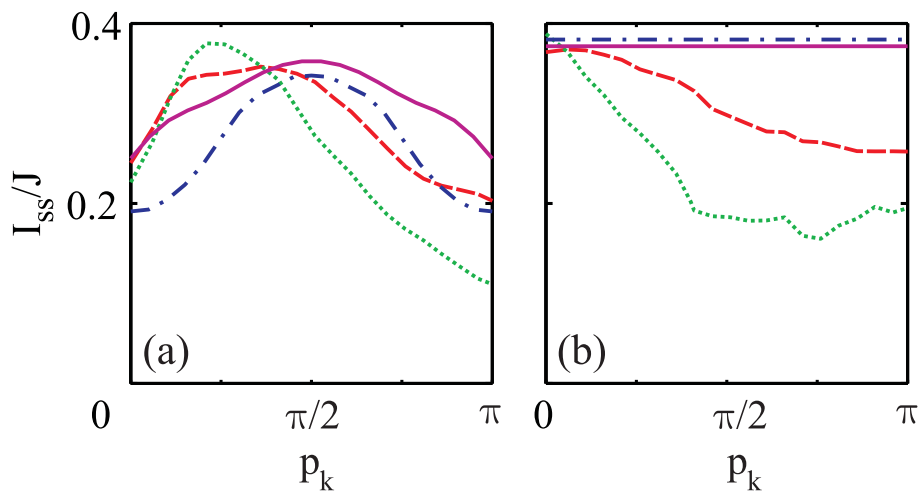


Figure 12.13. *Steady state currents through the SAT I_{SS} as a function of the kick parameter p_k , for $\Omega/J = 1$. These plots show the comparison of a Bose gas with different interaction strengths $U/J = 4$ (dotted line), $U/J = 10$ (dashed) and $U/J \rightarrow \infty$ (solid), and a Fermi gas (dash-dot), with (a) $n = 1/2$ and (b) $n = 1$. In both cases, $\Delta = U_{qb} = U_{bm} = 0$.*

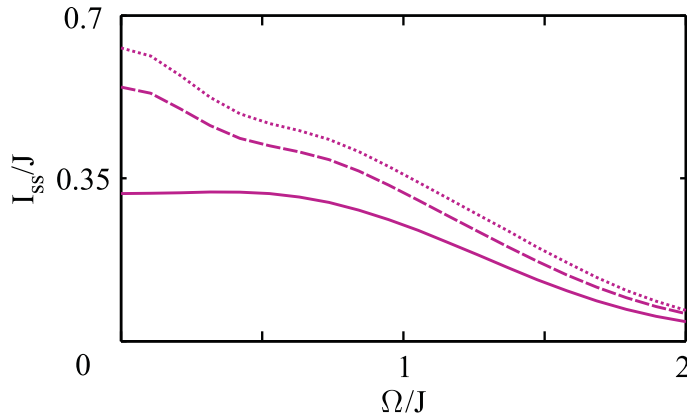


Figure 12.14. A comparison of steady state currents through the SAT, I_{ss} , as a function of Ω/J for $p_k = 0$ (solid line), $\pi/4$ (dashed), and $\pi/2$ (dotted). Here we consider a Tonks gas ($U/J \rightarrow \infty$) of bosonic probe atoms which is initially at half half-filling, $N = 15$, $M = 30$. $\Delta = U_{qb} = U_{bm} = 0$.

Dependence of the current on impurity-probe coupling, Ω

The steady state current I_{ss} is shown in Fig. 12.14 as a function of Ω . We observe the same strong decrease in the current due to the operation of the SAT for all of these curves, with the highest currents corresponding to the $p_k = \pi/2$ curve as expected. Note that the value of I_{ss} is affected equally for all of the kick strengths, and the ratio in the currents for different values of p_k is very similar for $\Omega = 0$ and $\Omega/J = 2$.

12.4 Summary

In summary, the SAT setup provides new experimental opportunities to study coherent transport of many atoms past a spin-1/2 impurity due to the relatively long coherence times that exist for systems of atoms in optical lattices. The resulting coherent many-body effects can be clearly seen in the difference between the atomic currents observed for fermions and bosons, and the non-trivial dependence of the current on interaction strength for bosons with finite interactions. Even stronger dependence on these interactions is observed when the probe atoms are initially accelerated to a non-zero momentum. The initial steady state currents would be directly accessible quantities in the experimental implementation of the SAT, and using recently developed methods for time-dependent calculation of many-body 1D systems, we have made quantitative predictions for the corresponding currents for a wide range of system parameters. We cannot be certain about the values the currents approach at long times, although it is possible that the system will settle eventually into a regime with a different steady state current. The high values of χ needed to reproduce this behaviour in our numerical calculations suggest that the currents in this regime could also be strongly sensitive to the coherence properties of the system, which would be very interesting to investigate in an experiment.

Acknowledgements

The authors would like to thank A. Micheli for advice and stimulating discussions, G. Vidal for helpful discussions on the numerical methods, and A. Kantian for his contributions to producing the number conserving version of the program code. AJD thanks the Clarendon Laboratory and DJ thanks the Institute for Quantum Optics and Quantum Information of the Austrian Academy of Sciences for hospitality during the development of this work. This work was supported by EU Networks and OLAQUI. In addition, work in Innsbruck is supported by the Austrian Science Foundation and the Institute for Quantum Information, and work in Oxford is supported by EPSRC through the QIP IRC (www.qipirc.org) (GR/S82176/01) and the project EP/C51933/1.

Bibliography

- [1] A. Micheli, A. J. Daley, D. Jaksch, and P. Zoller, *Phys. Rev. Lett.* **93**, 140408 (2004).
- [2] G. Nogues, A. Rauschenbeutel, S. Osnaghi, M. Brune, J. M. Raimond, and S. Haroche, *Nature* **400**, 239 (1999).
- [3] See, for example, G. Johansson, P. Delsing, K. Bladh, D. Gunnarsson, T. Duty, A. Käck, G. Wendin, A. Aassime, *cond-mat/0210163*.
- [4] L. S. Levitov, in *Quantum Noise in Mesoscopic Physics*, Ed. Y. V. Nazarov (Kluwer Academic Publishers, 2002).
- [5] See, for example, M. A. Cazalilla and J. B. Marston, *Phys. Rev. Lett.* **88**, 256403 (2002).
- [6] T. Stöferle, H. Moritz, C. Schori, M. Köhl, and T. Esslinger, *Phys. Rev. Lett.* **92**, 130403 (2004).
- [7] B. Paredes, A. Widera, V. Murg, O. Mandel, S. Fölling, I. Cirac, G. V. Shlyapnikov, T. W. Hänsch, and I. Bloch, *Nature* **429**, 277 (2004).
- [8] C. D. Fertig, K. M. O'Hara, J. H. Huckans, S. L. Rolston, W. D. Phillips, and J. V. Porto, *Phys. Rev. Lett.* **94**, 120403 (2005).
- [9] V. B. Braginsky and F. Y. Khalili, *Quantum Measurement*, (Cambridge University Press, UK, 1992).
- [10] G. Vidal, *Phys. Rev. Lett.* **91**, 147902 (2003); G. Vidal, *Phys. Rev. Lett.* **93**, 040502 (2004).
- [11] A. Micheli and P. Zoller, *cond-mat/0506498*.
- [12] For a review on techniques for manipulating atoms in optical lattices, see D. Jaksch and P. Zoller, *Annals of Physics* **315**, 52 (2005), and references therein.
- [13] D. Jaksch, C. Bruder, J. I. Cirac, C. W. Gardiner, and P. Zoller, *Phys. Rev. Lett.* **81**, 3108 (1998).

- [14] M. Greiner, O. Mandel, T. W. Hänsch and I. Bloch *Nature* **415**, 39 (2002); M. Greiner, O. Mandel, T. Esslinger, T.W. Hänsch and I. Bloch, *Nature*. **419** 51 (2002)
- [15] M. Köhl, H. Moritz, T. Stöferle, K. Günter, and T. Esslinger, *Phys. Rev. Lett.* **94**, 080403 (2005).
- [16] O. Mandel, M. Greiner, A. Widera, T. Rom, T. W. Hänsch, and I. Bloch, *Phys. Rev. Lett.* **91**, 010407 (2003).
- [17] E. L. Bolda, E. Tiesinga, and P. S. Julienne, *Phys. Rev. A* **66**, 013403 (2002).
- [18] E. A. Donley, N. R. Claussen, S. T. Thompson, and C. E. Wieman, *Nature* **417**, 529 (2002); T. Loftus, C. A. Regal, C. Ticknor, J. L. Bohn, and D. S. Jin, *Phys. Rev. Lett.* **88**, 173201 (2002).
- [19] M. Theis, G. Thalhammer, K. Winkler, M. Hellwig, G. Ruff, R. Grimm, J. Hecker Denschlag, *Phys. Rev. Lett.* **93**, 123001 (2004).
- [20] M. Lukin, *Rev. Mod. Phys.* **75**, 457 (2003).
- [21] See Fig. 3(a) in Ref. [1].
- [22] See, for example, S. Sachdev, *Quantum Phase Transitions*, (Cambridge University Press, UK, 1999).
- [23] M. Zwolak and G. Vidal, *Phys. Rev. Lett.* **93**, 207205 (2004).
- [24] F. Verstraete, J. J. Garcia-Ripoll, and J. I. Cirac, *Phys. Rev. Lett.* **93**, 207204 (2004).
- [25] F. Verstraete, and J. I. Cirac, cond-mat/0407066.
- [26] S. R. White, *Phys. Rev. Lett.* **69**, 2863 (1992); S. R. White, *Phys. Rev. B* **48**, 10345 (1993); U. Schollwöck, *Rev. Mod. Phys.*, **77**, 259 (2005).
- [27] A. J. Daley, C. Kollath, U. Schollwöck, G. Vidal, *J. Stat. Mech.: Theor. Exp.* P04005 (2004); S.R. White and A.E. Feiguin, *Phys. Rev. Lett.* **93**, 076401 (2004).
- [28] S.R. Clark and D. Jaksch, *Phys. Rev. A* **70**, 043612 (2004); S.R. Clark, C. Moura Alves, and D. Jaksch, *New J. Phys.* **7**, 124 (2005); C. Kollath, U. Schollwöck, and W. Zwerger, cond-mat/0504299; C. Kollath, U. Schollwöck, J. von Delft and W. Zwerger, cond-mat/0411403;
- [29] M. A. Nielsen and I. L. Chuang, *Quantum Computation and quantum communication*, (Cambridge University Press, Cambridge, 2000).
- [30] M. Suzuki, *Phys. Lett. A* **146**, 6 (1990); M. Suzuki *J. Math. Phys.* **32**, 2 (1991).

CHAPTER 13

FUTURE DIRECTIONS

The manipulation techniques for atoms in optical lattices discussed in part II of this thesis have significant potential applications to the experimental implementation of many strongly correlated systems and quantum computing schemes. The primary future direction for this work is, therefore, to see these ideas implemented in experiments. Similarly, it would be extremely interesting to see an experimental implementation of the Single Atom Transistor and the related measurements of steady state currents, as discussed in chapter 12. In addition, there are a series of clear theoretical extensions to this work, a few examples of which are outlined in this chapter.

As was already shown in chapter 6, for example, the dissipative process of creating excitations in an external reservoir gas, presented in chapter 5 has much broader applications than originally stated. This could be natural means to add controlled dissipation to systems of atoms in optical lattices, as, in contrast to other sources of decoherence such as spontaneous emission of photons, the energy scale of the phonons (or general excitations) generated is comparable to other energy scales in the system dynamics. In addition, the properties of emitted phonons and the emission rate can be controlled via the characteristics of the external reservoir gas. One potential application of such dissipation would be more general laser-assisted cooling schemes which could be used to cool the motional distribution of atoms within a particular Bloch band [1]. The spontaneous emission of phonons could also provide a controlled means to study the interplay between dissipation and coherent dynamics for atoms in optical lattices, especially the effects that dissipation may have on quantum phase transitions in these systems.

The emission of phonons also does not have to be dissipative: If the size of the external gas is comparable to the size of the lattice system and the lifetime of the excitation is engineered to be long, then the phonons could be used as an extra coherent degree of freedom. One could even imagine a system analogous to Cavity QED, but where phonons play the role of photons and the motional states of an atom confined in a lattice site play the role of electronic states in a real atom. The edge of the trap would be the equivalent of almost perfectly reflecting mirrors, and phonons could be introduced into the system by using a Raman process to excite the superfluid. Such a system could be used to study phonon-mediated entanglement between atoms.

The simulation methods discussed in part III of this thesis also have a large range of potential applications. With many extensions having been recently developed [e.g., the application of these methods to simulate master equations for dissipative systems and to study systems in two dimensions (see chapter 7)], the possibilities to perform computations on important systems is constantly growing.

The superposition of macroscopic states entangled with a spin-1/2 system that is seen in the Single Atom Transistor problem could also find additional applications. For example, it may be possible to produce a form of many-body wavefunction spectroscopy in which the inner product between two states is directly measured. Given the state

$$|\Psi(t)\rangle = |\uparrow\rangle \otimes |\psi_1(t)\rangle + |\downarrow\rangle \otimes |\psi_2(t)\rangle, \quad (13.1)$$

where $|\uparrow\rangle$ and $|\downarrow\rangle$ represent the state of the spin-1/2 atom in the z basis and $|\psi_1(t)\rangle$ and $|\psi_2(t)\rangle$ are the many-body wavefunctions, the complex inner product $\langle\psi_1(t)|\psi_2(t)\rangle$ may be determined by making measurements on the spin-1/2 atom in the x and the y basis. If the evolution of the states $|\psi_1(t)\rangle$ and $|\psi_2(t)\rangle$ can be controlled independently, this can be used to analyse the system time-dependently. For example, we could control the system evolution so that one of the states, $|\psi_1(t)\rangle$ crosses a quantum phase transition point in one direction and then the other (e.g., Mott Insulator \rightarrow superfluid \rightarrow Mott Insulator), whereas for the other many body state, $|\psi_2(t)\rangle$ remains in the same phase. The resulting overlaps measured would be of the form computed in chapter 8. This technique provides a comparison in the many-body sense of two interesting mesoscopic states, and provides the ultimate test for the return of the system to the original many-body state after crossing such a transition [2]. This would essentially constitute a step towards complete state tomography for many body wavefunctions.

Bibliography

- [1] A. Griessner et. al, work in progress.
- [2] A. J. Daley et. al, work in progress.

CURRICULUM VITAE

Andrew John Daley, July 2005

General

Current Address: Institute for Theoretical Physics
University of Innsbruck
Technikerstraße 25
A-6020 Innsbruck
Austria

Date of Birth: 24 October 1978

Citizenship: New Zealand

Languages Spoken: English (Native), German (Intermediate)

Education

2002- Studying for a PhD in Physics in Peter Zoller's group in the Institute for Theoretical Physics, University of Innsbruck.

2000-01 Master of Science with first class honours in Physics, University of Auckland. [Conferred September 2002]

1997-99 Bachelor of Science (in Physics and Mathematics), University of Auckland. [Conferred May 2000]

1992-96 Macleans College, Howick, Auckland. University Entrance via NZ University Bursary Examinations, 6 "Scholarship" grades in Physics, Chemistry, Mathematics with Statistics, Mathematics with Calculus, English and History.

1990-91 Bucklands Beach Intermediate School, Bucklands Beach, Auckland.

1983-89 Murvale Primary School, Bucklands Beach, Auckland.

Research Experience

- Sep 2002 - Present PhD Student in Peter Zoller's group at the Institute for Theoretical Physics, University of Innsbruck.
- Mar 2002 - Sep 2002 Temporary Research Assistant at the University of Auckland, studying topics in Quantum Chaos related to the Atom Optics Kicked Rotor.
- Dec 2000 - Feb 2002 MSc Thesis research at the University of Auckland, supervised by Dr. A.S. Parkins and Dr. R. Leonhardt working on topics in Quantum Chaos.
- Nov 1999 - Feb 2000 Summer Vacation Scholarship at the Australian National University (Canberra), supervised by Prof. S.J. Buckman, working in experimental Electron Physics.
- Dec 1998 - Feb 1999 Summer Research Scholarship at the University of Auckland, supervised by A-Prof. P.R. Wills, studying autonomous agents and protein folding systems.

Teaching Experience

- Oct 2003-Jan 2004 Tutor, Institute for Theoretical Physics, University of Innsbruck.
- Tutorial for Mathematical Methods in Physics 2.
- Mar 2002-Jul 2002 Limited Term Tutor, Department of Physics, University of Auckland.
- Laboratory demonstration for 2nd and 3rd year courses
 (+ marking experimental work)
- 15 Lectures on "Waves, Sound and Light" for first year "Basic Concepts in Physics" course (+ setting assignments, tests, final examination)
- 3 lectures for the second year "Electronics and Optics" course
- 1 Lecture in the second year "Physics in Action" course
 (on "Bose-Einstein Condensates")
- 2000-01 Limited Term Tutor, Department of Physics, University of Auckland.
- Laboratory demonstration for 2nd and 3rd year courses
 (+ marking experimental work)
- 1 Lecture in the second year "Physics in Action" course
 (on "Laser Cooling and its Applications")
- Tutor on a field trip for second year introductory geophysics course

Preprints

1. A. J. Daley, S. R. Clark, D. Jaksch, and P. Zoller, Numerical Analysis of Coherent Many-Body Currents in a Single Atom Transistor, quant-ph/0506256.

Publications - Articles

1. A. Griessner, A. J. Daley, D. Jaksch, and P. Zoller, Fault-Tolerant Dissipative Preparation of Atomic Quantum Registers with Fermions, accepted for publication in *Phys. Rev. A* (preprint available at [quant-ph/0502171](https://arxiv.org/abs/quant-ph/0502171)).
2. A. Micheli, A. J. Daley, D. Jaksch, and P. Zoller, A Single Atom Transistor in a 1D Optical Lattice, *Phys. Rev. Lett.* **93**, 140408 (2004) (preprint available at [quant-ph/0406020](https://arxiv.org/abs/quant-ph/0406020)).
3. A. J. Daley, C. Kollath, U. Schollwöck, and G. Vidal, Time-Dependent density-matrix renormalization-group using adaptive effective Hilbert spaces, *J. Stat. Mech.: Theor. Exp.* P04005 (2004) (preprint available at [cond-mat/0403313](https://arxiv.org/abs/cond-mat/0403313)).
4. A. J. Daley, P. O. Fedichev, and P. Zoller, Single Atom Cooling by Superfluid Immersion: A Non-Destructive Method for Qubits, *Phys. Rev. A* **69**, 022306 (2004) (preprint available at [quant-ph/0308129](https://arxiv.org/abs/quant-ph/0308129)).
5. M.E.K. Williams, M.P. Sadgrove, A.J. Daley, R.N.C. Gray, S.M. Tan, A.S. Parkins, R. Leonhardt, and N. Christensen Measurements of Diffusion Resonances for the Atom Optics Quantum Kicked Rotor, *J. Opt. B: Quantum Semiclass. Opt.* **6**, 28-33 (2004) (published online 2003, preprint available at [quant-ph/0208090](https://arxiv.org/abs/quant-ph/0208090)).
6. P. Rabl, A. J. Daley, P. O. Fedichev, J. I. Cirac, P. Zoller, Defect-Suppressed Atomic Crystals in an Optical Lattice, *Phys. Rev. Lett.* **91**, 110403 (2003) (preprint available at [cond-mat/0304026](https://arxiv.org/abs/cond-mat/0304026)).
7. A. J. Daley and A. S. Parkins, Early time diffusion for the quantum kicked rotor with narrow initial momentum distributions, *Phys. Rev. E* **66**, 056210 (2002) .
8. A. J. Daley, A. S. Parkins, R. Leonhardt and S. M. Tan, Diffusion Resonances in Action Space for an Atom Optics Kicked Rotor with Decoherence, *Phys. Rev. E* **65**, 035201(R) (2002). (preprint available at [quant-ph/0108003](https://arxiv.org/abs/quant-ph/0108003)).
9. A. J. Daley, A. Girvin, S. A. Kauffman, P. R. Wills and D. Yamins, Simulation of a Chemical "Autonomous Agent", *Z. Phys. Chem.* **216**, 41 (2002).

Publications - MSc Thesis

1. A. J. Daley, Action Space Diffusion Resonances for an Atom Optics Kicked Rotor with Decoherence and Amplitude Noise, MSc Thesis, University of Auckland (2002).

Contributions to Published Conference Proceedings

1. A. J. Daley, P. O. Fedichev, P. Rabl, P. Zoller, A. Recati, J. I. Cirac, J. Von Delft, and W. Zwerger, Spectroscopy of Strongly Correlated Cold Atoms, Proceedings of the XVI International Conference on Laser Spectroscopy, (Ed. by P. Hannaford, A. Sidorov, H. Bacher, and K. Baldwin), pp. 145-152 (World Scientific, Singapore, 2004).